Control of Power Electronic Interfaces for Photovoltaic Power Systems for Maximum Power Extraction

Polycarp Ifeanyi Muoka.

Master of Eng., in Computer Systems Engineering.

Bachelor of Eng., in Electrical Engineering.

A thesis submitted in fulfilment of the requirements for the degree of

Doctor of Philosophy

in

Electrical Engineering

University of Tasmania

Australia.

November, 2014

Declaration and Statements

Declaration of Originality

"This thesis contains no material which has been accepted for a degree or diploma by the University or any other institution, except by way of background information and duly acknowledged in the thesis, and to the best of my knowledge and belief no material previously published or written by another person except where due acknowledgement is made in the text of the thesis, nor does the thesis contain any material that infringes copyright."

Authority of Access

This thesis may be made available for loan and limited copying and communication in accordance with the Copyright Act 1968.

Statement Regarding Published Work Contained in the Thesis

"The publishers of part of the paper in chapter two hold the copyright for that content, and access to the material should be sought from the respective journals. The remaining non published content of the thesis may be made available for loan and limited copying and communication in accordance with the Copyright Act 1968."

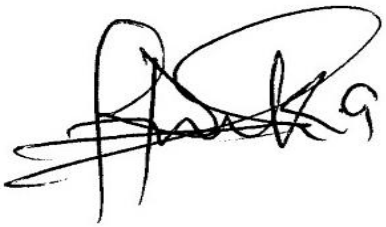

Polycarp Ifeanyi Muoka. Date: 4 November, 2014.

Acknowledgments

Firstly, my deepest gratitude goes to my creator, the Almighty God, who has kept me alive and well throughout the duration of my PhD programme.

Secondly, my sincere thanks go to my primary supervisor, Dr. Md. Enamul Haque for his invaluable contributions towards the completion of this work and for believing in me. I had an excellent working relationship with him.

Thirdly, I wish to express my thanks to the electrical workshop supervisor, Mr James Lamont, who provided immense assistance during the experimental phase of this project. My many thanks also go to all the academic staff members and postgraduate students who provided a friendly and cordial academic environment.

Finally, I express my sincere thanks to my wife, Mrs Rebecca Muoka, and to my senior sister, Mrs Elizabeth Tagbo, who always provided the necessary encouragement.

Abstract

As photovoltaic power plants provide an ever-increasing share of the world's electricity and assist in the mitigation of environmental degradation, engineers need to consider new challenges associated with the integration of this variable and intermittent source of energy into the grid. The associated challenges can only be solved by deploying appropriate technologies. This thesis proposes some technological solutions by developing control algorithms for power electronic interfaces involved in photovoltaic (PV) energy conversion. The overall objective is to develop control algorithms and the associated power converter topologies so as to efficiently harvest solar energy with minimal losses and at minimal cost, while providing the much-needed system reliability. The thesis details the analyses and modelling of photovoltaic subsystems, their simulation studies, the control approaches adopted, and the application of maximum power point tracking technique to extract maximum power from the photovoltaic system.

This thesis starts out with the development of a workable PV simulation model that considers the effects of environmental variables on system's performance for deeper understanding of PV characteristics and for accurate prediction of the PV system's behaviour in deployment. Also, introduced in the same chapter is a novel optimisation tool for the design of standalone PV power plants. To convert the "raw energy" from sunlight into usable regulated dc energy, the thesis proposes using a SEPIC (single ended primary inductance converter) dc-dc converter for the interfacing function. An in depth analysis and design of an 800W-capacity SEPIC converter is introduced and deployed for both simulation and experimental studies. Also developed for the SEPIC converter is a robust control system that is able to regulate the dc link voltage to the desired value, irrespective of changes in input voltage or system loading.

The thesis, also, proposes an improved maximum power point tracking (MPPT) algorithm derived from the incremental conductance MPPT technique. This ensures the efficient operation of the PV power plant by rapidly and accurately tracking the maximum power point (MPP) of the PV array regardless of changes in environmental conditions. In addition, in chapter 5, to ensure the reliability and availability of the PV power plant, the thesis proposes a control system for the bidirectional dc-dc converter that interfaces the energy storage system. The control system offers the desired management of the energy storage system by

ensuring proper charging and discharging, protection, and power balance between the PV subsystems. A 500W capacity of the converter is analysed, designed and later constructed in the laboratory.

To convert the generated dc energy into useful ac power, the thesis develops models and control strategies for the dc-ac converter (inverter) to ensure that sinusoidal waveform of the desired voltage magnitude and frequency is generated. Control strategies for three-phase operation in standalone and grid connected modes are also introduced.

The developed control algorithms and designed converters are subjected to rigorous simulation studies using MATLAB/Simulink/SimPowerSystems software. Such simulation studies provide useful insight into the PV system's behaviour when deployed in operation. However, simulation results without experimental backup offers limited practical value. Consequently, the thesis presents the hardware implementation of the entire PV power plant. It discusses the building of the power converter prototypes, the printed circuit boards (PCBs) for data acquisition, conditioning, isolation and gate-driving. The real time control of the plant using a digital signal processor platform is discussed in detail and the experimental results presented for the validation of the simulation results.

The main contributions of this thesis include: 1) the development of a workable photovoltaic power system simulation model for characterisation studies; 2) development of a software tool for the design of standalone PV plants; 3) development of an improved algorithm for maximum power point tracking; 4) development of an improved current mode based algorithm for control of the energy storage interface converter; 5) development of models for standalone and grid connected PV systems with the associated controls; and 6) experimental implementation of an effective, versatile, low-cost, low-component-count, data acquisition and conditioning system for a PV systems using dSPACE DS1104 DSP system.

Table of Contents

Declaration of Originality ii

Acknowledgements iii

Abstract iv

Table of Contents vi

List of Figures xii

List of Tables xvii

List of Symbols xviii

List of Abbreviations xix

Thesis Related Publications xx

Chapter 1 Introduction 1

1.1 General Overview 1

1.2 The Photovoltaic Process 3

1.3 Photovoltaic Power Systems: Classifications and Applications 4

1.3.1 Classifications of PV Power Systems 4

1.3.2 Applications of PV Power Systems 5

1.4 Problem Statement and Research Motivations 6

1.5 Objectives and Contributions of the Thesis 8

1.6 Thesis Organisation 9

Chapter 2 PV Modelling and Development of a New Optimisation Tool for Off-Grid PV Power Plant Design 11

2.1 Introduction 11

2.2 Review of PV Cell Technologies 11

2.2.1 Mono-crystalline Silicon Cells 12

2.2.2 Multi-crystalline or Polycrystalline Silicon Cells 12

2.2.3 Silicon-based Thin-film Technologies 13

2.2.4 Non-silicon Based Thin-film Technologies 13

2.2.5 Comparisons of Different PV Cell Technologies 13

2.3 Review of Analytical Model of the Solar Cell 15

2.3.1 Analysis of the Single Diode Model (SDM) 15

2.3.2 Module/Array Modelling 16
2.3.3 Dual Diode Model (DDM) 17
2.4 Proposed Simulation Model Development for Characterisation Studies 18
2.4.1 Model Implementation via Simulink Software 18
2.4.2 Simulation Results and Discussions 22
2.4.2.1 Effects of Irradiation Changes 22
2.4.2.2 Effects of Temperature Changes 22
2.5 A New Optimisation Tool for Off-grid PV Power Plant Design 24
2.5.1 System's Features 25
2.5.2 System's Description and Architecture 25
2.6 Development of Sub Models 28
2.6.1 Load Assessment Sub Model 28
2.6.2 PV Array Sizing Sub Model 29
2.6.3 Battery Bank Sizing Sub Model 30
2.6.4 Inverter 32
2.6.5 Charge Controller 33
2.7 Case Study and Simulation Results 33
2.7.1 Case Study 33
2.7.2 Simulation Results and Discussions 34
2.8 Conclusions 36

Chapter 3 Analysis, Design and Control of SEPIC DC-DC Converter for Photovoltaic Energy Harvesting 38

3.1 Introduction 38
3.2 Review of the Operation and Analysis of the SEPIC Converter 39
3.2.1 Features of the SEPIC Converter 39
3.2.2 Operation of the SEPIC Converter 40
3.2.3 DC Analysis of the SEPIC Converter 41
3.2.3.1 Derivation of Input/Output Voltage Relationship 41
3.2.3.2 Determination of Minimum inductance for Continuous Conduction 43
3.2.3.3 Output Voltage Ripple of the SEPIC Converter 44
3.3 Small Signal Model of the SEPIC Converter 44

3.4 Design of the Proposed 800W SEPIC Converter for the PV System 46
3.4.1 Power Components Sizing 46
3.5 The Proposed Closed-loop Control 51
3.5.1 Proportional-plus-Integral(PI) Controller Design 53
3.6 Simulation Studies of the SEPIC Converter Based PV System 54
3.6.1 Development of Dynamic Models for Simulation 54
3.7 Simulation Results and Discussions 56
3.7.1 Effects of Duty Cycle Variations on Open-loop Operation 56
3.7.2 Output Voltage Regulation 56
3.7.3 Robustness Analysis: Input Voltage Fluctuations 57
3.8 Conclusions 58
Chapter 4 Maximum Power Point Tracking of Photovoltaic Modules and Closed Loop Control Techniques for DC-DC Power Converters 59
4.1 Introduction 59
4.2 Review of MPPT Techniques 61
4.2.1 Perturb-and-Observe (P&O) Technique 61
4.2.2 Improved Versions of the P&O Technique 63
4.2.3 Incremental Conductance Technique 63
4.2.4 Ripple Correlation Control (RCC) Technique 65
4.2.5 Fuzzy Logic Technique 67
4.2.6 Fractional Open-Circuit Voltage Based MPPT 68
4.3 Review of Closed Loop Control Techniques for PV Converters 69
4.3.1 Voltage Mode Control 69
4.3.2 Current Mode Control Technique 70
4.3.2.1 Peak Current Control 70
4.3.2.2 Average Current Control 72
4.3.2.3 Hysteresis Current Control 73
4.4 Proposed Multi-loop System for MPPT and Current Mode Control 74
4.4.1 Development of an Improved Incremental Conductance MPPT with Variable Step-size Perturbation 74
4.4.2 Multi-loop System for MPPT and Current Mode Control 75
4.5 Simulation Model 76
4.6 Simulation Results and Discussions 78
4.6.1 Effect of Irradiance Changes 78

4.6.2 Effect of Ambient Temperature Changes 79
4.7 Conclusions 80
Chapter 5 Interfacing Energy Storage to PV Systems: Design of Converter and Control Systems. 81
5.1 Introduction 81
5.2 Review of Technologies for PV Energy Storage 82
5.2.1 Benefits of Integrating Energy Storage in PV Systems 82
5.3 PV Storage Technologies 83
5.3.1 Battery Energy Storage System (BESS) 83
5.3.2 Lithium Ion (Li-ion) Batteries 84
5.3.3 Sodium Sulfur (NaS) Batteries 85
5.3.4 Flow Battery Technologies 86
5.3.5 Ultracapacitors 88
5.3.6 Flywheel Energy Storage System (FESS) 88
5.3.7 Compressed Air Energy Storage System (CAES) 89
5.3.8 Pumped Hydro Storage 89
5.3.9 Hydrogen/Fuel Cell 89
5.3.10 Superconductive Magnetic Energy Storage 90
5.4 Power Electronics Interface for PV Energy Storage 90
5.4.1 Bidirectional DC-DC Converter Topology Selection and Analysis 91
5.4.2 Analysis of the Bidirectional DC-DC Converter 91
5.4.3 Design of a 500W Bidirectional DC-DC Converter 93
5.5 Proposed Multi-objective Control System for Battery Charging & Power Management 96
5.5.1 Multi-stage Algorithm for SLA Battery Charging 97
5.5.2 Power Management Technique 99
5.5.3 Controller Implementation 100
5.6 Simulation Model 102
5.7 Simulation Results and Discussions 104
5.8 Conclusions 109
Chapter 6 Control of Photovoltaic Inverter for Voltage and Frequency Regulation 110

6.1 Introduction 110
6.2 Review of Inverter Utilisation Topologies for PV Systems 111
6.3 Review of Inverter Schematic Topologies for PV Systems 114
6.3.1 Transformerless Topologies 116
6.3.1.1 H5 Inverter Topology 116
6.3.1.2 HERIC Inverter Topology 117
6.3.1.3 Other Transformerless Topologies 119
6.4 Review of Modulation Strategies for DC-AC Conversion 119
6.4.1 Bipolar (BP) Switching Scheme 119
6.4.2 Unipolar (UP) Switching Scheme 121
6.4.3 Hybrid Switching Scheme 122
6.5 Control of Three-phase Photovoltaic Power Plants 123
6.5.1 Grid Connected Mode 123
6.5.2 Standalone Mode 126
6.6 Review of Standards for Interfacing the DC-AC Converter 127
6.7 Proposed Control System for the PV Inverter 128
6.8 Simulation Model 130
6.9 Simulation Results and Discussions 132
6.9.1 Single-phase PV System 132
6.9.2 Three-phase Standalone PV System 134
6.10 Conclusions 135
Chapter 7 Hardware Implementation and Experimental Analysis of the PV System 137
7.1 Introduction 137
7.2 Data Acquisition and Conditioning 138
7.2.1 DS1104 R&D Controller Board Description 139
7.2.2 Real Time Implementation of the Complete PV System 140
7.3 Hardware Implementation 141
7.3.1 Voltage/Current Sensing & Conditioning 141
7.3.2 Isolation and Gate Drive Interface 143
7.3.3 Printed Circuit Board Design and Construction 144
7.3.4 Construction of the Power Converters 149
7.4 System Integration and Experimental Setup 152
7.4.1 Graphical User Interface Development in

ControlDesk Software 152
7.4.2 Installation of Solar Panels 153
7.4.3 Experimental Setup 154
7.5 Experimental Results and Discussions 155
7.5.1 Generation of Switching Pulses 155
7.5.2 Effects of Changing Ambient Temperature 156
7.5.3 Operation of the Bidirectional Converter 158
7.6 Conclusions 159
Chapter 8 Summary and Suggestions for Future Research 160
8.1 Summary 160
8.2 Contributions to Engineering Knowledge 163
8.3 Suggestions for Future Research 164

List of Figures

Fig. 1.1	Global annual PV installations from 2000 to 2013	3
Fig. 1.2	Classifications of PV power systems	5
Fig. 1.3	Block diagram of a decentralized PV system	5
Fig. 1.4	Block diagram of the PV system being studied	9
Fig. 2.1	Classifications of PV cell technologies	12
Fig. 2.2	Single diode model of a solar cell	16
Fig. 2.3	Functional relationship of PV cells, modules and arrays	17
Fig. 2.4	Dual-diode model of a solar cell	18
Fig. 2.5	Block diagram of the PV module simulation model using Simulink software	19
Fig. 2.6	Simulation model showing the major subsystems	19
Fig. 2.7	Details of the reverse saturation current subsystem	20
Fig. 2.8	Details of the saturation current subsystem	20
Fig. 2.9	Details of the photocurrent subsystem	21
Fig. 2.10	Mask dialogue box for the developed model showing some parameters of the PV module: BP 380 used for the study	21
Fig. 2.11	Influence of irradiation changes on module current and voltage output at constant temperature	23
Fig. 2.12	Influence of irradiation changes on the PV module power and voltage at constant temperature	23
Fig. 2.13	Variation of I-V characteristics with changes in temperature at constant irradiation	23
Fig. 2.14.	Variation of module power with changes in ambient temperature at constant irradiation	24
Fig. 2.15	Major subsystems of an off-grid PV power plant	26
Fig. 2.16	Simulation model showing the sub models in Simulink	27
Fig. 2.17	Simplified flowchart for the sizing tool	27
Fig. 2.18	Developed user interface in Simulink for sizing the battery bank sub model	32
Fig. 3.1	Schematic circuit of the SEPIC converter	40
Fig. 3.2	Mode 1: Power switch turned *ON*, diode turned *OFF*	41

Fig. 3.3	Mode 2: Power Switch turned *OFF*, diode turned *ON*	41
Fig. 3.4	Block diagram of the single-loop control for the SEPIC converter: (a) SEPIC converter with feedback loop; (b) functional block diagram of the feedback system	52
Fig. 3.5	Block diagram representation of the digital PI controller	53
Fig. 3.6	Simulation model for open loop operation: SEPIC converter with integrated two-panel PV array in Simulink/SimPowerSystems software	55
Fig. 3.7	Simulation model for closed-loop operation	55
Fig. 3.8	Variation of output voltage with duty cycle for open loop operation	56
Fig. 3.9	Regulated output voltage of the SEPIC converter	57
Fig. 3.10	Regulated output voltage for rapid drop in the ambient temperature	58
Fig. 4.1	The I-V curve of a PV module showing the maximum power point at 0.8 sun (800W/m^2)	60
Fig. 4.2	The P-V curve of a PV module showing the maximum power point at 0.8 sun (800W/m^2)	60
Fig. 4.3	Illustration of the P&O MPPT technique	62
Fig. 4.4	Flowchart of conventional P&O algorithm	63
Fig. 4.5	P-V curve of a PV array showing the three regions of the ICT search algorithm	65
Fig. 4.6	Flowchart of Incremental Conductance Algorithm	65
Fig. 4.7	Implementation of RCC-based MPPT technique	67
Fig. 4.8	Main components of a fuzzy logic controller	68
Fig. 4.9	Fuzzy logic controller-based MPPT implementation for a PV power plant	68
Fig. 4.10	Peak-current-controlled SEPIC converter. (a) Circuit. (b) CCM operation waveforms	71
Fig. 4.11	Principle of operation of the average current control mode	72
Fig. 4.12	SEPIC converter with hysteresis current control method	73
Fig. 4.13	Flowchart of the proposed variable step size incremental conductance MPPT technique	75
Fig. 4.14	Block diagram of the multi-loop system for MPPT and current mode control	76
Fig. 4.15	Simulation model of the PV system with MPPT and current mode control in Simulink	77

Fig. 4.16	Irradiation variation and maximum power point tracking @ 25^{o}C	78
Fig. 4.17	Ambient temperature variation and MPPT performance	79
Fig. 4.18	Temperature variation, MPP and regulated output voltage of the converter	80
Fig. 5.1	The operating principles of lithium-ion battery	84
Fig. 5.2	Operation of sodium sulfur cell	86
Fig. 5.3	Operating principles of ZnBr flow battery	88
Fig. 5.4	Half-bridge-based bidirectional buck-boost dc-dc converter	91
Fig. 5.5	Modes of operation of the bidirectional dc-dc converter	92
Fig. 5.6	Three-stage charging algorithm	99
Fig. 5.7	Power flow diagram of the system showing the converters and energy sources: PV array and battery energy storage.	100
Fig. 5.8	Controller configuration for battery charging	101
Fig. 5.9	Controller configuration for battery discharging	102
Fig. 5.10	Simulation model in Simulink/SimPowerSystems software	104
Fig. 5.11	Battery bank's voltage and dc link voltage during charging	105
Fig. 5.12	Battery current and inductor current during charging	106
Fig. 5.13	Battery power and state of charge after charging	106
Fig. 5.14	Battery bank's voltage and dc link voltage after discharge	108
Fig. 5.15	Battery current and inductor current during discharge	108
Fig. 5.16	Battery power and SOC after a discharge event	109
Fig. 6.1	Centralized inverter system topology	113
Fig. 6.2	String inverters topology	113
Fig. 6.3	Multistring inverters topology	113
Fig. 6.4	Module integrated inverter topology	114
Fig. 6.5	Basic H-bridge or full-bridge inverter with integrated PV array	115
Fig. 6.6	A diode-clamped multilevel inverter topology	116
Fig. 6.7	H5 inverter topology with integrated PV array	117
Fig. 6.8	HERIC Inverter Topology	118
Fig. 6.9	Bipolar PWM switching scheme	120
Fig. 6.10	Full-bridge topology with bipolar switching scheme	121
Fig. 6.11	Vector control scheme for a three-phase grid connected PV power plant	125
Fig. 6.12	Vector control scheme for a three-phase standalone PV power plant	127

Fig. 6.13	Block diagram of the proposed control system for the single-phase inverter	130
Fig. 6.14	Block diagram of the power circuit of the complete PV plant being modelled	131
Fig. 6.15	Simplified simulation model in Simulink showing the subsystems and the controls	131
Fig. 6.16	Line frequency of the system during the switching operation	132
Fig. 6.17	Load voltages and currents during the switching operation	133
Fig. 6.18	Load power flow during the switching operation	133
Fig. 6.19	Load frequency during three-phase operation	134
Fig. 6.20	Load current changes during switching operation	134
Fig. 6.21	Load power changes during the three-phase switching operation	135
Fig. 6.22	Screenshot of the instantaneous load current and voltage	135
Fig. 7.1	Block diagram of the signal acquisition and conditioning process used for the PV system	139
Fig. 7.2	System block diagram showing some analogue signals (green lines) to be measured and used for control purposes	140
Fig. 7.3	Hall-effect voltage sensor circuitry using LV 25P	142
Fig. 7.4	Schematic diagram of 1-channel of the voltage sensing and conditioning circuitry based on LV 25P and INA 118	142
Fig. 7.5	Schematic diagram of 1-channel of the current sensing and conditioning circuitry based on LV 25P and INA 118	142
Fig. 7.6	Opto-coupler circuitry used for isolation of the IGBT switching signals	143
Fig. 7.7	Block diagram of signal flow for one channel of the printed circuit board	145
Fig. 7.8	Schematic diagram in Altium Designer software of the four-channel sensor board for the SEPIC converter	145
Fig. 7.9	Layout drawing in Altium Designer software showing the four-channel PCB for the SEPIC converter	146
Fig. 7.10	Schematic diagram in Altium Designer of the sensor board for the bidirectional dc-dc converter	146
Fig. 7.11	Layout drawing in Altium Designer software showing the four-channel PCB for the bidirectional dc-dc converter	147

Fig. 7.12	Schematic diagram in Altium Designer of the sensor board for the inverter	147
Fig. 7.13	PCB layout drawing in Altium Designer of the sensor board for the inverter	148
Fig. 7.14	The finished PCBs for the three converters	148
Fig. 7.15	Prototype of the SEPIC converter in perspex housing	150
Fig. 7.16	Prototype of the inverter board in perspex housing	151
Fig. 7.17	Prototype of the bidirectional dc-dc converter	151
Fig. 7.18	Experimental setup for the PV system	155
Fig. 7.19	SEPIC converter gating signals	156
Fig. 7.20	Inverter gating signals	156
Fig. 7.21	Effects of changing ambient temperature on system performance	157
Fig. 7.22	Output of the bidirectional dc-dc converter	158
Fig. 7.23	Battery bank terminal voltage during charging	159

List of Tables

Table 1.1	PV global cumulative installed capacities as at 2011	2
Table 2.1	Comparisons of silicon based cell technologies	14
Table 2.2	Comparisons of silicon and non-silicon based thin-film technologies	14
Table 2.3	Electrical loads for a Perth household	35
Table 2.4	Input design parameters	35
Table 2.5	Simulation results - sizing parameters	36
Table 4.1	Electrical parameters of BP 380 solar module @ STC	77
Table 5.1	Comparisons of BESS Technologies	87
Table 5.2	Bidirectional dc-dc converter specifications	93
Table 5.3	Controller parameters defined	102
Table 6.1	Switching sequence for the H-bridge topology	115
Table 6.2	Switching states for H5 inverter topology	117
Table 6.3	Switching states for HERIC inverter topology	118
Table 6.4	Switching states using unipolar switching scheme	122
Table 6.5	Advantages, disadvantages and limitations of some modulation schemes	123
Table 7.1	Major components used for the power converters	152

List of Symbols

A	Diode Ideality factor
E_B	Band gap energy
G	Solar insolation
I_L	Output current of solar cell model
I_D	Shockley diode current
I_{MPP}	Current at maximum power point
1_{PH}	Photo current
I_{pv}	Photovoltaic current
I_{sat}	Saturation current of diode in equivalent circuit
I_{SC}	Short-circuit current of solar cell
K_B	Boltzman constant
P	Power (W)
P_{MAX}	Maximum power
q	Electron charge
T_C	Cell working temperature
V_d	Diode voltage in solar model
V_{MPP}	Voltage at maximum power point
V_{OC}	Open circuit voltage
V_{PV}	Photovoltaic voltage
W_P	Peak watts
ΔP	Incremental change of photovoltaic power
ΔV	Incremental change of photovoltaic voltage
ΔI	Incremental change of photovoltaic current

List of Abbreviations

AC	Alternating Current
ADC	Analogue to Digital Converter
BESS	Battery Energy Storage System
CAES	Compressed Air Energy Storage
CIS	Copper Indium Diselenide
DAC	Digital to Analogue Converter
DC	Direct Current
DSP	Digital Signal Processor
GUI	Graphical User Interface
HERIC	Highly Efficient and Reliable Inverter Concept
IEEE	Institute of Electrical and Electronics Engineers
ICT	Incremental Conductance Technique
IGBT	Insulated Gate Bipolar Transistor
I-V	Photovoltaic Current versus Voltage
NaS	Sodium Sulfur
MPP	Maximum Power Point
MPPT	Maximum Power Point Tracking
PCB	Printed Circuit Board
PI	Proportional-Integral
P & O	Perturb and Observe
PLL	Phase Locked Loop
PV	Photovoltaic
P-V	Photovoltaic Power versus Voltage
PVPS	Photovoltaic Power Systems
PWM	Pulse Width Modulation
RCC	Ripple Correlation Control
SDM	Single Diode Model
SEPIC	Single Ended Primary Inductance Converter
STC	Standard Test Conditions
UPS	Uninterruptible Power Supply
VRLA	Valve Regulated Lead Acid

Thesis Related Publications

Journals:

- P. I. Muoka, M. E. Haque, A. Gargoom, and M. Negnevitsky, "DSP Based Hands-on Laboratory Experiments for Photovoltaic Power Systems," *IEEE Transactions on Education*. (In press).

- P. I. Muoka, M. E. Haque, and A. Gargoom, "A DSP Controlled Smart Battery Charger for Photovoltaic Power Systems," *Australian Journal of Electrical & Electronics Engineering*. (In press).

- P. I. Muoka, M. E. Haque, and A. Gargoom, "An Optimization Tool for Designing, Costing and Economic Analysis of off-grid Photovoltaic Power Plants," *International Journal of Renewable Energy Technology (IJRET)*. (Under Review).

- "Control of a PV System in Standalone and Grid Connected Modes". (Under development).

Conference Publications:

- P. I. Muoka, M. E. Haque, A. Gargoom, and M. Negnevitsky, "Modeling and Experimental Validation of a DSP Controlled Photovoltaic Power System with Battery Energy Storage, *IEEE Power & Energy Society Annual General Meeting*, Vancouver, BC, Canada, July 21-25, 2013.

- P.I. Muoka, M. E. Haque, A. Gargoom, and M. Negnevitsky, "Modelling, Simulation and Hardware Implementation of a PV Power Plant in a Distributed Energy Generation System," *IEEE Power & Energy Society Innovative Smart Grid Technologies Conference*, Washington, D.C., USA, Feb. 24-27, 2013.

- P.I. Muoka, M. E. Haque, A. Gargoom, and M. Negnevitsky, "Modelling and Simulation of a SEPIC Converter based Photovoltaic System with Battery Energy Storage," *Australasian Universities Power Engineering Conference (AUPEC)*, Bali, Indonesia, Sept. 26 – 29, 2012.

- M. M. Chowdhury, M. E. Haque, A. Gargoom, M. Negnevitsky, and P.I. Muoka, "Enhanced Control of a Direct Drive Grid Connected Wind Energy System with STATCOM," *Australasian Universities Power Engineering Conference (AUPEC)*, Bali, Indonesia, Sept. 26 – 29, 2012.

- S. Lyden, M. E. Haque, A. Gargoom, M. Negnevitsky, and P. I. Muoka, "Modelling and Parameter Estimation of Photovoltaic Cell," *Australasian Universities Power Engineering Conference (AUPEC)*, Bali, Indonesia, Sept. 26 – 29, 2012.

- D. Das, M. M. Chowdhury, M.E. Haque, A. Gargoom, P.I. Muoka, and M. Negnevitsky, "Operation and Control of Grid Integrated Hybrid Wind-Fuel Cell System with STATCOM," *Australasian Universities Power Engineering Conference (AUPEC)*, Bali, Indonesia, Sept. 26 – 29, 2012.

- P.I. Muoka, M.E. Haque, and M. Negnevitsky, "A New Tool for Design Optimization and Cost Estimation of Stand-alone Photovoltaic Power Plants," *IEEE Power & Energy Society Annual General Meeting*, Detroit, Michigan, USA, July 24-29, 2011.

Chapter 1
Introduction

1.1 General Overview

As the world's population increases, the demand for energy usage also increases proportionally. Meeting this energy requirement using fossil fuels (oil, natural gas and coal) based technologies has environmental and socioeconomic consequences. Environmental concerns range from environmental pollution and degradation to global warming and the attendant climate change, while the socioeconomic implications involve the depletion of scarce non-renewable resources and, even wars between nations in the quest for these resources [1-3]. To mitigate these problems, it is necessary for humanity to resort to the use of sources of energy that are non-polluting, renewable and sustainable. The sun, the earth's primary source of energy, provides us such valuable resource either in the form of solar thermal energy or in the form of photovoltaic (direct conversion of sunlight to electric energy) energy, which is the focus of this thesis [4], [5].

There is a worldwide boom in the deployment of both large-scale and small roof-mounted solar photovoltaic (PV) power systems. This has resulted in photovoltaics becoming an indispensable part of the energy mix of many countries. Even with reduced or no government subsidization, demand is growing in many parts of the world to the extent that photovoltaics is increasingly becoming the first choice for building new peak load power plants in countries like Canada, China, Thailand and India [6]. Globally, the installed capacity in 2011 was 29,665MW bringing the cumulative global installed capacity to 69,684MW as at the end of 2011 [7]. Table 1.1 shows the distribution of this installed capacity and cumulative capacity among countries of the world, while Figure 1.1 shows the global annual PV installations from the year 2000 to an expected increase to about 35GW in year 2013 [7-9]. This rapid and impressive development is driven by the following factors [1-3], [7-10]:

- The need by many national governments for long term energy security, diversification of their energy portfolio, as well as ecological security.
- Introduction of incentives like feed-in-tariff (FiT), and investment tax credits in many countries.

- Replacement of shuttered nuclear power plants with renewables, especially for Japanese market after the March 2011 Fukushima nuclear disaster.
- More and more people striving for sustainability living for the mitigation of global warning and energy independence from utility companies.
- The falling prices of PV modules and balance of systems (BOS) – as at the end of 2012 the spot market price for Chinese made crystalline silicon (c-Si) modules fell to USD 0.74/W_P and consequently solar electricity production costs have fallen below 10c/KWh in sunny places like California and Arizona in USA.
- Attainment of the long-awaited cost-competitiveness with fossil-fuel electricity in some European countries.
- Inevitable increase in petroleum prices and depleting hydrocarbon reserves worldwide.
- General increase in energy bill worldwide occasioned by increased fuel costs of conventional power plants.

Table 1.1: PV global cumulative installed capacities as at 2011 [7].

Country	Installed Capacity (MW)	Cumulative Capacity (MW)	Share of Global Cumulative Capacity (%)
Germany	7,485	24,678	36
Italy	9,284	12,754	18
Japan	1,296	4,914	7
Spain	372	4,400	6
USA	1,855	4,384	6
China	2,200	3093	4
France	1,671	2,659	4
Belgium	974	2,018	3
Czech Republic	6	1,959	3
Australia	774	1,298	2
Rest of the world	807	7,529	11

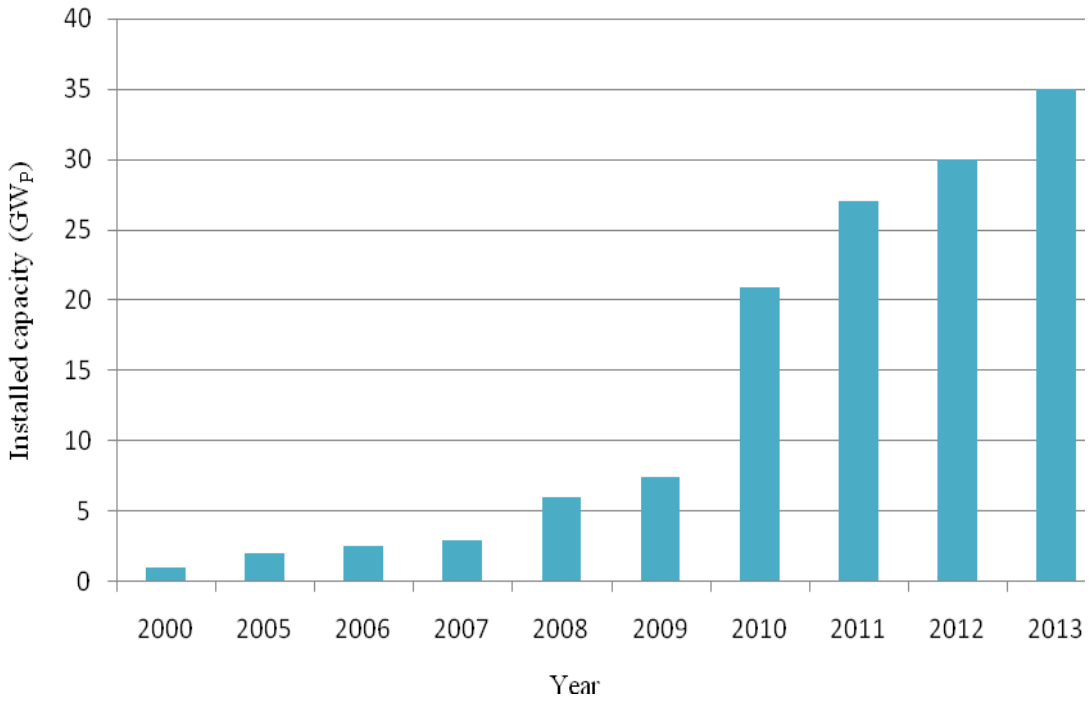

Fig.1.1: Global annual PV installations from 2000 to 2013 [8].

1.2 The Photovoltaic Process

Photovoltaic (PV) technology is based on the photovoltaic effect (the development of electrical potential between two dissimilar materials when their common junction is exposed to sunlight) to convert solar radiation into direct current (dc) electricity. When incoming light energy (photons) are absorbed by a semiconductor crystal, electron-hole pairs are released from their bonding state [1], [4].

The basic components of a solar cell are the n-type layer and a p-type layer of a semiconductor crystal. The n-type layer can emit electrons while the p-type layer can absorb electrons. At the interface of the two layers (the p-n junction) an electric field is formed. This electric field then separates the photon-generated charge carriers (the electron-hole pairs) when they are prevented from recombining. Thus, the electric field produces a proportional voltage at the terminals of the solar cell [1], [4]. Direct current is then able to flow when these contacts are connected.

For practical use, the solar cells are packaged into modules by connecting them in series so as to deliver a useful higher voltage.

1.3 Photovoltaic Power Systems: Classifications and Applications

1.3.1 Classification of PV Power Systems

Generally, photovoltaic power systems are broadly classified as shown in Fig. 1.2. The stand-alone or off-grid systems do not have a connection to the public electricity grid [11]. The simplest of such systems consist of a PV module and a dc load such as a water pump. However, in situations where a 24-hour supply of electricity is required, the system is combined with an energy storage system – often a deep cycle battery system. Stand-alone systems can be either dc systems or ac systems with an inverter, or combination of dc and ac systems [11], [12].These days, on-site production of solar power in the MW (mega-watts) range by energy-intensive companies to meet their energy needs exist [8-9].

The hybrid system integrates an auxiliary power supply as a backup or complement for the PV power system. The auxiliary supply may be a fossil-fuelled generator or another renewable energy source (example, wind, hydropower, biomass or fuel cell) [13-15]. The hybrid system is often used in situations where the security of supply is very critical.

The grid-connected PV systems have a connection to the public electricity grid. The two main components of such systems are the PV modules (the array), and the dc-ac converter (the inverter). The two classifications of grid-connected systems are [1], [4]:

- Decentralized grid-connected PV (DGCPV) systems: these often have smaller power ranges and mostly installed in rooftops or integrated into building facades. Energy storage is not really necessary for these systems. Excess energy is supplied to the grid during sunny days and is drawn from the grid during night times or periods of low insolation. Figure 1.3 is an illustration of a typical decentralized grid-connected PV system.
- Centralized grid-connected PV (CGCPV) systems: These have power capacities up to the MW range and so they are often fed directly into the medium or high voltage grid. The outputs of these large-scale PV power plants are fast achieving scales equal to those of conventional coal-fired power plants as exemplified by the installation of a 290MW solar park connected to the grid in Arizona, USA, in 2012 and a 579MW capacity solar power plant which is expected to come upstream by 2015.

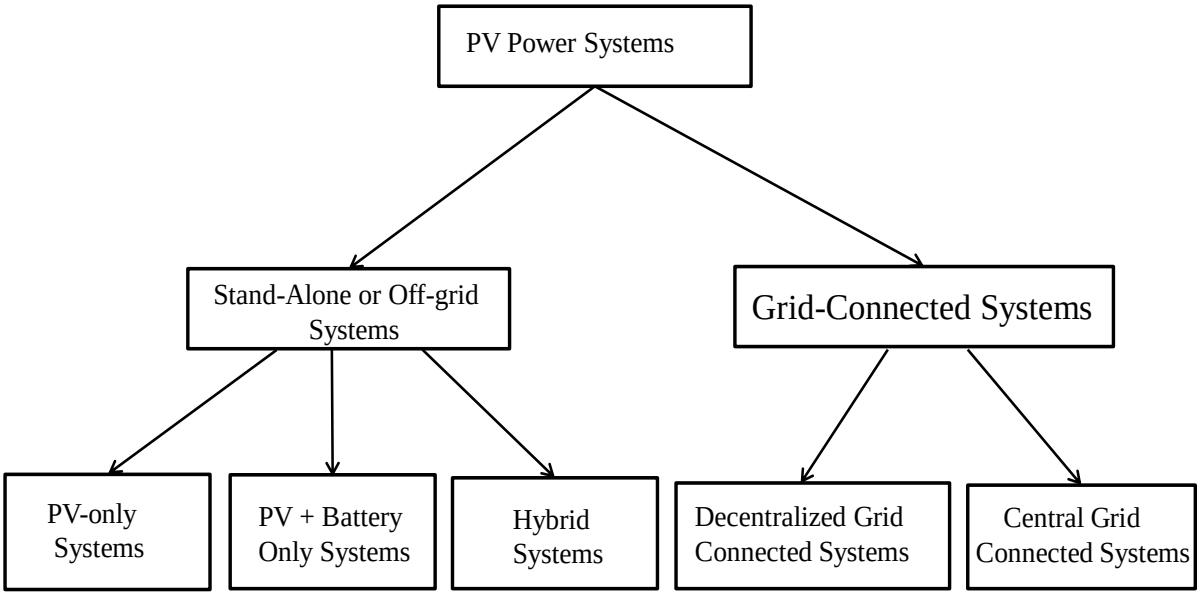

Fig. 1.2: Classifications of PV power systems.

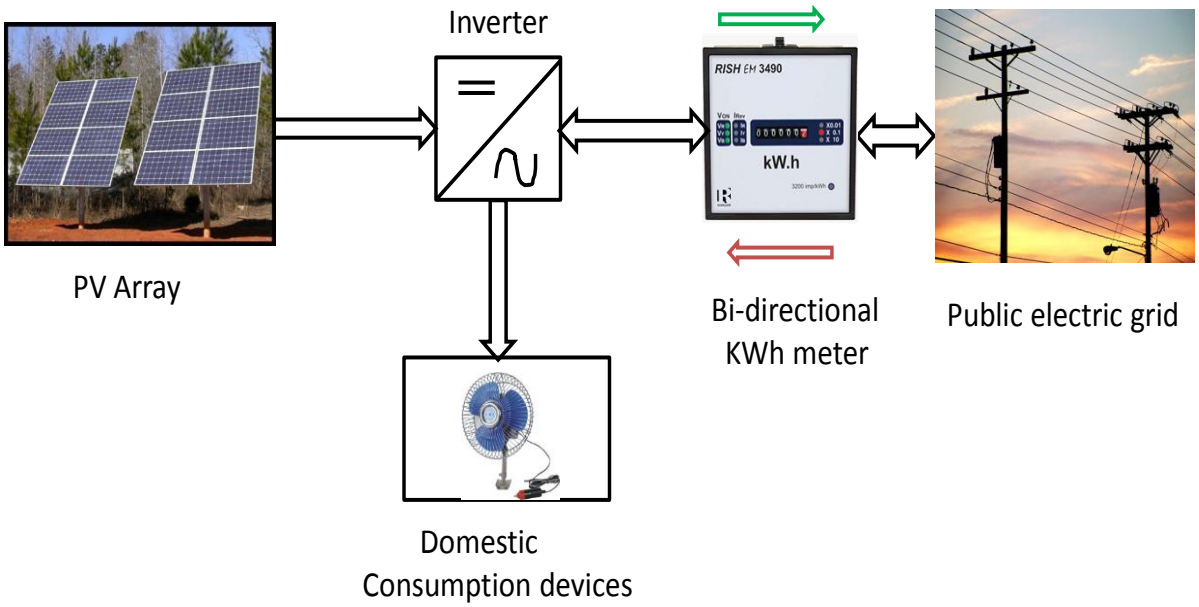

Fig. 1.3: Block diagram of a decentralized PV system

1.3.2 Applications of PV Power Systems

Photovoltaic energy systems, unlike other sources of energy, have these unique advantages [4], [5] : 1) direct conversion of sunlight into electricity, 2) long lifetime of up to 25 years because no mechanical moving parts, 3) no pollution of the environment, 4) based on

ubiquitous, free and inexhaustible source – the sun, 5) modularity and scalability that makes it flexible for system expansion, 6) availability mostly during hours of peak demand, and 7) comparatively shorter construction lead time. These unique advantages have made the technology popular in numerous areas of applications, including the following [1], [2], [16]:

- *Space applications*: Because of its ability to work reliably and without maintenance for a long time, PV technology has been used in space vehicle power supplies since 1958 when it was first used for the Vanguard satellite.
- *Consumer electronics:* for items like calculators, watches, organizers, and battery chargers where a small PV module is integrated as part of the product.
- *Autonomous grids:* In remote regions, far away from the power grid, they are cost-competitive compared to grid extension or reliance on diesel generators that also pollute the environment. Such autonomous systems can be used in schools, hospitals, entire villages or island in the form of a *micro grid*. This is often in combination with other backup systems in the form of hybrid systems.
- *Support for unreliable power grid:* Operating the PV system in parallel with the grid is necessary in situations, obtainable in developing nations, where the public grid is unreliable or where a large consumer (a factory, for example) is connected to a weak grid.
- *Solar water pumping systems*: These are used as replacements for hand pumps and diesel-engine-driven pumps for both irrigation and drinking water, especially in developing countries.
- *Use in weather stations, navigational aids, transmitter masts and traffic lights.*
- *Solar home systems.*
- *Transportation applications*: Applications in these areas, though not yet commercially mature, include solar cars, boats, unmanned zeppelins, and solar planes. These areas hold great promise for the foreseeable future. Also, solar PV technology is used in charging electric vehicles.

1.4 Problem Statement and Research Motivations

A photovoltaic power plant has the main objective of extracting as much energy as possible from the solar modules (array) when sunlight impinges on them while maintaining acceptable

power quality, reliability and cost-competitiveness. However, achieving this objective is fraught with the following challenges [6], [17-23]:

- Low conversion efficiency: The output of a solar generator depends on three major factors: 1) module efficiency, 2) insolation, and 3) temperature. PV generators generally have low conversion (sunlight-to-electricity) efficiency. Even monocrystalline silicon based PV generators – which have the highest efficiency – boast of efficiency of only 13-19%.
- Cost issues: Prior to 2012, solar energy was not cost-competitive in relation to fossil-fuel based electricity. This had hampered the global spread of this mature technology especially in developing nations where it is needed most. Even the substantial drop in system costs witnessed in late 2012 has not brought the much desired global price parity with energy from coal fired power stations due mainly to the high "soft costs" in some countries. These soft costs include permission, labour, inspection and interconnection costs for grid-connection. This parity is needed to spur much more demand for PV based energy systems.
- Intermittency and variability: Unlike fossil-fuel based power stations, the amount of electricity that a solar power plant generates varies and is very intermittent in nature. This is due to its dependence on the vagaries of the weather – mainly on solar insolation and ambient temperature that varies throughout the day.
- Power quality issues: The voltage quality is expected to fulfil stipulated national and international standards. However, voltage variations occasioned by the intermittent and variable nature of the PV generator is often the case. Moreover, voltage flicker, voltage transients, and harmonics caused by the presence of non-linear loads and the power electronic converters in the system are often serious issues.
- Load variations: The mismatch between power generation and power demand is a big issue. This mismatch arises because electricity consumption varies from moment-to-moment, hour-to-hour over the course of the day.
- Integration issues: When the various components of a PV power plant are integrated, transient instability can be an issue because of disturbances on system performance arising from variations in load and the stochastic nature of the PV generator output. Ensuring transient stability using energy storage is a challenge.

Addressing some of the above challenges is the motivation for this thesis and requires investigative research as discussed in the following subsection.

1.5 Objectives and Contributions of the Thesis

To solve the issues raised in the preceding subsection requires research in the following key areas:

i) Application of appropriate control strategies for optimal energy conversion.
ii) Improvement of conversion efficiency by improving the spectral response of the module.
iii) Effective coordination of the various subsystems for efficient system operation.
iv) Proper selection of subsystems especially the energy storage system.
v) Application of effective voltage and frequency regulation strategies.
vi) Application of appropriate protection strategies.

Making a contribution by addressing the aforementioned challenges for system performance enhancement are the motivations for this thesis. Consequently, the broad objective of this study is the optimization of a PV power plant performance through the application of innovative and efficient control techniques. By applying appropriate control algorithms at the different subsystems of the PV power plant, Fig. 1.4, performance improvement are achieved via seamless integration, interaction and matching of the subsystems. The following four integrated digital control algorithms are implemented:

i) An MPPT (maximum power point tracking) controller for efficient harvesting of solar energy.
ii) A SEPIC topology based converter controller for dc voltage regulation
iii) A dc-dc bidirectional converter controller for management of the energy storage system.
iv) A dc-ac (inverter) converter controller for sinusoidal wave generation based on the grid voltage and frequency requirements.

In addition to the development of control algorithms for the PV power electronic interfaces, this thesis has also made the following contributions:

- ✓ Development of the simulation models for the PV power plant subsystems.
- ✓ Development of a software tool for the design of standalone PV power plants.
- ✓ Development of a complete integrated simulation model of a PV power plant.
- ✓ Software and hardware platforms for evaluation of the performance of maximum power point tracking techniques.

- ✓ Practical implementation of a real-time digital controlled PV power plant with maximum power point tracking.
- ✓ Implementation of advanced control algorithms for energy storage system with integrated bi-directional dc-dc converter.
- ✓ Experimental implementation of an effective, versatile, low-cost, low-component-count, data acquisition and conditioning system for a PV systems using dSPACE DS1104 DSP system.

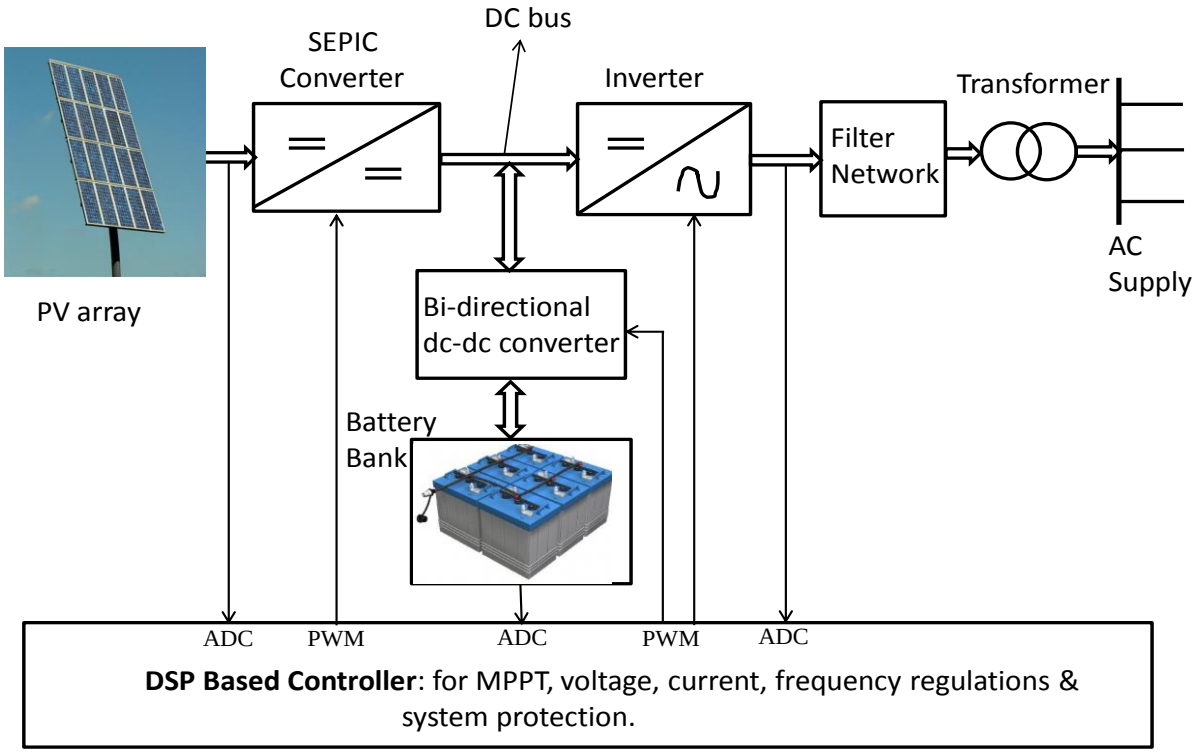

Fig. 1.4: Block diagram of the PV power system.

1.6 Thesis Organisation

This thesis is organised as follows:

- Chapter 2 presents the development of a simulation model for a photovoltaic module using the Matlab/Simulink software platform. The developed model is used in simulation for PV characterization studies. The second part of the chapter introduces a novel Matlab based optimisation tool for the sizing of a photovoltaic standalone power system.
- Chapter 3 presents the analysis and design of the SEPIC converter used as the dc-dc power converter for interfacing the PV array in the study. The performance of the converter in both open-loop and closed-loop operation is analysed.
- Chapter 4 reviews various algorithms for the implementation of maximum power point tracking (MPPT) in a photovoltaic module integrated with a dc-dc converter. It also reviews the current mode control methodologies for power converters. Finally, the chapter proposes a novel multi-loop integrated MPPT and current mode control for the SEPIC converter to ensure optimal system performance.
- Chapter 5 reviews the roles and types of energy storage systems in PV applications. A bidirectional dc-dc converter for interfacing the energy storage system is designed and a novel battery management and power flow controller is presented.
- Chapter 6 reviews various topologies and modulation approaches for photovoltaic inverters in both single-phase and three-phase operational modes. Also reviewed are the applicable international standards for photovoltaic inverters. Finally, a control scheme to ensure voltage and frequency regulation is presented.
- Chapter 7 discusses the hardware implementation and experimental analysis of the entire PV power system using the DS1104 DSP controller. It discusses the building of the prototypes – the power converters and the data acquisition and conditioning systems – prior to systems integration.
- Chapter 8 presents summary of the thesis and the suggestions for future research.

Chapter 2

PV Modelling and Development of a New Optimisation Tool for Off-Grid PV Power Plant Design

2.1 Introduction

The first part of this chapter focuses on the development of a simulation model for a photovoltaic module. Prior to this, the electrical model of the solar cell/module is introduced and analysed in detail. This is used as a basis for the development of the proposed simulation model using the Matlab/Simulink software. Through simulation studies, the developed model will help in understanding the characteristics of PV modules and such understanding is necessary in developing proper interfacing and control strategies for the entire PV power system. The chapter starts with a review of the classifications and comparisons of solar technologies based on cell material and cell thickness.

In the final part of the chapter, a new user-friendly optimisation tool for designing an off-grid PV power plant is developed. Such tools are invaluable to PV system designers. They not only hasten the design process but also help ensure the system's reliability, durability, maintainability, safety and cost-competitiveness. The developed tool is used in a case study to size the key components of a typical PV power system.

2.2 Review of PV Cell Technologies

While the first generation photovoltaics technology is based on crystalline silicon, the second generation is based on thin–film technology and the third generation includes mainly new technologies like organic solar cells, which are still at the embryonic level of their developments. The motivating factors for progression from one generation to the other are mainly [7], [24], [25]:

- The desire to improve cell conversion efficiency, and
- The desire to reduce module cost, for cost-competitiveness with other sources of energy, especially coal-fired power plants.

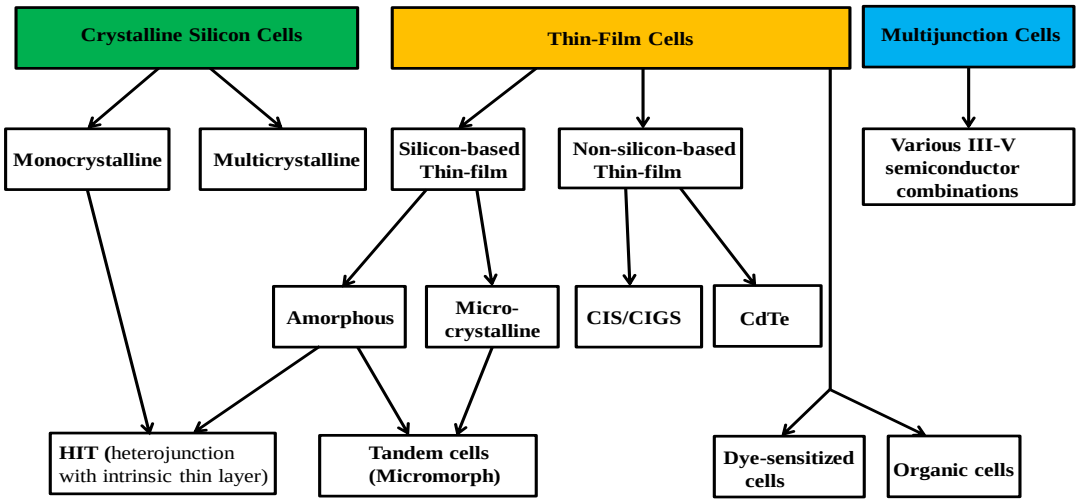

Fig. 2.1: Classifications of PV cell technologies.

Despite the many types of solar technologies already developed in laboratories, only five have achieved commercial success. Differences between cell technologies are based fundamentally on: 1) the type of semiconductor material used, and 2) the crystalline structure of the cell [26], [27]. Figure 2.1 shows the broad classifications for the first, second and third generation solar cell technologies [4], [7]. A brief description of some of the mature technologies follows in the subsequent subsections.

2.2.1 Mono-crystalline Silicon Cells

In mono-crystalline PV cells, each cell is made from a single crystal of silicon. It is the most efficient of all PV cell technologies, but the manufacturing process is slow and energy intensive. Its energy conversion efficiency ranges between 14 to 18%. Mono-crystalline cell technology is also a common choice for concentrator cells: which are used for sun-tracking concentrating dish or trough systems [4], [26], [27].

2.2.2 Multi-crystalline or Polycrystalline Silicon Cells

This is produced from multiple crystals. The production method is relatively fast and low-cost in comparison to the mono-crystalline technology. The conversion efficiency is also lower and typically ranges between 11 and 13%. This lower conversion efficiency implies lightly larger size per watt of output power compared to mono-crystalline module. Because of

its random crystal structure, it does not degrade in operation and is becoming so popular in commercial applications [4], [26-28].

2.2.3 Silicon-based Thin-film Technologies

The main necessity for using thin film technology is cost reduction because of their low-material consumption – a thickness of about 1µm is used [4]. Amorphous silicon (a-Si) is used in silicon-based thin-film technology because it has superior light absorbing capability than crystalline silicon. However, a-Si based modules have low conversion efficiency in the range of 6-8% [4] because impinging sunlight generates charge carriers with low mobility. They have the advantage of flexibility and so can be manufactured to very large dimensions. To improve the stabilized low efficiency of a-Si modules, microcrystalline silicon (µc-Si) is added to the amorphous silicon. This stacking produces tandem or micromorph solar module with improved spectral response and improved conversion efficiency of up to 10% [7], [29].

2.2.4 Non-silicon Based Thin-film Technologies

The major types of non-silicon based thin-film PV cell technologies include:

a) Copper indium diselenide (CIS) based PV technology. Alloying this with gallium is often used in the production of CIGS modules. CIS and CIGS based modules have efficiencies between 7 and 12% - making them the most efficient of all thin-film technologies. Compared to crystalline technology, they have the disadvantages of lower efficiency and uncertain durability in deployment arising from degradation over time [7], [27].

b) Cadmium Telluride (CdTe): Modules based on this technology have low production cost with relatively high efficiency of 11% - making them the most economical thin-film technology [27]. The lower conversion efficiency means that more space and hardware are required to produce the same output power when compared to the crystalline technology. The low production cost accounts for the popularity of this technology in utility-scale solar installations [30].

2.2.5 Comparisons of different PV cell technologies

Tables 2.1 and 2.2 below show the differences between the major solar cell technologies.

Table 2.1: Comparisons of silicon based cell technologies [24-29].

Parameter	**Mono-crystalline cell technology**	**Poly-crystalline cell technology**	**Amorphous cell technology**
Cell thickness (μm)	200 - 400	200 - 400	1 - 2
Cell conversion efficiency (%)	14 - 18	11 - 13	4 -9
Spectral response	High sensitivity to high wavelengths. Low sensitivity to short wavelengths.	High sensitivity to high wavelengths. Low sensitivity to short wavelengths.	High sensitivity to short wavelengths and low sensitivity to high wavelengths.
Module reliability in operation	Good long-term reliability: greater than 20 years.	Good long-term reliability.	Long-term reliability problems.

Table 2.2: Comparisons of silicon and non-silicon based thin-film technologies [24-29].

Parameter	**Silicon crystalline** cell technology	**Ga-As** cell technology	**CIS** cell technology	**CdTe** cell technology
Band-gap energy (eV).	1.12	1.42	0.96 – 1.04	1.45 – 1.5
Spectral response	Weaker optical absorption.	Stronger optical absorption.	Stronger optical absorption	Stronger optical absorption
Band-gap transition	Indirect	Direct	Direct	Direct
Module reliability	Long-term reliability: greater than 20 years.	Long-term reliability issues because of moisture ingression.	Module degradation occurs over time.	Module degradation occurs over time.
Cell thickness (μm)	200 - 400	Less than 1.0	Less than 1.0	Less than1.0
Space/Mounting hardware requirements.	Average	More space and hardware required because of lower efficiency.	More space and hardware required because of lower efficiency.	More space and hardware required because of lower efficiency.

2.3 Review of Analytical Model of the Solar Cell

A solar cell is basically a p-n junction fabricated from a thin layer (wafer) of semiconductor material. In the dark, the solar cell has characteristics similar to that of a diode. When the cell is illuminated by solar energy, the photon-generated current, which is proportional to the incident radiation flows in the external circuit when the cell is short-circuited. When the cell is open-circuited, the current is shunted internally by the intrinsic p-n junction diode. Thus, the characteristic of this diode is the basis of the characteristics of the solar cell [31-33]. Consequently, a solar cell is often represented by the electrical equivalent single-diode model shown in Fig. 2.2.

Where the circuit parameters are defined as: I_{PH} is the light-generated current or photo-current; I_D is the diode current; I_{SH} is the shunt-leakage current; I_L is the net current at the output terminal; R_{SH} is the shunt resistance of the diode; and R_S is the series resistance, which normally lies between 0.05 to 0.10Ω; and V_{OUT} is the output voltage.

2.3.1 Analysis of the Single Diode Model (SDM)

From the equivalent electrical circuit in Fig. 2.2,

$$I_L = I_{PH} - I_D - I_{SH} \tag{2.1}$$

The Shockley diode current, $I_{D,}$ is given by the classical expression [33]

$$I_D = I_o\left[\exp\left(\frac{qV_d}{AK_BT_C}\right)-1\right] \tag{2.2}$$

Where,

q = electron charge =1.6x10^{-19} C.

A = diode ideality factor.

K_B = Boltzmann Constant = 1.38x10^{-23}J/^{o}K.

T_C = cell working temperature, K.

V_d = diode voltage in volts.

Substituting (2.2) in (2.1) gives:

$$I_L = I_{PH} - I_S[\exp(\frac{qV_d}{AK_BT})-1] - \frac{V_d}{R_{SH}} \tag{2.3}$$

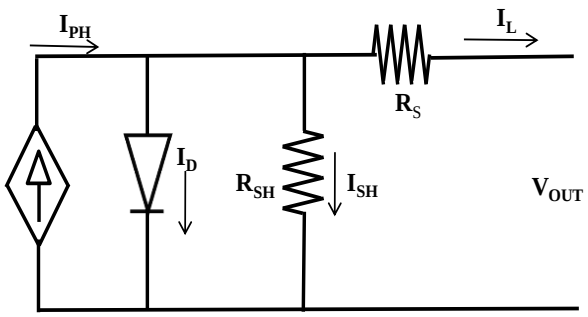

Fig. 2.2: Single diode model (SDM) of a solar cell.

Where R_S is assumed to be zero. That is, no series loss. The photo-current, I_{PH}, depends mainly on the solar insolation, G, and the cell's working temperature, T_C. It is given by the relationship [31], [32]:

$$I_{PH} = [I_{SC} + K_1(T_C - T_{Ref})]G \tag{2.4}$$

Where I_{SC} is the short-circuit current at standard test condition (25^{o}C and 1000W/m^2); K_1 is the cell's short-circuit temperature coefficient, $T_{Ref,}$ is the cell's reference temperature and G is the solar radiation.

The diode saturation current, I_S, which is temperature-dependent can be determined from the following relationship [33]:

$$I_S = I_{RS}(\frac{T_C}{T_{Ref}})^3 \exp[qE_B(\frac{1}{T_{Ref}} - \frac{1}{T_C}) / K_B A \tag{2.5}$$

Where I_{RS} is the reverse saturation current at reference temperature and solar radiation; E_B is the band-gap energy of the semiconductor material and A is the ideality factor which is PV technology dependent. The series resistance of a PV cell is very small (approximately 0.1Ω) at short circuit, so it can be neglected. Thus the photocurrent can be assumed to be equal to the short-circuit current. That is,

$$I_{PH} = I_{SC} \tag{2.6}$$

2.3.2 Module/Array Modelling

Since a PV cell on its own produces less than 3W at 0.5Vdc approximately, cells must be connected in series-parallel configurations to produce enough power for high power

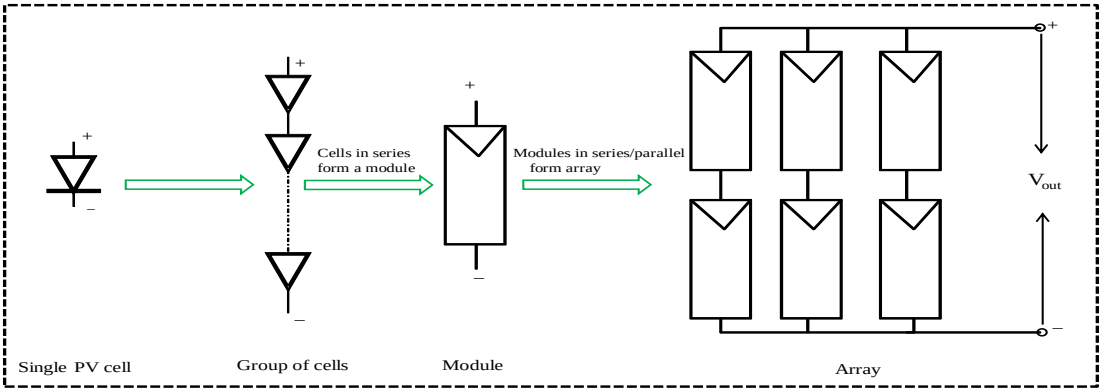

Fig.2.3: Functional relationship of PV cells, modules and arrays.

applications. A group of cells make up a *module* and a group of modules make up an *array*. Fig.2.3 is an illustration of how cells are configured into modules and how modules are connected as arrays to achieve high voltage and power for any application [27], [28].

Thus, the generalised equivalent circuit of a module with cells in series and a number of parallel arrangements is given by:

$$I_L = N_P I_{PH} - N_P I_S [\exp(qV / N_S K T_C A) - 1] \tag{2.7}$$

Where N_S is the number of cells in series and N_P is the number of parallel connections. Also, ignoring the shunt leakage current, the reverse saturation current at reference temperature is given as [31-36]:

$$I_{RS} = \frac{I_{SC}}{[\exp(qV_{oc} / N_S K A T_C) - 1]} \tag{2.8}$$

2.3.3 Dual Diode Model (DDM)

An alternative model for PV cells is the dual-diode model which uses two diodes to define the behaviour of the solar cell. This is shown in Figure 2.4. Although the dual-diode model is more accurate than the single-diode model, it is not widely used in PV applications because of its complexity [4], [28], [29].

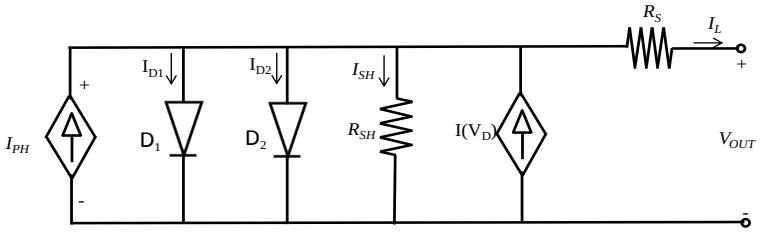

Fig. 2.4 Dual-diode model of a solar cell.

2.4 Proposed Simulation Model Development for Characterisation Studies

To develop a simulation model that can help to accurately predict the performance of the PV solar power plant used in this study, Matlab/Simulink software is used. The model, by using the ever-changing environmental temperature and irradiation and the parameters of any given solar module, is able to accurately predict the characterisation (current-voltage and power-voltage behaviour) of the module and its power output. The details of the proposed modelling approach and the simulation results are discussed in the subsections below.

2.4.1 Model Implementation via Simulink Software.

This model is used to study and predict the performance of the module with variation in temperature and irradiation. It is based on the temperature and irradiation dependent analytical relationships described in Section 2.3.1. Using these relationships that describe the dark diode current, the saturation current and the output current, in conjunction with Simulink built-in blocks, the model is constructed as shown in Fig. 2.5, which shows the block diagram of the model in Simulink. The major subsystems of the model are shown in Fig. 2.6, while the details of the three major subsystems are shown in Figs. 2.7 - 2.9.

The user is able to input the following parameters to the model:

- Ambient temperature, as shown in the Figs. 2.5 and 2.6.
- Solar irradiation, as shown in Figs. 2.5 and 2.6.
- Parameters of the solar module under study. This can be inputted via the dialogue box of the developed mask for the model. Fig. 2.10 shows a dialog box of the mask for the BP 380 solar module used for this study.

Also, the user can assess the following output parameters, as shown in Figs. 2.5 and 2.6:

- Module output voltage.

- Module output current.
- Module output power.
- Module power-voltage (P-V) characterisation plot.
- Module current-voltage (I-V) characterisation plot.

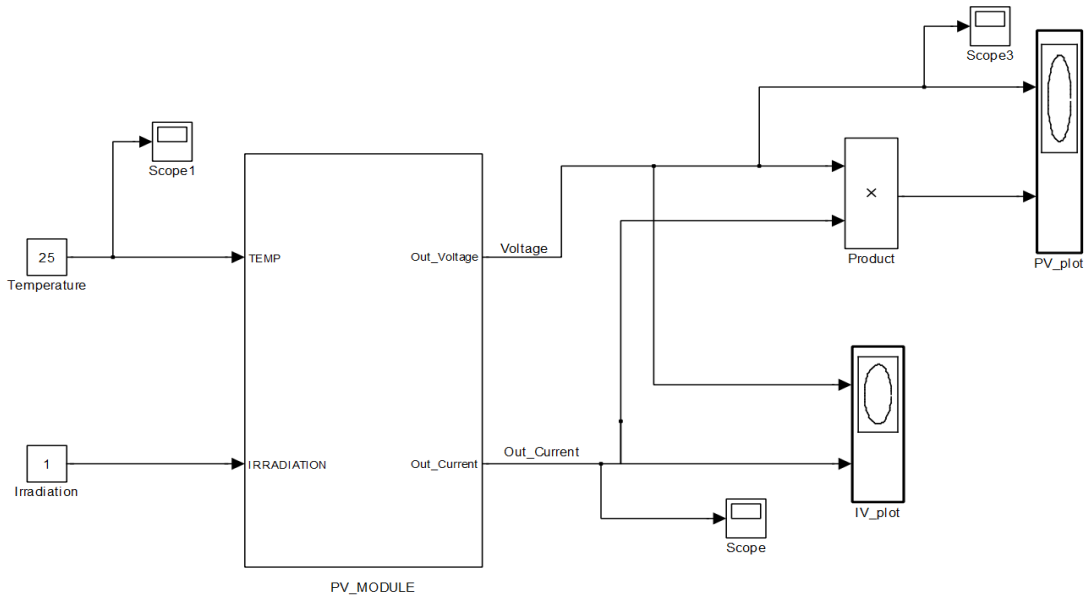

Fig. 2.5 Block diagram of the PV module simulation model using Simulink software.

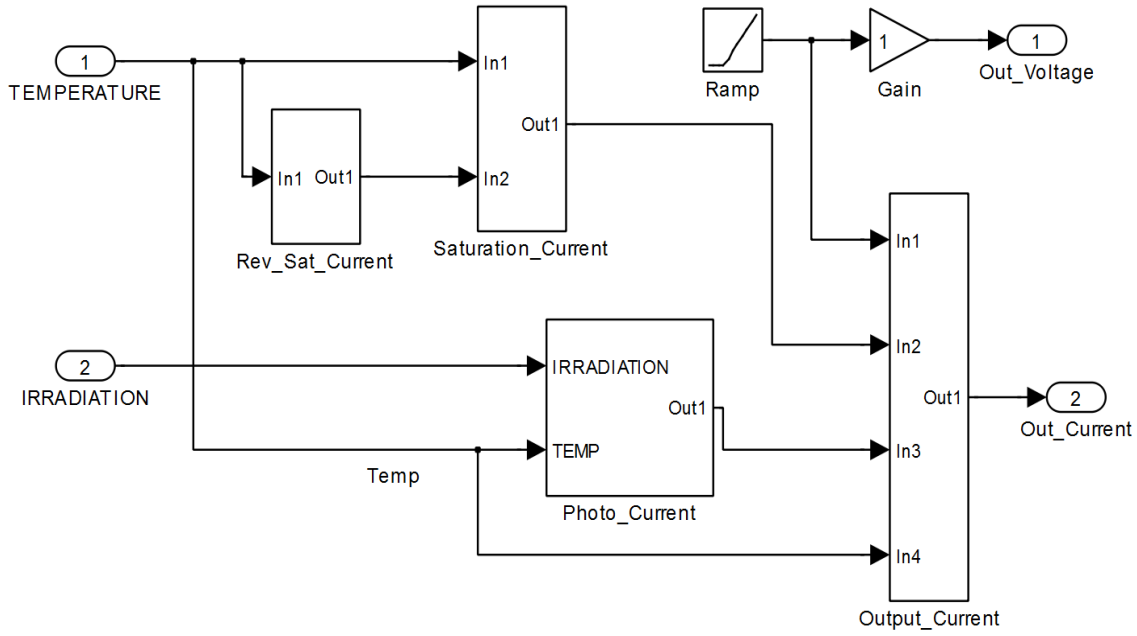

Fig. 2.6 Simulation model showing the major subsystems.

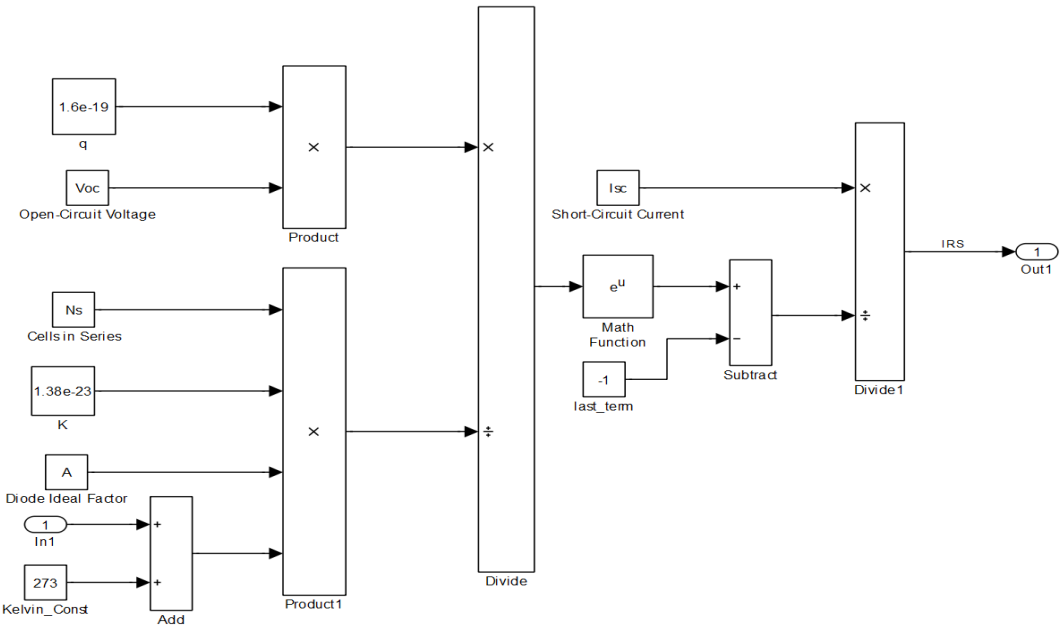

Fig. 2.7 Details of the reverse saturation current subsystem.

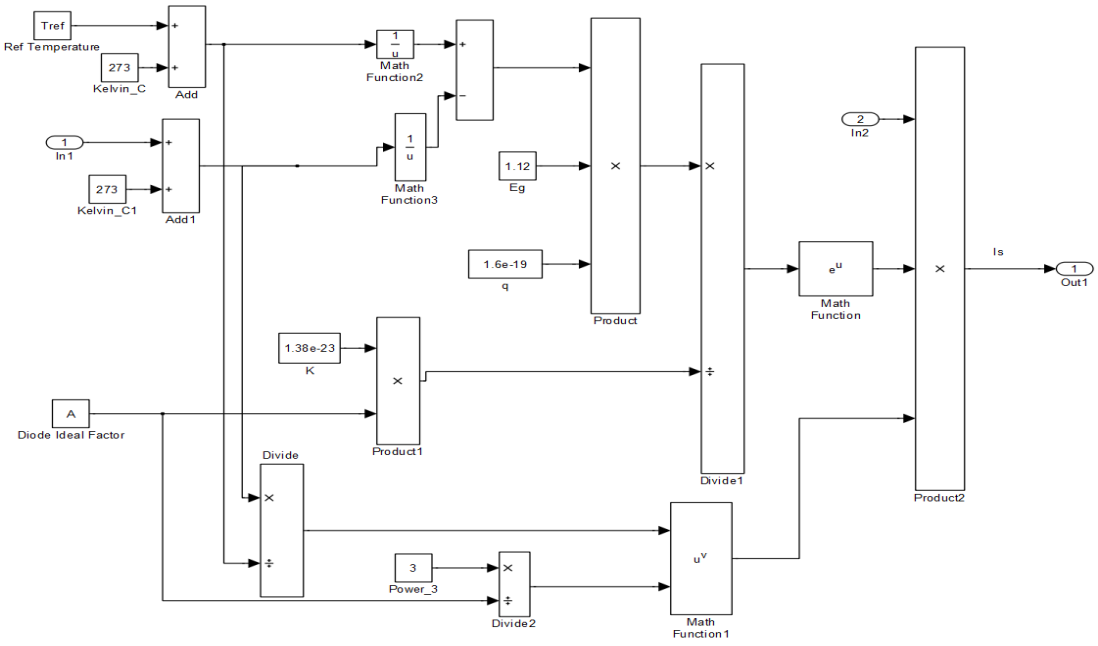

Fig. 2.8 Details of the saturation current subsystem.

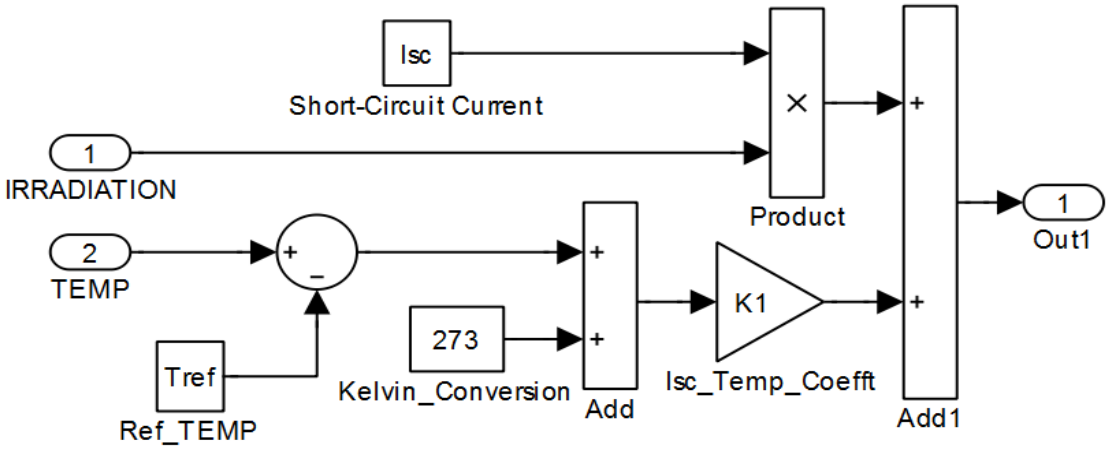

Fig. 2.9 Details of the photocurrent subsystem.

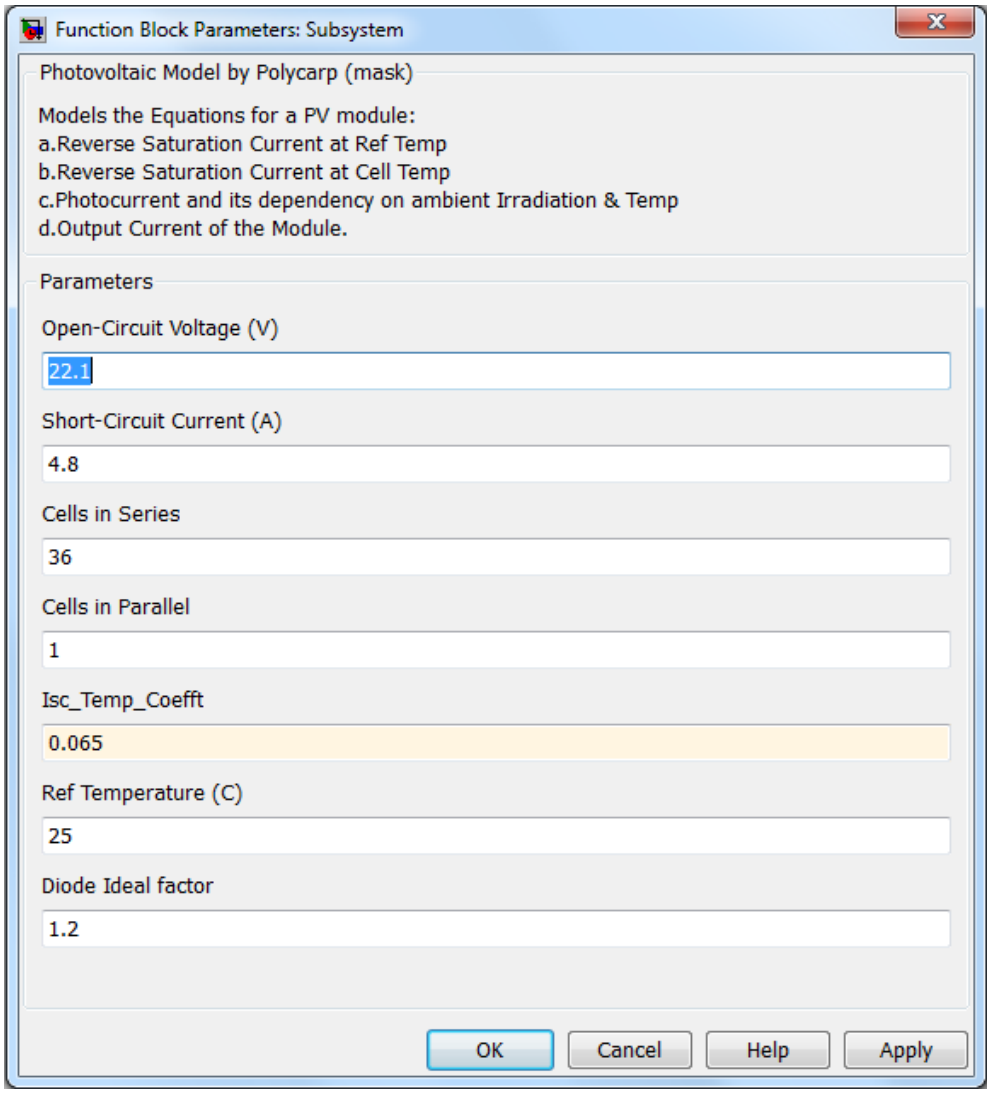

Fig. 2.10 Mask dialogue box for the developed model showing some parameters of the PV module: BP 380 used for the study.

2.4.2 Simulation Results and Discussions

The three major environmental variables that affect the performance of a solar module are: 1) irradiation, 2) temperature, and 3) cloud cover. The irradiation and temperature effects are most pronounced and are simulated in this study. The study does not consider the effect of cloud cover. The results obtained using the developed model to study the effects of these two ever-changing environmental variables are shown in Figs. 2.11-2.14. While Figs. 2.11 and 2.12 consider the effect of changing solar irradiation at constant temperature, Figs. 2.13 and 2.14 consider the effect of changing temperature at constant irradiation.

2.4.2.1 Effects of Irradiation Changes

From Fig. 2.11, it is seen that, at constant temperature, an increase in the solar intensity (irradiation) results in an increase of the module current, while a decrease in solar intensity results in a decrease of the module current. The irradiation is measured in '*suns*', where 1sun =1000W/m^2. Thus, the current-voltage (I-V) curve of Fig. 2.11 shifts up with increased solar radiation and down with a decrease in solar radiation. It is also seen that the effect of irradiation changes on the module's output voltage change is very minimal. Similarly, in Fig. 2.12, the module output power increases as the solar intensity increases and decreases as the intensity decreases. This P-V characteristic is expected since the module's output power is the product of the module current and voltage.

2.4.2.2 Effects of Temperature Changes

For the temperature effects at constant solar irradiation, it is seen from Fig. 2.13 that the module voltage is inversely proportional to the ambient temperature. That is, a rise in temperature produces a proportional decrease in the output voltage. The effect of temperature variations on the output current is seen to be very minimal. Similarly in Fig. 2.14, the module output power decreases as the temperature increases.

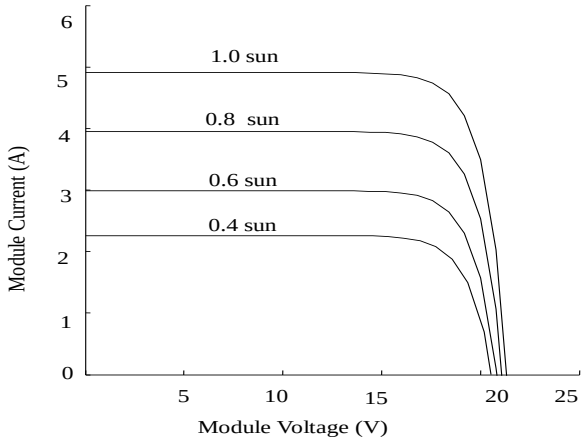

Fig. 2.11 Influence of irradiation changes on module current and voltage output at constant temperature.

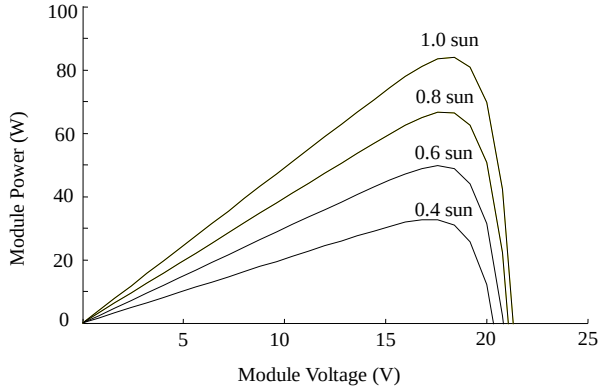

Fig. 2.12 Influence of irradiation changes on the PV module power and voltage at constant temperature.

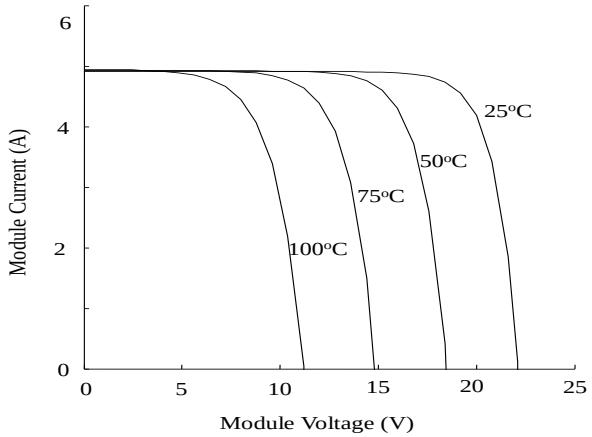

Fig. 2.13 Variation of I-V characteristics with changes in temperature at constant irradiation.

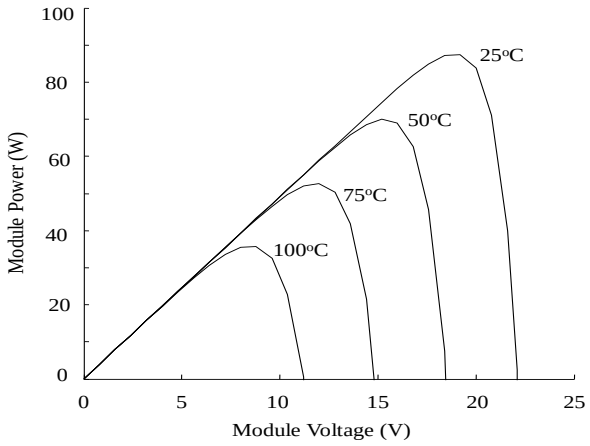

Fig.2.14. Variation of module power with changes in ambient temperature at constant irradiation.

2.5 A New Optimisation Tool for Off-grid PV Power Plant Design

An off-grid (stand-alone system) PV power plant, which is very popular in areas with no grid access, is an integrated system designed to generate electricity from sunlight 24/7. To ensure system reliability and availability, energy storage system and power converters are invaluable components. It is necessary that PV systems designers ensure that only the highest quality PV systems are designed and deployed in operation. This is because good design, proper systems integration and installation of the PV plant will ensure [37]:

- System longevity.
- System reliability and availability by avoiding premature failures of the BOS (balance-of-system) which have lower lifetimes compared to the PV modules.
- Safety to system users by avoidance of shock hazards, battery fires and explosions, and lightning hazards.
- Cost competitiveness of the system.

Achieving such desired high quality design is possible only with the help of reliable and robust software tools. This final part of the chapter discusses the development of a robust and user-friendly Matlab/Simulink software based optimisation tool for designing a PV power plant. It uses site-specific parameters to size the system's components. Discussed in the following subsections are: features of the developed tool, description and architecture of the tool, and the development of the various sub models. Finally, the simulation analysis of a case study using the developed tool is also presented.

2.5.1 System's Features

The optimisation tool provides the following features [38]:

- User-friendly interface inherited from the Simulink software masking features.
- Utilises relatively accurate and robust calculation algorithms, based on the equations discussed in subsequent sections.
- It keeps the designer in the loop by offering transparency of the calculation methods, equations and assumptions used via the help function.
- It provides intermediate results at each simulation stage for verification of the output of each of the sub models.
- It offers a design process that is not necessarily linear – parts of the design may have to be revisited over and over and different choices made as the design progresses. That is, it allows for design iterations to get the best possible choice of components.
- It provides a library of components that are re-usable in other systems designs.

2.5.2 System's Description and Architecture

Fig. 2.15 is a typical off-grid PV power plant showing the major subsystems. These major subsystems are:

- The PV array, which is a collection of PV modules, which converts the solar energy into dc electricity.
- The battery bank, a group of series/parallel connected deep cycle batteries, for energy storage. This supplies the needed energy during night time or during periods of little or no sunlight like cloudy weather.
- The inverter to convert the *dc* energy to *ac* energy suitable for use by the loads.
- The charge controller that changes the dc output of the solar array into another dc level suitable for charging the battery bank and for use by the inverter. It ensures that the battery is neither overcharged nor over discharged.
- The loads. These are *ac* or *dc* loads connected to the system by the end users. Nowadays, these are mostly *ac* loads.

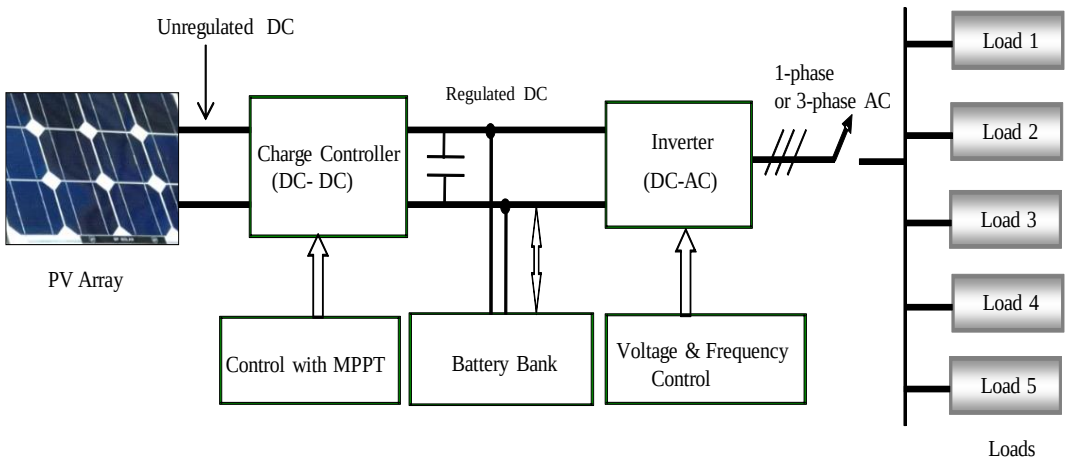

Fig. 2.15: Major subsystems of an off-grid PV power plant.

These subsystems are used as the basic building blocks to develop the model in Simulink. The developed model is shown in Fig. 2.16 and comprises the following four sub models:

- System load assessment sub model: for calculating all the loads connected to the system.
- PV array sizing sub model: for calculation of the actual size of the array needed to meet the load requirements.
- The battery bank sizing sub model: for the calculation of the capacity of the battery bank needed to meet the system's requirements.
- Power conditioner sizing sub model: for calculating the size of the inverter and the charge controller.

Each of these four sub models has a user-friendly interface developed using the masking features of Simulink that enables the designer to input the desired parameters prior to simulation. Firstly, the PV system's designer initiates the design process by doing the assessment of the system's loads. He inputs the desired loads via the user-friendly interface. The output of this sub model provides the inputs to the other sub models and is the basis for the sizing of the array, the battery bank, and the power conditioners – inverter and charge controller. The system designer also uses the user-friendly interface of each sub model to input other desired system parameters prior to system simulation. Fig. 2.17 is a simplified flowchart of the model's operation. Details of the four sub models are discussed in the subsequent sections.

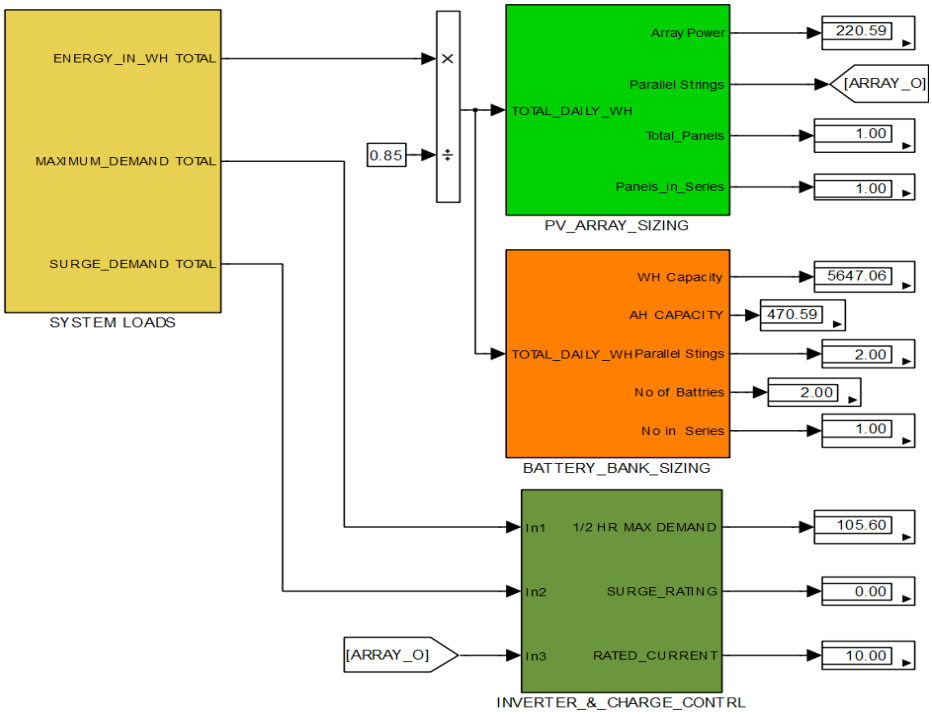

Fig. 2.16: Simulation model showing the sub models in Simulink.

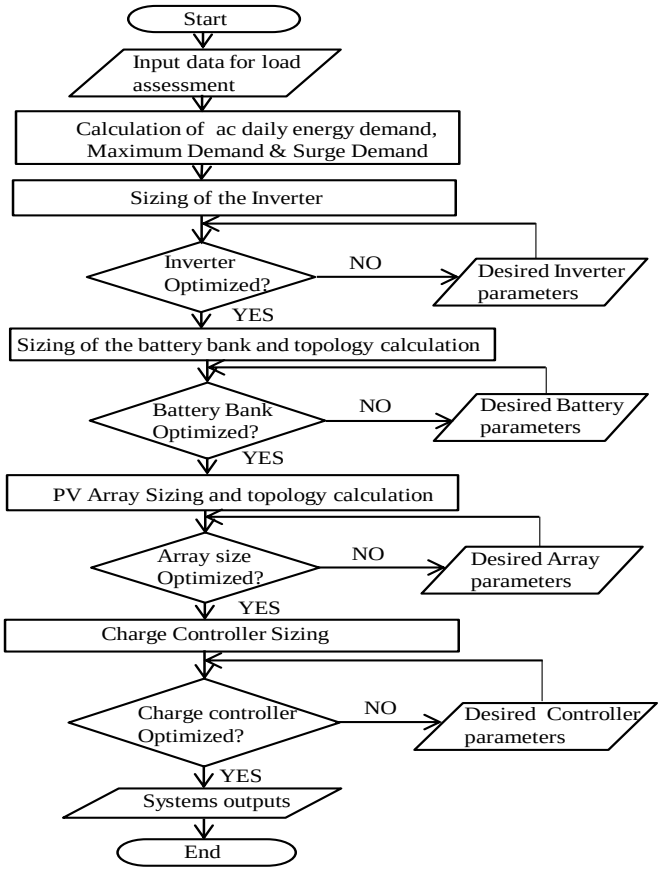

Fig. 2.17 Simplified flowchart for the sizing tool.

2.6 Development of Sub Models

2.6.1 Load Assessment Sub Model

The first stage of the design process for any off-grid PV system is the estimation of the loads to be powered. To meet a particular electricity demand, the daily energy requirements and the electrical characteristics of the loads must be known. Once the peak power consumption and the duty cycle (usage hours per day) of all loads are compiled, the product of the two gives the actual share of the energy requirement of that load on the system during the course of the day. Thus the algorithm for this sub-model is based on the following relationship [5]:

$$E_{dc} = \sum_{i=1}^{n} P_i \times hrs \tag{2.9}$$

where E_{dc} is the total energy consumed per day (Wh/day) by all dc loads, if they are used; P_i is the power consumption of each individual load in watts, and *hrs* is the duty cycle or usage hours of each individual load. Similarly, for ac loads,

$$E_{ac} = \sum_{i=1}^{n} P_i \times hrs \tag{2.10}$$

And the total energy in Wh/day, E_{TOT}, drawn from the *dc* bus by both *dc* and *ac* loads is given by:

$$E_{TOT} = E_{dc} + E_{ac} = E_{dc} + \frac{E_{ac}}{\eta_{inv}} \tag{2.11}$$

Where η_{inv} is the efficiency of the inverter.

In general, the designer's input data for each of the loads are:

- Power rating of the load in watts.
- The number of the particular type of load.
- The number of hours of usage (duty cycle) of the load.
- The power factor of the load.
- The surge factor of the load, if applicable.

The load assessment sub model then provides the following outputs on simulation:

- Daily energy used by the system in Wh/day, E_{TOT}. This forms the basis of all subsequent evaluation by the other sub models for sizing the battery bank and the PV array.

- Maximum demand, D_{max}, which is needed for the sizing of the inverter.
- The surge demand, S_{surg}, also needed for the sizing of the inverter to withstand surge loads.

The designer enters the data via the user-friendly interface created using Simulink's masking features. The algorithm for the desired load management strategy to properly size the inverter is done using the embedded Matlab function and consequently, the user only has to input "1" or "0" to indicate which loads to include or not to include in evaluating the maximum demand and the surge demand.

2.6.2 PV Array Sizing Sub Model

A stand-alone photovoltaic system must maintain the energy balance over its specified period, usually a day. Thus, it must be sized to satisfy the energy balance equation between the PV array, the batteries, the load, the power conditioning components, and the system losses, over the course of a day. Consequently, the sizing algorithm for this sub model is developed from the following relationship [39 - 41]:

$$P_{array} = \frac{E_{TOT}}{PSH \times \eta_{pvss} \times f_{derate}} \tag{2.12}$$

where P_{array} is the peak array power in watts; E_{TOT} is the total energy demand from the *dc* bus in watt-hour; PSH is the peak sun hours at the site of interest; f_{derate} is the temperature and operating point derating factor; η_{pvss} is the sub-system (from the PV array to the *dc* bus) efficiency. That is,

$$\eta_{pvss} = \eta_{pvr} \times \eta_{Reg} \times \eta_{RB} \times \eta_{Batt} \tag{2.13}$$

where η_{pvr} accounts for the PV to regulator wiring loss; η_{Reg} is the regulator efficiency; η_{RB} accounts for the regulator to battery wiring loss and η_{Batt} is battery efficiency. Equations (2.12) and (2.13), via the user interface, thus offer the system designer the chance of choosing a wide range of parameters for sizing the array.

Having calculated the total PV array power from equation (2.12), the designer can choose the desired module type with the appropriate peak power, W_P and voltage, V_{mod} to achieve the intended array configuration via the algorithm-embedded relationships in (2.14) - (2.16):

$$N_P = \frac{P_{array}}{W_P} \tag{2.14}$$

$$N_S = \frac{System\ Voltage}{V_{\mathrm{mod}}} \tag{2.15}$$

$$N_T = N_P \times N_S \tag{2.16}$$

Where the designer rounds $N_{P,}$ the number of modules in parallel, up or down if equation (2.14) gives a fractional value; N_S is the number of modules in series and N_T is the total number of modules in the array.

2.6.3 Battery Bank Sizing Sub Model

The major factors in calculating the capacities of batteries in any photovoltaic power system are [37], [42], [43]:

- Total daily energy demand from the system in watt hours, $E_{TOT,}$ derived from the load assessment process.
- Nominal system voltage, V_{dc}.
- The number of storage days or days of autonomy, $D_{A,}$ to account for those periods (night time and cloudy days) when there is no energy from the solar panels. The choice of this depends on factors like the critical nature or otherwise of the loads, climate at site, access to site, regularity of system monitoring and the consequences of system failure.
- The design maximum Depth of Discharge (DOD_{max}). The life of the batteries depends on the value chosen. Excessive DOD_{max} (low state of charge, SOC) will shorten the battery life while shallow DOD_{max} increases the size of the battery bank and the solar array required.
- Temperature derating factor for cold climates, $D_{T.}$
- Charge/Discharge efficiency, D_{CH}, of the battery.

Based on these factors, the algorithm for this sub model is derived from (2.17) [40].

$$C_X = \frac{E_{TOT} \times D_A}{V_{dc} \times DOD_{\max} \times D_T \times D_{CH}} \tag{2.17}$$

where C_X is the battery capacity in ampere-hours (Ah) at a given discharge rate, usually C/20 or C/100 for PV systems. Also, based on equation (2.17), the software tool offers the designer a wide range of choices in selecting the design parameters to properly size the batteries.

The battery bank may contain batteries in series or parallel or series/parallel connections to achieve desired capacity and system voltage. For batteries connected in series, the voltage of the string is additive while the amp-hour rating is the same as for a single battery since the same current flows through the string. For parallel connected batteries, the voltage across each remains the same while the amp-hour is additive. Hence, the designer can choose the desired configuration and topology for the battery bank based on equations (2.18) – (2.20), also embedded in the algorithm [40-44].

$$N_P = \frac{C_X}{C_{CH}} \tag{2.18}$$

$$N_S = \frac{V_{dc}}{V_{bat}} \tag{2.19}$$

$$N_T = N_P \times N_S \tag{2.20}$$

where N_P is the number of batteries to be connected in parallel. If N_P is a fractional number, the system designer must decide whether to round up, to round down or to use a battery of different size; C_{CH} is the capacity of the individual battery the designer has chosen for the design; N_S is the number of batteries to be connected in series to achieve the system voltage; V_{bat} is the voltage of the battery chosen to achieve the system voltage; N_T is the total number of batteries in the series-parallel battery bank.

The number of parallel strings is generally chosen to be less than four to provide better balance of battery currents. The designer can ensure this by choosing higher capacity batteries. Fig. 2.18 is the user-interface developed to help the designer input the desired battery parameters.

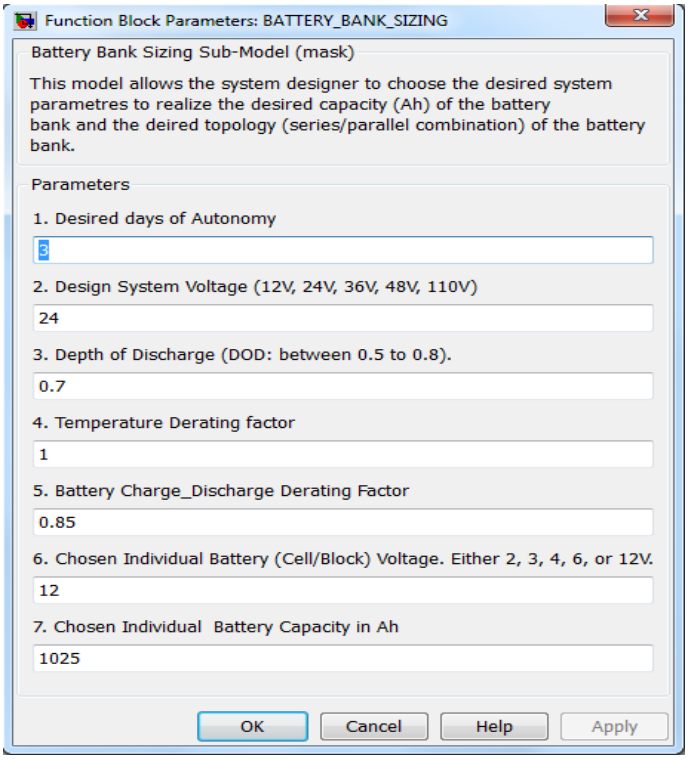

Fig. 2.18: Developed user interface in Simulink for sizing the battery bank sub model.

2.6.4 Inverter

Proper sizing of the inverter requires the specification of the following [44]: 1) dc input voltage, which corresponds to the system voltage, 2) ac output voltage for operation of the 1-phase or 3-phase loads, 3) continuous power handling capability, and 4) surge power capability, that defines the amount of power it can effectively supply for brief periods of time. The designer selects the desired system voltage based on the trade-off between using higher voltage and lower current or lower voltage and higher current. The maximum demand and the surge demand values in VA or kVA are the outputs of the load assessment sub model.

The maximum demand is based on the summation of the power demands of all loads that could operate simultaneously, while the surge demand is based on loads with larger starting currents (surges), especially inductive loads. The inverter is selected to meet these two requirements. That is, [44], [45]:

$$P_{INVC} > D_{\max} \tag{2.21}$$

$$P_{INVS} > S_{surg} \tag{2.22}$$

where P_{INVC} is the continuous power rating of the inverter, D_{max} is the maximum demand of ac loads, P_{INVS} is the surge power rating of the inverter, and S_{surg} is the surge demand of the highest rated ac load.

Thus, the algorithm for this sub model allows the designer to choose the design parameters for an inverter to meet the desired specifications and make provision for future load growth based on his chosen load management strategy. A safety factor, S_F, is also included to allow a small margin of oversize to account for uncertainty in the load data.

2.6.5 Charge Controller

The charge controller performs the following three main functions [45]: 1) it prevents the overcharging of the battery bank; 2) it prevents over discharge of the batteries, and 3) it performs system monitoring. The charge controller is sized to satisfy the following conditions:

$$I_R = 1.25 \times I_{SC} \tag{2.23}$$

$$V_R \geq V_{Nom} \tag{2.24}$$

where I_R is the current rating, I_{SC} is the short-circuit current of the PV array or sub-array being regulated; V_R is the voltage rating, and V_{Nom} is the nominal voltage of the PV array.

2.7 Case Study and Simulation Results

This section deals with the following:

- Testing of the tool for accuracy and robustness via the use of a case study, and
- Discussions of the simulation results.

2.7.1 Case Study

Table 2.3 shows the electrical loads for a household, which is to be supplied with ac power by a sine wave inverter [46]. The load management strategy agreed with the client is that:

- It is possible that any or all lights may be on at once.

- The computer may be on at any time, but the laser printer is used infrequently.
- Ironing is not done at the same time as vacuum cleaning, washing or drilling.

The location of the site is about 200 km from Perth in Western Australia. This case study describes the design of an off-grid PV-only power system that will meet these requirements using the developed software tool.

2.7.2 Simulation Results and Discussions

The input design parameters, entered via the user-interfaces of the sub models, used for the simulation of this case study are shown in Table 2.4. The simulation results which give the sizing values of the components are shown in Table 2.5. From Table 2.5, it is seen that the system's daily energy requirement of 3.32kWh needs an array power of 1.123kW for an average peak sun hour of 5.8 at the site. To meet this requirement, an array topology of *1S x 4P* **(**1 series x 4 parallel connections**)** of 300Wp modules is required to give a plant installed capacity of 1.2kW$_{P.}$

Similarly, a battery bank with capacity of 821.30Ah is required to meet the requirement, even for 3 days without sunlight (autonomy) and the topology is *2S x 1P* with the chosen battery of 1025Ah @ C/100 discharge rate. For the power conditioners, an inverter with maximum demand of 2.8kVA and a surge demand of 4.8kVA is capable of meeting the load requirement and so also is a charge controller with a current rating of 40A.

Table 2.3: Electrical loads for a Perth household [46].

Appliance Name	Number	Power (W)	Surge Apparent Power (VA)	Usage Hours
Compact fluorescent lamps	3	15		5.0
Incandescent lamps	3	60		0.25
370-litre refrigerator	1	200	1400	10.0
TV/Stereo	1	40		1.5
Computer	1	20		3.0
Laser printer	1	500		0.5
Vacuum cleaner	1	1000	3000	0.14
Washing machine	1	300	2100	0.11
Electric drill	1	600	1800	0.07
Iron	1	1200		0.14

Table 2.4: Input design parameters.

Design Parameters	Chosen Value
System voltage (V)	24.0
Peak sun hours (PSH) for Perth	5.8
Battery days of autonomy	3.0
Maximum depth of discharge (DOD)	70%
Chosen battery voltage (V)	12
Chosen battery capacity (Ah) @ C/100	1025
Charge/discharge efficiency of battery	85%
Temperature derating factor for batteries	1.0
Inverter efficiency, η_{INV},	85%
Safety factor for inverter sizing	10%
Chosen module peak power (W_P)	300
Chosen module nominal voltage (V)	24
Sub-system efficiency, η_{SS},	75%
Module derating factor for soiling & degradation	0.8
Balance of systems (BOS) factor	1.3

Table 2.5: Simulation results - sizing parameters.

System parameter	Output value
Total daily energy consumption (Wh)	3,323.0
Peak array power required (W)	1,123.0
Number of modules in parallel	4.0
Number of modules in series	1.0
Total number of modules	4.0
Total battery capacity required (Ah)	821.30
Number of batteries in parallel	1.0
Number of batteries in series	2.0
Total number of batteries in the bank	2.0
Suggested inverter maximum demand (kVA)	2.8
Suggested inverter surge demand (kVA)	4.8
Suggested charge controller current rating (A)	40.0

2.8 Conclusions

The first part of this chapter has reviewed the various PV cell technologies available in the market and presented a comparative analysis of them. An analysis of the photovoltaic cell is followed by the development of the simulation model using Matlab/Simulink software. The developed model has been subjected to the vagaries of temperature and irradiation and their effects on system performance studied. It is evident from the simulation studies using the developed model that: 1) the module output current is directly proportional to the solar intensity, 2) the module output voltage is inversely proportional to the ambient temperature, 3) the module power has a positive linear relationship with the irradiation and a negative linear relationship with the ambient temperature, 4) module efficiency decreases with increasing ambient temperature, and 5) solar generation intermittency and variability are mainly due to the ever-changing irradiation and ambient temperature.

The final part of this chapter has presented a robust, user-friendly design tool based on the Matlab/Simulink software. To ensure high level of reliability, the design procedure involved

three levels of iterative testing phases. The unit-level testing phase was done repeatedly to ensure to satisfactory working of the individual programme units (the sub models) while the integration-level testing phase ensured compatibility of the various sub models. Finally, the system-level testing ensured system stability, functionality and robustness. Series of test-find fault-fix cycles were performed for each of these levels of testing. This three-level approach to reliability ensured the accuracy of the simulation results.

Chapter 3

Analysis, Design and Control of SEPIC DC-DC Converter for Photovoltaic Energy Harvesting

3.1 Introduction

Power converters are electronic circuits associated with the conversion, control and conditioning of electric power. The efficient conversion of energy from one stage to another is essential for renewable energy systems to achieve optimum performance. The variable and intermittent output of a photovoltaic power generator needs to be converted, controlled and conditioned properly before utilization in a stand-alone system or connection to the grid to avoid grid instability or failure [47].

The utilization of power electronics in renewable energy systems has grown in the last decade for the following reasons [48]:

i) The development of fast semiconductor switches that are capable of handling high power and switching at high frequencies. This is especially the case with insulated gate bipolar transistors (IGBTs) and metal oxide semiconductor field effect transistors (MOSFETs).

ii) The availability of microcontrollers and digital signal processors with capabilities for processing advanced and complex control algorithms. These offer the possibility of implementation of precise and fast control of system voltage, current and frequency.

In a photovoltaic power system, a dc-dc conversion stage is followed by a dc-ac conversion stage to make the power suitable for ac load utilization. The dc-dc converter is responsible for boosting the PV array voltage up and ensuring maximum utilization of the PV power. It converts the variable output of the solar array into a regulated and stabilized output irrespective of load or input variations. The dc-dc converter has to provide a voltage high enough to meet the requirements of the dc-ac converter that is often connected to its output in

a two-stage cascaded connection. Different dc-dc converter topologies that can be used for PV applications include the following non-isolated converters [49], [50]:

- Buck converter: this is a step-down topology that provides a lower output voltage than the input voltage.
- Boost converter: this is a step-up topology which provides an output voltage higher than the input.
- Buck-boost converter: the output voltage of this converter may be less than or greater than the input voltage and has a reverse polarity.
- SEPIC (single ended primary inductance converter) converter: this is a boost-buck topology, and is the converter chosen for this study because of the features described later.

Also, the isolated dc-dc converters which incorporate high frequency transformers to provide isolation between the input and the output are frequently used in PV applications. Some converters in this group include: half-bridge, full-bridge, fly-back, forward, and push-pull dc-dc converters [49].

This chapter delves into the analysis and design of the SEPIC converter topology, which directly interfaces the solar array for this study. A detailed review of both dc analysis and the small signal analysis of the SEPIC converter is carried out first, then an 800W SEPIC converter is designed. This is followed by the development of a control strategy based on a single loop control. The designed SEPIC converter, the developed control system, and a two-panel solar array - developed earlier in Chapter 2, are then integrated and used for simulation studies in the Simulink/SimPowerSystems platform. The developed simulation model is then used to investigate the dynamic responses of the PV system in both open-loop and closed-loop operations. Responses to changes in duty cycle, input voltage fluctuations with changes in environmental variables – temperature and irradiation - are presented and discussed.

3.2 Review of the Operation and Analysis of the SEPIC DC-DC Converter

3.2.1 Features of the SEPIC Converter

The Single Ended Primary Inductance Converter (SEPIC) is a dc-dc converter topology that has recently become of much interest to design engineers following the recent expiration of

its patent [50]. The SEPIC converter has been chosen for implementation of the dc-dc conversion stage in this study because of the following unique merits [51-53]:

a. It has the ability to either step-up or step-down the input dc voltage.
b. Unlike the traditional buck-boost converter, the SEPIC topology produces a non-inverted output. That is, the output voltage has the same polarity as the input voltage.
c. The input and output voltages are dc isolated by a coupling capacitor. With this capacitive isolation, failure of the power switch will short the input without affecting the output. Thus, the output load is protected. The capacitor also prevents unwanted current flow from the input supply to the output, thus overcoming the limitation of the simple boost converter.
d. It has a true shutdown mode: when the power switch is turned off, its output drops to zero.
e. It uses two low cost inductors to transfer energy from input to the output.
f. It is operable over wide input voltage range.
g. It needs low ESR (equivalent series resistance) capacitors and these are now widely available.
h. It maintains the same ground reference for both input and output, which reduces control complexity.

3.2.2 Operation of the SEPIC Converter

A schematic circuit of the basic SEPIC topology is shown in Fig. 3.1. The operation of the SEPIC is better understood via its two modes of operation: *Mode1* - when the power switch, Q1, is turned *ON* and *Mode 2*, when the power switch is turned *OFF*. These two modes are depicted in Figs. 3.2 and 3.3 below [51].

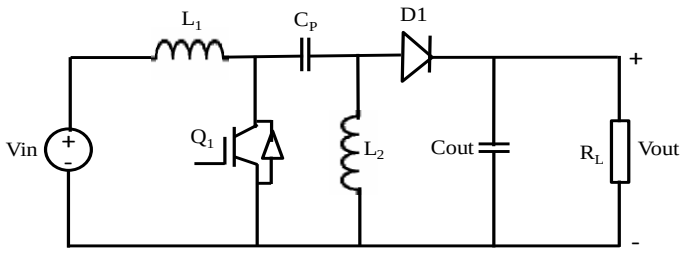

Fig. 3.1: Schematic circuit of the SEPIC converter.

Mode1 Operation:

In *Mode1* operation, the power switch, *Q1*, is turned *ON* and the diode, *D1*, is turned *OFF*, as in Fig. 3.2. When this occurs, the input inductor, L_1, is charged from the input voltage source, V_{in}. The output inductor, L_2, takes energy from the coupling capacitor, C_p, and the output capacitor, C_{out}, is left to supply the load current. Thus, L_1 and L_2 are both disconnected from the load when the switch is turned *ON* [53].

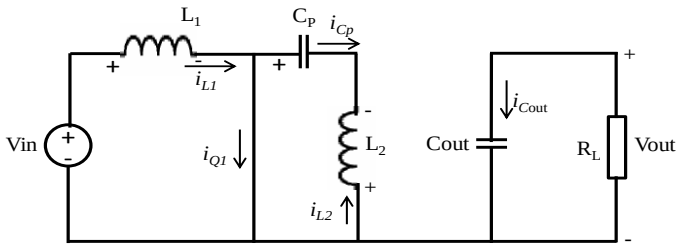

Fig. 3.2: Mode 1: Power switch turned *ON*, diode turned *OFF*.

Mode2 Operation:

In *Mode2* operation, the power switch is turned *OFF* and the diode turned *ON* as in Fig. 3.3. When this occurs, the input inductor, L_1, charges the coupling capacitor, C_p, and also supplies current to the load. The output inductor, L_2, also supplies the load current during this mode and the output capacitor sees a burst of current during this time [53].

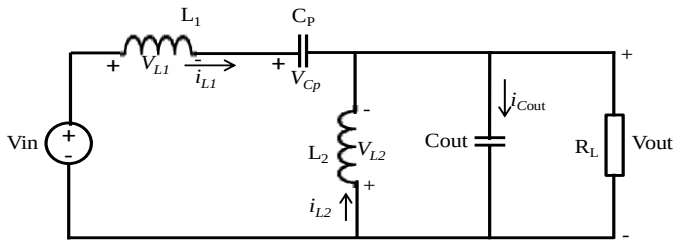

Fig. 3.3: Mode 2: Power Switch turned *OFF*, diode turned *ON*.

3.2.3 DC Analysis of the SEPIC Converter

3.2.3.1 Derivation of Input/Output Voltage Relationship

The derivation of the input/output transfer function is based on the following assumptions [51]:

1. The inductor currents are continuous.
2. The input and output inductors are large with constant currents.
3. The capacitor values are large and they have constant voltages.

4. The operation is in steady state.
5. The power switch is *ON* for time *DT* and *OFF* for time, *(1-D) T*, where *D* is the duty ratio and *T* is the switching period.
6. The components are assumed ideal.

A) Analysis for Mode1 Operation (Power Switch ON):

When the power switch, *Q1*, is *ON*, the diode is reverse biased and is *OFF* and the resulting equivalent circuit is as in Fig. 3.2. Applying Kirchhoff's voltage law, KVL, to this circuit gives [51]:

$$-V_{in} + V_{L1} + V_{Cp} - V_{L2} = 0.$$

Since for periodic currents, the average voltage across an inductor is zero,

$$-V_{in} + 0 + V_{Cp} - 0 = 0.$$

Thus, the average voltage across the capacitor, C_P, is

$$V_{Cp} = V_{in} \tag{3.1}$$

Also, from the equivalent circuit, the voltage across L_1 for this *ON* interval, *DT* is given by:

$$V_{L1} = V_{in} \tag{3.2}$$

B) Analysis for Mode 2 Operation (Power Switch OFF):

When the power switch is *OFF*, the diode is *ON* and the equivalent circuit is as shown in Fig. 3.3 above. Applying KVL to the outermost loop gives [51]:

$$-V_{in} + V_{L1} + V_{Cp} + V_{out} = 0. \tag{3.3}$$

Substituting equation (3.1) into equation (3.3) gives

$$-V_{in} + V_{L1} + V_{in} + V_{out} = 0$$

This simplifies to:

$$V_{L1} = -V_{out} \tag{3.4}$$

Since the average voltage across an inductor is zero for periodic waveform, combination of equations (3.2) and (3.4) give:

$$V_{in}(DT) - V_{out}(1-D)T = 0$$

Giving the average output voltage as [51], [53]:

$$V_{out} = V_{in} \frac{D}{1-D} \tag{3.5}$$

where D is the duty ratio. Equation (3.5) can be re-written as:

$$D = \frac{V_{out}}{V_o + V_{in}} \tag{3.6}$$

3.2.3.2 Determination of Minimum Inductance for Continuous Conduction

From power balance relation, $P_{in} = P_o$, where P_{in} is the input power from the dc source and P_o is the output power. Therefore,

$$V_{in} \times I_{in} = V_{out} \times I_{out} \tag{3.7}$$

And the input current, I_{in}, is the same as in inductor, L_1.Thus, equation (3.7) becomes

$$V_{in} \times I_{L1} = V_{out} \times I_{out} \tag{3.8}$$

Thus, the average inductor current which is also the source current is given by [50], [51]:

$$I_{L1} = I_{in} = \frac{V_{out} \times I_{out}}{V_{in}} \tag{3.9}$$

The peak-to-peak ripple current, ΔI_{L1}, is found from the inductor relation when the switch is closed, as [51]:

$$V_{L1} = V_{in} = L_1 \frac{di_{L1}}{dt} = L_1 \frac{\Delta i_{L1}}{\Delta t} = L_1 \frac{\Delta i_{L1}}{DT} \tag{3.10}$$

Solving for Δi_{L1} gives,

$$\Delta i_{L1} = \frac{V_{in} \times D \times T}{L_1} = \frac{V_{in} \times D}{L_1 \times f_s} \tag{3.11}$$

Where f_s is the switching frequency. Therefore, from equation (3.11), the desired value of inductance, L_1, for continuous conduction is given by [50], [51]:

$$L_1 = \frac{V_{in} \times D}{\Delta i_{L1} \times f_s} \tag{3.12}$$

Similar analysis for inductor, L_2, gives the critical value for continuous conduction as

$$L_2 = \frac{V_{IN} \times D}{\Delta i_{L2} \times f_s} \tag{3.13}$$

3.2.3.3 Output Voltage Ripple of the SEPIC Converter

In practice, due to the finite value of the output capacitance, some fluctuations in output voltage or ripple exist [50], [51]. The peak-to-peak voltage, ΔV_o, of the output capacitor can be calculated from the capacitor output waveform. From the capacitor charge relationship, the charge in the capacitor is given by:

$$\Delta Q = \frac{V_{out}}{R} \times DT = C_{out} \Delta V_{out}$$

This gives the ripple voltage as:

$$\Delta V_o = \frac{V_{out} \times D \times T}{R \times C_{out}} = \frac{V_{out} \times D}{R \times C_{out} \times f_s} \tag{3.14}$$

This can be expressed as:

$$\frac{\Delta V_{out}}{V_o} = \frac{D}{R \times C_{out} \times f_s} \tag{3.15}$$

This gives the output capacitance as:

$$C_{out} = \frac{D}{R \times \frac{\Delta V_{out}}{V_{out}} \times f_s} \tag{3.16}$$

Similarly, for the coupling capacitor, C_p, the value of capacitance is given by:

$$C_P = \frac{D}{R \times \frac{\Delta V_{Cp}}{V_{out}} \times f_s} \tag{3.17}$$

3.3 Small Signal Model of the SEPIC Converter

To design the complete SEPIC converter with the integrated feedback control, a dynamic model of the converter is required. By the use of the ac equivalent circuit model, the dynamics introduced by the inductors, capacitors and the semiconductor devices are taken into account. This dynamic model provides physical insight into the system's behaviour. The developed small signal model can be solved using conventional circuit techniques to find the small-signal transfer function, output impedance and other frequency dependent properties. The three popular analytical approaches used in small-signal modelling are [53-56]:

- Circuit averaging;
- State-space averaging; and
- PWM switch model.

The best way to analyse the ac characteristics of the SEPIC converter is by using the PWM switch model [53].According to [53], the analysis of the SEPIC converter, which is a fourth order converter, yields the following result for the control-to-output transfer function:

$$\frac{v_o(s)}{d(s)} = \frac{1}{D^{'2}} \times \frac{\left(1 - s\frac{L_1}{R} \times \frac{D^2}{D^{'2}}\right) \times \left(1 - s\frac{C_1(L_1 + L_2)R}{L_1}\right) \times \frac{D^{'2}}{D^2} + s^2 \frac{L_2 C_1}{D}}{\left(1 + \frac{s}{\omega_{o1} Q_1} + \frac{s^2}{(\omega_{o1})^2}\right) \times \left(1 + \frac{s}{\omega_{o2} Q_2} + \frac{s^2}{(\omega_{o2})^2}\right)} \tag{3.18}$$

Where the first resonance is given by:

$$\omega_{o1} = \frac{1}{\sqrt{L_1\left(C_2 \times \frac{D^2}{D^{'2}} + C_1\right) + L_2(C_1 + C_2)}} \tag{3.19}$$

The first quality factor is given by:

$$Q_1 = \frac{R}{\omega_{o1}\left(L_1 \times \frac{D^2}{D^{'2}} + L_2\right)} \tag{3.20}$$

The second resonance is given by:

$$\omega_{o2} = \sqrt{\frac{1}{L_2 \times \left(\frac{(C_1 C_2)/(D^2 D^{'2})}{(C_1/D^2) + (C_2/D^{'2})}\right)} + \frac{1}{L_1 \times \frac{C_1 C_2}{C_1 + C_2}}} \tag{3.21}$$

And the second quality factor is given by:

$$Q_2 = \frac{R}{\omega_{o2}(L_1 + L_2) \times \frac{C_1}{C_2} \times \frac{\omega^2_{o1}}{\omega^2_{o2}}} \tag{3.22}$$

Also,

$C_1 = C_p$ of Fig. 3.1; $C_2 = C_{out}$ of Fig. 3.1; D is the duty cycle and $D' = 1\text{-}D$.

3.4 Design of the Proposed 800W SEPIC Converter for the PV System

Design Specifications:

Input voltage range, V_{in}: 12 – 48VDC.

Output voltage, V_{out} : 180VDC.

Output power, $P_{out:}$ 800W.

Current ripple, ΔI_L: 30% of $I_{in.}$

Voltage ripple, ΔV_{out}: 2%.

Desired efficiency, η: > 90%

3.4.1 Power Components Sizing

Step 1: Choice of Switching Frequency:

The three factors that influenced the choice of the switching frequency for this design are [50], [54]:

- The switching power losses,
- The size of the components – inductors and capacitors,
- The limitations of the controller, DS1104, used for the implementation of the prototype. This is considered in details in Chapter 7.

To satisfy these three requirements, a switching frequency, *Fs*, of 25 kHz is chosen for this design.

That is,

$\underline{Fs = 25\ \text{kHz.}}$

Step 2: Calculation of the Operating Duty Cycle:

The minimum value of the duty cycle, D_{min} is evaluated using the relationship [55]:

$$D_{\min} = \frac{V_{out}+V_d}{V_{out}+V_{in(\max)}+V_d} \tag{3.23}$$

Where V_d is the voltage drop across the diode, *D1*. Substituting values in equation (3.23) yields:

$$D_{\min} = \frac{180+0.5}{180+48+0.5} = 0.79$$

where $V_d = 0.5$.

$$\therefore D_{\min} = 0.79$$

Similarly, the maximum Duty cycle, D_{max}, is evaluated using the relationship [55]:

$$D_{\max} = \frac{V_{out} + V_d}{V_{out} + V_{in(\min)} + V_d} \tag{3.24}$$

Substituting values gives

$$D_{\max} = \frac{180 + 0.5}{180 + 12 + 0.5} = 0.93$$

$$\therefore D_{\max} = 0.93$$

Step 3: Calculation of the Inductances:

From the specifications, the inductor ripple current, ΔI_L = 30% of maximum input current at minimum input voltage, $V_{in.}$ That is,

$$\Delta I_L = 30\% I_{in} \tag{3.25}$$

From the power balance relation,

$$P_{out} = \eta \times P_{in} \tag{3.26}$$

Therefore,

$$I_{in} = \frac{V_{out} \times I_{out}}{\eta \times V_{in(\min)}} \tag{3.27}$$

From equations (3.25) and (3.27),

$$\Delta I_L = 30\% I_{in} = \frac{0.3 \times V_{out} \times I_{out}}{\eta \times V_{in(\min)}} \tag{3.28}$$

Where I_{out} = 800/180 = 4.44 Amperes.

Substituting values in equation (3.28) yields:

$$\Delta I_L = \frac{0.3 \times 180 \times 4.44}{0.9 \times 12} = 22.2A.$$

The minimum value of inductance is given by:

$$L_1 = L_2 = \frac{V_{IN(\min)} \times D_{\max}}{\Delta I_L \times f_s} \tag{3.29}$$

Substituting values in equation (3.29) gives:

$$L_{1(\min)} = L_{2(\min)} = \frac{12 \times 0.93}{22.2 \times 25 \times 1000} = 20.12\mu H$$

To achieve 90% efficiency at the minimum input voltage, the power loss in the inductor has to be limited to around 2 - 3% of the total output power. Using 3% loss in the inductor, L_1 gives:

$$P_{L1} = 0.03 \times V_{o(\max)} \times I_{o(\max)} \tag{3.30}$$

$$= 0.03 \times 180 \times 4.44 = 24W$$

Assuming an 80 - 20% ratio in the inductor losses between resistive and core losses, the DC resistance (*DCR*) of the inductor has to be less than [50]:

$$DCR < \frac{0.8 \times P_{L1}}{I_{in(\max)^2}} \tag{3.31}$$

Where,

$$I_{in(\max)} = \frac{V_{out} \times I_{out}}{\eta \times V_{in(\min)}} \tag{3.32}$$

Therefore, from (3.31) and (3.32),

$$\underline{\text{DCR} < 0.004\ \Omega}$$

Also, the inductors are chosen such that their peak current values meet the following conditions:

$$I_{L(pk)} > I_{out} + 0.5\Delta I_L \tag{3.33}$$

Substituting values gives:

$$I_{L(pk)} > (4.44 + 0.5 \times 22.2)A = 15.5A$$

$$\therefore I_{L(pk)} > 15.5A$$

Thus, the inductors *L1* and *L2* are chosen to satisfy these three conditions:

a) Inductance value must be greater than 20.12µH**.**
b) Must have a dc resistance of about 0.004 Ω**.** The nearest practical value is chosen.
c) A saturation current greater than: 15.5A.

The actual values used in simulation and for the prototype, to satisfy these conditions, are:

L1 = 85 µH.

L2 = 85µH.

Step 4: Calculation of the Coupling Capacitor Value:

The selection of this capacitor depends on three factors:

(i) The rms current, which is given by [55]

$$I_{Cp(rms)} = I_{out} \times \sqrt{\frac{V_{out} \times V_D}{V_{in(\min)}}} \tag{3.34}$$

$$= 4.44 \times \sqrt{\frac{180 \times 0.5}{12}}$$

$$= 12.2 \text{ A}$$

(ii) The peak-to- peak ripple voltage on C_p, which is given by:

$$\Delta V_{C_p} = \frac{I_{out} \times D_{\max}}{C_P \times f_s} \tag{3.35}$$

This gives:

$$C_P = \frac{I_{out} \times D_{\max}}{\Delta V_{C_P} \times f_s} \tag{3.36}$$

Design assumption: Let ripple voltage = 5% of minimum input voltage.

That is,

$$\Delta V_{C_p} = 5\% \times V_{in} = \frac{5}{100} \times 12 = 0.6V$$

Therefore from equation (3.36):

$$C_P = \frac{4.44 \times 0.93}{0.6 \times 25{,}000}$$

$$= 275\mu\text{F}$$

(iii) Voltage rating greater than the maximum input voltage of 48VDC.

Thus the coupling capacitor, C_p, must satisfy the following three conditions:

a) Current Rating must be greater than 12.2A.

b) Capacitance must be greater than 275µF.

c) Voltage rating must be greater than 48VDC.

The capacitor chosen for this design to satisfy these conditions is:

Cp = 330 µF

Step 5: Calculation of the Output Capacitor Value:

The output capacitor must meet the following requirements:

(i) The rms current rating, $I_{Cout(\text{rms})}$, must satisfy the condition [50], [55]:

$$I_{C_{out(rms)}} > I_{out} \times \sqrt{\frac{V_{out} + V_d}{V_{in(\min)}}} \tag{3.37}$$

Substituting values give

$$I_{C_{out(rms)}} > 4.44 \times \sqrt{\frac{180 + 0.5}{12}}$$

Therefore, $I_{C_{out(rms)}} > 17.2A$

The equivalent series resistance, *ESR*, must satisfy the following condition:

$$ESR \leq \frac{V_{ripple} \times 0.5}{I_{L_{1(pk)}} + I_{L_{2(pk)}}} \tag{3.38}$$

Assume, $V_{ripple} = 2\% V_{out}$

Therefore,

$$ESR \leq \frac{0.02 \times 180 \times 0.5}{15.5 + 15.5}$$

$$\therefore ESR \leq 58m\Omega$$

(ii) The capacitance must satisfy [51]:

$$C_{out} \geq \frac{I_{out} \times D_{\max}}{V_{ripple} \times 0.5 \times f_s} \tag{3.39}$$

Substituting values yields:

$$C_{out} \geq \frac{4.44 \times 0.93}{0.02 \times 180 \times 0.5 \times 25{,}000} = 91.76\mu F$$

Therefore, the capacitor, C_{out}, must satisfy the following conditions:

i) Current capability >> 17.2A.

ii) ESR << 58mΩ

iii) Capacitance >> 91.76µF.

Therefore, the practical value chosen to satisfy these conditions is:

C_{out} = 100 µF

Step 6: Sizing the Output Diode:

The diode is selected to meet these two requirements:

i) The current rating ,I_D, must satisfy the relation:

$$I_D > (I_{L_{1(pk)}} + I_{L_{2(pk)}}) \tag{3.40}$$

Substituting values gives,

$$I_D > (15.5 + 15.5) = 31A.$$

ii) The peak inverse voltage, PIV, rating must satisfy this condition:

$$PIV > (V_{in(\max)} + V_{out} + V_D) \tag{3.41}$$

Substituting values give:

$$PIV > (48 + 180 + 0.5) = 228.5V$$

Using a safety margin of 15%, the PIV rating of the Schottky diode becomes: 1.15 x 228.5 = 263V.Thus, for this design, the diode chosen is a:

270V, 35A Schottky diode.

Step 7: Sizing the IGBT Power Switch:

The switch voltage requirement, $V_{SQ,}$ is given by:

$$V_{SQ} > (V_{in(\max)} + V_{out} + V_D)$$

$$\therefore V_{SQ} > (48 + 180 + 0.5) = 228.5V$$

$$\therefore V_{SQ} > 228.5V$$

Using a safety margin of 15% as in the case of the diode, V_{SQ} =1.15x228.5 =263V,

The switch current requirement, I_{SQ}, is given by:

$$I_{SQ} > (I_{L1(pk)} + I_{L2(pk)})$$

$$\therefore I_{SQ} > (15.5 + 15.5) = 31A$$

$$\therefore I_{SQ} > 31A$$

Thus, for this design, the power switch chosen is a:

600V, 35A IGBT switch.

3.5 The Proposed Closed-loop Control

The output voltage of the SEPIC converter must be kept constant regardless of changes in the input voltage from the photovoltaic array, which is ever-changing, or changes in the system's loading or variations in component values. The closed-loop control circuit has to be designed with care, since the duty cycle has to be continually varied to maintain the output voltage at the desired set value. An effective closed-loop control would ensure good transient performance by reducing transients and good steady state performance by effectively tracking the reference output value [54]. In addition, such a system should be stable. To accomplish these functions, a Proportional-plus-Integral (PI) controller is designed for this study.

A block diagram of a single loop feedback system based on the voltage mode control is shown in Fig. 3.4. While Fig. 3.4(a) shows the single loop control of the SEPIC converter, Fig. 3.4(b) shows the functional block diagram of the associated feedback loop. The output voltage, $v_o(t)$ is measured using a voltage sensor. In the prototype implementation discussed in Chapter 7 of this thesis, the sensor circuit is based on the Hall-effect voltage sensor with integrated signal conditioner/amplifier using the instrumentation amplifier - INA118. The sensor output signal is compared with the reference input voltage, v_{ref}. The aim is to make the sensor output equal to the reference voltage regardless of the disturbances or component variations in the PWM, the compensator or the power converter components.

The error signal, $v_e(t)$ is the difference between the reference input and the sensor output. The error signal is used by the compensator to generate the control signal, $v_c(t)$. The compensator used for this project is based on the proportional-plus-integral (PI) controller, which conditions the error signal to achieve the desired transient response, steady state value and required system stability. The details of this controller are discussed in the subsection below. The control signal is then used in the pulse width modulator, PWM, to compare a triangular carrier signal waveform. The output of the PWM block is a series of pulses, the duty cycle, d, used to control the power switch.

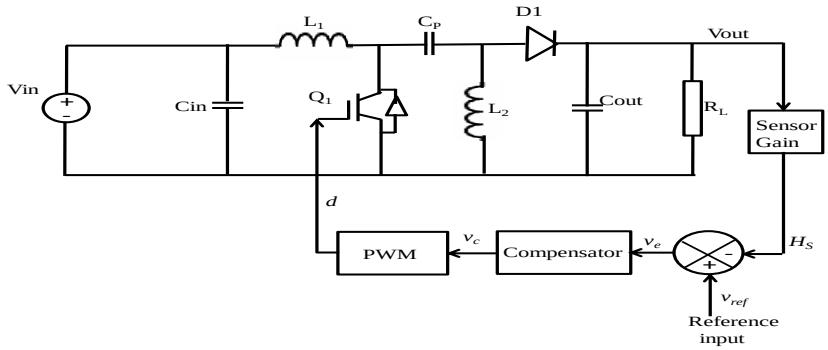

(a)

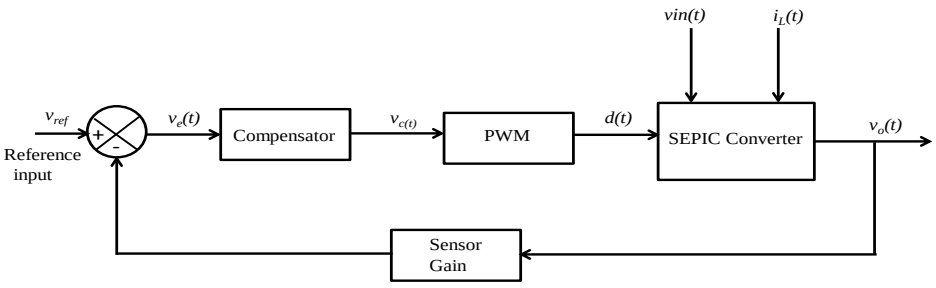

(b)

Fig. 3.4: Block diagram of the single-loop control for the SEPIC converter: (a) SEPIC converter with feedback loop; (b) functional block diagram of the feedback system.

3.5.1 Proportional-plus-Integral (PI) Controller Design

The key design goals of any dc-dc converter are to achieve the following [54], [56]:

- Steady output voltage in the face of load current variations;
- Steady output voltage in the face of input voltage variations;
- Desirable transient response time for disturbances in the load current or input voltage so as to quickly restore the output voltage to the desired value.
- Limited overshoot in the transient response.

Meeting each of these requirements imposes constraints on the loop gain of Fig. 3.4(b). Consequently, the design of any dc-dc power supply feedback control system invariably involves the modification of the loop gain. This modification is done via the compensating network. The compensation methodology adopted for the SEPIC converter feedback control system discussed in this chapter is based on the lag compensator, popularly known as the *Proportional-plus-integral*, or *PI* controller. By increasing the low-frequency gain, the inclusion of the PI controller ensures that the steady state output voltage is perfectly regulated by the rejection of disturbances. The *PI* controller has the transfer function [57], [58]:

$$G_{c(s)} = K_p + \frac{K_i}{s} \tag{3.42}$$

Where:

$G_{c(s)}$ represents the controller transfer function; K_p represents the proportional term gain; K_i represents the integral term gain. The block diagram representation of the digital *PI* controller, which is realised in software using the Simulink software, is shown in Fig.3.5.

From Fig. 3.4(b) and the previous analysis of Section 3.3 on the small signal modelling of the SEPIC converter, the analytical expression for the loop gain of the system is given by the cascade connection of all the blocks in (3.43).

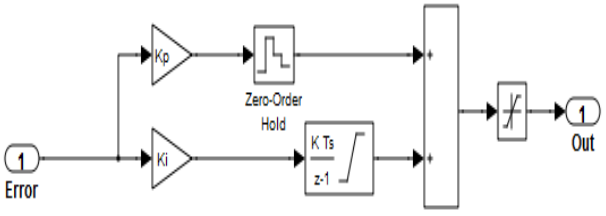

Fig. 3.5: Block diagram representation of the digital PI controller.

System loop gain = [converter open-loop control-to-output transfer function] x [PI controller transfer function] x [feedback gain] x [PWM gain] (3.43)

That is,

Loop gain= [equation (3.18)] x [equation (3.42)] x [feedback gain] x [PWM gain] (3.44)

In the design approach adopted for this paper, the proportional gain, K_p, and the integral gain, K_i, of the *PI* controller are tuned in Simulink to meet the desired system response. The values of these parameters are optimised using the method of Ziegler and Nichols [60], [61]. Some iteration is needed to tune these control parameters so that the closed-loop system gives satisfactory results during start up and abrupt load or input changes. The values used for the simulation studies in Section 3.6 are:

$K_p =$ 100; $K_i =$ 0.05.

3.6 Simulation Studies of the SEPIC Converter based PV System

3.6.1 Development of Dynamic Models for Simulation

To design a complete dc-dc converter incorporating the feedback system, a dynamic model of the switching converter is needed. The model is implemented using a dynamic system software simulator – in this case, the SimPowerSystems of Matlab/Simulink. To use component models that approximate the physical behaviour of the devices, the non-ideal component models of the IGBT-based power switch and the power diode of the SimPowerSystems software are used as shown in Figs 3.6 and 3.7. Such models provide physical insight into the switching transitions, switching losses, instantaneous voltage and current stresses, and responses to load or input transients.

Figs 3.6 and 3.7 integrate the two-panel PV array model developed earlier in Chapter 2, as the dc source, and the 800W SEPIC converter designed in Section 3.4 for the simulation models. The use of the PV array model is necessary to capture the effects of changing environmental variables on system performance. While Fig. 3.6 depicts the open-loop model, Fig. 3.7 shows the closed-loop model. The feedback loop of Fig. 3.7 incorporates the designed *PI* controller discussed in previous section, the unit delay to model the calculation delays associated with the PWM process and analogue-to-digital conversion, and the PWM block for the generation of the pulse train used to drive the IGBT-based power switch.

The variable output voltage of the two-panel solar array is boosted up to generate a regulated dc voltage of 180V – as indicated by the reference value, V_{ref}. The regulated output voltage serves as the input to the other subsystems discussed in subsequent sections – the bidirectional dc/dc converter, and the dc-ac converter. To achieve voltage regulation, the voltage mode rather than the current mode technique is used in this simulation studies. This technique is used in this section to show its capability. However, a superior control technique using a multi-loop approach integrating the current mode control and the maximum power point tracking technique is discussed and implemented in Chapter 4.

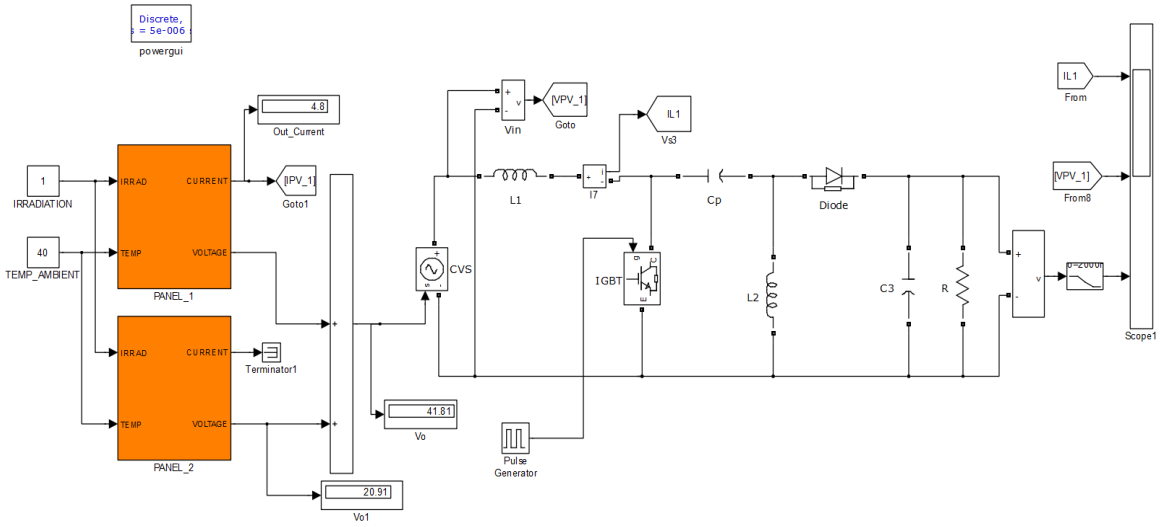

Fig. 3.6: Simulation model for open loop operation: SEPIC converter with integrated two-panel PV array in Simulink/SimPowerSystems software.

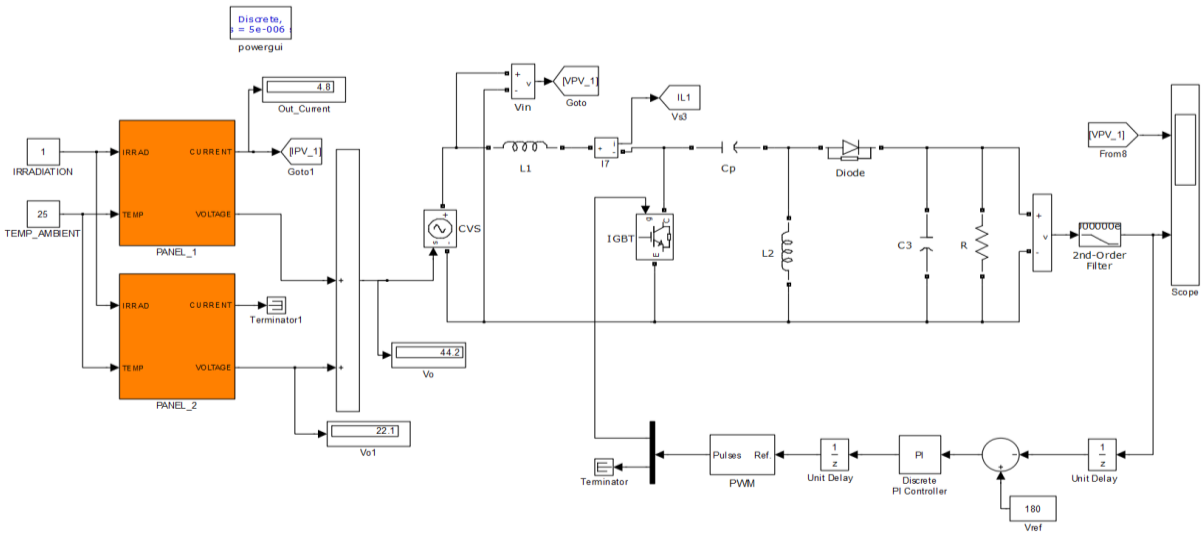

Fig. 3.7: Simulation model for closed-loop operation: SEPIC converter with integrated two-panel PV array in Simulink/SimPowerSystems software.

3.7 Simulation Results and Discussions

The responses of the PV power conversion system in both open-loop and closed-loop systems are investigated through simulations as discussed below.

3.7.1 Effect of Duty Cycle Variations on Open-loop Operation

The three major parameters that affect the output voltage of any dc power system – input voltage variation, load variations, and changes in the duty cycle values – are investigated for operation in the open-loop mode, Fig. 3.6. Specifically, Fig. 3.8 shows the variation in output voltage of the PV system with changes in the duty cycle. It is observed that increasing the duty cycle increases the output voltage, and similarly decreasing the duty cycle decreases the output voltage. This is the same situation with variations in input voltage. The essence of Fig. 3.8 is to show that without a controlled feedback loop, the system's performance in terms of voltage regulation and stability cannot be guaranteed.

3.7.2 Output Voltage Regulation

The closed-loop operation of Fig. 3.7 is simulated with a reference voltage of 180V, as shown. With the parameters of the *PI* controller tuned and the switching frequency of 25 kHz, the output voltage is shown in Fig. 3.9 for an input voltage of 44.2V at 1000W/m^2 and 25^{o}C (standard test condition) from the PV solar array – first subplot. An overshoot of approximately 240V occurs during the transient response when the simulation is first started

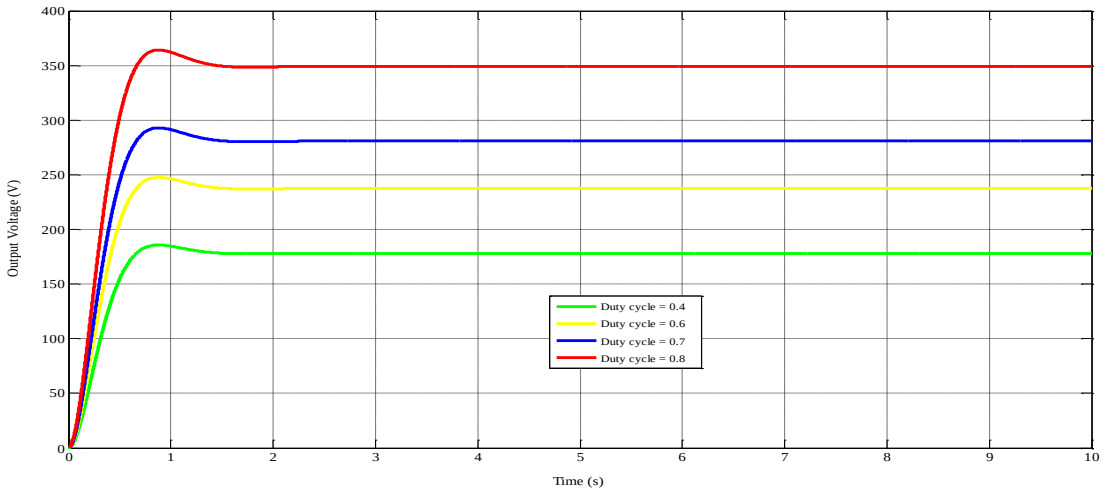

Fig. 3.8: Variation of output voltage with duty cycle for open loop operation.

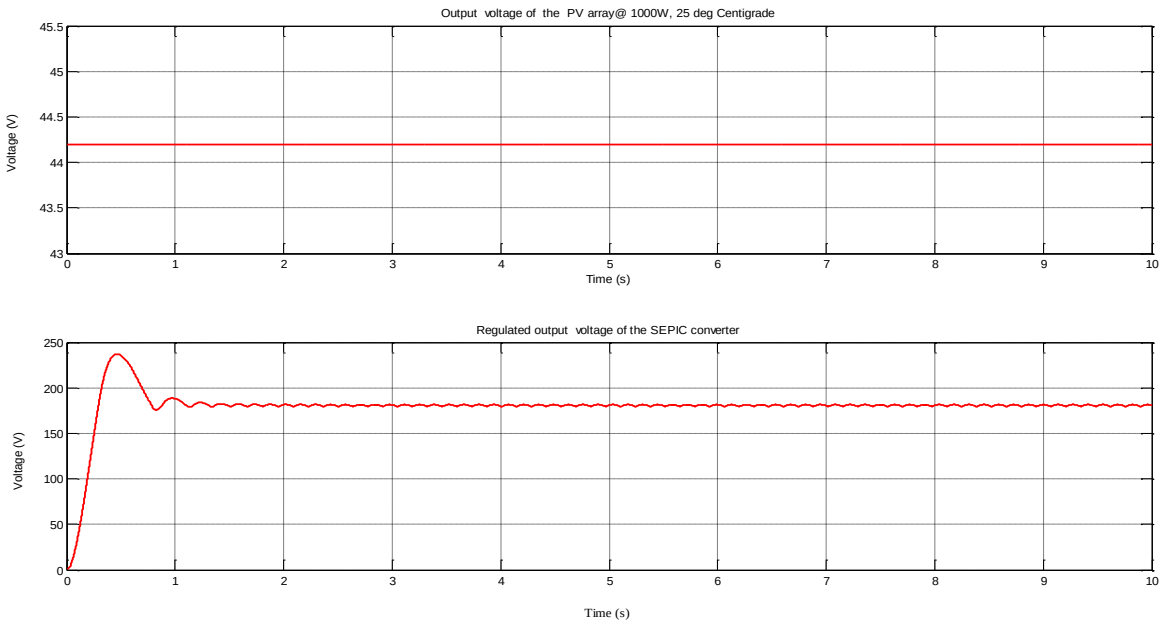

Fig. 3.9: Regulated output voltage of the SEPIC converter for a given PV array voltage. Top subplot shows the output of the PV array; bottom subplot shows the regulated output voltage of the converter.

(system start-up). The simulation shows that it takes approximately 1.1 seconds for the output voltage to reach ±2% of the desired output voltage of 180V. Thus, the steady-state error is almost eliminated. Also, comparison with the open-loop response of Fig.3.8 shows that the closed loop systems apart from providing the desired regulated voltage has a faster transient response, and hence attains the steady state value faster following system start-up.

3.7.3 Robustness Analysis: Input Voltage Fluctuations.

The two major environmental variables that affect the output of a PV array are temperature and irradiation. The response of the controlled converter to changes in the output voltage of the PV array occasioned by changes in the ambient temperature is considered in this section. The topmost subplot in Fig. 3.10 shows a drop in the ambient temperature from 25^{o}C to 15^{o}C, at step time 5seconds. This drop in temperature results in an increase in the output voltage of the PV array from 44.2V to 45.8V – shown in the middle subplot. For this drop in temperature and the associated rise in the output voltage of the PV array, the output voltage of the SEPIC converter (bottom subplot) is regulated at the desired output voltage of 180V.

The transient response and the steady-state error are within the desired ranges. This shows the robustness of the *PI* controlled PV system.

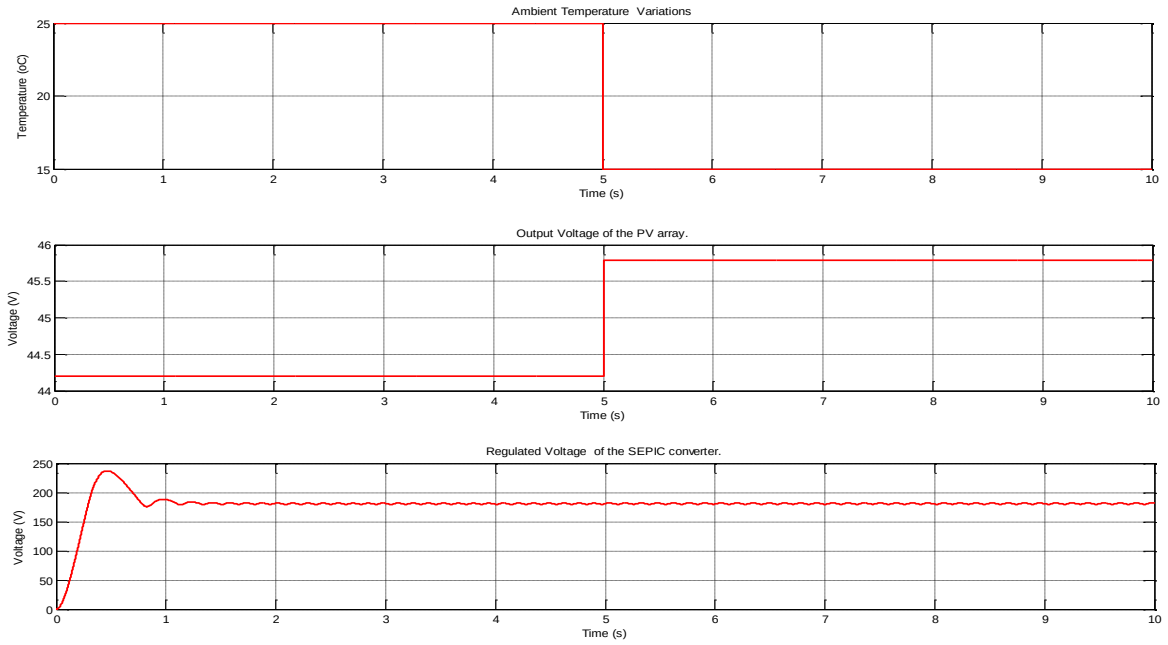

Fig. 3.10: Regulated output voltage for rapid drop in the ambient temperature. Topmost subplot is the drop in ambient temperature; middle subplot shows accompanying rise in PV output; bottom subplot is the regulated response of the converter to these changes.

3.8 Conclusions

Effectively converting the "raw energy" from sunlight into usable electrical energy requires a dc-dc converter. This chapter has presented the design and modelling of such a converter based on the SEPIC topology. The designed converter is integrated with a PV array model to study the performance of a PV power plant under open-loop and closed-loop controls. The open-loop PV power plant is seen to be sensitive to input disturbances – input voltage variations, system load changes, duty cycle variations and component variations – and lacks the ability to correct these disturbances. On the other hand, the closed-loop system compensates for these disturbances. The closed-loop offers the PV power plant greater accuracy, and the transient response and the steady-state error are more conveniently controlled using a compensator – a *PI* controller in this simulation. Moreover, any adjustment of the *PI* compensator parameters required to achieve a desired response can be made by changes in software.

Chapter 4

Maximum Power Point Tracking of Photovoltaic Modules and Closed Loop Control Techniques for DC-DC Power Converters.

4.1 Introduction

The power output of any photovoltaic module is a function of environmental variables like insolation (incident solar radiation), temperature, shading (from trees and cloud cover) and load conditions [62]. However, insolation and temperature conditions are the prime variables. Thus, the current-voltage (I-V) characteristics and the power-voltage (P-V) characteristics of solar modules are affected by the insolation and temperature levels. The output current and hence the output power increases linearly with insolation while the output voltage and hence the output power decreases with increasing temperature. These two environmental variables change constantly throughout the day and consequently give rise to the intermittency and variability associated with the production of energy by solar modules. However, the PV module has a single operating point where the values of the current and voltage of the module result in a maximum power output [62-64]. Fig. 4.1 and 4.2 show such an operating point for the current-voltage characteristics and power-voltage characteristics. As is seen in the figures, such a maximum power point (MPP) occurs at the knee of the curve. At this point, the module delivers the maximum power from the source to its load [64]. Ensuring that the PV module operates at this desired *MPP* and hence at the highest efficiency, requires a robust control strategy to track this ever-changing point [65], [66].

This tracking task is often implemented using maximum power point tracking (MPPT) control algorithm – several of which exist in the literature [67], [68]. Extraction of this maximum power is often done in conjunction with a power conditioning unit (dc-dc converter or dc-ac converters) as the interface between the PV modules and the system electrical load [62], [69]. Such power conditioning unit, in addition to ensuring operation at the *MPP* must also ensure the regulation of the output voltage and current irrespective of load and input voltage variations. Realisation of this robust regulation function requires the use of a closed-loop feedback system – which was briefly introduced in Chapter 3. A robust closed-

loop operation requires the use of current-mode control methodology rather than the voltage-mode approach, which was used earlier in the previous chapter.

This chapter discusses these two control approaches that ensure that the SEPIC converter based PV power system operates: 1) efficiently by extracting the maximum available power from the PV module and, 2) offers robust regulation of the output voltage and current using current-mode technique. Firstly, a review of the existing *MPPT* techniques is carried out, highlighting the pros and cons of each approach. This is followed by a review of some current-mode control methodologies. Thirdly, a robust multi-loop control system incorporating the *MPPT* and current-mode control is proposed and used to control the SEPIC converter and the PV array output. Finally, the performance of the proposed control system is studied via simulations using the simulation model developed in the Simulink/SimPowerSystems software.

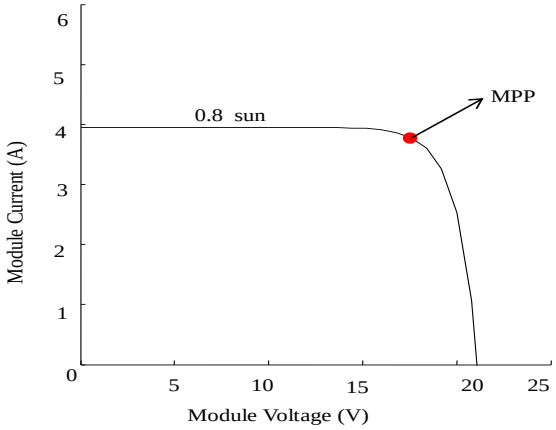

Fig. 4.1: The I-V curve of a PV module showing the maximum power point at 0.8 sun (800W/m^2).

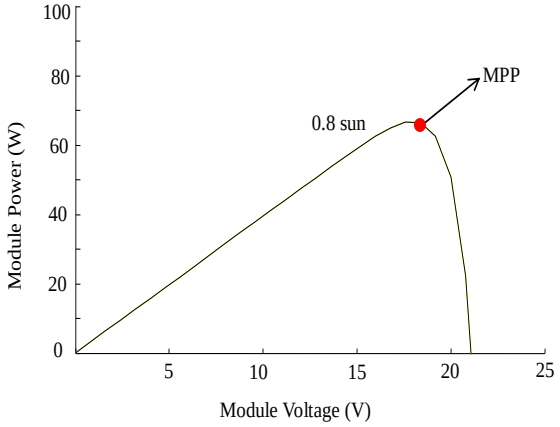

Fig. 4.2: The P-V curve of a PV module showing the maximum power point at 0.8 sun (800W/m^2).

4.2 Review of MPPT Techniques

As shown in Fig. 4.1 and Fig. 4.2, the nonlinear characteristics of the PV module give rise to a unique maximum power point (MPP) at which the module delivers the highest output power to the load and hence operates most efficiently. The decrease of current in the I-V curve of Fig. 4.1 beyond the *MPP* and the decrease of power in the P-V curve of Fig. 4.2 beyond the *MPP* can be explained by the inherent characteristics of the p-n junction diode which is the basic building block of PV cells and, hence modules. In trying to track this *MPP* that depends heavily on the ever-changing environmental temperature and solar radiation, the searching algorithm aims to operate the converter in such a way that the current and voltage of the PV module is set within a specified range [65], [66], [70].

Different maximum power point tracking (MPPT) algorithms are characterised by factors such as [64], [69]: speed of response, tracking accuracy, ease of implementation, cost, steady state and transient response, digital or analogue implementation, range of effectiveness, and usage of sensors. The subsections below review some of the popular *MPPT* techniques, highlighting their pros and cons.

4.2.1 Perturb-and-Observe (P&0) Technique

The P & O technique [71-74] is the most commonly used *MPPT* tracking algorithm because of its ease of implementation. It is based on a hill climbing approach to the maximum power point of the power-voltage characteristics of the PV module as illustrated in Fig. 4.3. It uses the fact that the slope of such a curve is zero at the *MPP*, positive on the left hand side of the *MPP* (increasing power zone), and negative on the right hand side of the *MPP* (decreasing power zone) [71-74]. This is explained mathematically by equations (4.1- 4.3) [73], [74].

$$\frac{dP}{dV} = 0 \quad \text{At the } MPP. \tag{4.1}$$

$$\frac{dP}{dV} > 0 \quad \text{Left side of the } MPP. \tag{4.2}$$

$$\frac{dP}{dV} < 0 \quad \text{Right side of } MPP. \tag{4.3}$$

The operating criterion of this algorithm is based on the perturbation (increase or decrease) of the solar PV module variable of interest - either voltage or current. If the variable (say

voltage) is perturbed in a given direction, the algorithm checks for a corresponding increase or decrease in the array power by comparing it with that of the previous perturbation cycle. If an increase is detected, it means the operating point is on the left side of the *MPP* and therefore the operating voltage must be further perturbed in the same direction. Otherwise, for power decrease, the operating point is on the right side of *MPP* and therefore operating voltage must be perturbed in the reverse direction. This iterative process is repeated until the *MPP* is tracked. The flowchart for the algorithm is illustrated in Fig.4.4.

The P&O technique offers the following advantages [72], [73]:

- Ease of implementation
- Low cost of implementation.

The disadvantages include: [72-74]:

- Energy losses arising from oscillation of operating point around the *MPP* at steady state operation.
- In rapidly changing atmospheric conditions, the P&O algorithm performance becomes very questionable since it exhibits slow dynamic response.
- Slow tracking speed.

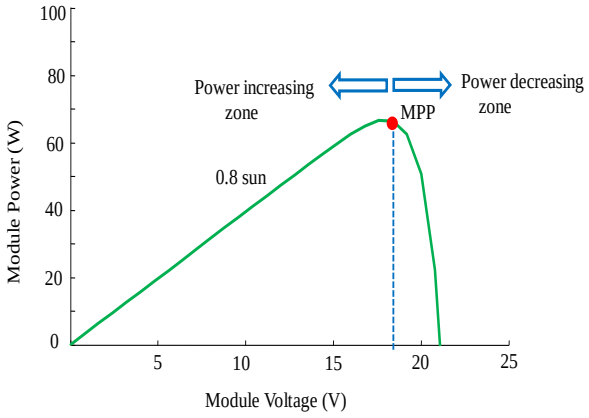

Fig. 4.3: Illustration of the P&O MPPT technique.

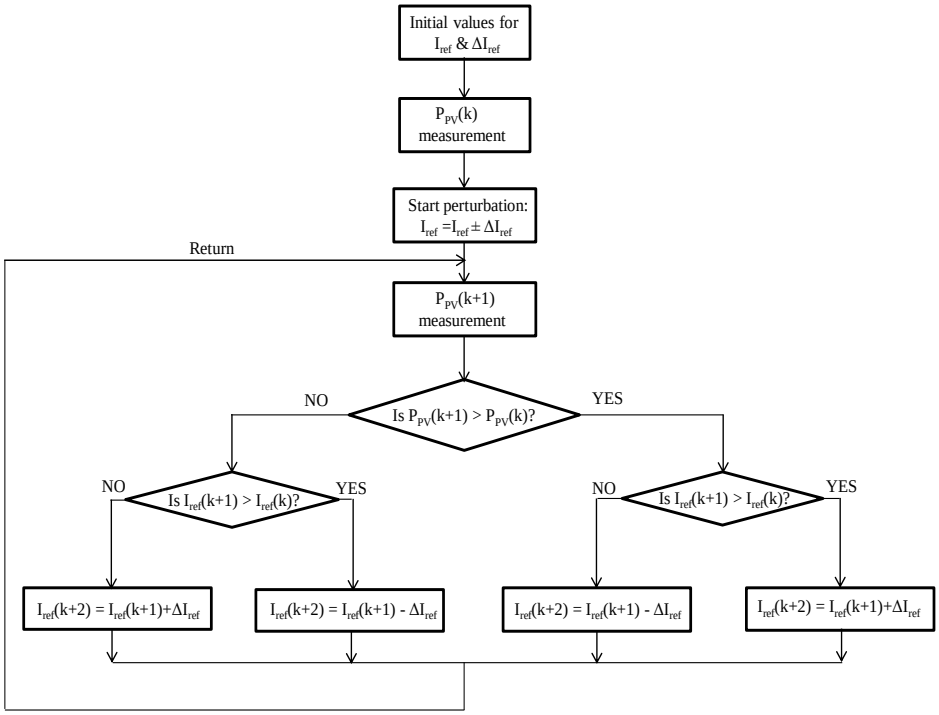

Fig. 4.4: Flowchart of conventional P&O algorithm.

4.2.2 Improved Versions of the P&O Technique

Many variations of the conventional P&O technique described above exist in the literature [72]. These variations attempt to overcome the shortcomings of the conventional P&O and improve the performance. These modified techniques often involve:

- Using variable step size instead of fixed step size for perturbation. This is the so-called Adaptive P&O technique [71].
- Use of larger or smaller fixed step size for the perturbation. Larger values cause oscillation while smaller values result in slow response [63]. Thus, the need for effective trade-off between fast response and oscillation often arises.
- Utilization of the converter duty ratio as the perturbation signal instead of using the array voltage or current [71], [73].

4.2.3 Incremental Conductance Technique

The Incremental Conductance Technique (ICT) is based on the fact that the *MPP* can be tracked accurately by comparing the incremental conductance ($\Delta I/\Delta V$) with the instantaneous conductance (I/V) of the PV array [75-81]. The sum of these two values is zero at *MPP*, negative on the right side of *MPP* and positive on the left side of *MPP* as shown in Fig.4.5.

Thus, the algorithm searches for the *MPP* using equations (4.4 – 4.6). That is, if the operating point is to the left of *MPP*, equation 4.4, increase the control variable and hence the duty cycle.

$$\frac{\Delta I}{\Delta V} > -\frac{I}{V} \tag{4.4}$$

Similarly, if he operating point is to right of *MPP*, equation 4.5, decrease the control variable and hence the duty cycle.

$$\frac{\Delta I}{\Delta V} < -\frac{I}{V} \tag{4.5}$$

And when the operating point is at *MPP*, equation 4.6, keep the previous value of the variable and hence the duty cycle.

$$\frac{\Delta I}{\Delta V} = -\frac{I}{V}, \tag{4.6}$$

The detailed operation of the algorithm is explained with the help of the flowchart in Fig.4.6. The algorithm starts its iterative process by obtaining the input voltage, V(t), and current, I(t), from the panel. These values are compared with values at the end of the preceding cycle, V(t-1) and I(t-1). Thus, the incremental change is [76]:

$$\Delta V = V(t) - V(t-1). \tag{4.7}$$

The next step in the cycle is the checking of the conditions given (equations 4.4 - 4.6) as explained before. In practice, it is difficult to satisfy equation 4.6 due to noise and errors and hence the condition is modified with good approximation by [66]:

$$abs(\frac{\Delta I}{\Delta V} + \frac{I}{V}) < \varepsilon. \tag{4.8}$$

Where ε is a positive small value.

The Incremental conductance algorithm has the following advantages [75-78]:

- High accuracy in tracking the *MPP* in rapidly changing environmental conditions.
- Medium implementation complexity.

The disadvantages of the method include [79-81]:

- Increased hardware and software complexity when compared to the P&O algorithm.
- Increased computational time occasioned by the complexity of the hardware.

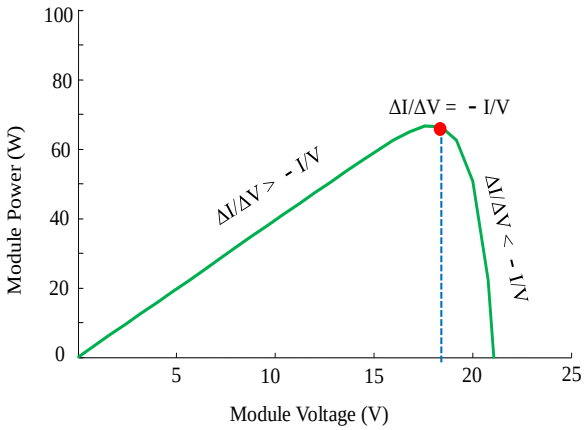

Fig. 4.5: P-V curve of a PV array showing the three regions of the ICT search algorithm.

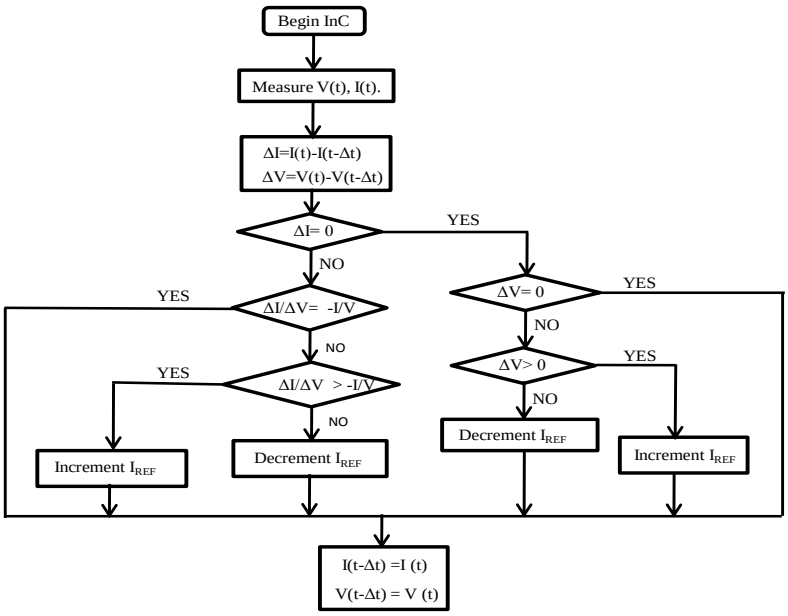

Fig. 4.6: Flowchart of Incremental Conductance Algorithm

4.2.4 Ripple Correlation Control (RCC) Technique

The switching actions of power converters (weather dc-dc or dc-ac) result in the generation of current and voltage ripples. These ripples are usually injected into the PV array line. The *RCC* technique uses these ripples to extract information about the power gradient and evaluate if the PV system is operating close to the maximum power point [82]. Thus, the *RCC* technique finds the correlation between the time derivative of the time-varying PV power and the time derivative of the time-varying array current or voltage. For a PV power curve (P-V characteristics) the RCC technique is explained by the following relationships [82], [83]:

$$\frac{dP}{dt} \times \frac{dV}{dt} > 0 \Rightarrow V_{pv} < V_{mp} \tag{4.9}$$

$$\frac{dP}{dt} \times \frac{dV}{dt} < 0 \Rightarrow V_{pv} > V_{mp} \tag{4.10}$$

$$\frac{dP}{dt} x \frac{dV}{dt} = 0 \Rightarrow V_{pv=V_{mp}} \tag{4.11}$$

Where V_{pv} is the operating voltage and V_{mp} is the voltage at the *MPP*.

Equation (4.9) shows that the operating point is below (to the left side) the *MPP* if the ripple voltage or the ripple current is increasing and the power is also increasing. Similarly (4.10) shows that the operating point is above (to the right side) the *MPP* if the ripple current or voltage is increasing while the power is decreasing. Equation (4.11) locates the *MPP*. Thus, it is seen that the phase relationship between the power ripple and the array voltage or current decides the tracking direction and the associated change in the duty ratio. Controlling the duty ratio of the converter based on the relationship in equations (4.12 - 4.13) continuously tracks the MPP [82], [84].

$$d(t) = -K \int \frac{dP}{dt} \times \frac{dV}{dt} dt \tag{4.12}$$

$$d(t) = K \int \frac{dP}{dt} \times \frac{dI}{dt} dt \tag{4.13}$$

Where d is the duty ratio of the converter and K is a positive constant. Fig. 4.7 is an illustration of the implementation of the *RCC* MPPT technique.

The *RCC* technique has the following advantages [82-85]:

- Ease of implementation since the technique is PV array independent. That is, it yields parameter-insensitive MPPT of the PV system.
- It offers fast tracking speed even under rapidly changing environmental conditions.
- Low cost of implementation.

However, the RCC technique has the following disadvantages:

- The technique offers low accuracy; and
- Unsuitable for high switching frequency.

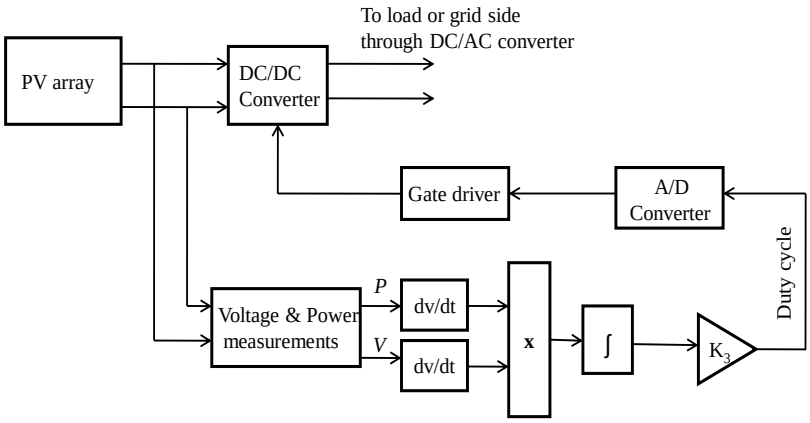

Fig. 4.7: Implementation of RCC-based MPPT technique

4.2.5 Fuzzy Logic Technique

The advent of microcontrollers and digital signal processors (DSPs) has made fuzzy logic controllers (FLC) attractive in MPPT applications. This is because of their inherent advantages of: 1) having the ability to work on nonlinear systems, 2) not needing dynamic mathematical models, 3) ability to use imprecise inputs and 4) ability to control unstable systems [86].The basic structure of any fuzzy logic controller is shown in Fig.4.8, where the three major components are also shown. The fuzzification stage converts the input variables into linguistic variables based on the membership functions. The fuzzy inference engine processes the inputs according to the rules set and produces the fuzzy outputs while the defuzzication stage produces the crisp real value for the fuzzy output [86].

For fuzzy logic-based MPPT controller, the error (4.14), and the change of error, (4.15), are used as inputs to the fuzzifier since at *MPP*, *dP/dV* approaches zero [86].

$$E(n) = \frac{P(n) - P(n-1)}{V(n) - V(n-1)} \tag{4.14}$$

$$\Delta E(n) = E(n) - E(n-1) \tag{4.15}$$

The crisp input values of the error and change of error are then fuzzified into a set of fuzzy values by using appropriate membership functions. Based on the designed fuzzy rule base, the fuzzy inference engine derives a set of fuzzy results [87]. Finally, the output stage which is the defuzzifier combines and transforms the fuzzy results to a crisp output value. The defuzzification process produces an analogue output signal, a change in the duty ratio, which controls the power output of the *MPPT* system. Fig. 4.9 shows the implementation of FLC-based MPPT system for a photovoltaic power plant [86], [88].

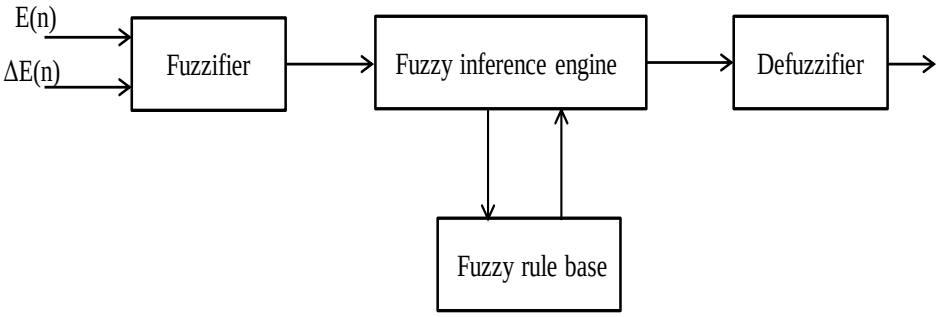

Fig. 4.8: Main components of a fuzzy logic controller.

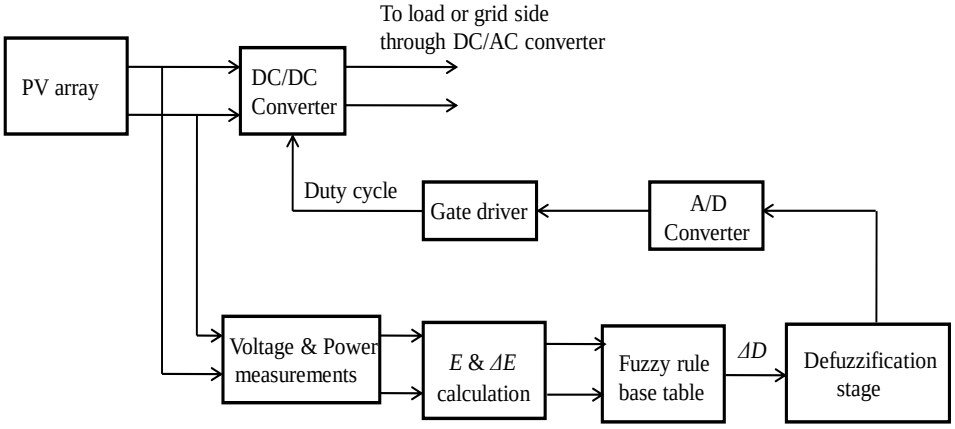

Fig. 4.9: Fuzzy logic controller-based MPPT implementation for a PV power plant.

The advantages of the FLC-based MPPT include [86-88]:

- Has more flexibility and intelligence than conventional MPPT techniques.
- Effectively handles systems with nonlinearities and imprecise inputs.
- Good performance under varying weather conditions.

It has the major disadvantage of requiring more memory space for implementation when compared to other MPPT techniques.

4.2.6 Fractional Open-Circuit Voltage-Based MPPT

This technique is based on the fact that the voltage at the maximum power point, *Vmpp*, is proportional to the open circuit voltage, *Voc*, under varying irradiance and temperature conditions. That is,

$$Vmpp = kVoc \tag{4.16}$$

Where *k*, is a constant which is dependent on the characteristics of the PV panel. This control technique requires measurement of the *Voc* and *Vmpp* at different irradiance and temperature levels for the determination of the constant. Generally this value is between 0.71 and 0.78 [69]. With the determined value of the constant, the voltage at the maximum power point is easily determined from (4.16). To overcome problems associated with the constant disconnection of the PV output terminals to take measurements of *Voc*, pilot cells which are exposed to the same environmental conditions are used.

This technique has the advantages of ease of implementation because it does not require complex control system and it is cheap to implement [69]. The disadvantages of the technique include [69], [70]:

- Temporary loss of power as a result of disconnection of PV array from the converter when taking measurements.
- Use of extra pilot cells for measurement.
- Unreliable performance under partial shading conditions.

4.3 Review of Closed Loop Control Techniques for PV Converters

To obtain a precise and well-regulated output voltage that is irresponsive to load changes and input voltage changes, a feedback technique is always used in modern switch-mode power converters [49]. For pulse-width modulation (PWM) based converters, while the early converters used only voltage-mode control technique, modern converters rely heavily on the use of the current-mode control technique [49]. The subsections below briefly explain the working principles of these two broad approaches to the control of power converters.

4.3.1 Voltage Mode Control

This control approach was earlier briefly introduced in Chapter 3. In this control approach, the output voltage to be regulated is sensed and fed back through an amplifier. For a PWM controlled converter, the feedback signal is then compared with a precision reference voltage [49], [89]. The comparator generates an error voltage, v_e, which is fed to the compensator network to generate the input to the pulse width modulator. The pulse width modulator which has an embedded saw tooth reference signal, V_{cr}, then generates the switching pulses used to control the converter. That is [89],

$$D = \frac{v_e}{V_{cr}} \tag{4.17}$$

Where *D* is the duty cycle of the switching pulses. From equation (4.17) it is seen that when the output voltage is lower than the desired dc value (reference voltage), a higher error voltage is produced and consequently the duty cycle is increased to cause a subsequent increase in the output voltage. The opposite happens when the output voltage is higher than the reference voltage. Thus, by constantly controlling *D*, the output voltage is regulated [49].
The advantages of the voltage mode control are [89]: 1) ease of implementation and simplicity and, 2) good load regulation. The shortcomings of this method include [49], [50]:

- Slower line regulation reaction because changes in input must first be translated into changes in output voltage and then fed back before corrective action is taken.
- The slower response makes it unsuitable, when used alone, in PV applications that are characterized by fast dynamic changes.

4.3.2 Current Mode Control Technique

Current mode control is one of the mostly used control techniques employed in the control of switch-mode power converters. It relies on the use of a current loop feedback in addition to the voltage loop. This multiple-loop approach to control uses either the inductor or switch current and the output voltage error signal as the control variables. The use of multiple control variables results in improved line and load transient response [85], [90].These variables are used to generate inputs to the PWM modulator or gate pulses which are the final switching signals. Several variants of the current mode control exist in the literature [90-94]. A short review of some of the variants is presented in the subsections below.

4.3.2.1 Peak Current Control

While the conventional voltage-mode control has only one feedback loop with the output voltage as the control variable, the peak current control methodology utilizes the inductor current as an additional control variable, and thus achieves an improved input transient response [85], [90]. Fig. 4.10 (a) shows a variant of the peak-current control method applied to a SEPIC converter. In the inner loop (red dotted enclosure), the resistor, R_c, senses the inductor current, i_L, to generate the voltage, v_c, which is the feedback control variable for this loop. The outer loop (dotted green enclosure) uses the feedback control variable, v_e, which is

the amplified error signal between the desired output voltage, V_{ref}, and the actual output voltage, $V_{o.}$

Fig. 4.10(b) depicts the waveforms involved in peak-current control and explains the operation. At the beginning of the switching cycle the switch *Q1* is turned ON and the diode, *D1*, turned OFF. Turning ON *Q1* causes the inductor current, $i_{L,}$ and the associated voltage drop, v_c, across the sensing resistor to increase linearly from the initial value. When v_c increases to v_e, the amplified error signal from the outer loop of the voltage mode control, *Q1* is turned OFF and *D1* is turned ON. This makes i_L and v_c to decrease linearly until the end of the switching cycle. Thus, the meetings of the peak of v_c with v_e control the switching of *Q1* [93].

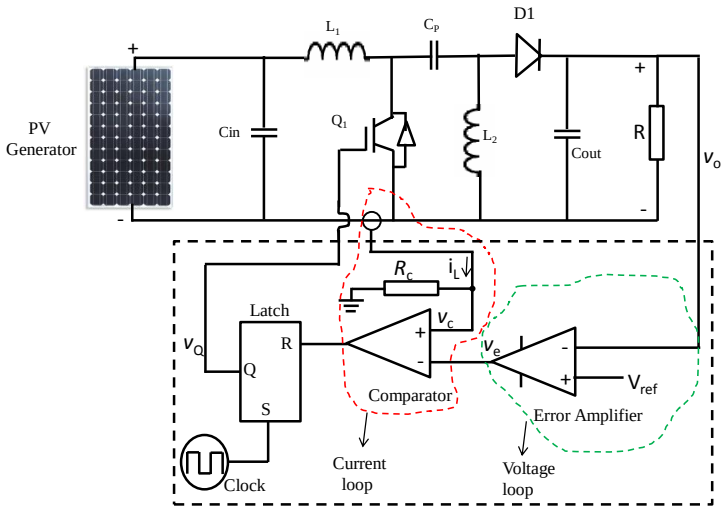

(a)

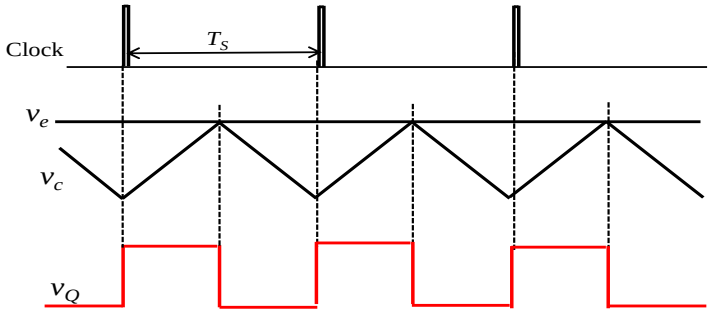

(b)

Fig. 4.10: Peak-current-controlled SEPIC converter. (a) Circuit. (b) CCM operation waveforms.

4.3.2.2 Average Current Control

This control scheme utilizes two cascaded loops that are dynamically separated, Fig. 4.11. The inner current loop is faster than the outer voltage loop [90]. Fig. 4.11 explains the operation of this control methodology. It is seen from Fig. 4.11 that the outer voltage loop (green enclosure) compares the sensed output voltage, V_o, with the fixed reference voltage, V_{ref}. The difference, v_e, is amplified by the compensator (a proportional-plus-integral network) to generate Kv_e as the error output. Kv_e acts as a current reference for the inner current loop (red enclosure), where the sensed current is acquired via the sense resistor, R_S. The sensed voltage of R_S, V_{in}, is compared with Kv_e to generate the output error, i_e , which is amplified and used for comparison in the pulse-width modulator to generate the gate switching pulses.

This mode of control has the following merits [90-92]:

- Faster transient response to load and input voltage changes when compared to voltage mode control or peak current mode control.
- Tracks the reference current with a high degree of accuracy.
- Slope compensation is not necessary.
- It offers excellent noise immunity.

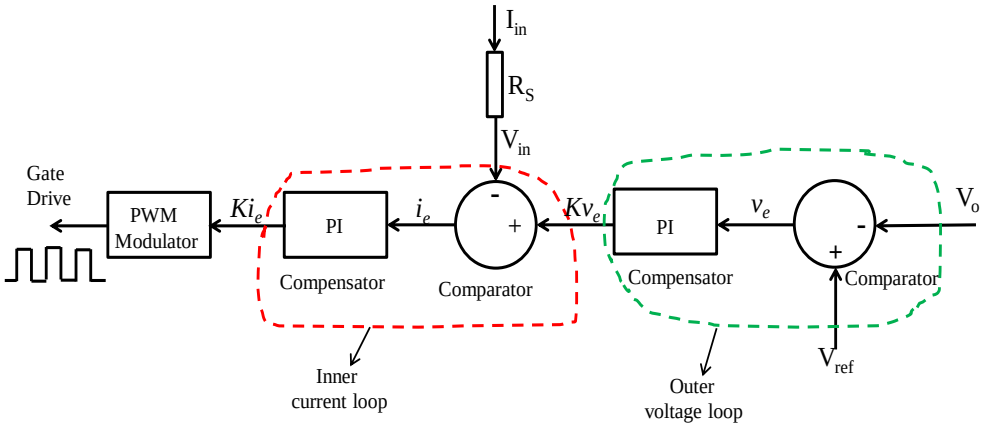

Fig. 4.11: Principle of operation of the average current control mode.

4.3.2.3 Hysteresis Current Control

Hysteresis control is the control method in which the controlled variable, often the inductor current, is maintained between pre-set upper and lower limits [50]. The control scheme turns the switch OFF when the inductor current reaches the upper limit and turns it OFF when the current reaches the lower limit. Thus, the average inductor current is set at the average of the upper and lower thresholds. Fig. 4.12 shows the hysteresis current control method applied to the SEPIC converter. The operation of the circuit is explained as follows [64]. The zero current detector, ZCD, is used to sense the inductor current, $i_{L.}$ Thus, the ZCD sets the SR-latch and turns *ON* the switch to initiate a switching cycle. In addition to the inductor current, the switch current, i_{SQ}, is also monitored and compared to a reference voltage that is proportional to the input voltage, V_{PV}. When equality is achieved between the sensed current and the reference, the latch is reset and the switch is turned *OFF*.

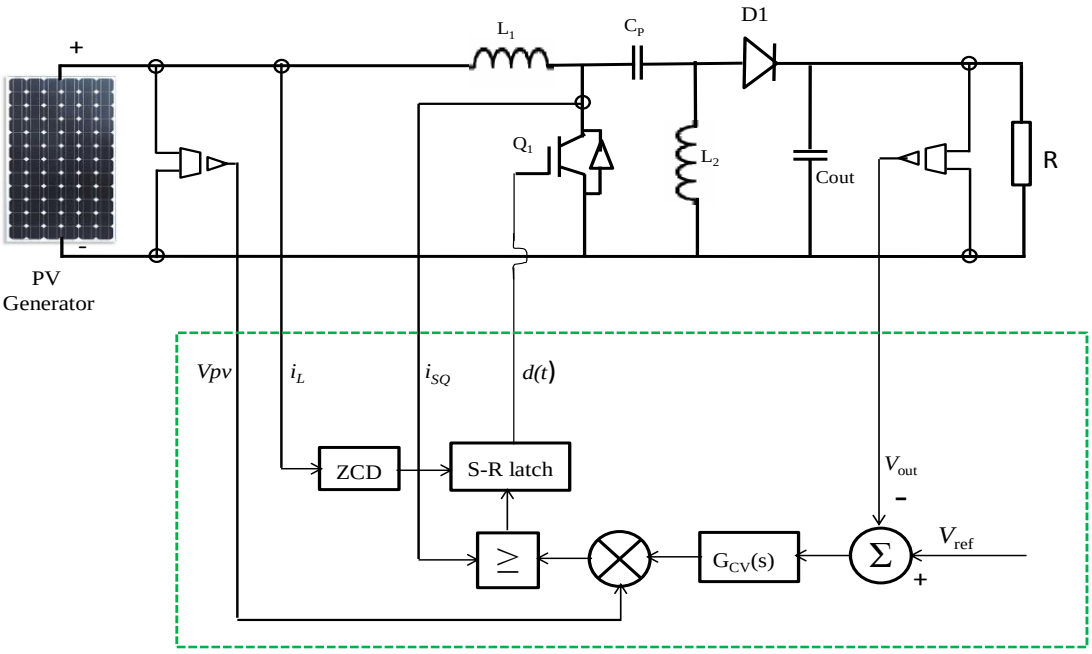

Fig. 4.12: SEPIC converter with hysteresis current control method.

4.4 Proposed Multi-Loop System for MPPT and Current Mode Control

4.4.1 Development of an Improved Incremental Conductance MPPT with Variable Step-size Perturbation

As seen in Section 4.2.3, in the conventional incremental conductance *MPPT* technique, a fixed, small iteration step size determined by accuracy and tracking speed requirement is used. With the use of such a fixed iteration step size, it is very difficult to achieve rapid dynamic response and good steady state accuracy simultaneously. If this step size is increased, the tracking speed is increased but with reduced tracking accuracy [75-78]. Conversely, if the step size is reduced, the tracking speed is reduced but the tracking accuracy is increased. To overcome these limitations, this paper proposes an improved version of the incremental conductance *MPPT* technique based on the application of variable step size for the perturbation. Compared to the conventional incremental conductance technique which uses a fixed step size for perturbation, this improved algorithm simultaneously offers: 1) improved *MPPT* speed and, 2) improved *MPPT* accuracy.

In the proposed approach, the perturbation step-size, δ V, is tuned automatically based on the PV array characteristics. When the operating point is far from the *MPP*, the step size is automatically increased and the tracking speed is thus increased. Conversely, when the operating point is close to the *MPP*, the step size is automatically decreased with the resultant decrease of the steady state oscillation. The flowchart of this *MPPT* approach is shown in Fig. 4.13. The step size is defined by:

$$\delta V = K \times abs(\Delta P / \Delta V) \tag{4.18}$$

Where *K* is the scaling factor.

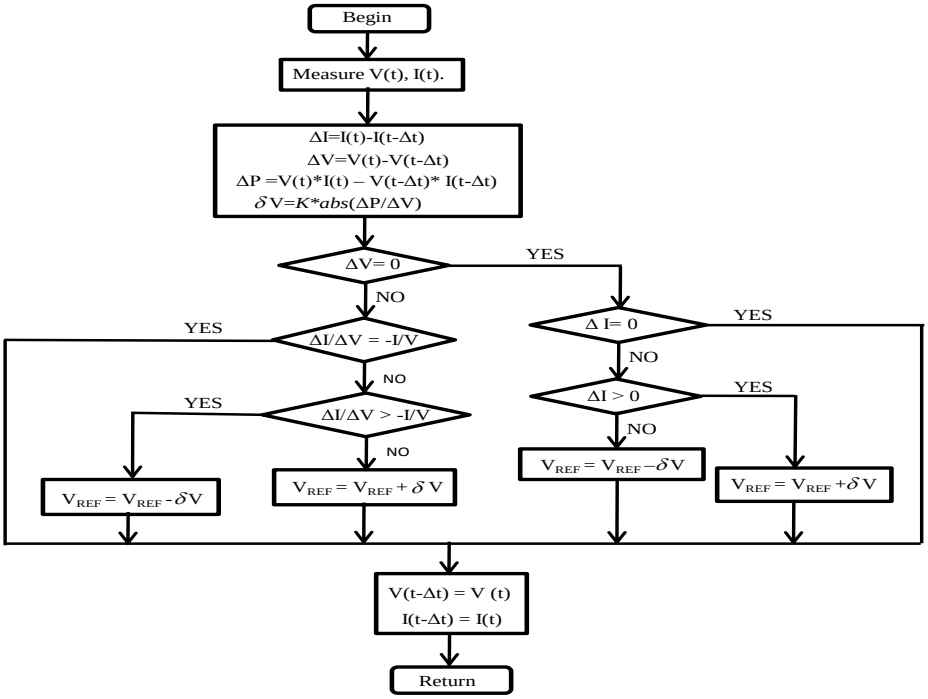

Fig. 4.13: Flowchart of the proposed variable step size incremental conductance MPPT technique.

4.4.2 Multi-loop System for MPPT and Current Mode Control

A multi-loop, multi-objective control system is developed to achieve the following desired aims simultaneously:

- Tracking the maximum power point using the modified incremental conductance technique introduced in the above section.
- Regulation of the output voltage of the SEPIC converter in the face of changes in the input or load.
- Controlling the inductor current.
- Ensuring the system's stability.

Fig. 4.14 shows block diagram of the multi-loop system. In Fig. 4.14, the MPPT block of *Loop 1*, monitors the voltage and current at the terminals of the PV array and generates a reference voltage, V_{mpp}, which it uses to control the input voltage of the converter by forcing the PV array to operate at this voltage using the PI controller. The voltage controller of *Loop 2* ensures the regulation of the output voltage of the converter while the innermost loop, *Loop 3*, ensures the control of the inductor current, i_L, using the average current mode control technique. The PWM block then produces the pulse train that operates the gate of the switch.

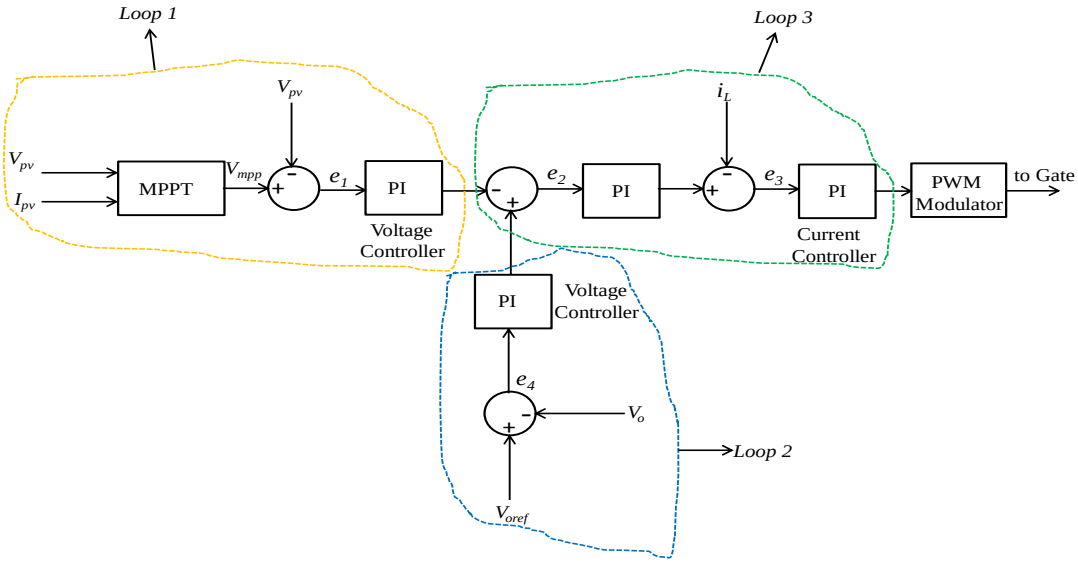

Fig. 4.14: Block diagram of the multi-loop system for MPPT and current mode control.

4.5 Simulation Model

A simulation model is developed using MATLAB/Simulink/SimPowerSystems dynamic system simulation software in order to verify the operation of the control system developed in the previous section. The Simulink model of the photovoltaic module, developed earlier in Chapter 2, is used as the PV source. The model takes solar irradiation and ambient temperature as inputs and generates PV module current and voltage, and hence module power as output. Different parameters of the BP 380 module used for the study such as the open circuit voltage, short circuit current, voltage and current at the maximum power point and the temperature-based coefficients (alpha, beta, and gamma) can also be set in the model. The parameters of the BP 380 solar module used are shown in Table 4.1.

The SEPIC converter designed earlier in Chapter 3 is used as the dc-dc power conversion interface. The dc-dc converter is to generate the 180V output and implement the *MPPT* of the PV module based on the tracking algorithm. The PV model uses the ambient temperature and insolation to generate the voltage, current and hence power, which characterises the BP 380 solar module used for the study. The produced power is processed by the SEPIC converter. For the implementation of the control strategy for the *MPPT* and current-mode operation, the PV module voltage, current, power, and the inductor current are continuously monitored. To transfer the *MPPT* algorithm into the Simulink platform, the flowchart of Fig.4.13 is coded using the Embedded Matlab function block of Simulink. This *MPPT* controller generates a

reference voltage. This reference voltage, the inductor current and the feedback voltage are used in the multi-loop feedback system. Fig. 4.15 shows the simulation model for the MPPT with the integrated current mode control.

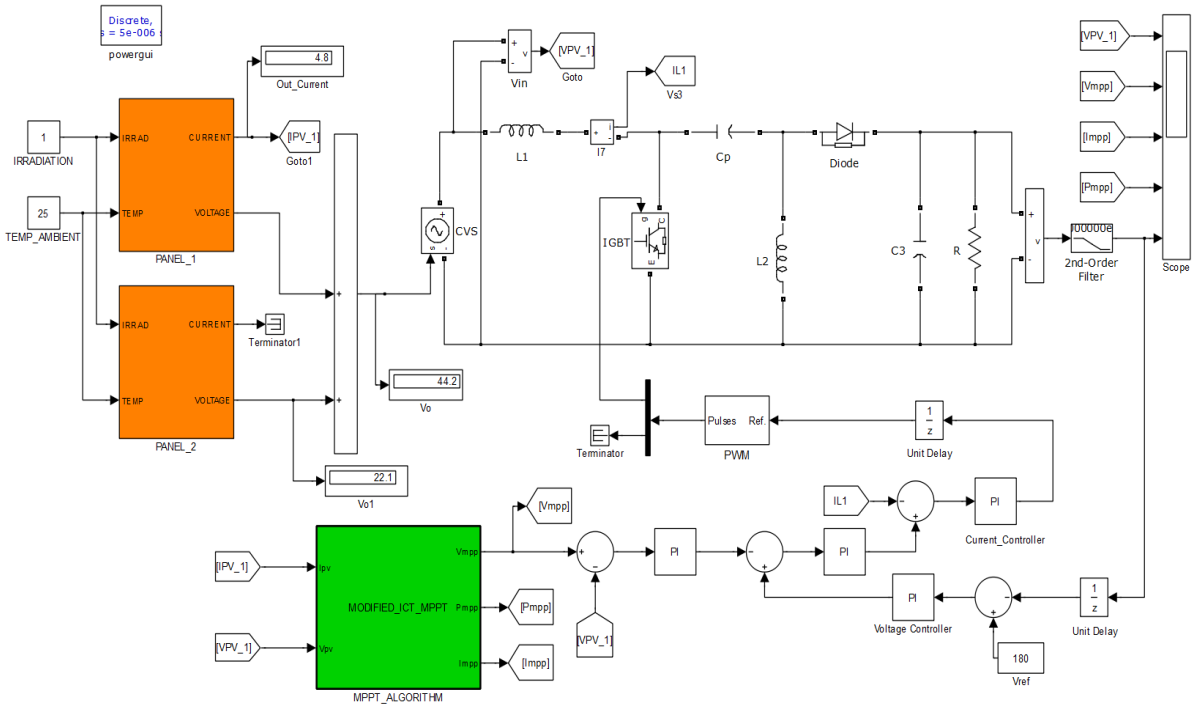

Fig. 4.15: Simulation model of the PV system with MPPT and current mode control in Simulink.

Table 4.1 Electrical parameters of BP 380 solar module @ STC.

Electrical Parameter	**Value**
Maximum power (P_{max})	80W
Voltage at P_{max} (V_{mp})	17.6V
Current at P_{max}(I_{mp})	4.55A
Short-circuit current (I_{sc})	4.8A
Open-circuit voltage (V_{oc})	22.1V
Temperature coefficient of I_{sc} (alpha)	(0.065±0.015)%/^{o}C
Temperature coefficient of V_{oc} (beta)	-(80±10)mV/^{o}C
Temperature coefficient of Power (gamma)	-(0.5±0.05)%/^{o}C
Nominal Operating Cell Temperature(NOCT)	47±2^{o}C
Maximum system voltage	600V.

4.6 Simulation Results and Discussions

The model, Fig. 4.15, was simulated under different irradiance and ambient temperature conditions so as to study the effectiveness of the developed algorithm. The details are presented in the following subsections.

4.6.1 Effect of Irradiance Changes

To verify the performance of the improved *MPPT* technique with the current mode control, the PV system is simulated with a series of values of solar irradiance at constant ambient temperature. The simulation results, Fig. 4.16, show the solar irradiance changing abruptly from 500W/m^2 (0.5 sun) to 800W/m^2 (0.8 sun) at the step time of 5seconds, when the ambient temperature is constant at 25^{o}C. It is observed that the maximum power tracked changes correspondingly from 80W to 128W at the same step time of 5 seconds. The MPP changes rapidly with the same rapidity as the irradiance change and therefore ensures that optimum use of the PV array power is made.

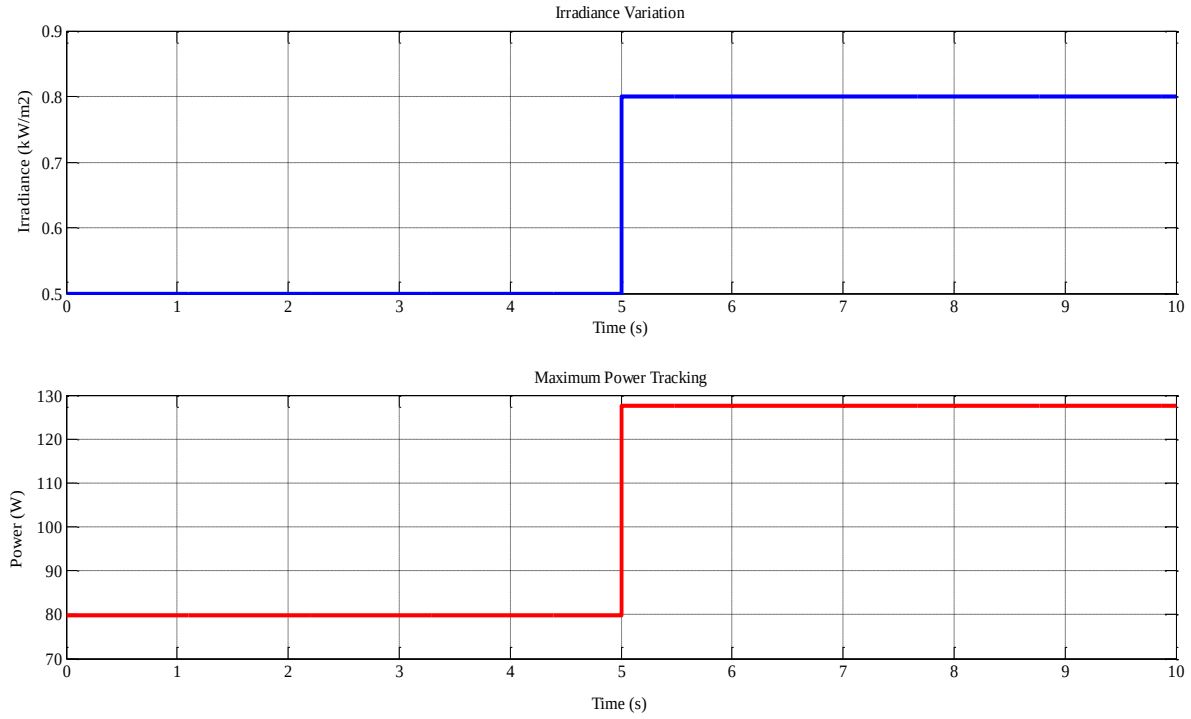

Fig. 4.16: Irradiation variation and maximum power point tracking @ 25^{o}C.

4.6.2 Effect of Ambient Temperature Change

Figs. 4.17 and 4.18 show the results of the simulation for varying ambient temperature at constant irradiance of 1000W/m^2. In this system, the SEPIC converter input voltage is controlled to follow the reference voltage (Vmpp) determined by the improved incremental conductance algorithm. Fig. 4.17 shows the ambient temperature increasing abruptly from 20^{o}C to 33^{o}C at a step time of 5 seconds. For this increase, the PV array output voltage is seen to decrease from the initial value of 45V to 42.9V, while the algorithm generated voltage drops from 35.8V to 34.2V at the same step time. Consequently, the tracked maximum power decreases from 152W to 145W at the same step time. The speed and accuracy of the tracking algorithm is obvious. Fig. 4.18 also shows that despite the increase in ambient temperature from 20^{o}C to 33^{o}C and the attendant drop in the tracked power, the integrated current mode controller achieves a good regulation of the output voltage at the desired value of 180V.

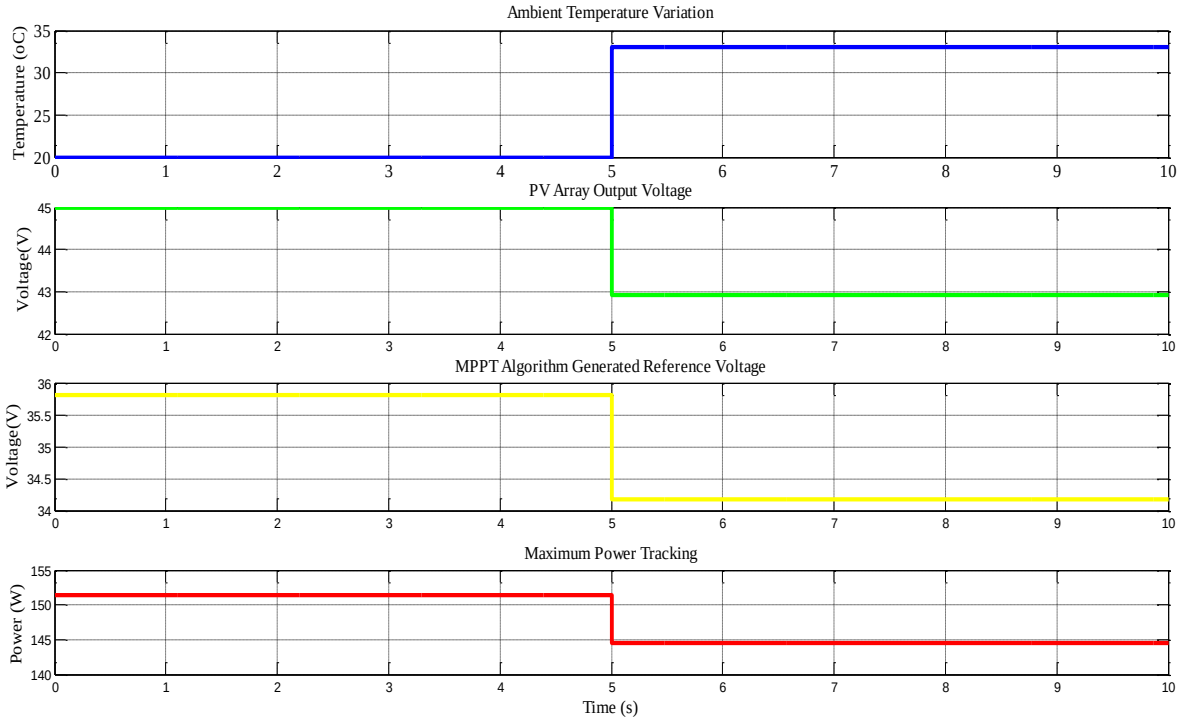

Fig. 4.17: Ambient temperature variation and MPPT performance.

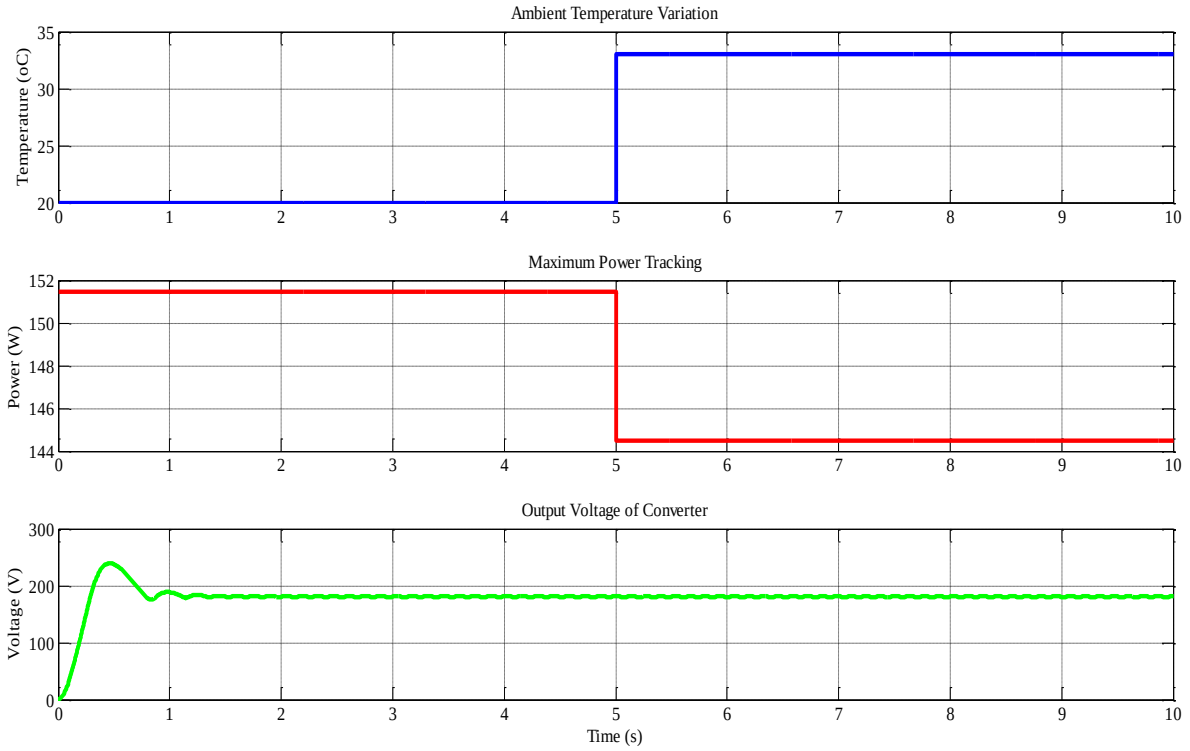

Fig. 4.18: Temperature variation, MPP and regulated output voltage of the converter.

4.7 Conclusions

This chapter has reviewed the major existing MPPT techniques, highlighting the merits and the demerits of each approach. Similarly, the different approaches to current mode control have been reviewed. An improved MPPT technique based on the incremental conductance technique has been proposed. The proposed technique with an integrated current mode control multi-loop system has been used to control the PV-SEPIC converter system. The results show that the developed multi-loop system can effectively track the MPP rapidly and accurately under different solar irradiance changes and changes in ambient temperature. Moreover, the system is seen to offer robust voltage regulation and improved dynamic response in the face of changing environmental variables.

Chapter 5
Interfacing Energy Storage to PV Systems: Design of Converter & Control Systems

5.1 Introduction

The variability and intermittency of renewable energy sources like wind and solar in a distributed generation system pose some challenges. At low levels of PV penetration, the impact on the system may be negligible but at high penetration levels the impact offers enormous challenges. Some of these challenges include [95-98]:

- Meeting the load demand when the intermittent source is unavailable or low in supply, especially during night times or periods of cloudy weather.
- Matching generation with load demand.
- Dealing with excess energy when generation exceeds demand.
- Managing the induced increased cycling (frequent start up and shut down, ramp up and down) of the fossil-fuelled generators.

For grid integrated systems, mismanagement of these issues can cause network failures. To mitigate these challenges requires two major backup infrastructures: energy storage and power electronics interfaces [95].These infrastructures ensure that energy production from such intermittent resources is matched with demand at all times, 24 hours a day, 365 days a year.

This chapter focuses on the development of control strategies for integrating energy storage system into a photovoltaic power plant. Firstly, a review of energy storage technologies applicable to photovoltaic power systems is presented. This is followed by the analysis and design of a 500W bi-directional dc-dc converter, based on the half-bridge topology, used for interfacing the energy storage system used for this study. Thirdly, a novel multi-objective technique for battery management and system power balance control is proposed. A simulation model for the proposed control system is developed and its performance verified via simulation studies using MATLAB/Simulink/SimPowerSystems software. Finally, the simulation results are presented and discussed.

5.2 Review of Technologies for PV Energy Storage

5.2.1 Benefits of Integrating Energy Storage in PV Systems

To increase the renewable energy content of their generation, utilities often rely on costly reserves based on fossil fuels. However, this central reserve approach could be replaced with distributed storage or on-site storage [99]. The inclusion of energy storage increases system availability, reliability and makes the system dispatchable. In general, the benefits of integrating energy storage into a PV system are summarized below [99-103]:

- Energy storage provides power on demand.
- Daily load shifting: off-peak energy is stored for usage during peak periods. Combining storage with PV will reduce the demand for utility power during higher-rate hours of the day by charging the storage system with PV-generated energy early in the day to support the load later in the day.
- Provision of spinning reserve: to restore the balance of supply and demand on a system after the sudden loss of a power line or generator or sudden, unexpected increase in load.
- Peak shaving: This is used to minimize demand charges for a customer or to reduce peak loads by the utility. Peak shaving utilizing PV-storage systems involves the PV providing all required power above a specified limit and if PV is not available, energy storage comes on to fill the gap. Such application of energy storage for peak shaving can be used by utilities to defer substation transformer upgrades.
- Regulation services to reduce voltage flickers, harmonics, and improve voltage stability and hence overall power quality improvement.
- Storage of PV generated energy for use when needed and so mitigating variability and intermittency issues of PV generated energy.
- Lowering GHG (greenhouse gas) emission generation by replacing fossil fuel based peaking and reserve units.
- Use as an uninterruptible power supply (UPS) in case of power outage.
- In residential and commercial applications, it results in the reduction of customer utility bills.
- As an indispensable part of the smart grid infrastructure.
- Reduction of the wear and tear of fossil-fuelled generators and hence the overall maintenance cost due to reduced cycling of these generators.

5.3 PV Storage Technologies

Integrating storage technologies to PV systems benefits utilities, homeowners and commercial customers through greater reliability, improved power quality and overall reduced energy costs. Generally, energy storage systems (ESSs) convert electrical energy to some form of energy that can be stored and released when needed. Generally, the storage of PV energy can be in any of the following three broad forms [98]:

- Chemical energy: e.g. battery energy storage system (BESS).
- Electrical energy: e.g. supercapacitors.
- Mechanical energy: e.g. compressed air, flywheel and pumped hydro storage.

An optimal PV-Storage system in grid-tied system should involve a mixture of [6]:

- Small, decentralized, short-term storage, and
- Large seasonal storage systems.

A more detailed analysis of these approaches to PV storage is done in the subsections below.

5.3.1 Battery Energy Storage System (BESS)

Lead acid battery technology is the most mature and common of BESS because of its popularity in the automotive industry. It has a cathode made of spongy lead and an anode of lead dioxide both of which are immersed in an electrolyte of dilute sulphuric acid. During discharge, both electrodes are converted to lead sulphate while the charging operation restores the anode to lead dioxide and the cathode to metallic lead as depicted in (5.1) [28].

$$Pb + 2H_2SO_4 + PbO_2 \leftrightarrow PbSO_4 + 2H_2O + PbSO_4 \tag{5.1}$$

Unlike the shallow-cycle version of lead acid battery technology which is used in automobiles, the deep-cycle version is designed for repeated discharge by as much as 80% depth-of-discharge (DOD) [28]. This ability to withstand repeated full charge and discharge cycles at high *DOD* makes them suitable for PV energy storage applications, especially in decentralized systems. The two versions of valve regulated lead acid (VRLA) batteries– absorbed glass mat(AGM) and gelled [5], [28] – are particularly attractive in residential PV applications because they are safer to use than the flooded version. Their ruggedness, high round-trip efficiency during charge/discharge, wide availability, low cost and ease of charging and discharging, account for the popularity of this battery technology in PV-Storage

systems [28],[103]. However, like all lead-acid batteries, they have the shortcomings of low energy densities and relatively limited cycle lives [104].

The properties of the major *BESS* technologies are compared in Table 5.1.

5.3.2 Lithium Ion (Li-ion) Batteries

The operation of lithium-ion battery is based on the migration of lithium ions from the negative electrode to the positive electrode during discharge and the reverse migration during the charging process. This to-and-fro movement is the so-called "rocking chair or Swing or Shuttlecock" design [105] and is illustrated in Fig.5.1

Besides being popular in mobile applications, they have also become popular in residential PV energy storage. This is mainly due to[105],[106]: 1) their high energy density(150Wh/kg) and hence light weight; 2) longevity because of high charge cycles (up to 7,000); 3) ability to withstand high charging current and hence can be charged quickly; 4) unaffected by low temperatures; 5) high charge/discharge efficiency (nearly 100%); and 6) higher cell voltage(3.5V compared to 2.0V for lead acid and 1.2V for other electro-chemistries). However, because of the shortcomings of high cost and elaborate battery management system required for its protection, the present usage of Li-ion technology in utility-scale storage is limited to short-time duration applications for regulation and power management services.

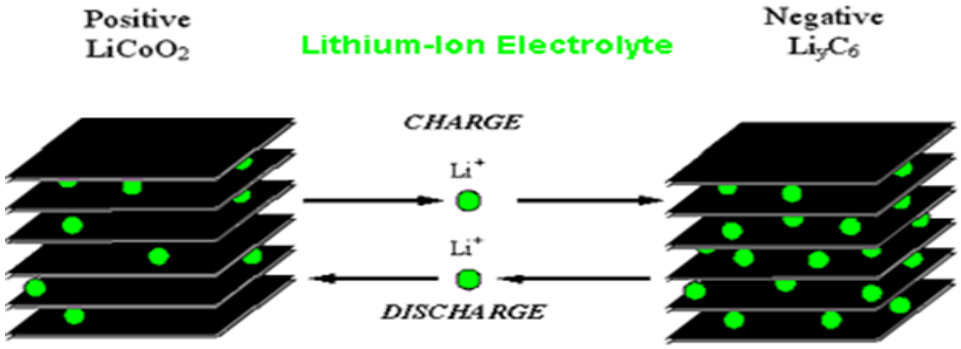

Fig. 5.1: The operating principles of lithium-ion battery [105].

5.3.3 Sodium Sulfur (NaS) Batteries

The *NaS* battery consists of molten sulphur at the positive electrode (cathode) and molten sodium at the negative electrode (anode), Fig. 5.2, [103]. The two molten electrodes are separated by beta-alumina solid electrolyte (BASE) membrane. The BASE selectively conducts only the positive sodium ions, Na^+, that combine with sulphur to form sodium polysulfides [107]. During the discharge phase the Na^+ ions flow through the BASE and result in current flow in the external circuitry with cell voltage of about 2 volts. The discharge phase results in a drop in the sodium level while the charging phase restores this level. *NaS* batteries have operating temperatures ranging from 300^{o}C to 360^{o}C and are usually equipped with electric heaters to maintain a minimum operating temperature. *NaS* batteries have the following favourable attributes [108], [109]:

- High energy density - 3 to 5 times that of lead acid batteries, thus optimizing space.
- Insensitivity to ambient temperature - because of its high operating temperature range.
- High durability - the use of the durable porcelain-like BETA material to separate the electrodes gives *NaS* batteries a life span of about 15 years and more than 2500 charge/discharge cycles for 100% depth of discharge (*DOD*).
- High efficiency - up to 89% charge/discharge efficiency and not prone to self-discharge.
- High short-time power rating - up to 5 times nominal rating.
- Remote operation and monitoring and minimal maintenance.

The main drawbacks of this technology are [110]:

- High cost compared to conventional battery technologies.
- Requirement of elevated temperature (300^{o}C) for operation. Maintaining this temperature results in losses associated with the heating process.

This advanced battery technology is popular in utility applications for multi MW load-levelling, peak shaving, and emergency power supply applications. It has been deployed in many sites in Japan and USA for substation upgrade because of its high capacity [108], [109].

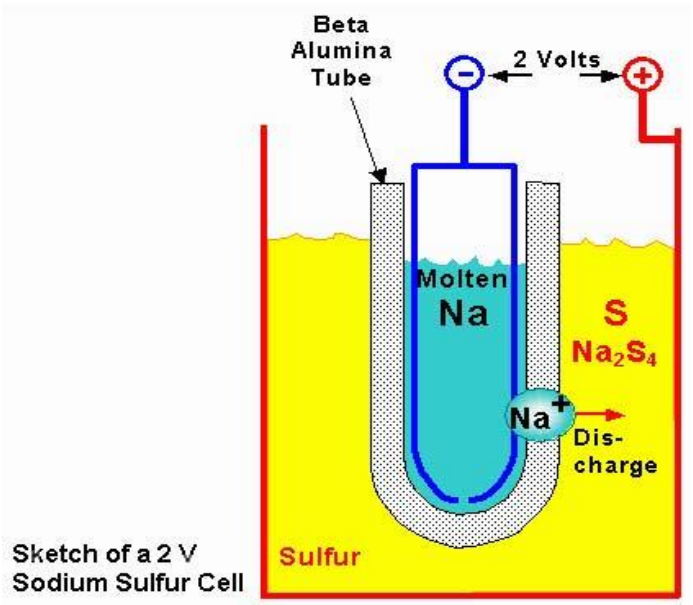

Fig. 5.2: Operation of sodium sulfur cell [105].

5.3.4 Flow Battery Technologies

Flow batteries have two major components: cell stacks, where power is converted from electrical form to chemical form during the charging phase, and two external tanks for the storage of the electrolytes, Fig. 5.3. The energy is stored chemically in the electrolytes. The electrolytes are pumped simultaneously through the two half-cells of the cell stacks, which are separated by a thin membrane through which selected ions flow [107].

During the charging phase, a chemical reduction reaction occurs in one of the electrolytes while oxidation reaction occurs in the other. During the discharge phase, the stored chemical energy in the electrolytes is released in the form of electrical energy from the electrodes. The most popular flow battery types on the market are [107]:

- Zinc Bromine (ZnBr) Batteries.
- Polysulfide Bromide (PSB) Batteries.
- Vanadium Redox Batteries (VRB).

Flow batteries are truly large-scale batteries used for load levelling applications and mitigation of substation congestion.

Table 5.1: Comparisons of BESS Technologies [5], [28], [104-109].

Parameter	Pb-acid	NiCd	NiMH	Zinc-air	Li-ion	NaS	ZnBr
Specific energy (Wh/kg)	30 - 40	40-60	50-65	140-180	90-120		
Energy density (Wh/L)	70-75	70-100	140-200	200-270	200 - 250	1000	600
Specific power (W/kg)	250	150	200	105	300		
Nominal cell voltage(V)	2.0	1.2	1.2	1.65	3.6	2.08	1.8
Overcharge tolerance	High	Medium	Low		Very low		
Cycle life in full discharge (cycles)	500-1000	1000 - 2000	1000-2000	200 -300	1500 - 2000	2500	2500
Calendar life in years	5-8	10-15	8-10	-	-	15	
Self discharge (%/month at 25ºC)	3 - 5	20 - 30	20 - 30	4 - 6	5 - 10	No	Yes
Electrical efficiency (%)	80	60 - 85	Up to 80		> 90	90	75
Operating temperature range (C)	-10 to 50	-20 to 50	-10 to 50		10 to 45	290 to 360	20 -50
Auxiliaries	water					heater	pump

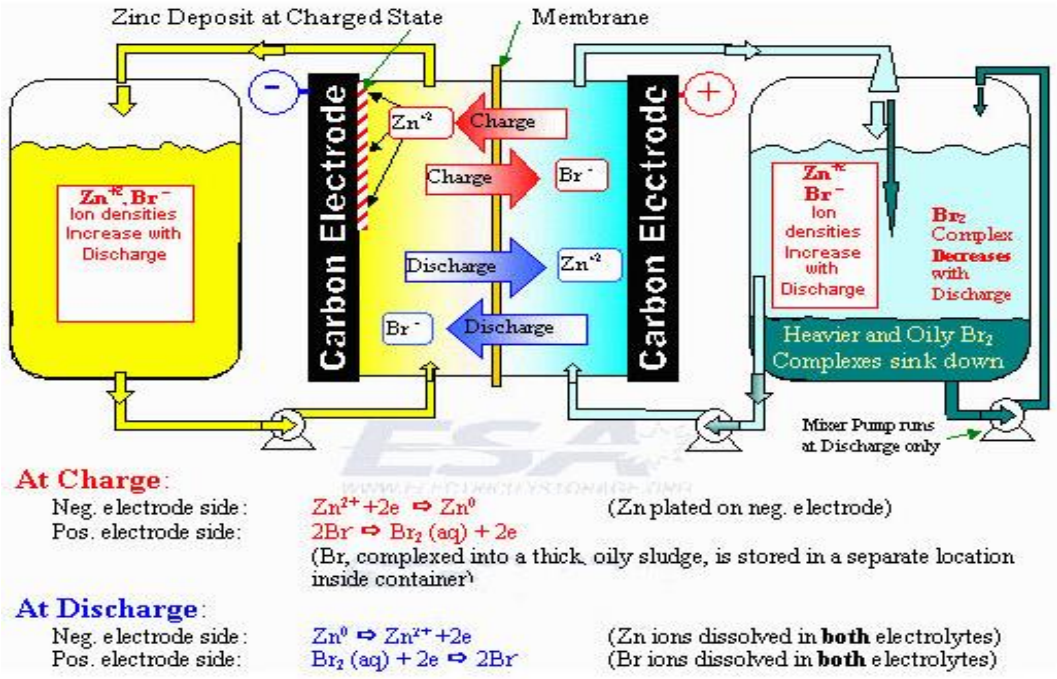

Fig. 5.3: Operating principles of ZnBr flow battery [107].

5.3.5 Ultracapacitors

Ultracapacitors or electric-double layer capacitors (EDLCs) store energy by means of an electrolyte solution between two solid conductors rather the conventional capacitor which has a solid dielectric between the electrodes [102]. This arrangement is responsible for their high capacitance (in farads and kilofarads) and high energy density in very compact form [107], [110]. They are popular in UPS (uninterruptible power supply) and grid applications where their ability to charge and discharge very fast at high efficiency is used in power quality mitigations [111]. In addition to their power cycling capability, they offer robust performance over wide temperature extremes and have high cycle life. In hybridized energy storage systems, when combined with batteries, the operational life of the system is increased because while the batteries optimize the energy capability, the ultracapacitors optimize the power capability [112].

5.3.6 Flywheel Energy Storage System (*FESS*)

FESS uses kinetic energy stored in a rotor spinning at high velocities. The unit is integrated with a motor/generator unit and power converter to handle the mechanical-to-electrical energy conversion [113]. During charging the flywheel is accelerated by the electric motor

which later operates as a generator during the discharge process. During a discharge event, the stored energy is converted to fixed frequency and voltage supply via the integral power converter. *FESS* is typically employed in power quality mitigations that require large number of charge-discharge cycles to provide up to 15 seconds ride-through for power interruptions or to bridge the shift when transferring from one power source to another [102],[103].

5.3.7 Compressed Air Energy Storage (*CAES*)

This technology stores energy as compressed air for later use. For PV-Storage system, photovoltaic power is used to compress the air which is then stored at high pressure in underground reservoirs. Excess energy from the PV system is used for the compression during periods of low demand and then converted back to electric energy via a turbine-generator set when electricity demand is high [103]. Using PV energy for the compression cycle, the fuel normally used is reduced substantially [102]. *CAES* have been used for numerous grid problems mitigations including support and load levelling. Installed commercial system capacities range from 35-300MW [103]. Recent ongoing research works explore the use of above-ground pipelines for the storage of compressed air for CAES applications [102], [103].

5.3.8 Pumped Hydro Storage

This mature technology can also be used in conjunction with photovoltaic power system. In this approach, the PV energy is used during off peak hours to pump water from a lower reservoir to a higher one. The stored water is later released during peak demand and turns the turbine to generate the needed electricity. The drawback of this storage medium for PV application include: 1) hard-to-find suitable geographical location, 2) need for large reservoir, 3) high total capital cost and the long time required to plan and build [5],[[28].

5.3.9 Hydrogen/Fuel Cell

A fuel cell is an electrochemical device that generates electricity by a chemical reaction without altering the electrodes and the electrolyte materials, as is the case with electrochemical batteries. By combining hydrogen and oxygen, electricity and water are produced. Thus, the main fuel used in a fuel cell is hydrogen. This hydrogen is often generated by the electrolysis process in an electrolyser [5]. Photovoltaic energy can easily be

used to initiate this electrolysis process so as to generate the needed hydrogen which is stored for future use. The hydrogen fuel can be stored in the following forms [5]: 1) underground for large quantities of gas and for long-term storage, 2) as liquid hydrogen in storage tanks, and 3) as compressed gas in cylinders for short storage times. Despite having long cycle life, the limitations of this storage technology include: 1) high initial cost, 2) complexity of the control system, and 3) life degradation in dynamic applications [64]. Fuel cells are successfully being applied for use in UPS applications and in grid-connected plants for load levelling and to meet peak demand.

5.3.10 Superconductive Magnetic Energy Storage (SMES)

Superconductive magnetic energy storage (SMES) is an enabling technology for the integration of renewable energy systems, especially wind and photovoltaic system. It involves storing energy in a magnetic field created by direct current flowing through a superconducting coil which is cryogenically cooled to a temperature below its superconducting critical temperature [103]. SMES have high energy densities and have the major advantage of high storage efficiency. Also, they have high dynamic response [103], [104].

5.4 Power Electronics Interface for PV Energy Storage

Augmenting PV energy source with energy storage to provide power on demand and mitigate the intermittency and variability shortcomings of PV energy generation requires the incorporation of a dc-dc power converter with bidirectional power flow capabilities. The dc-dc converter is required to perform the following functions: 1) to match (by stepping up) the lower voltage of the battery bank to the higher dc link voltage value required by the inverter, 2) to match (by stepping down) the higher dc link voltage to the level suitable for charging the battery bank, and 3) to control the power flow under steady state and transient conditions so as to achieve the system's needed power balance [115].

This section details the analysis and design of a 500W bidirectional dc-dc converter based on the half-bridge topology that is used for interfacing the energy storage system for this study.

5.4.1 Bidirectional DC-DC Converter Topology Selection & Analysis

Numerous topologies for possible implementation of bidirectional dc-dc converters have been reported in the literature [115]. Generally they are divided into two broad categories: 1) non-isolated (transformer-less) converters, and 2) isolated (transformer-inclusive) converters [116]. While the isolated converters have the advantage of providing isolation between the source and the load sides, the transformer-less versions have advantages of improved efficiency, reduced size and weight, and lower cost [115], [116]. Based on the aforementioned advantages, and coupled with simplicity, a half-bridge based, non-isolated, buck-boost topology shown in Fig.5.4 is adopted for this work. In this topology the switch cells, *SW1* and *SW2*, consist of IGBT power switches (*Q1*) in parallel with diode *D1* and *Q2*

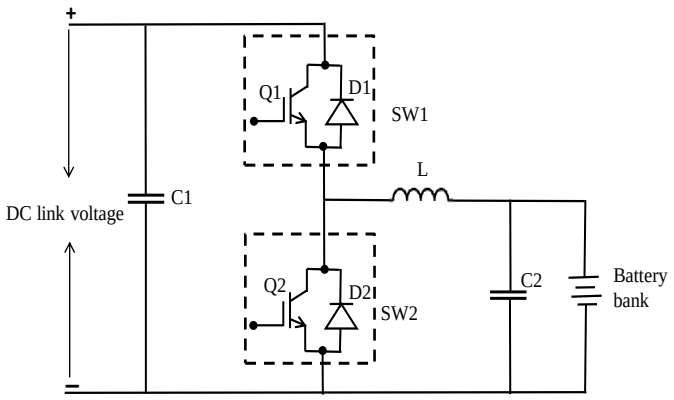

Fig. 5.4: Half-bridge-based bidirectional buck-boost dc-dc converter.

in parallel with diode *D2* to provide the bidirectional capability of the converter. For the PV application of this thesis, the buck converter operation (battery charging) is achieved by modulating *Q1*, with *D2* operating as the buck-mode diode. Similarly, the boost converter operation (battery discharging) is achieved by modulating *Q2*, with *D1* serving as the boot-mode diode.

5.4.2 Analysis of the Bidirectional DC-DC Converter

The operating principle of the bidirectional dc-dc converter, Fig. 5.4, in steady state is based on four modes [117]. The four operational modes are described below and illustrated in Fig. 5.5.

- Mode 1: *Battery-energy-to-inductor-transfer* mode. In this mode, Fig. 5.5a, *Q2* is turned *ON* and the battery energy is transferred to the inductor, *L*. *Q1* is turned *OFF*, while the diodes (*D1 & D2*) are reverse biased.
- Mode 2: *Battery-energy-release-from-inductor* mode. In this mode (Fig. 5.5b), *Q1* & *Q2* are both *OFF*; *D1* conducts to release the energy now in the inductor to the dc link.
- Mode 3: *PV-energy-to-inductor transfer* mode. For this mode (Fig. 5.5c), *Q1* is turned *ON* to transfer the PV energy to the inductor; *Q2* is turned *OFF*; *D1* & *D2* are reverse biased.
- Mode 4: *PV-energy-release-from-inductor* mode. For this mode (Fig. 5.5d), *Q1* & *Q2* are turned *OFF*; *D2* conducts to release the PV energy for battery charging.

Modes 1 and 2 constitute the battery discharge phase, when the converter is stepping up the battery voltage to the required value of the dc link voltage. This is during periods of little or

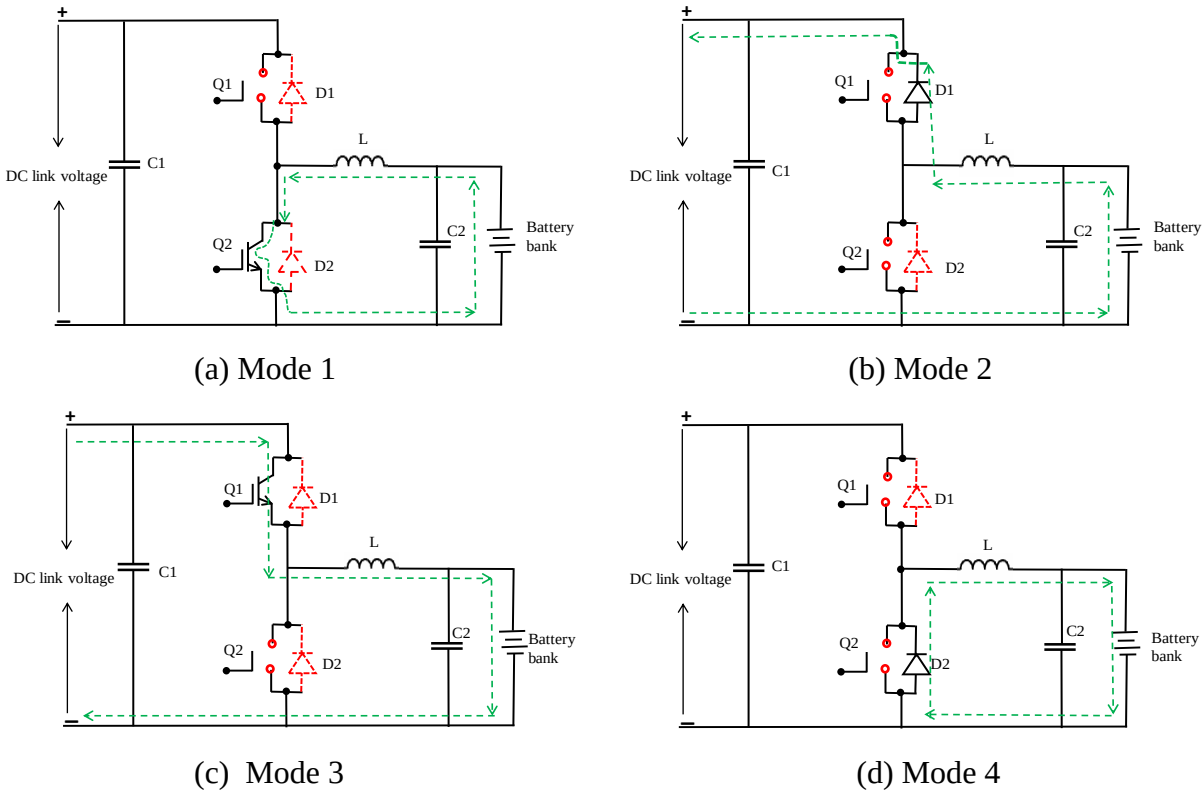

(a) Mode 1 (b) Mode 2

(c) Mode 3 (d) Mode 4

Fig. 5.5: Modes of operation of the bidirectional dc-dc converter.

no insolation from the solar panels. Modes 3 and 4 constitute the battery charging phase when the converter steps down the higher voltage of the dc link to charge the battery bank. This

situation is obtainable during periods of excess solar radiation, when the solar array can supply both the load (the inverter) and at the same time charge the battery bank.

5.4.3 Design of a 500W Bidirectional DC-DC Converter

The specifications for the converter are shown in Table 5.2. The design is done such that components must satisfy both the buck mode and the boost mode of operating conditions. Hence, the following calculations consider both cases before choosing the higher values.

Table 5.2: Bidirectional dc-dc converter specifications.

Parameter	**Value**
Input voltage from battery bank, V_{IN}	40 – 60V
DC link voltage, V_{DC}	180V
Average output voltage for battery charging.	60V
Maximum power, P_o	500W
Switching frequency, F_S	50kHz
Inductor current ripple, Δi_L	30%
Output voltage ripple, ΔV_o	2%

Inductor selection:

a) *Buck mode*: For this mode, the converter has to step down the dc link voltage from 180V to an output voltage of 60V needed for charging the battery bank of 48V 200Ah batteries. The inductor value, L_{BUCK}, and its peak current value are determined using the specified maximum inductor current ripple based on equation (5.2) [51], [118].

$$L_{BUCK} = \frac{V_o \times (1-D)}{\Delta_{iL} \times F_s} \tag{5.2}$$

Where, D is the duty cycle of the power switch, defined as the fraction of the switching period that the switch is closed. And for buck mode of operation equation (5.3) holds.

$$V_o = V_{IN} \times D \tag{5.3}$$

Substituting (5.3) into (5.2) and using values from Table 5.2 gives:

$$L_{BUCK} = \frac{V_o \times \left(1 - \frac{V_o}{V_{IN}}\right)}{\Delta i_L \times F_S} = \frac{60 \times \left(1 - \frac{60}{180}\right)}{0.3 \times \left(\frac{500}{60}\right) \times 50000} = 320\mu H$$

Where Δi_L = 30 %(Io) = 30% (P_o/V_o) = 0.3 x 8.333 =2.5A.

The inductor peak current is:

$$I_{pk} = I_o + \frac{\Delta i_L}{2}$$

$$= 9.58A$$

b) *Boost mode***:** For this mode, the converter has to step up the battery bank voltage from the input range of 40 - 60V to the dc link voltage, V_{DC}, of 180V. Thus, the circuit must be analysed for both input extremes from the battery bank to determine the worst case condition. For V_{BAT} = 40, the duty ratio, D, is given by [119]:

$$D = 1 - \frac{V_{BAT}}{V_{DC}} = 1 - \frac{40}{180} = 0.78$$

The average inductor current is given by [51], [119]:

$$I_L = \frac{V_o \times I_o}{V_{BAT}} = \frac{P_o}{V_{BAT}} = \frac{500}{40} = 12.5A$$

Thus, the variation in inductor current to meet the 30% specification in Table 5.2 is:

Δi_L= 0.3x12.5 = 3.75A.

The inductor value, L_{BOOST1}, is thus given by [51], [119]:

$$L_{BOOST1} = \frac{V_{BAT} \times D}{\Delta i_L \times F_S} = \frac{40 \times 0.78}{3.75 \times 50000} = 166.4\mu H$$

Repeating the calculations for V_{BAT} = 60V,

$$D = 1 - \frac{V_{BAT}}{V_{DC}} = 1 - \frac{60}{180} = 0.66$$

$$I_L = 500/60 = 8.33A$$

Δi_L = 0.3x8.33 = 2.5A.

The re-calculated value of the inductor becomes:

$$L_{BOOST2} = \frac{V_{BAT} \times D}{\Delta i_L \times F_S} = \frac{60 \times 0.66}{2.5 \times 50000} = 316.8\mu H$$

Thus the higher value, L_{BOOST2}, is chosen to satisfy the specifications for the variations in the voltage of the battery bank. This is then compared to the calculated value for the buck mode of operation and the higher of the two values is chosen. Therefore, the value of the inductance for the bidirectional converter is:

L = 320µH

Selection of Capacitors:

The value of the output capacitance, C_2, is given by [51]:

$$C_2 = \frac{1-D}{8 \times L \times (\frac{\Delta V_o}{V_o}) \times F_S{}^2} = \frac{1-0.33}{8 \times 320 \times 10^{-6} \times 0.02 \times (50000)^2} = 5.2 \mu F$$

In this design, a low ESR (equivalent series resistance) capacitor of 10µF is chosen. The ESR must be low so as to be able to absorb the high frequency ripple current generated. Thus, C_2 is chosen to be a capacitor of rating:

10µF, 100V.

Similarly, the hold-up capacitor at the dc link, C_1, is chosen to have the same capacitance but with a voltage rating more than the dc bus voltage of 180V. Thus, C_1 is chosen to be a capacitor of rating:

10µF, 250V.

Switching devices selection:

a) IGBT Switches, Q1 and Q2:

The average current, I_A, for the switch *Q1* for buck operation is:

$$I_A = D \times I_{IN}$$

For *Q1*, I_{IN} = 8.33A, for the buck mode and D = 0.3. Thus,

$$I_A = 0.3 \times 8.33 = 2.5A$$

And the rms current, I_{rms}, for *Q1* is:

$$I_{rms} = \sqrt{D} \times I_{IN} = \sqrt{0.3} \times 8.33 = 4.6A$$

The peak voltage seen by *Q1* during buck-mode is equal to the dc link voltage of 180V. Applying a 50% safety rating for the voltage withstand capability and 300% capability to the current rating because of losses, result in *Q1* with the following parameters chosen:

$$\boldsymbol{V_{Q1}} \geq (180\times 1.5 = 270\text{V})$$

$$\boldsymbol{I_{rms}} \geq (3\text{x}4.6 = 13.8\text{A}).$$

Similarly for *Q2* for boost operation:

$$I_{IN} = \frac{I_o}{1-D} = \frac{(P_o/V_o)}{1-D} = \frac{(500/180)}{1-0.66} = 8.2A$$

And the average current and the rms value of the current are:

$$I_A = D \times I_{IN} = 0.66 \times 8.2 = 5.4A$$

$$I_{rms} = \sqrt{D} \times I_{IN} = \sqrt{0.66} \times 8.2 = 6.67A$$

Using the same safety ratings as in *Q1*, *Q2* is chosen to satisfy the following conditions:

$$\boldsymbol{V_{Q2}} \geq (180\times 1.5 = 270\text{V})$$

$$\boldsymbol{I_{rms}} \geq (3\text{x}6.67 = 20\text{A}).$$

b) Diodes, D1 and D2:

The diodes chosen are body diodes to *Q1* and *Q2* and so are rated to withstand the same voltage and current as the IGBTs.

5.5 Proposed Multi-Objective Control System for Battery Charging & Power Management

This section discusses the development of a multi-objective control system that achieves the following control objectives necessary for the integration of energy storage into the PV system:

- *Control objective 1*: To balance the power flow, P_{PV}, from the PV array to the battery bank, P_{BAT}, and the load, P_{LOAD}, irrespective of the irradiation, temperature and load changes.
- *Control objective 2*: To ensure the PV power is harvested and utilized effectively by operating at the maximum power point, MPP, at all operating conditions using the modified incremental conductance MPPT algorithm developed in Chapter 4.
- *Control objective 3*: To effectively regulate the dc link voltage at the desired value of 180V during power balancing, battery charging and battery discharging.
- *Control objective 4*: To ensure that the battery is charged effectively with 3-stage charging algorithm without overcharging via the bidirectional dc-dc converter.

- *Control objective 5*: To ensure effective discharge of the battery when insolation is low or non-existent without over discharging, using the bidirectional dc-dc converter.

Achieving these control objectives require the development of the appropriate controllers and algorithms. Firstly, the three-stage charging algorithm used in charging the SLA battery bank is presented. This is followed by the development of a power management technique that ensures proper power balance between the PV array, the battery bank and the system load for all cases of solar insolation and ambient temperature. These approaches are discussed in the subsections below.

5.5.1 Multi-Stage Algorithm for SLA Battery Charging

Because of the advantages of cost, maturity of the technology and familiarity by users, the lead acid battery technology is popular in PV applications [120]. Consequently, the deep-cycle sealed lead acid (SLA) variant, otherwise called valve-regulated lead acid (VRLA), is used as the energy storage medium in this study. The three-stage charging algorithm adopted and incorporated into the control system for the bidirectional dc-dc converter is discussed in the following sections.

The bidirectional dc-dc converter implements the three-stage charging algorithm using the PWM technique. With the PWM technique, the dc link voltage, V_{DC}, and the incoming current from the panels via the SEPIC converter is switched *ON* and *OFF* with a variable duty cycle, β. Battery charging is done via the IGBT switch *Q1* of the bidirectional buck-boost converter, Fig. 5.4, which has to operate in the buck mode. Thus, the average output voltage used for battery charging, V_{CH}, is given by:

$$V_{CH} = \beta \times V_{DC} \tag{5.4}$$

Where,

$$\beta = \frac{T_{ON}}{T_{ON} + T_{OFF}} \tag{5.5}$$

and T_{ON} is the *ON* time of *Q1*, T_{OFF} is the *OFF* time and V_{DC} is given by:

$$V_{DC} = V_{PV} \times \frac{\beta}{1-\beta} \tag{5.6}$$

Where V_{PV} is the input voltage from the solar array.

The controller uses this PWM technique to progressively increase and decrease the duty cycle to achieve the three-stage charging (bulk, absorption, and float) algorithm [121]. The three-stage charging algorithm is described below and illustrated in Fig.5.6, where the charge voltage set points are [121]:

- Bulk/absorption = 2.45V per cell@ 25ºC.
- Float = 2.30V per cell @ 25ºC.

Bulk charging: In this mode the charger applies constant current (*CC*) from the solar panels to the battery. This charge rate is based on the maximum power point current, I_{MPP}, of the solar panel. For SLA batteries, the bulk mode restores the battery to about 70% SoC (state of charge) and takes up roughly 50% of the required charge time of between five to ten hours of bright sunlight (1000W/m^2) [121]. The end-of-charge voltage for restoring this 70% SoC is set by the controller at 2.45V per cell for this SLA battery bank. The *CC* is maintained until the battery voltage reaches this pre-defined safety limit at which the constant voltage charging, the absorption phase starts, as shown in Fig.5.6.

Absorption charging: This mode commences once the end-of-charge voltage in the bulk mode is attained. The controller transits from constant current (*CC*) to constant voltage (*CV*) operation and remains at this constant voltage value of 2.45V per cell. The charge rate is reduced progressively as the battery charges up. The *CV* charging ensures the restoration of the remaining capacity of the battery. The capacity returned is approximately the remaining 30% SoC. This mode also ensures that the battery is never undercharged, thus avoiding the problem of sulfation [45], [121].

Float charging: The float charge maintains the battery at full charge and is used mainly to avoid the usual self-discharge associated with batteries [45], [121]. This mode commences at the expiration of the absorption mode when the charger transitions to another voltage level as shown in Fig.5.6. The charge rate is maintained at its reduced lowest value.

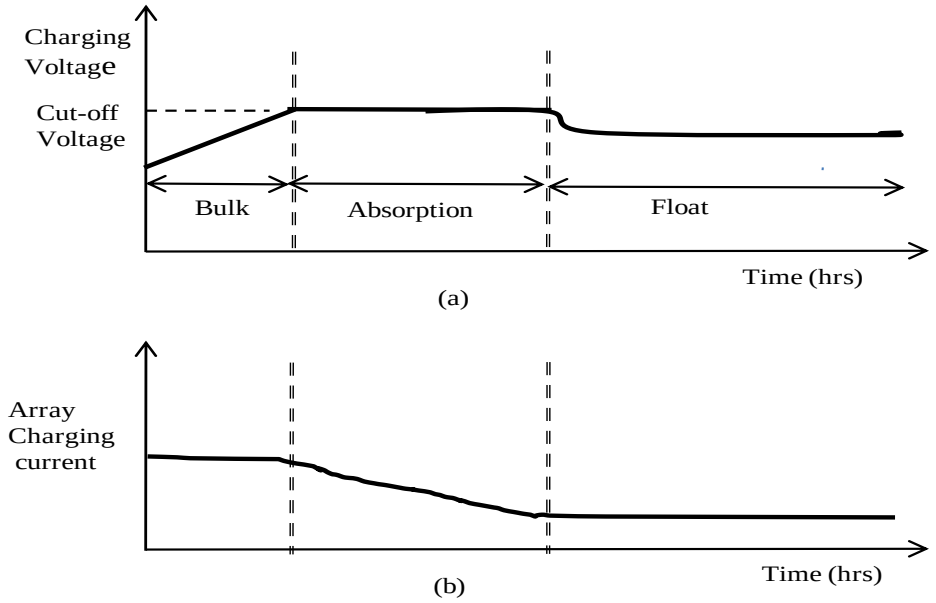

Fig. 5.6: Three-stage charging algorithm. (a) Voltage profile. (b) Current profile.

5.5.2 Power Management Technique

The power flow diagram of this two-source (PV array and battery bank) system is shown in Fig.5.7. Three key parameters of Fig. 5.7 determine the direction of power flow and the mode of operation**.** These parameters are: 1) the PV array power, P_{PV}, 2) battery state of charge, SoC, and 3) the load. Depending on the condition of these parameters, the proposed control system can operate in any of the following three modes:

i) *Full charging mode*: This occurs when the PV array power is greater than the power demand of the load. If this occurs and the state-of-charge, *SoC*, of the battery energy storage is below the desired maximum, SoC_{MAX}, then battery charging is initiated, Fig. 5.8a. Also, the pre-set value of the charging current, I_{BP}, is used for the charging process. That is, the conditions for this mode are:

$$P_{PV} > P_{LOAD} \tag{5.7}$$

$$S_oC < S_oC_{MAX} \tag{5.8}$$

$$I_B = I_{BP} \tag{5.9}$$

Operation of this mode activates the power switch, Q1, of the bidirectional converter as shown in Fig. 5.8a.

ii) *Discharging mode:* This occurs when the energy from the solar generator is insufficient to power the load. In this case, for system availability, the battery is discharged.

However, the *SoC* must be above a certain minimum level to avoid over-discharge of the battery. That is, the conditions for battery discharge, Fig. 5.9, when *Q2* of the bidirectional converter is activated are:

$$P_{PV} < P_{LOAD} \tag{5.10}$$

$$S_oC > S_oC_{MIN} \tag{5.11}$$

iii) *Partial charging mode*: This mode occurs when the PV array power is greater than the load power and the battery state of charge is below maximum. However, the charging current, I_B, is below the pre-set value, I_{BP}. That is, the conditions for this charging mode are:

$$P_{PV} > P_{LOAD} \tag{5.12}$$

$$S_oC < S_oC_{MAX} \tag{5.13}$$

$$I_B < I_{BP} \tag{5.14}$$

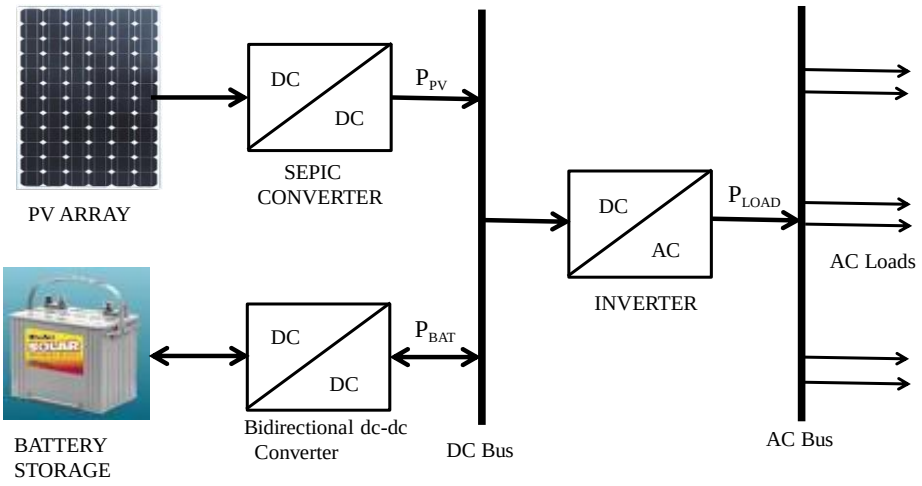

Fig. 5.7: Power flow diagram of the system showing the converters and energy sources: PV array and battery energy storage.

5.5.3 Controller Implementation

The development of this multi-objective control system requires the monitoring of the following systems variables:

- PV array variables – voltage and current.
- Battery variables – voltage and current.
- Inductor current and switch current.
- Dc link voltage.

- Load voltage and current.

The proposed control system (Fig. 5.8 and Fig.5.9 integrated) is a multi-loop system with current-mode control loop, MPPT loop, and battery charging/discharging loop. Based on the power output of the PV module, the battery *SoC* and the load, the mode selector switch determines whether the bidirectional converter is to charge or discharge the battery by switching *ON* the *IGBT*, *Q1*, for battery charging and *Q2* for battery discharging. Fig. 5.8 shows the control system operation in battery charging mode. In this mode, the average current mode is used with an outer PV voltage regulating loop. The combination of the MPPT and the battery charging loop is used to achieve the desired power balance control described earlier, and to charge the battery with the three-stage charging algorithm described in the previous section.

The control loop for battery discharging is shown in Fig. 5.9, where the control goal is to attain the desired dc link voltage without over discharging the battery. The variables in Fig.5.8 and Fig.5.9 are as defined in Table 5.3.

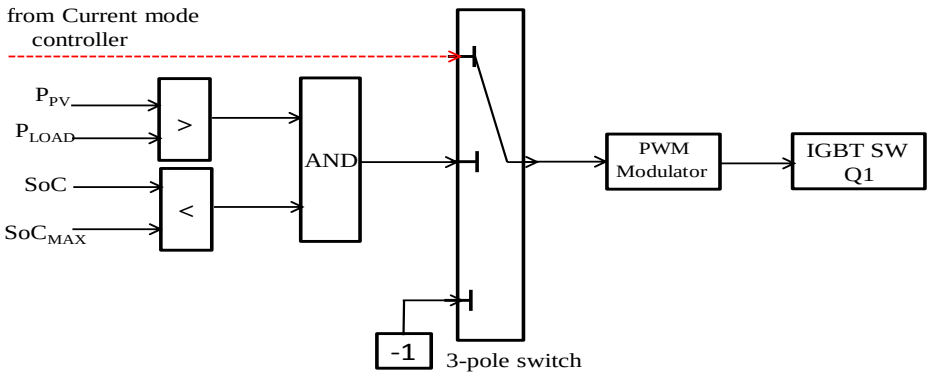

(a) Charging mode selector

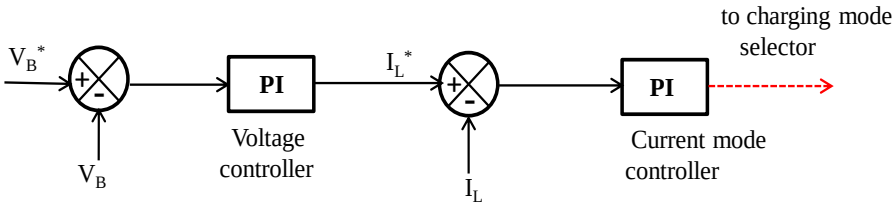

(b) Charging loop.

Fig. 5.8: Controller configuration for battery charging.

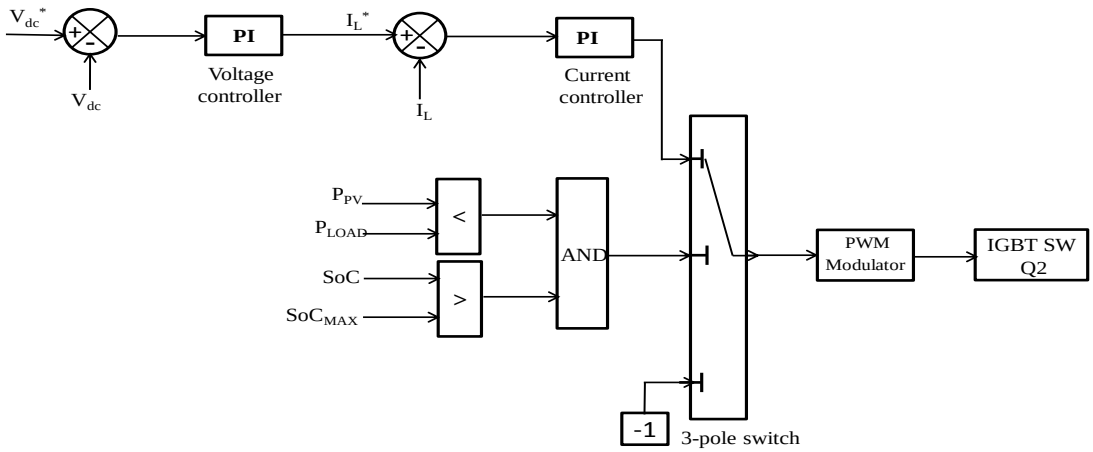

Fig. 5.9: Controller configuration for battery discharging.

Table 5.3: Controller parameters defined.

Parameter	Meaning
P_{PV}	PV array power
P_{Load}	Load power
SoC	Battery state of charge
I_L	Inductor current.
I_L^*	Reference value of inductor current.
V_B	Battery voltage.
V_B^*	Reference value of battery voltage during charging.
V_{dc}^*	Reference dc link voltage.
V_{dc}	Dc link voltage

5.6 Simulation Model

Fig. 5.10 shows the simulation model developed in the Simulink/SimPowerSystems software to investigate the ability of the designed bidirectional dc-dc converter to work seamlessly with the other subsystems of the PV power plant by providing the necessary charging and discharging control functions for the battery energy storage system. Integrated in the model are: 1) the PV array as the source of power; 2) the SEPIC converter to step up and regulate the fluctuating output of the PV array while also implementing the MPPT; 3) the designed bidirectional dc-dc converter to interface the energy storage system via charging and discharging functions, and 4) the battery energy storage system to serve as a back-up source

of power during night time or periods of low solar irradiation. This simulation model uses the generic battery model provided by the Matlab/Simulink's SimPowerSystems package. Despite the shortcomings of not taking into account the dynamic behaviour of the battery and the ageing effect, this battery model is chosen for its simplicity – the parameters of the battery can easily be set in the model.

In Fig. 5.10, the SEPIC converter is controlled using the current-mode technique to regulate the dc link voltage at 180V. This serves as the input to the bidirectional converter which steps this down to a nominal value of 60V needed for charging the SLA battery bank of 200Ah, 48V. The converter is also able to step up this 48V nominal voltage of the battery bank to the dc link voltage of 180V during the discharge mode. The multi-objective control system integrates the following: 1) MPPT loop, 2) dc link voltage regulating loop, 3) discharge loop, 4) the charging loop, and 5) the charge/discharge manager. Fig. 5.10(b) shows the detailed view of the charge/discharge manager which determines the mode of operation of the bidirectional converter.

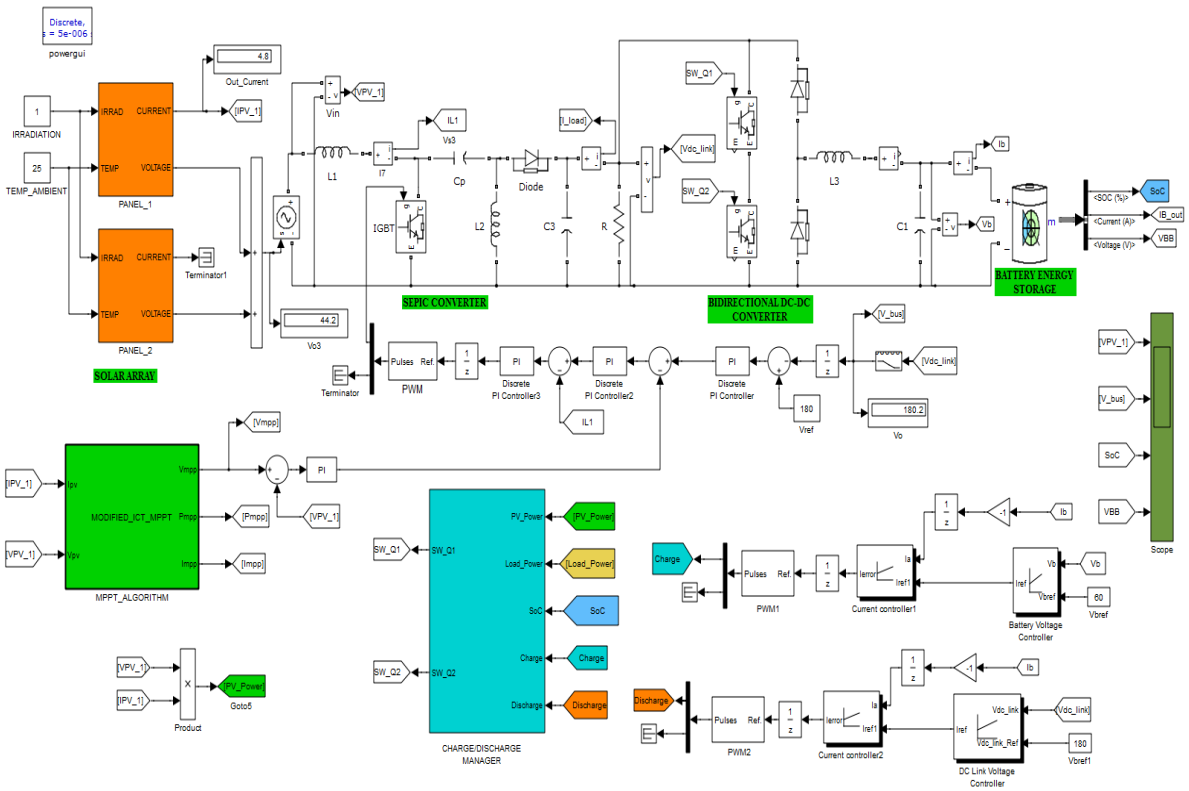

(a)

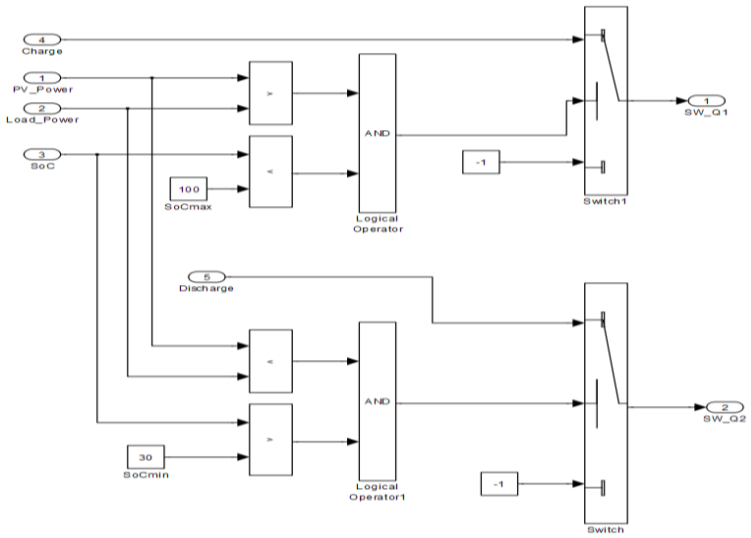

(b)

Fig. 5.10: Simulation model in Simulink/SimPowerSystems software showing: (a) the PV array, the SEPIC and bidirectional converters, and the battery energy storage system and the controls; (b) detailed view of the charge/discharge manager subsystem.

5.7 Simulation Results and Discussions

Using the simulation model of Fig. 5.10, simulations were performed using the parameters of the PV module, BP 380. A two-panel array, a battery bank of 48V nominal voltage and a dc link voltage of 180V were used for the simulations. The following discussions analyse the performance of the designed bidirectional dc-dc converter and the associated control system.

When there is sufficient solar power from the array, it is used to power the load while the excess is used to charge the battery via the bidirectional converter. As discussed earlier, the bidirectional dc-dc converter acts as a buck-boost converter. In the charging mode, it converts the dc link voltage of 180V to a nominal voltage of 60V sufficient to charge the battery bank of 48V nominal voltage. Whereas in its discharge mode, the converter boosts the battery bank's terminal voltage to the desired dc link voltage of 180V.

The bidirectional converter performance during the charging mode is illustrated in Figs. 5.11-5.13. In Fig. 5.11(a) the battery bank's terminal voltage is seen to have risen from the initial value of 58 V to a stabilised value of 60V, as dictated by the reference value set by the control algorithm. While the charging operation is going on, the dc link voltage is effectively

maintained at the desired value of 180Vdc as illustrated in Fig. 5.11(b). The current injected into the battery during the charging process is indicated in Fig. 5.12(a), while the inductor current is shown in Fig. 5.12(b) following the desired reference value. The charging process injects power into the battery as shown in Fig.5.13 (a) while the battery state of charge (SOC) following the charging process is shown in Fig. 5.13(b). It is seen that the SOC ramps up from the initial value - indicating an increase in the available capacity of the battery, as a consequence of the charging operation.

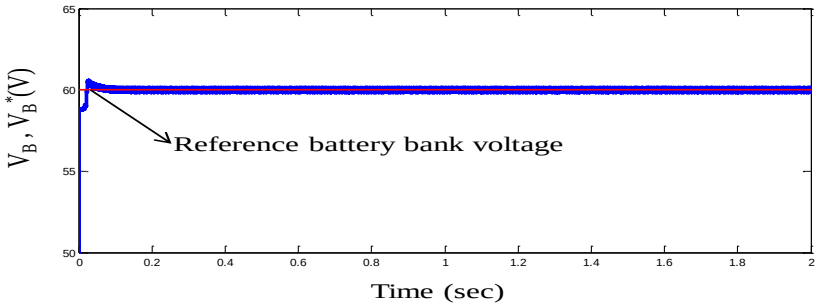

(a) Battery bank voltage and reference bank voltage.

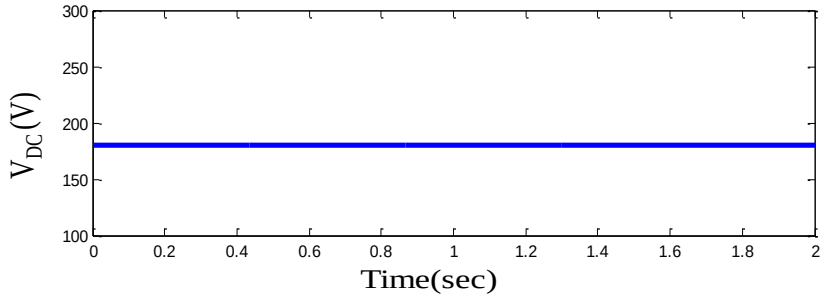

(b) DC link voltage.

Fig. 5.11: Battery bank's voltage and dc link voltage during charging operation.

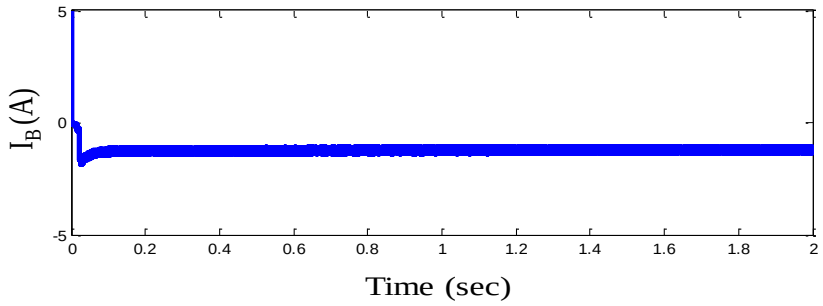

(a) Battery current during charging.

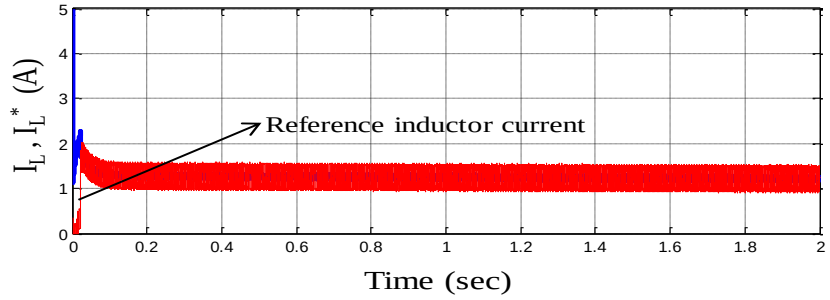

(b) Inductor current and reference inductor current.

Fig. 5.12: Battery current and inductor current during charging.

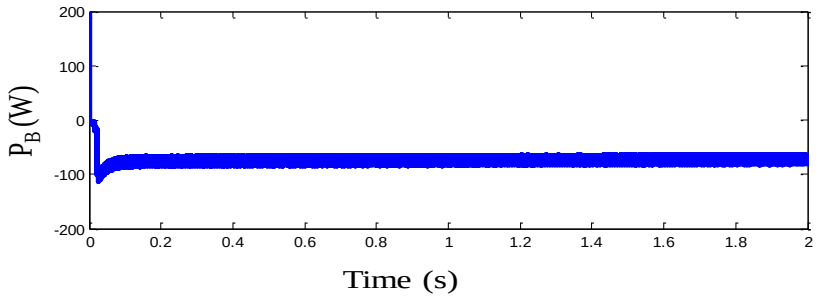

(a) Power injected into battery during charging.

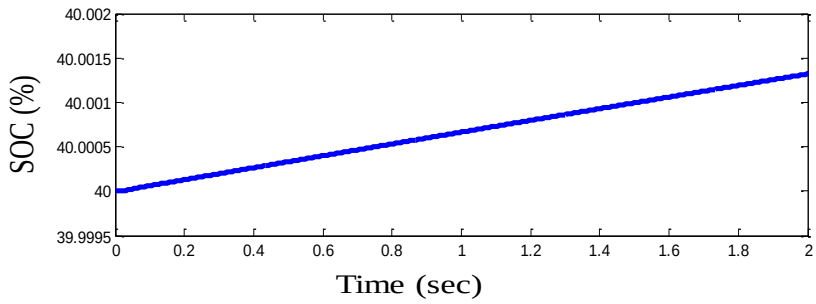

(b) Battery SOC during charging.

Fig. 5.13: Battery power and state of charge following charging.

During periods of none or insufficient solar power, the battery bank is discharged to ensure the system's reliability. In this simulation, during the discharge operation, the system is subjected to a step load decrease from 300 Ω to 156 Ω to test the robustness of the control algorithm. The bidirectional converter's performance for this discharge mode is shown in Figs. 5.14-5.16. In Fig. 5.14(a), at turn-on, the battery bank's voltage settles at a steady value of 57V after 0.2 second following the transient period. However, at the step time of 1 second the step load decrease is introduced. This results in the sudden increase in the voltage which then settles again after 1.1 seconds. Conversely, Fig. 5.14(b) shows the corresponding response of the dc link voltage. It is seen that despite the sudden decrease in the battery's voltage as a result of the step load decrease, the dc link voltage is maintained at the desired voltage of 180V. This indicates the ability of the control algorithm to effectively regulate the dc link voltage in the face of changing battery voltage.

Similarly, Fig. 5.15 shows the battery current and the inductor current in both transient and steady state operation during the same discharge conditions. The inductor current and the battery current, as expected, show sudden decrease in values with the introduction of the step load decrease. The inductor current is seen to follow its reference value. In Fig.5.16, for the same discharge conditions, the battery power is seen to decrease from the initial steady of 200W to about 120W with the sudden reduction in the load while the battery SOC decrease slightly from the initial value of 80%.

The ability of the bidirectional dc-dc converter to regulate the dc link voltage and follow the assigned reference currents indicates the robustness of the integrated control algorithms.

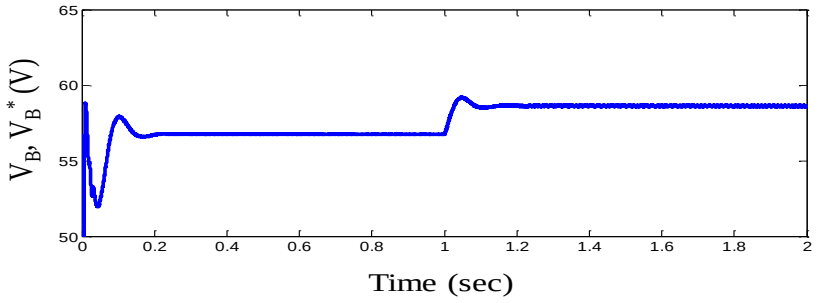

(a) Battery bank voltage and reference bank voltage in discharging mode.

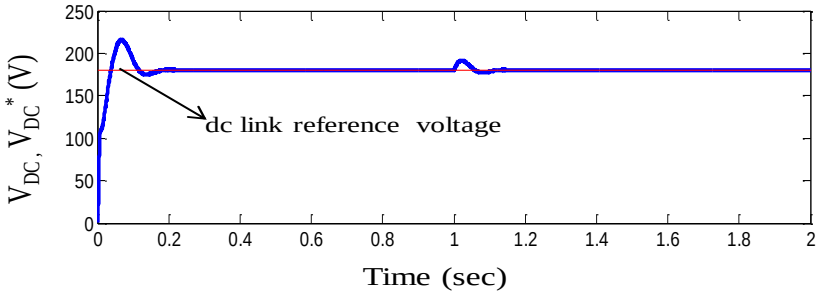

(b) DC link voltage.

Fig. 5.14: Battery bank's voltage and dc link voltage during discharge.

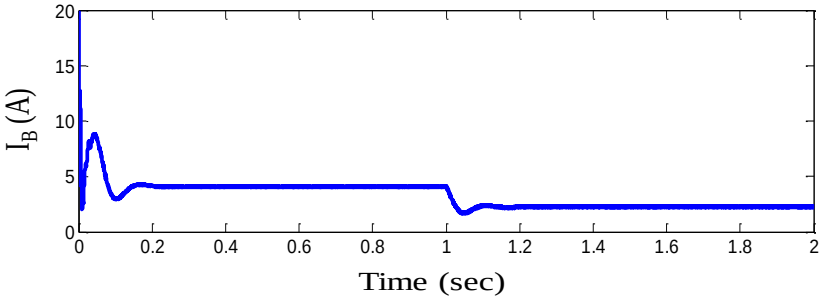

(a) Battery bank current during discharge mode.

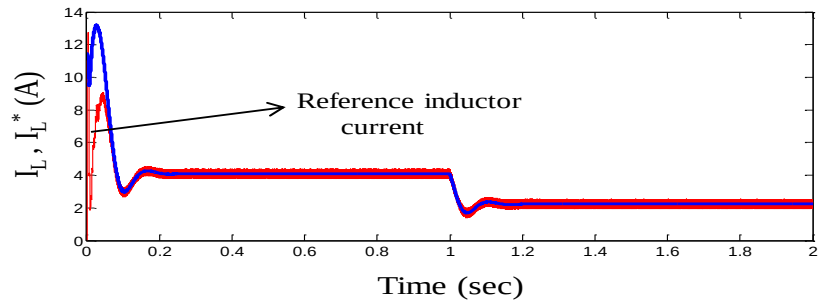

(b) Inductor current and its reference.

Fig.5.15: Battery current and inductor current during discharge.

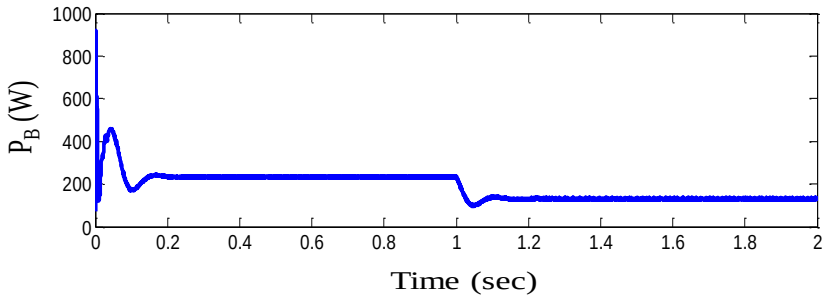

(a) Power discharge by the battery.

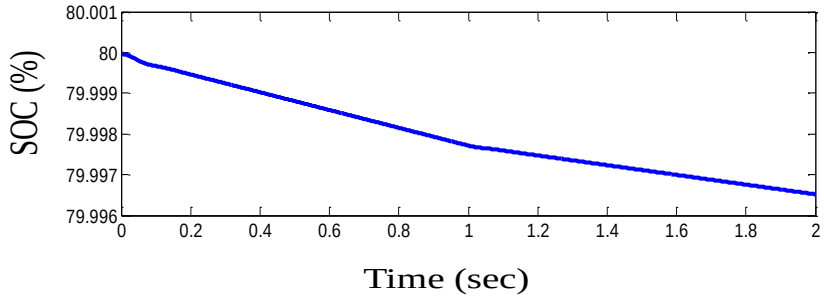

(b) SOC following a discharge.

Fig. 5.16: Battery power and state of charge after a discharge event.

5.8 Conclusions

This chapter has discussed the interfacing of energy storage system to a PV power plant using a simple, low-cost bidirectional dc-dc converter based on the half bridge topology. A multi-objective, multi-loop control system has been designed and implemented to control the dc link voltage, track the maximum power, implement battery charging and discharging functions without overcharging or over discharging, and manage the power transfer among the various subsystems. Simulation results show that the proposed control system is able to effectively implement these functions. This attests to the robustness of the integrated control algorithms.

Chapter 6
Control of Photovoltaic Inverter for Voltage and Frequency Regulation

6.1 Introduction

The photovoltaic (PV) inverter is the key power electronic interface for both the grid-connected PV power systems and for off-grid (standalone) systems. It has the main function of converting the dc power generated by the PV array into grid-synchronized *ac* power. To ensure the reliable delivery of power to consumers from the renewable energy generator, the inverter has to ensure that the frequency and magnitude of the generated voltage are within the acceptable limits. The frequency must be within the range of 50Hz ± 0.4% for a 50Hz system [122]. In any power system, this requirement for the supply frequency to be within a narrow band is necessary for the following reasons [122]:

(i) It ensures that motor-based loads in both industrial and domestic applications operate at the required constant speeds. This is because the speed of *ac* electrical drives is frequency sensitive.
(ii) As a basis for timing various processes in electronic applications.
(iii) For the safe operation of power transformers. Transformers are generally sensitive to frequency changes and may be overloaded if the frequency drifts substantially from the nominal value.

Effective control of the magnitude and frequency of the *ac* output voltage requires a robust control technique. The PWM (pulse width modulation) technique is a popular method for achieving such effective control, with the sinusoidal PWM variant being able to provide output voltages close to a sine wave by reducing the low order harmonics to a negligible level [123], [124]. In addition to controlling both the voltage magnitude and frequency, efficiency consideration has been a major driving factor of PV inverter technology due to the high cost of PV solar energy. Compared to motor drive inverters, PV inverters are more complex in both hardware and functionality. Such inverters, in addition to the primary function of dc-ac conversion, may also feature the following functionalities [47], [125]: 1) maximum power

point tracking (MPPT); 2) anti-islanding: for grid-connected systems; 3) grid synchronization; and 4) data logging.

The main focus of this chapter is the development of control algorithms that can effectively regulate the magnitude and frequency of the generated output *ac* voltage with minimal harmonics for photovoltaic power plants in the following modes of operation: a) single-phase operation, b) three-phase grid connected operation, and c) three-phase standalone operation. Firstly, a review of dc-ac converter interfaces classified according to their utilization topologies is done. This is followed by a review of such converters based on their schematic topologies. Thirdly, a review of the popular modulating strategies for dc-ac conversion used in single-phase applications is done. This is followed by a review of the vector control scheme applied for the control of a three-phase PV power plant in both the grid connected mode and in a standalone mode. Also reviewed briefly is the applicable standards for the integration of PV inverters to the grid. This is followed by the development of the proposed control system for a single-phase inverter to achieve a sinusoidal output waveform. Finally, the simulation results and discussions are presented, followed by the chapter conclusions.

6.2 Review of Inverter Utilization Topologies for PV Systems

To decrease the cost and increase the efficiency of PV systems, many inverter utilization topologies have been developed. The four most popular of these topologies are discussed below [47], [125-126]:

- *Centralized Inverter Topology*: In this topology, Fig. 6.1, the PV modules are connected in series and parallel in order to achieve a higher power – typical unit sizes range from 100 to 1000kW with three-phase topology. One common central inverter connected to the common dc bus is used to achieve this higher power. Despite the advantage of not requiring pre-inverter voltage boost converter because of use of series-connected strings to achieve high voltages, this topology has the following disadvantages [126]: 1) power losses due to mismatch between PV modules, 2) losses in string diodes, 3) losses due to common MPPT, 4) use of high voltage dc cables between PV panels and inverter, and 5) limited system reliability due to dependence on a single inverter – failure of which throws the entire plant out of operation.
- *String Inverter Topology*: In this topology, Fig.6.2, the PV plant is divided into several parallel strings with each string having a separate inverter. These string

inverters are paralleled and connected to the grid (or the *ac* bus for off-grid systems). Each of these string inverters is equipped with MPPT capability to increase the energy yield by the mitigation of PV mismatch and shading losses. The advantages of this topology include [126], [127]: 1) use of fewer PV panels, since dc-dc converters can easily be incorporated to boost the string voltage, 2) no losses in the string diodes, and 3) enhanced supply reliability due to dependence on more than one inverter. This topology has evolved as the standard for grid connected PV systems for lower power applications ranging from 0.4 -2kW, especially for small roof-top plants.

- *Multi-string Inverter Topology:* This topology, Fig.6.3, is a derivative of the string topology used for higher power applications – typically in the 1.5-6kW range for medium large roof-top plants. Each string is equipped with a separate dc-dc converter integrated with MPPT capability. These strings with the dc-dc converters and MPPT functionalities are then paralleled through a common dc-ac inverter. The unique advantages of this topology include [126],[127]: 1) compactness and cost-competitiveness, 2) combines advantages of central and string topologies, 3) ability to incorporate PV strings of different technologies and different orientations.
- *Module Integrated Inverter Topology:* In this topology, Fig. 6.4, a single PV module is directly connected to the grid via its own integrated inverter with MPPT functionality. The advantages of this topology include [126],[127]: 1) reduced mismatch losses, 2) better optimization of power extraction due to separate MPPT, 3) modularity of usage because of the plug-and-play nature. However, it has the following disadvantages [126]: 1) low efficiency occasioned by boosting of the low dc voltage of the panel to a higher level needed by the inverter, 2) low power conversion, 3) limited to low wattage applications – just one panel integrated.

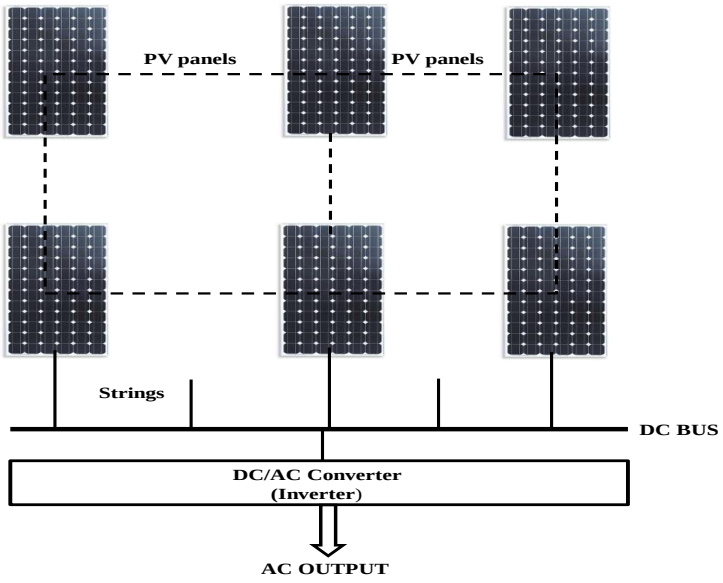

Fig. 6.1: Centralized inverter system topology.

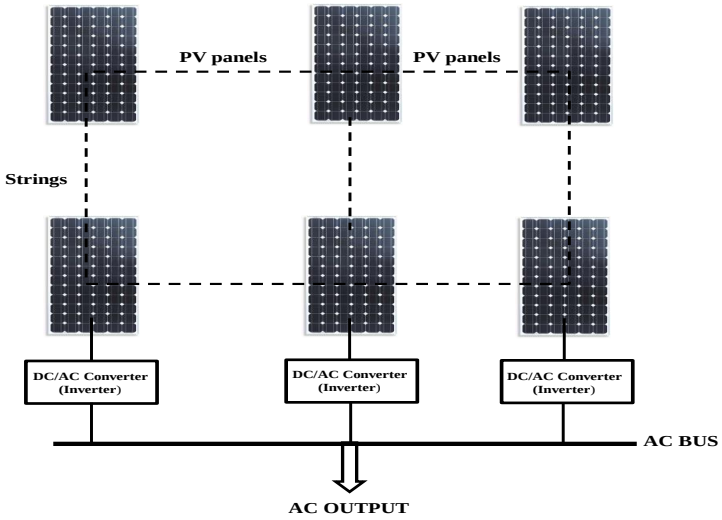

Fig.6.2: String inverters topology.

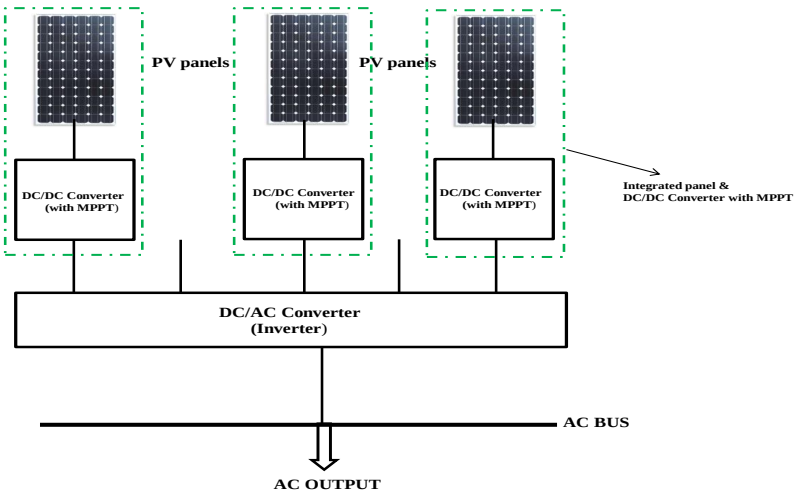

Fig. 6.3: Multistring inverters topology.

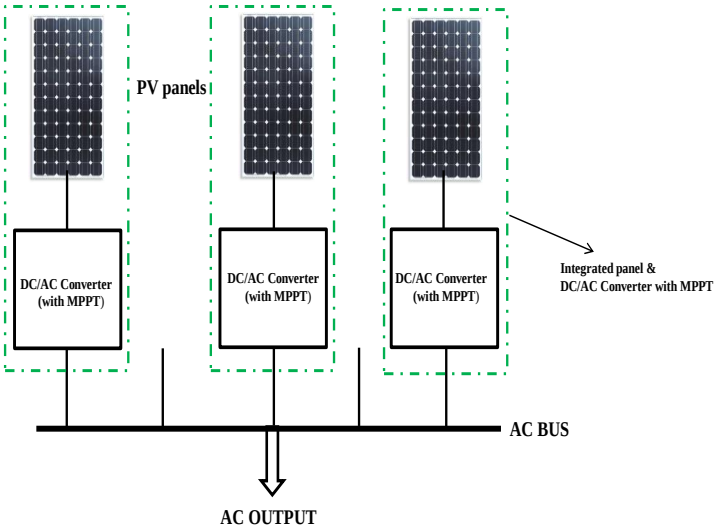

Fig. 6.4: Module integrated inverter topology.

6.3 Review of Inverter Schematic Topologies for PV Systems

New innovative topologies have recently been developed for PV inverters. The primary driving factor is increasing system's efficiency. Other considerations include cost reductions and increasing system's lifetime. Efficiency improvement (of between 1-2%) has been achieved by the elimination of galvanic isolation provided by integration of either high frequency (HF) transformer in the boost converter section or low frequency (LF) transformer in the output section [123]. While the transformerless PV inverter topologies offer advantages of: 1) improved efficiency, 2) lower manufacturing cost, 3) size and mass reductions; they introduce the following issues to the system [128-130]:

- No galvanic isolation between the *ac* and *dc* sections of the inverter, with the associated safety issues in faulty situations.
- DC current injection into the *ac* network with the negative consequences of poor performance of the grid system.
- PV array voltage fluctuation due to capacitive leakage currents arising from the sandwich structure of a PV panel developing a capacitance to earth, with safety and EMC issues.

Modern inverter topologies have tried to address these issues of efficiency and safety using the following two well- known converter topologies [47], [124], [130]:

- H-bridge or Full-bridge: This is the basic circuit used to synthesize *ac* power from *dc* power by sequential opening and closing of the power switches. Figure 6.5 shows the basic full-bridge topology with integrated PV array as the dc source. The output voltage of the topology can take various levels ($+V_{PV}$, $-V_{PV}$, or 0) depending on the sequence of closing the switches [51]. The normal switching sequence for this topology is depicted in Table 6.1.
- Multilevel inverter topology: The multilevel inverter approach uses an aggregation of H-bridges to produce additional voltage levels [51], [122]. The production of these voltage levels results in a staircase waveform that closely approaches a sinusoid. Multilevel inverters are becoming popular in medium and high power inverter applications for interfacing renewable energy to the grid. Figure 6.6 is a diode clamped type of multilevel inverter topology.

A brief discussion of some modern derivatives of these two topologies is presented below.

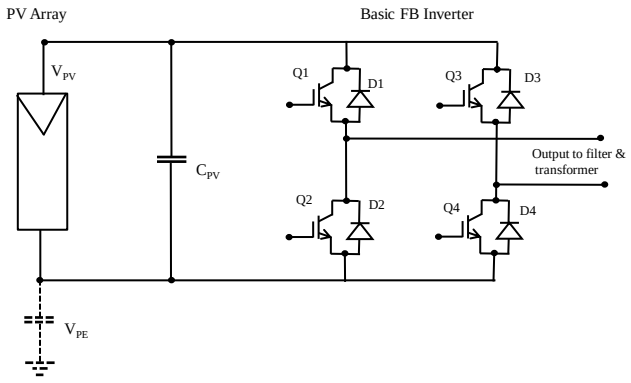

Fig. 6.5: Basic H-bridge or full-bridge inverter with integrated PV array.

Table 6.1: Switching sequence for the H-bridge topology.

Switch Sequence	Output voltage level
Q1 & Q4 closed	$+V_{PV}$
Q3 & Q2 closed	$-V_{PV}$
Q1 & Q3 closed	0
Q2 & Q4 closed	0

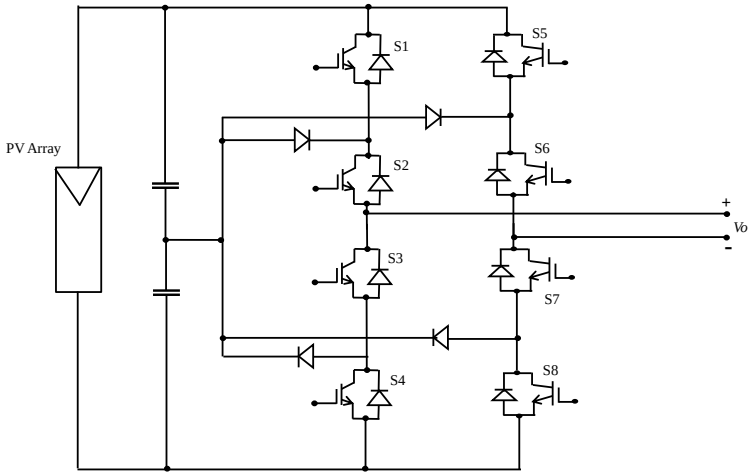

Fig. 6.6: A diode-clamped multilevel inverter topology

6.3.1 Transformerless Topologies

This section presents the key operational features of some state-of-the-art transformerless PV inverter structures that have addressed the shortcomings of the transformerless designs discussed earlier. They are all derivatives of the basic H-bridge topology.

6.3.1.1 H5 Inverter Topology

This topology (a patent of SMA, Germany) is a classical H-bridge with an integrated extra fifth switch (hence the name) in the positive bus of the dc link [125], [130] as shown in Fig. 6.7. The switching scheme is based on the hybrid method, which is a variant of the unipolar scheme (explained in section 6.4.2). With this switching scheme, *Q5*, *Q4* and *Q2* are switched at high frequency while *Q1* and *Q3* are switched at the grid frequency. Two zero output voltages are available when *Q5* is *OFF*, and *Q1* & *Q3* are *ON*. The details of the switching states are shown in Table 6.2. The inclusion of the extra fifth switch, *Q5*, helps to achieve the following [125], [129]:

- Isolation of the PV array from the grid during zero voltage state.
- Avoidance of dc current injection into the grid during the zero voltage state.

The H5 topology has the following advantages [125], [129]:

- The use of three-level modulation ($+V_{dc}$, 0, $-V_{dc}$) yields lower core losses.
- A higher efficiency of up to 98% due to no dc current injection during the zero voltage state.
- Low leakage current and low electromagnetic interference (EMI).

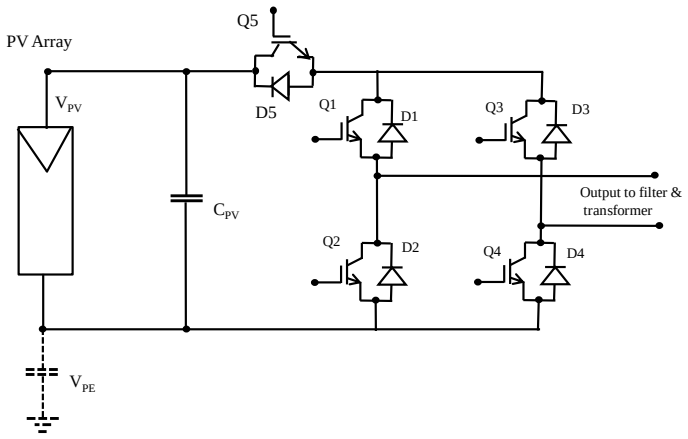

Fig. 6.7: H5 inverter topology with integrated PV array.

Table 6.2: Switching states for H5 inverter topology.

Switching state	Switches ON	Switches OFF	Output voltage
1	Q1, Q4, Q5	Q2, Q3	$+V_{dc}$
2	Q1	Q2, Q3, Q4, Q5	0
3	Q2, Q3, Q5	Q1, Q4	$-V_{dc}$
4	Q3	Q1, Q2, Q4, Q5	0

Despite these advantages, it has the disadvantage of a higher switch count because of the use of extra switch. However, since the H5 topology isolates the PV panels from the grid during zero voltage state using the extra switch, possess high efficiency, and has low leakage current and low EMI, it is very suitable for use in transformerless PV applications [125], [129], [130].

6.3.1.2 HERIC Inverter Topology

This topology (patented by Sunways, Germany, in 2006) is a derivative of the classical H-bridge. The HERIC (highly efficient and reliable inverter concept) topology incorporates a bypass leg in the *ac* side of the H-bridge topology using two back-to-back IGBT switches, as shown in Fig. 6.8. The *ac* bypass provides the following functionality [128-130]:

- Isolation of the PV array from the grid during zero voltage state.
- Avoidance of dc current injection into the grid during the zero voltage state.

The switching scheme is: *Q1*, *Q4* and *Q2*, *Q3* are switched at high frequency while *Q5* and *Q6* are switched at the grid frequency. The details of the switching states are shown in Table 6.3.

While having the drawback of high switch count because of the inclusion of the two extra switches, the HERIC topology has the following advantages [128-130]:

- Lower core losses because of unipolar operation.
- Decouples the PV array from the grid during zero voltage state on the *ac* side.
- High efficiency of up to 97% due to no current injection during zero voltage state.
- Low leakage current and low EMI.

These advantages make the HERIC topology very suitable for use in transformerless PV applications.

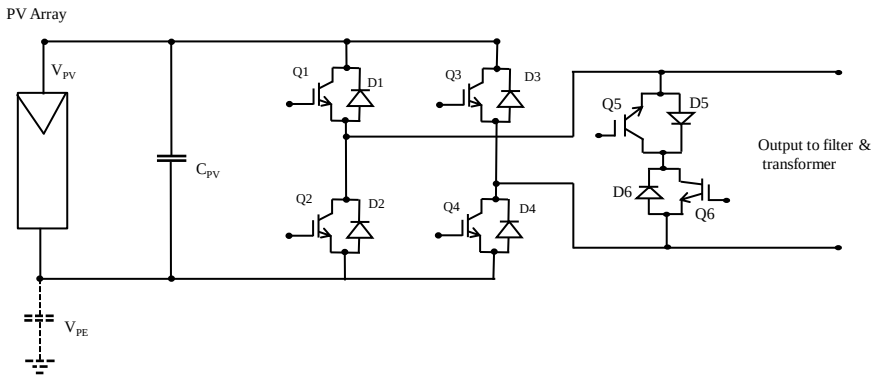

Fig. 6.8: HERIC Inverter Topology.

Table 6.3: Switching states for HERIC inverter topology.

Switching state	Switches ON	Switches OFF	Output voltage
1	Q1, Q4, Q6	Q2, Q3,Q5	$+V_{dc}$
2	Q6	Q1, Q2, Q3, Q4,Q5	0
3	Q2, Q3, Q5	Q1, Q4,Q6	$-V_{dc}$
4	Q5	Q1, Q2, Q3, Q4,Q6	0

6.3.1.3 Other Transformerless Topologies

Other state-of-the-art transformerless topologies for PV applications that try to overcome the shortcomings of non-inclusion of a transformer, discussed earlier, include [125], [128-130]:

(i) The REFU Inverter – a patent of Refu Solar. This is a derivative of the classical H-bridge topology.

(ii) The Full-Bridge Zero Voltage Rectifier –FB-ZVR, which is a derivative of the HERIC topology.

(iii) Neutral Point Clamped (NPC) Half-Bridge Inverter.

6.4 Review of Modulation Strategies for DC-AC Conversion

The pulse-width modulation (PWM) is the most popular modulation strategy that optimizes the PV inverter circuit operation for both single-phase and three-phase operations [124]. The PWM technique basically controls each power switch by comparing a sinusoidal reference wave with a triangular carrier wave and producing an output voltage having a fundamental frequency of same value as the reference waveform [123],[125]. The amplitude of the output is also dependent on the relative amplitudes of the reference and the carrier signals. The three variants of PWM techniques used for the optimization of PV inverters based on the popular H-bridge topology and their derivatives are briefly reviewed in the following sub-sections.

6.4.1 Bipolar (BP) Switching Scheme.

The bipolar switching scheme, illustrated in Fig. 6.9, is based on the synchronization of a sinusoidal reference signal with a triangular carrier signal. The instantaneous value of the sine reference, v_{sine}, is compared with the triangular carrier, v_{triangle}, to generate the output voltage. Mathematically, the operating principle is [123], [124]:

$$v_o = +V_{dc} \quad \text{for } v_{\text{sine}} > v_{\text{triangle}} \tag{6.1}$$

$$v_o = -V_{dc} \quad \text{for } v_{\text{sine}} < v_{\text{triangle}} \tag{6.2}$$

where V_{dc} is the dc supply voltage and v_o is the output voltage.

Thus, the output voltage alternates between two voltage levels ($+V_{dc}$ and $-V_{dc}$) as shown in Fig. 6.9(b). The term bipolar is because this switching scheme alternates between plus and

minus the dc supply voltage – a two-level operation. Application of the bipolar switching scheme to the single-phase full-bridge topology is shown in Fig. 6.10 where the switching sequence is based on [123], [124]:

Q1 & Q4 are *ON* when $v_{\text{sine}} > v_{\text{triangle}}$ ($v_o = +V_{dc}$). (6.3)

Q2 & Q3 are *ON* when $v_{\text{sine}} < v_{\text{triangle}}$ ($v_o = -V_{dc}$). (6.4)

While the power switches are turned *ON* diagonally, the switches of a switching leg must not be turned *ON* at the same time to avoid short circuit across the dc source – a condition known as shoot-through fault [124]. Inclusion of switching transition times, known as deadtime, is often used to avoid shoot-through occurrence [51].

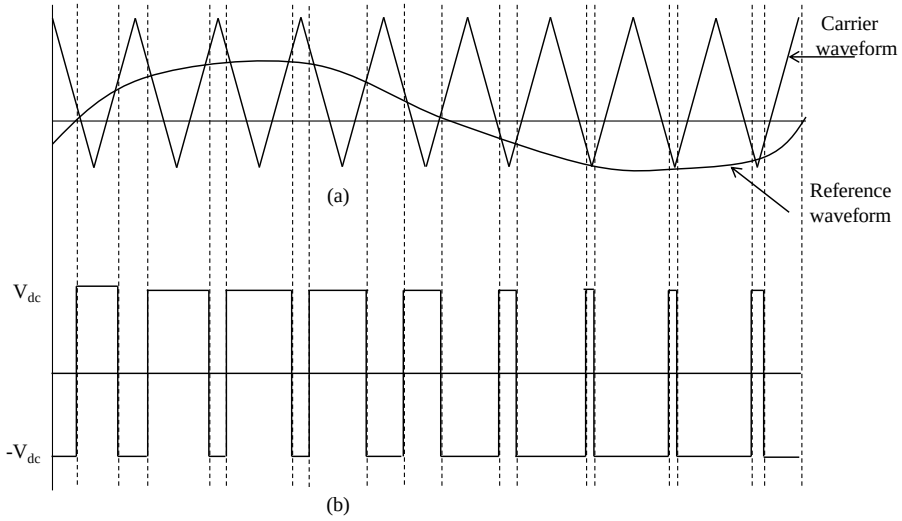

Fig. 6.9: Bipolar PWM switching scheme.

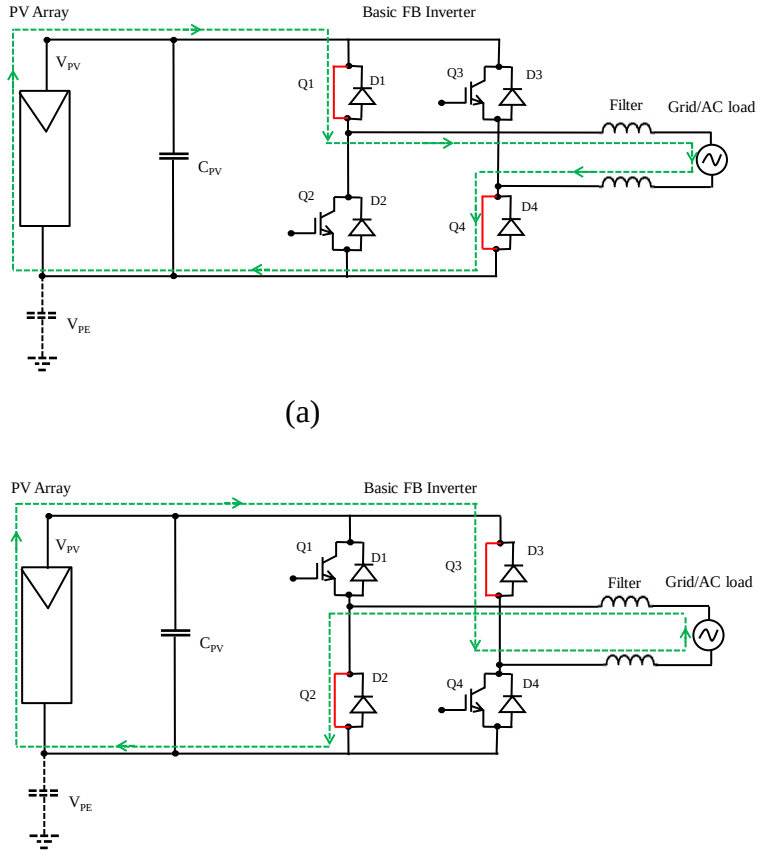

Fig. 6.10: Full-bridge topology with bipolar switching scheme :(a) *Q1* and *Q4* turned ON and (b) *Q3* and *Q2* turned ON.

6.4.2 Unipolar (UP) Switching Scheme.

In a unipolar switching scheme, the inverter output voltage switches between three levels ($+V_{dc}$, 0 and $-V_{dc}$) over a complete fundamental cycle. This is achieved by modulating the phase legs with 180 degrees opposed reference waveforms – that is, with a mirrored sinusoidal reference for each phase leg [124]. For the full-bridge topology, the switching states based on the unipolar switching scheme are shown in Table 6.4. The output voltage of the full-bridge inverter controlled with the unipolar switching scheme is given by [123]:

$$v_o(t) = V_{dc} \times M_a \times Sin\omega t + harmonics \tag{6.5}$$

Where $\omega = 2\pi f$ is the frequency of the sine wave in radians per second and f is the frequency in Hz; M_a is the amplitude modulation index which is defined as the ratio of the peak of the sine waveform, v_{sine}, to that of the triangular waveform, $v_{triangle}$.

Table 6.4: Switching states using unipolar switching scheme.

Switching State	ON Switches	OFF Switches	Output Voltage
1	Q1 and Q4	Q2 and Q3	V_{dc}
2	Q2 and Q4	Q1 and Q3	0
3	Q2 and Q3	Q1 and Q4	$-V_{dc}$
4	Q1 and Q3	Q2 and Q4	0

From (6.5) it is clear that for the unipolar switching scheme, the peak of the fundamental component of the output voltage has a peak value proportional to amplitude modulation index. In general, for the UP switching scheme, the frequency and magnitude of the output voltage is controlled by the reference sine wave, whereas the harmonic content of the output voltage depends on the frequency modulation index, M_f, defined as the ratio of the frequency of the triangular wave to that of the sine wave used for the modulation process [123], [124].

6.4.3 Hybrid Switching Scheme.

The hybrid switching scheme is a variant of the unipolar scheme in which one phase leg is switched at the grid low frequency while the other phase leg is switched at the high carrier frequency to generate the three output voltage levels ($+V_{dc}$, 0 and $-V_{dc}$) [125]. Thus, it has two high-frequency switches and two low-frequency switches.

Table 6.5 summarizes the advantages, disadvantages and limitations of these inverter modulation strategies with integrated H-bridge topology for transformerless PV applications [125], [128-130].

Table 6.5: Advantages, disadvantages and limitations of some modulation schemes.

Modulation Scheme	Advantages	Disadvantages	Limitations
Bipolar scheme	1. Very low leakage current. 2. Low EMI.	1. Higher filtering requirements. 2. High core losses due to two voltage levels produced. 3. Lower efficiency-96.5%.	Reduced efficiency in transformerless PV applications with full-bridge topology.
Unipolar scheme	1. Lower filtering requirements. 2. Lower core losses due to three voltage levels produced. 3. High efficiency of up to 98% due to reduced core losses during zero voltage states.	1. High leakage current. 2. High EMI.	Unsuitable in transformerless PV application with full-bridge topology due to high leakage current.
Hybrid scheme	1. Lower core losses 2. Higher efficiency, up to 98%.	1. Higher filtering requirements. 2. High leakage current peaks.	Unsuitable in transformerless PV application with full-bridge topology due to high leakage current.

6.5 Control of Three-phase Photovoltaic Power Plants

6.5.1 Grid Connected Mode

The main control issues for the grid-connected three-phase photovoltaic power plants include [131], [132]:

- Management of the dc link voltage: The dc voltage can be subjected to transient conditions arising from the variability of the power produced by the PV array. An increase in the produced power results in voltage overshoot while a decrease results in voltage undershoot. Thus, power changes in the output of the PV array results in

variation of the dc link voltage. The control of the dc link voltage is often done via the control of the frontend dc-dc converter.

- Maximum power point tracking (MPPT) of the operating point of the PV array to ensure operation at the highest efficiency at any operating condition.
- Control of AC voltage
- Control of AC current
- Grid synchronisation
- Anti-islanding detection
- Grid monitoring

For such grid-connected photovoltaic power systems, one of the most important considerations in the control of the inverter is the proper synchronisation with the three-phase utility voltages. Such inverters interact with the grid at the point of common coupling (PCC) in order to attenuate voltage disturbances and reduce their undesirable consequences [132]. Moreover, such inverters are particularly sensitive to voltage disturbances which might affect the controllability of their control systems. For such inverters, proper three-phase synchronisation can only be achieved with a well-designed control system since the three phases of a three-phase system do not work autonomously. Since in a balanced three-phase system, the phases have equal amplitude, frequency and phase shifts, the synchronisation system should be able to detect any voltage vector disturbances. The control system of such an inverter should also be able to react to ride-through such operating conditions and the inverter partakes in supporting the grid frequency and voltage to ensure grid stability and safety.

The vector control scheme of a grid-connected three-phase photovoltaic power plant for the control of grid side inverter is shown in Fig.6.11. The control loops in Fig.6.11 include [132], [133]:

- Two inner current control loops for the translated *dq* axis currents, i_{dg} and $i_{qg.}$
- One dc link voltage control loop to regulate the dc link voltage.
- The three-phase phase-locked loop (PLL).
- The maximum power point tracking (MPPT).
- The cross-feedback decoupled network.

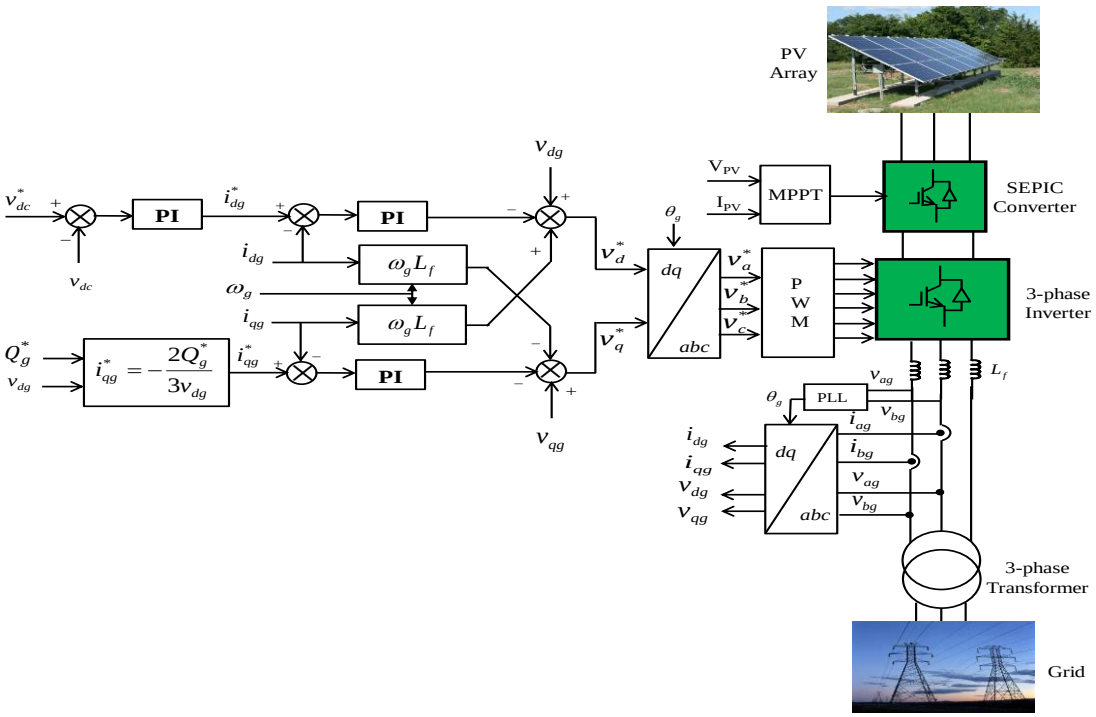

Fig. 6.11: Vector control scheme for a three-phase grid connected PV power plant.

The outer loops regulate the power flow of the system by controlling the active and reactive power injected into the grid. This is because of the dependence of the active and reactive powers on the direct and quadrature current components as given below [131], [134]:

$$P_g = \frac{3}{2}\left(v_{dg} i_{dg}\right) = \frac{3}{2}\left|v_g\right| i_{dg} \tag{6.6}$$

$$Q_g = \frac{3}{2}\left(v_{dg} i_{qg}\right) = \frac{3}{2}\left|v_g\right| i_{qg} \tag{6.7}$$

The overall inductance, L_f, downstream with respect to the inverter has the following voltage balance [131], [134]:

$$\begin{bmatrix} v_{ag} \\ v_{bg} \\ v_{cg} \end{bmatrix} = R_f \begin{bmatrix} i_{ag} \\ i_{bg} \\ i_{cg} \end{bmatrix} + L_f \frac{d}{dt} \begin{bmatrix} i_{ag} \\ i_{bg} \\ i_{cg} \end{bmatrix} + \begin{bmatrix} v_{a1} \\ v_{b1} \\ v_{c1} \end{bmatrix} \tag{6.8}$$

Where R_f is the overall line resistance; i_{ag}, i_{bg}, i_{cg}, represent the line currents, while v_{a1}, v_{b1}, v_{c1}, represent the inverter output voltages.

In the control scheme of Fig. 6.11, the three-phase synchronous phase-locked loop, PLL, is used for the detection of the phase angle and amplitude of the grid voltage; while the PWM

scheme is used for the modulation of the inverter. The cross-feedback decoupling network is used to cancel out the effect of oscillation at 2ω on the synchronous reference voltage of the PLL [132].

6.5.2 Standalone Mode

In this subsection, a three-phase PV power plant not connected to a main grid is considered. These types of plants are often autonomous, isolated or in the form of a microgrid for the following reasons [125]:

- Far distance of the users from the grid, which makes the cost of grid extension prohibitive.
- Difficult terrain to the load centre.
- Size of the load.

The main technical problem with such standalone plants is related to frequency and voltage magnitude control, since unlike in the grid-connected system, synchronisation is not an issue. The vector control structure for the inverter of a standalone three-phase photovoltaic power plant is shown in Fig. 6.12 with the decoupled current controllers. The control system consists of the output voltage controller, the dc link voltage controller, the current controller, MPPT controller, and the pulse width modulator (PWM) for the generation of the switching pulses. Proportional-plus-Integral (PI) controllers are used for the regulation of the output voltage and currents. The outer loop is the voltage controller while the inner loop is current controller. The absence of the phase-locked loop (PLL) is obvious since there is no grid for synchronisation functionality.

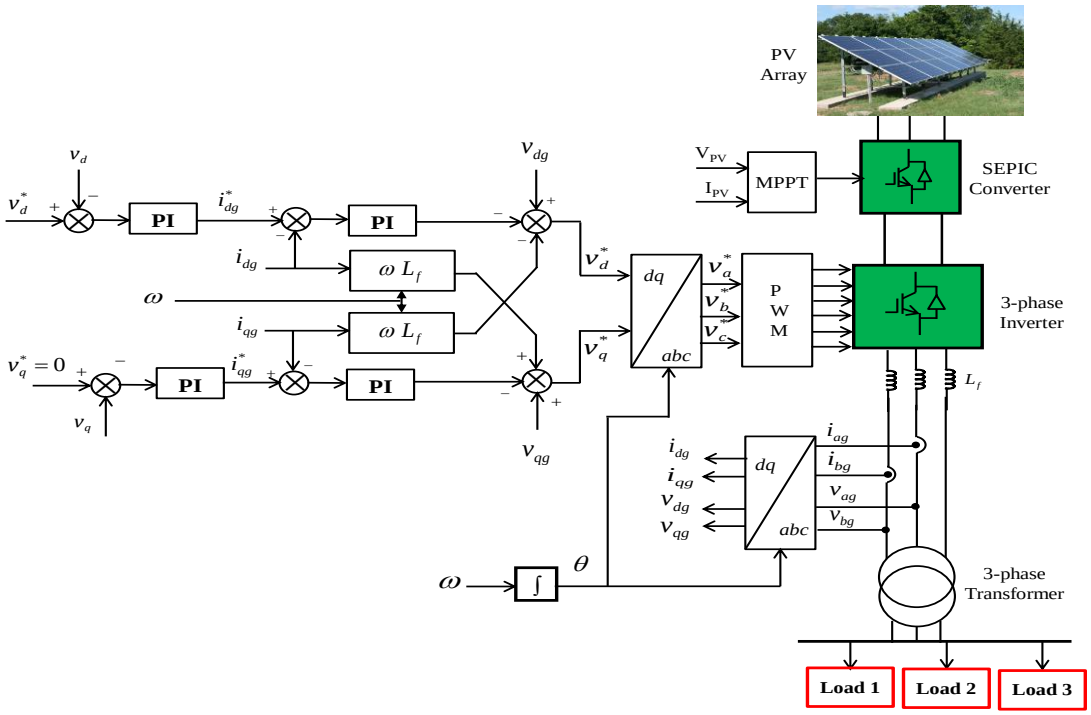

Fig. 6.12: Vector control scheme for a three-phase standalone PV power plant.

6.6 Review of Standards for Interfacing the DC-AC Converter

To ensure safety and seamless transfer of electric power to the grid and for the local *ac* loads, the inverter - as the main component for PV system's interface - needs to comply with a series of requirements. While local regulations are imposed by grid operators in most countries, efforts are made at the global level to impose some standard grid requirements for PV inverters to be adopted by various countries for purposes of harmonisation. The most relevant international bodies involved in the development of these standards for grid requirements are [125]: 1) USA based IEEE (Institute of Electrical and Electronic Engineers); 2) Switzerland based IEC (International Electrotechnical Commission); and 3) DKE in Germany.

The most important and relevant of these standards are [133-139]:

- IEEE 1547-2003: *Standard for Interconnecting Distributed Resources with Electric Power Systems.*
- IEC 61727-2004: *Photovoltaic (PV) Systems – Characteristics of the Utility Interface.*

- VDE 0126-1-1-2006: *Automatic Disconnection Device between a Generator and the Public Low-Voltage Grid.*
- IEC 61000-3-2: *Electromagnetic Compatibility (EMC – low frequency).*
- EN 50160: *Voltage Characteristics of Public Distribution System.*

The most relevant requirements of these standards in relation to PV systems are classified into the following broad areas [135-141]:

- Response to abnormal grid conditions: This requirement deals with the need for the PV inverter to disconnect within a specified time (in seconds) from the grid in the event of abnormal voltage or frequency in the grid. Disconnection is essential for safety of personnel and to avoid damage to connected equipment while the time delay is to ride through short-term disturbances so as to avoid nuisance tripping. It also deals with the conditions for reconnection after such disconnections.
- Power quality issues: This requirement deals with practices and standards on voltage, flicker, frequency, harmonics and power factor. Deviations from recommended values represent out-of-bound conditions that require the PV system to be disconnected from the utility. It considers and sets limits on issues like: 1) dc current injection into the grid system, which is harmful to transformers; 2) current harmonics generated by the converters; and 3) average power factor.
- Anti-islanding requirements: The consequences of islanding – failure of the inverter to disconnect after the tripping of the grid to which it is connected – include: a) line or equipment re-tripping which is hazardous to the equipment, and b) shock/electrocution risks to line workers who assume the lines are de-energized. To avoid these negative consequences, safety measures called anti-islanding are integrated as part of these standards.

6.7 Proposed Control System for the PV Inverter

This section discusses the control strategy proposed to meet power quality requirements – 240V, 50Hz – for the single-phase voltage source inverter. The control structure proposed is shown in Fig. 6.13.The control structure is designed to achieve the following control objectives [58]:

- Synthesize a single-phase sinusoidal *ac* output voltage from the *dc* input from the PV array or from the battery bank.

- Control of the magnitude of the *ac* output voltage to achieve 240V rms.
- To control and maintain the output frequency at 50Hz.
- Reduction of the harmonic content of the generated output voltage.
- AC output current monitoring and control.
- Ensure shoot-through fault does not occur between switches of the same phase leg.

It should be noted that the control strategy developed does not consider the issue of islanding detection and control. Also, the maximum power point tracking and the dc link voltage management are both implemented via the preceding SEPIC converter; hence they are not detailed in this section.

Operationally, the control system of Fig. 6.13 uses the unipolar modulation scheme integrated with current mode control. The unipolar scheme ensures frequency control by using two sinusoidal signals with a phase difference of 180 degrees and the desired fundamental frequency of 50Hz for the modulation process. Each phase leg is modulated separately but switched cooperatively as shown in Fig. 6.13. The modulator is chosen with a triangular carrier frequency of 25 kHz. Two of the four generated pulse trains of the modulator are inverted to provide the complementary signals needed for the switching of the lower switch of each phase leg, *Q2 or Q4*. This ensures that the problem of shoot-through – a short circuit condition when switches of each phase leg switch *ON* simultaneously – does not occur. The current mode control is used to regulate the generated output current while ensuring that the output voltage is also regulated for an rms value of 240V. The modulated output of the inverter which contains a lot of harmonics is filtered using the low pass *LC* filter. The filter removes the higher frequency harmonics not removed by the modulation process. Finally, the output transformer with a transformation ratio of 1:2 steps the voltage up to 240V *ac* before utilisation by the load or before integration to the grid.

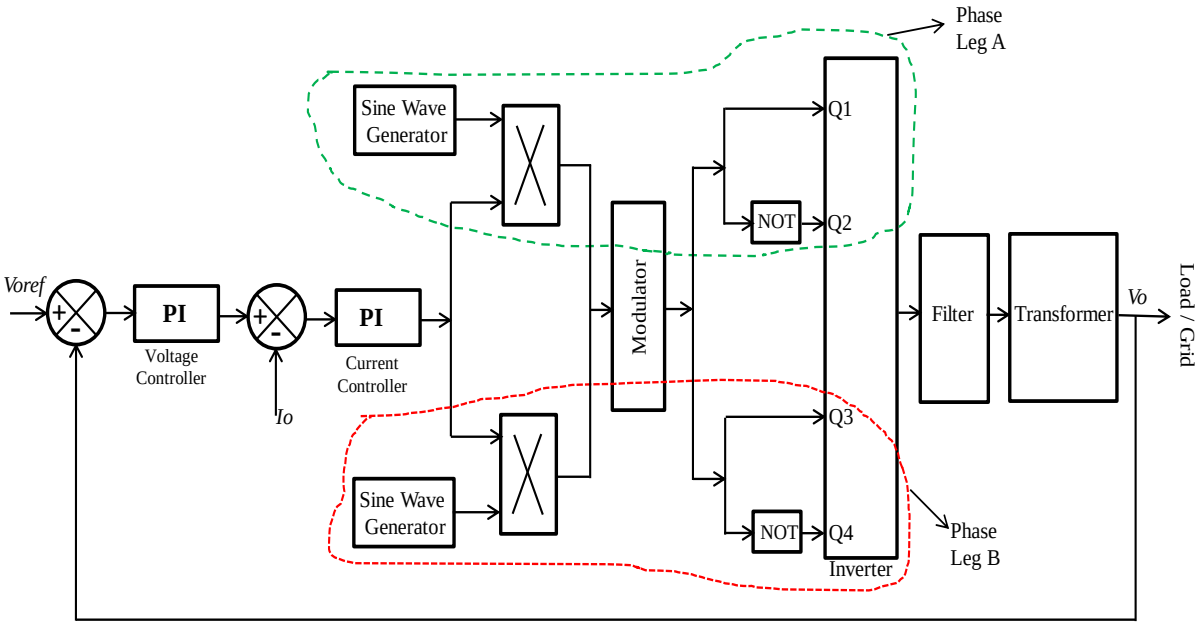

Fig. 6.13: Block diagram of the proposed control system for the single phase inverter.

6.8 Simulation Model

To investigate the behaviour of the inverter and its performance in relation to the other subsystems, a simulation model is developed using MATLAB/Simulink dynamic systems software. Previous chapters of this thesis have discussed the modelling of the other major subsystems of the complete PV power plant, Fig. 6.14. Those models are now integrated with the voltage source inverter based on the H-bridge topology to realise the complete model of Fig. 6.15. In Fig. 6.15, the PV array is the primary power source and generates a dc power. This is stepped up by the SEPIC converter to provide a dc link voltage of 180V. This voltage is used as input to the inverter and as a source to the bidirectional dc-dc converter to charge the energy storage system as explained earlier in Chapter 5. The bidirectional dc-dc converter also operates during periods of low insolation or night time to discharge the battery bank which serves as a backup power supply. The LC filter which is integrated with the transformer in the model filters out the high frequency harmonics generated from the switching action of the inverter. Since the 180V of the *dc* link is not enough to provide the needed *ac* output voltage of 240V, the filtered output is stepped up by the line frequency transformer.

Figure 6.15 also shows the various control blocks: 1) the MPPT for efficient extraction of PV energy; 2) the *dc* link voltage regulator to ensure the *dc* voltage is maintained at 180V; 3) the

battery bank manager which determines when the battery bank is to be charged or to be discharged; and 4) the inverter controller which implements the unipolar sinusoidal PWM discussed in the previous section.

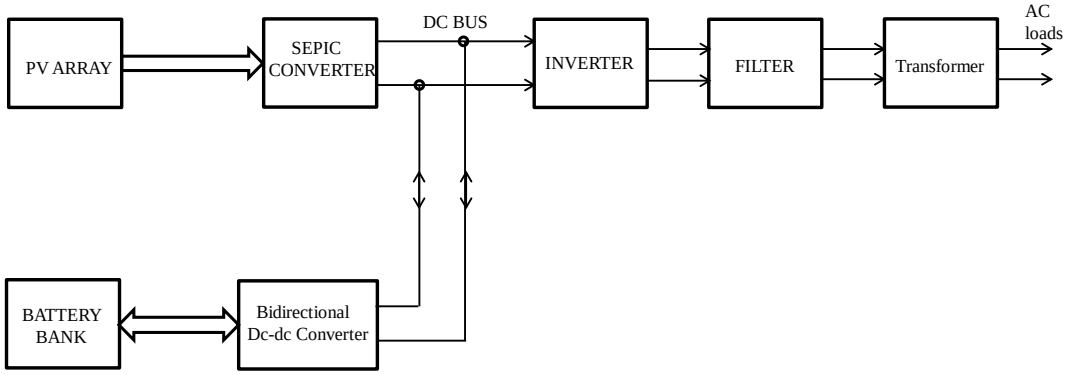

Fig. 6.14: Block diagram of the power circuit of the complete PV plant being modelled.

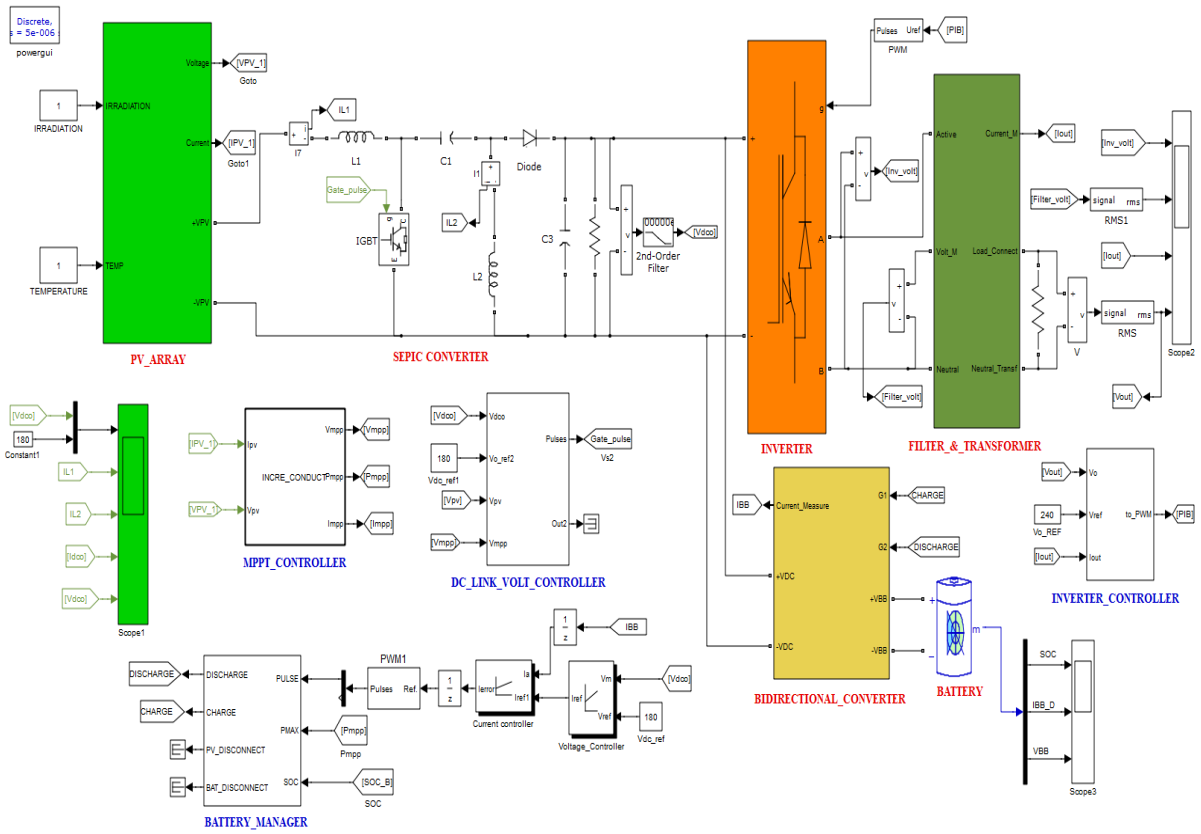

Fig. 6.15: Simplified simulation model in Simulink showing the subsystems and the controls

6.9 Simulation Results and Discussions

The controllers developed were used in simulation studies for both the single-phase operation and for three-phase operation in the standalone mode. For the single-phase operation, the results are shown in Figs. 6.16 – 6.18, while the results for the three-phase operation are shown in Figs. 6.19 – 6.22. The detailed discussions are presented below.

6.9.1 Single-phase PV System

For the single-phase operation, at a step time of 1second, a circuit breaker switches on a load of 3.5kW into the system and switches it off at the step time of 1.5 seconds. The variation of the line frequency during the switching operation is shown in Fig. 6.16. It is observed that the frequency deviation from the nominal value of 50Hz is minimal and within acceptable limits. The instantaneous values and rms values of the load voltages and currents during this switching operation are shown in Fig. 6.17 in per unit values. The current transitions (increment and decrement) during the switching operation are obvious in Figs. 6.17(c) and 6.17(d). Also shown in Fig. 6.18 is the corresponding power flow during the switching operation.

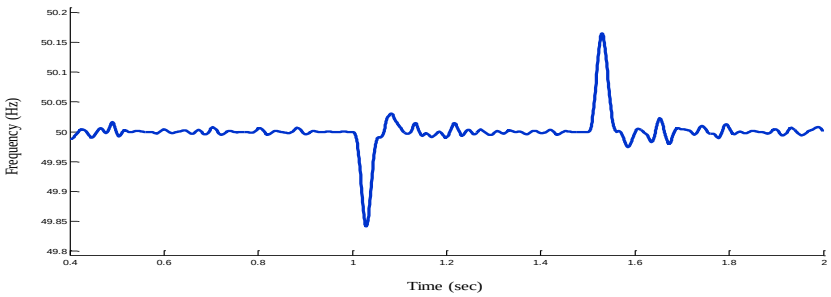

Fig. 6.16: Line frequency of the system during the switching operation.

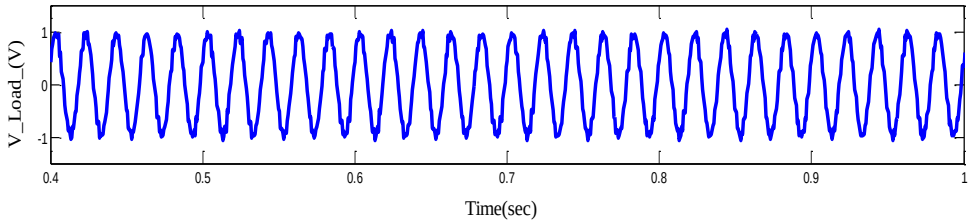

(a) Instantaneous load voltage during operation.

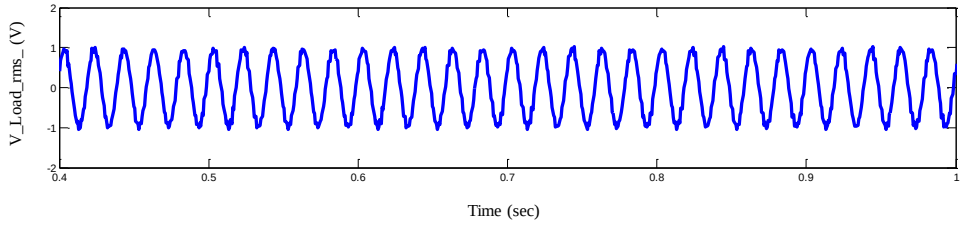

(b) The rms load voltage during operation.

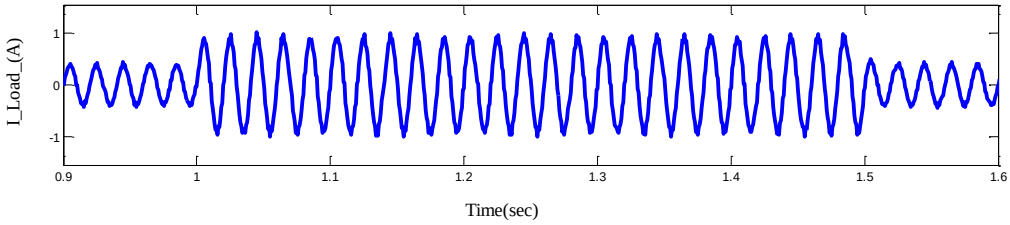

(c) The instantaneous load current.

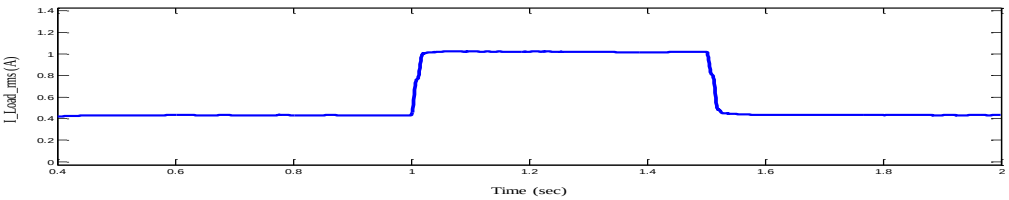

(d) The rms load current.

Fig. 6.17: Load voltages and currents during the switching operation.

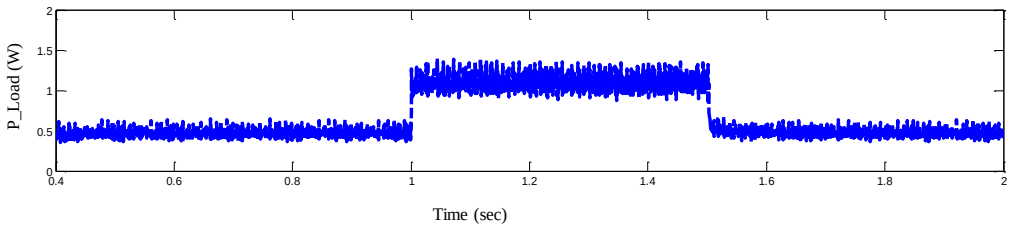

Fig. 6.18: Load power flow during the switching operation.

6.9.2 Three-phase Standalone PV System

For the three-phase system, Fig. 6.12, at a step time of 1second a 3-phase load of 2.5kW is switched on, while an additional load of 3.5kW is also switched on at a time of 1.5 seconds. The results for this double switching operation are shown in Figs. 6.19 -6.22. Fig.6.19 shows the frequency deviations obtained. Like in the single-phase case, this is still maintained within the required limits. The instantaneous and rms load currents in per units are shown in Fig. 6.20, with the current transitions at the switching times obvious. The power flow is shown in Fig. 6.21 while Fig. 6.22 is a screenshot showing the three-phase instantaneous load current (upper) and the instantaneous load voltage (bottom) during the same switching operations.

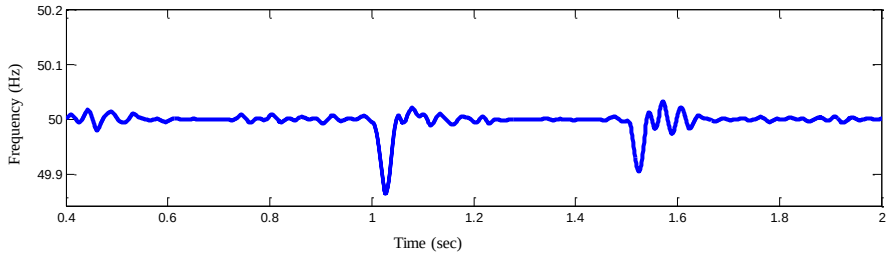

Fig. 6.19: Load frequency during three-phase operation

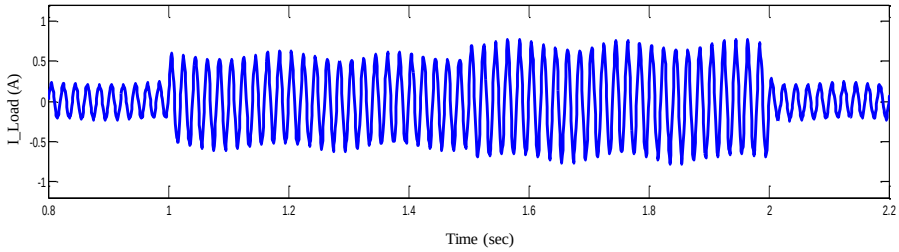

(a) The instantaneous load current in three-phase operation.

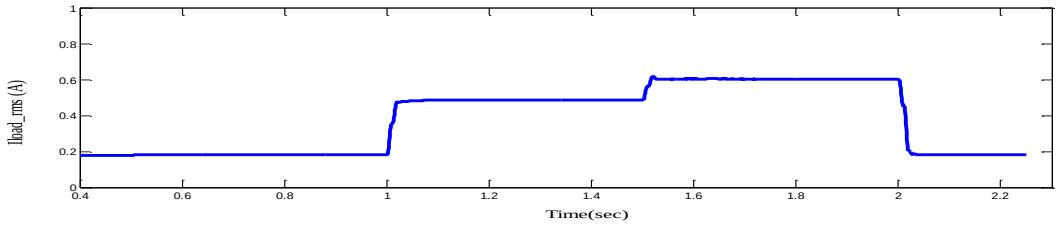

(b) The rms load current

Fig. 6.20: Load current changes during the switching operation.

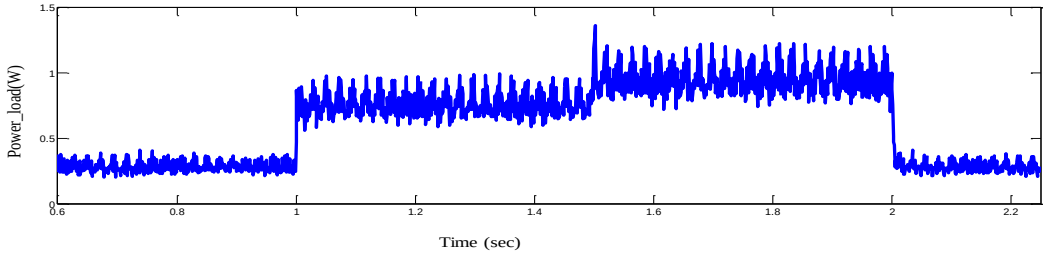

Fig. 6.21: Load power changes during the three phase switching operation.

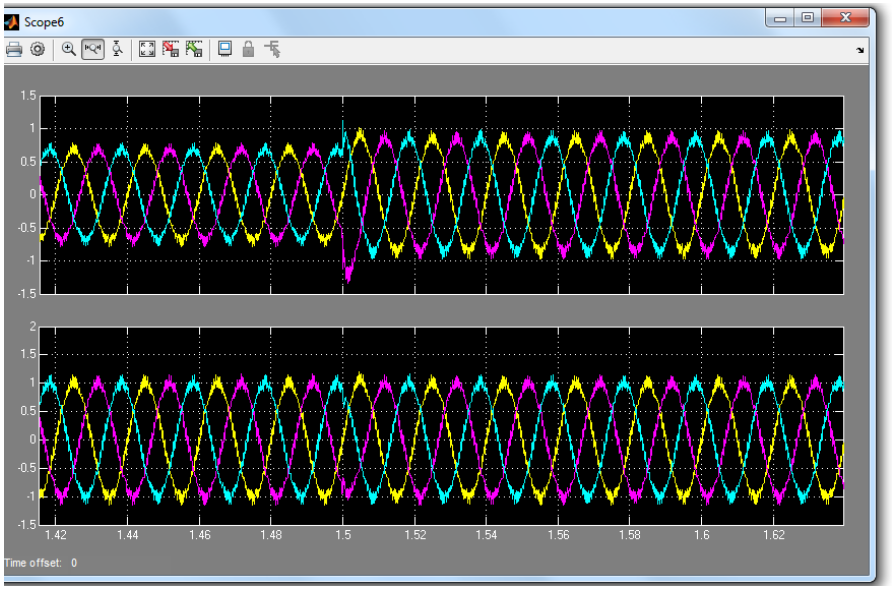

Fig. 6.22: Screenshot of the instantaneous load current (upper) and voltage (bottom).

6.10 Conclusions

The topologies and different modulating strategies of the H-bridge based photovoltaic inverters have been presented. A modulation scheme based on the unipolar sinusoidal PWM technique has been proposed and used for the inverter switching operation. The simulation studies confirm the feasibility and effectiveness of the control strategy. The proposed control strategy is able to synthesise *ac* voltage from the *dc* voltage from the solar array or the backup battery energy storage system. It is evident that the control strategy is able to provide a sinusoidal output voltage with the harmonics reduced to the barest minimum after minimal filtering.

Moreover, the robustness of the control system has been demonstrated by the ability of the system to maintain the load frequency and voltage magnitudes, in both single-phase and

three-phase operations, within the required limits even in the events of changes in the system loading.

Chapter 7
Hardware Implementation and Experimental Analysis of the PV System.

7.1 Introduction

Previous chapters of this thesis have investigated, via simulation studies, the theoretical processes of voltage mode control, current mode control and pulse width modulation strategies for the control of power converters for interfacing photovoltaic energy. The understanding that comes from such simulation studies is invaluable since it provides useful insight into how the power converters should be controlled to achieve the intended performance outcomes. However, simulation studies without experimental backup offer limited value. Building the physical system to achieve the desired switching performance as closely as possible, not only consolidates the learning process, it also offers the satisfaction of the realization of the engineering transformative process of building a product out of an idea.

To implement real time control of the converters discussed in the previous chapters using the developed control algorithms, a digital signal processor (DSP)-based hardware/software platform using dSPACE DS1104 DSP board is used [138]. The DSP controller produces logic level outputs as commands to turn particular switches *ON* and *OFF*. These outputs are translated by hardware (opto-isolators and gate drivers) into actual gate control signals which eventually control the switches in the converter system. Also, for the converters to work properly and effectively, analogue signals must be acquired via appropriate sensors, conditioned and converted into digital forms before processing by the controller [124], [143].

This chapter is the culmination of the work of the previous simulation studies – it discusses the hardware implementation of the entire photovoltaic power system. Firstly, the data acquisition and conditioning methodology is presented. This is followed by the discussion of the dSPACE DS1104 DSP board and the interfacing with the Simulink software. Thirdly, the building of the hardware subsystems – voltage and current sensor boards with integrated opto-isolator and gate drivers; the IGBT based power boards for the SEPIC converter, the bidirectional dc-dc converter, and the PV inverter, is presented. Finally, the experimental results and discussions are presented followed by the conclusions.

7.2 Data Acquisition and Conditioning

The analogue inputs of a typical power converter have a wide range of operational voltage and current values. These field signals require proper conditioning to convert them to the low-power, low-voltage levels required by the digital controller. To create a robust input/output (I/O) circuitry that reliably interfaces to the digital controller requires proper choice of sensors and amplifiers [124], [143]. Figure 7.1 show the process of acquiring these converter signals by the sensor, conditioning by the amplifier circuitry, and then converting the conditioned signal into digital form using the ADC (analogue-to-digital-converter) before processing by the controller. Also, shown in Fig. 7.1 is the conversion of the processed digital signal to analog form using the DAC (digital-to-analog-converter). The processed and reconverted signals (switching pulses) are then conditioned to the level needed to turn *ON* and turn *OFF* the power switches by the gate driver circuitry.

The choice of a DSP based controller for this project is because of the following advantages of the digital approach compared to the analogue approach [58], [116], [124], [143]:

- It offers greater flexibility and potential for implementation of sophisticated control algorithms.
- Offers greatly improved reliability and repeatability.
- High speed signal processing.
- Availability of low cost, high performance DSP controllers with enhanced and integrated ADC, DAC, and pulse width modulators.
- Offers real-time hardware-software interface functionality.
- Less susceptible to ageing and environmental variations.
- Offers better noise immunity.
- Ability to incorporate additional functionality like protective features, communication features, operator interface, and field transducer control signals.

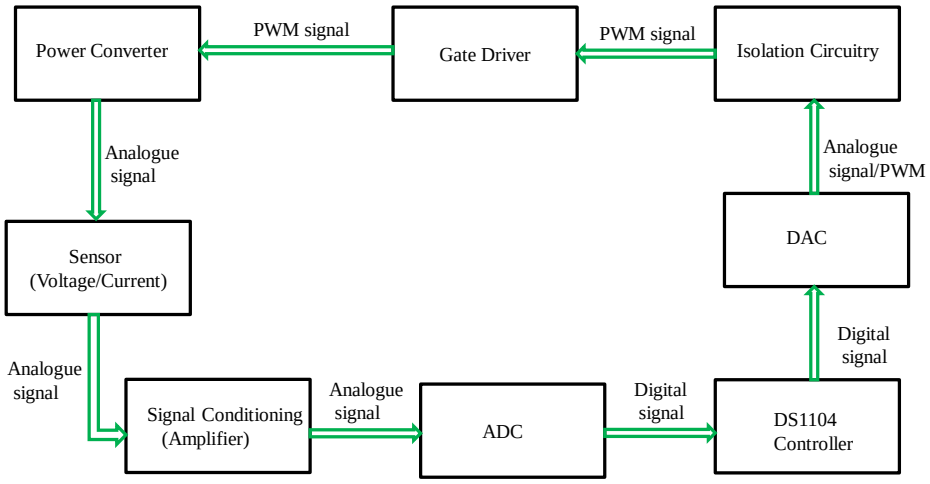

Fig. 7.1: Block diagram of the signal acquisition and conditioning processes used for the PV system.

7.2.1 dSPACE DS1104 DSP Board Description

The DS1104 DSP board used for this project, a product of dSPACE GmbH Germany, is a standard board that can be inserted into the peripheral component interconnect (PCI) slot of a host PC. It is designed for the development of high-speed multivariable digital controllers and for real-time simulation. Specifically, this real- time controller incorporates the following [142], [144]:

- A Master DSP – 603 PowerPC floating point processor, with a clock frequency of 250MHz.
- A slave DSP system based on the TMS320F240 DSP microcontroller.
- 100-pin I/O connector for linking field signals, via an adapter cable.
- Two different types of analog/digital converters (ADCs): a) one 16-bit *ADC* with four multiplexed input signals: ADCH1 – ADCH4; b) four 12-bit parallel *ADCs* with one input signal each: ADCH5 –ADCH8.
- A digital/analog converter (DAC) with 8 parallel *DAC* channels: DACH1—DACH8.

In addition, the following interface connectors allow communication between the controller and external devices [140], [142]:

- The CP1104 connector panel: this provides easy-to-use connections between the dSPACE DS1104 DSP board and the field devices, via BNC connectors and Sub-D connectors.

- The CLP1104 Connector /LED Combi panel which provides an array of LEDs for visual indication of the digital signals.

7.2.2 Real Time Implementation of the Complete PV System

For the real time control of the complete PV system, Fig. 7.2, the controllers designed in the previous chapters using Matlab/Simulink software are integrated with the desired dSPACE blocksets to form the complete real time model. The four major blocksets used for this project include: 1) ADC blocks for capturing the analog inputs, 2) DAC blocks for reconversion of the digitally processed signals back to analog form, 3) PWM (pulse width modulation) blocks for generation of the signals used for switch activation, and 4) the digital input/outs (I/Os) used for system protection. During the build process, the Real-Time Interface (RTI) automatically generates real time code from the Simulink model and implements this code on the dSPACE real-time hardware – the dSPACE DS1104 DSP board, used for this project [144].While the experiment is running, the user can change system parameters via the functionality of the controller's associated software – the ControlDesk.

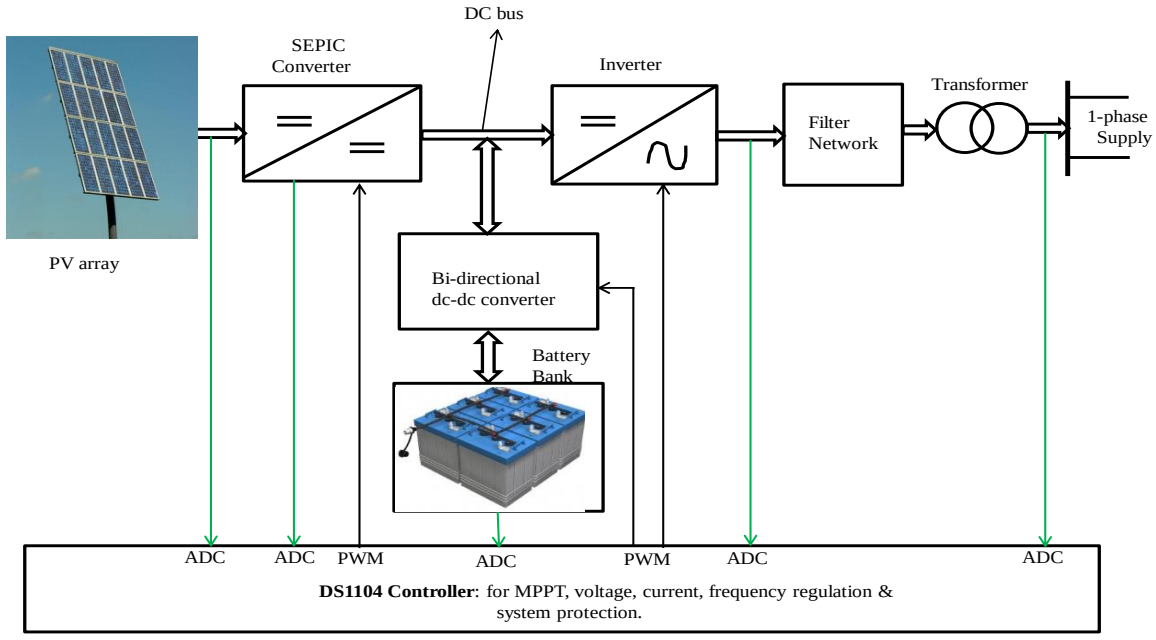

Fig. 7.2: System block diagram showing some analogue signals (green lines) to be measured and used for control purposes.

7.3 Hardware Implementation

7.3.1 Voltage/Current Sensing & Conditioning

All power electronic control systems require certain input signals to operate. These signals, often in analogue forms, must be acquired, scaled and conditioned from their external voltage and current levels to match the controller's input/output (I/O) levels [124],[143]. Fig. 7.2 shows some of the important analogue signals (in green lines) needed to be acquired, scaled and conditioned for the implementation of the control algorithms of this project.

The voltage sensor circuits are designed to measure the output of the PV array, the SEPIC converter, the battery bank, and the filtered output of the inverter. The measured voltage is processed as explained in subsection 7.2. The voltage sensing circuits for this project are based on the Hall-effect based voltage transducer [145]: LV-25P by LEM Components, Fig. 7.3. Operationally, the voltage to be sensed is fed into the primary of the transducer to produce a proportional current through the primary resistor, R_P. This current generates a proportional current, based on the conversion ratio (2500: 1000) of the transducer, in the secondary side. The secondary current then develops an output voltage proportional to the secondary resistor, R_S. For optimum accuracy, R_P is chosen such that the nominal voltage to be measured corresponds to a primary current of 100mA.

The voltage and current conditioning circuits used for this project are based on the instrument amplifier [146] – INA 118 by Burr-Brown Corporation. Figure 7.4 shows one channel of the voltage sensor circuitry incorporating the voltage sensor and the voltage conditioner. The INA 118 is used to process the sensed signals. The output of the amplifier is connected through the dSPACE connector panel CP1104 through the ADC channel to the DS1104 controller for processing, as explained earlier in Fig. 7.1.

To sense the PV current, battery current and inductor currents, Hall-effect based current transducers [147], LA 55P by LEM Components, are used. Like in the voltage sensing circuitry, the output of the current transducer is conditioned using the instrumentation amplifier: INA 118. The conditioned signal is fed to the controller for processing via the dSPACE connector panel CP1104, Fig. 7.5.

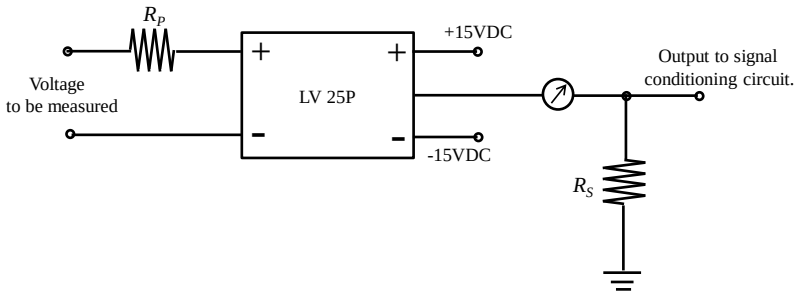

Fig. 7.3: Hall-effect voltage sensor circuitry using LV 25P.

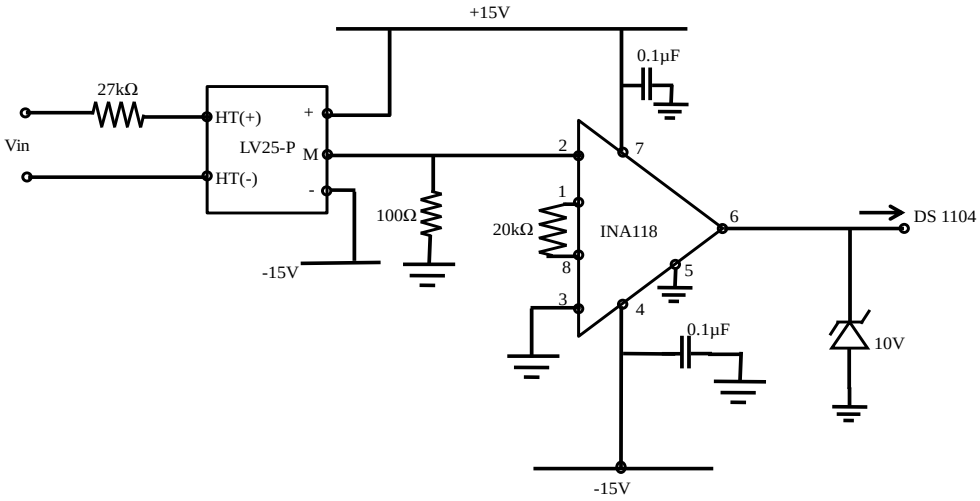

Fig.7.4: Schematic diagram of 1-channel of the voltage sensing and conditioning circuitry based on LV 25P and INA 118.

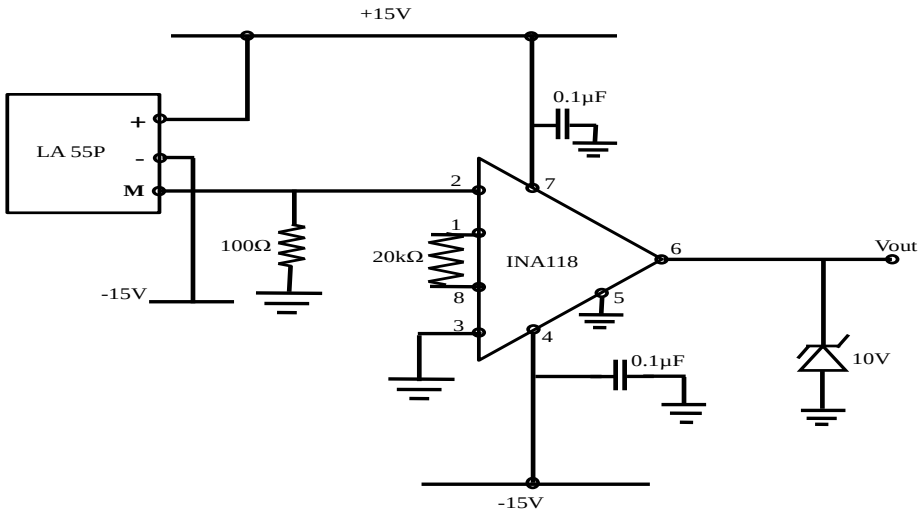

Fig. 7.5: Schematic diagram of 1-channel of the current sensing and conditioning circuitry based on LV 25P and INA 118.

7.3.2 Isolation and Gate Drive Interface

For the DS1104 controller to drive the IGBT power switches, the logic signals from the controller must firstly be coupled into the gate driver circuit using an isolation system. This isolation is necessary to avoid interference from the high di/dt and dv/dt associated with the switching transition propagating into the controller and causing either damage or malfunction of the controller logic. The strategy adopted in this project to achieve isolation is via optical interfacing using high-speed opto-couplers. The integrated circuit HCPL-3120 by Agilent Technologies is the opto-coupler chosen [148]. The connection of this IC for the project is as shown in Fig. 7.6.

The gate driver performs the function of converting the logic command generated by the DS1104 controller into a suitable voltage and current level required to turn *ON* and turn *OFF* the power switches of the converters. To turn an IGBT power switch *ON* requires that an initial burst of current must be injected into the gate, followed by a holding voltage (of between 10 to 20V) to keep the switch *ON*. Also, to turn *OFF* the IGBT, a similar burst of opposite polarity current is needed to discharge the gate capacitance, with a zero or negative holding voltage to keep the switch *OFF*. Moreover, the gate driver must provide a low output impedance to ensure that accidental switch state transitions do not occur [124].

While the SEPIC converter topology has a low side power switch, the bidirectional dc-dc converter and the dc-ac (inverter) converter each has both low-side and high-side switches. To be able to drive these low-side and high-side switches, the integrated circuit, IR 2110 by International Rectifier, is incorporated into the circuitry. By operating in the bootstrap mode this high-side and low-side driver provides very fast switching speed and low power dissipation.

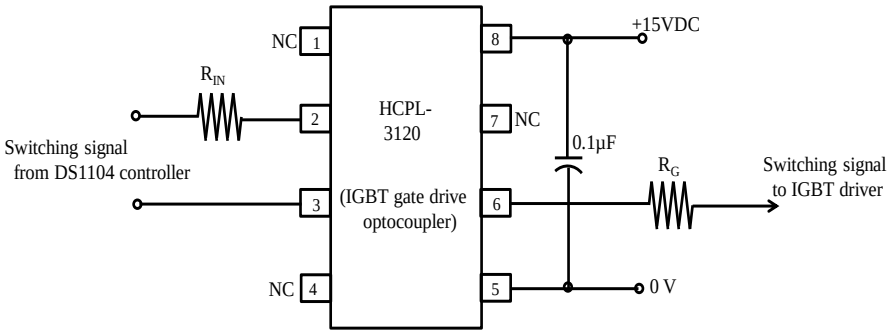

Fig. 7.6: Opto-coupler circuitry used for isolation of the IGBT switching signals.

7.3.3 Printed Circuit Board Design and Construction.

The voltage/current sensor circuitries, the signal conditioner circuitry, the opto-coupler circuitry, and the gate driver circuitry described in the previous subsections are all integrated to form a single circuit board. Figure 7.7 shows the block diagram of the elements of the integrated board with the sequence of signal flow for a single channel. Multiple channels are integrated onto the same board based on the number of analogue inputs to be acquired. The board development is started via bread-boarding of the prepared circuit schematic diagram and subsequent testing and troubleshooting. With a functional circuit on the breadboard, the transition to electronic design automation (EDA) platform based on the Altium Designer software follows. The schematic capture tool, the PCB layout tool, the analysis tool, and the routing tool of the Altium Designer are used to develop the following printed circuit boards (PCBs):

- A four-channel single-sided PCB for the SEPIC converter. Figure 7.8 shows schematic diagram in Altium software while the layout drawing is shown in Fig. 7.9. The finished PCB with populated components is shown in Fig. 7.14.
- A four-channel single-sided PCB for the bidirectional dc-dc converter. The associated schematic drawing and layout drawing are shown in Figs. 7.10 and 7.11, while the finished PCB with populated components is included in Fig. 7.14.
- A single-sided PCB for the inverter power circuitry. The associated schematic drawing and layout drawing are shown in Figs. 7.12 and 7.13, while the complete PCB is included in Fig. 7.14.

Each of the single-sided PCBs is assembled with the following main components [145-149]:

- Hall-effect voltage sensors (LV 25P) and current sensors (LA 55P).
- Instrument amplifiers: INA 118 by Burr-Brown Corporation.
- Opto-couplers: HCPL-3120 by Agilent Technologies.
- IGBT gate driver ICs: IR2110 by International Rectifier.

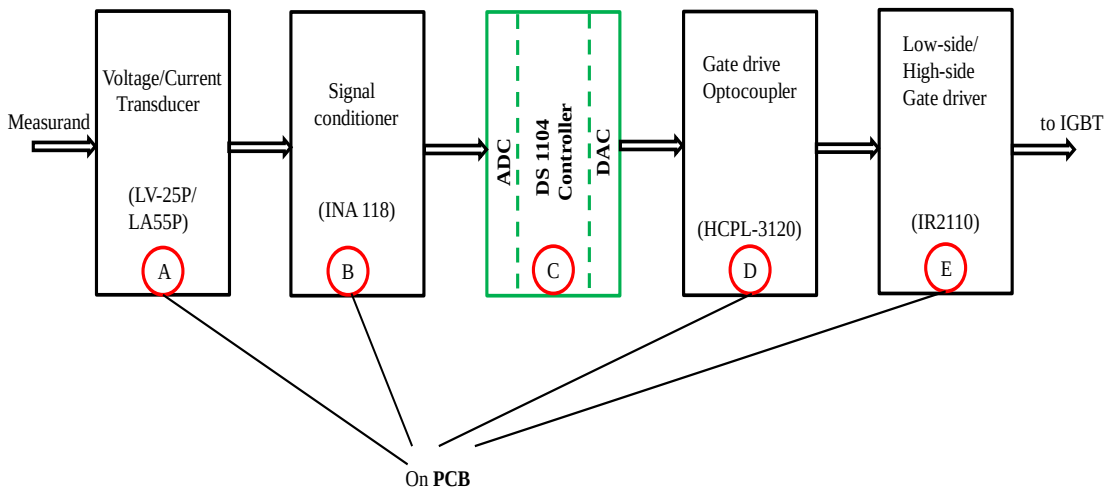

Fig. 7.7: Block diagram of signal flow for one channel of the printed circuit board.

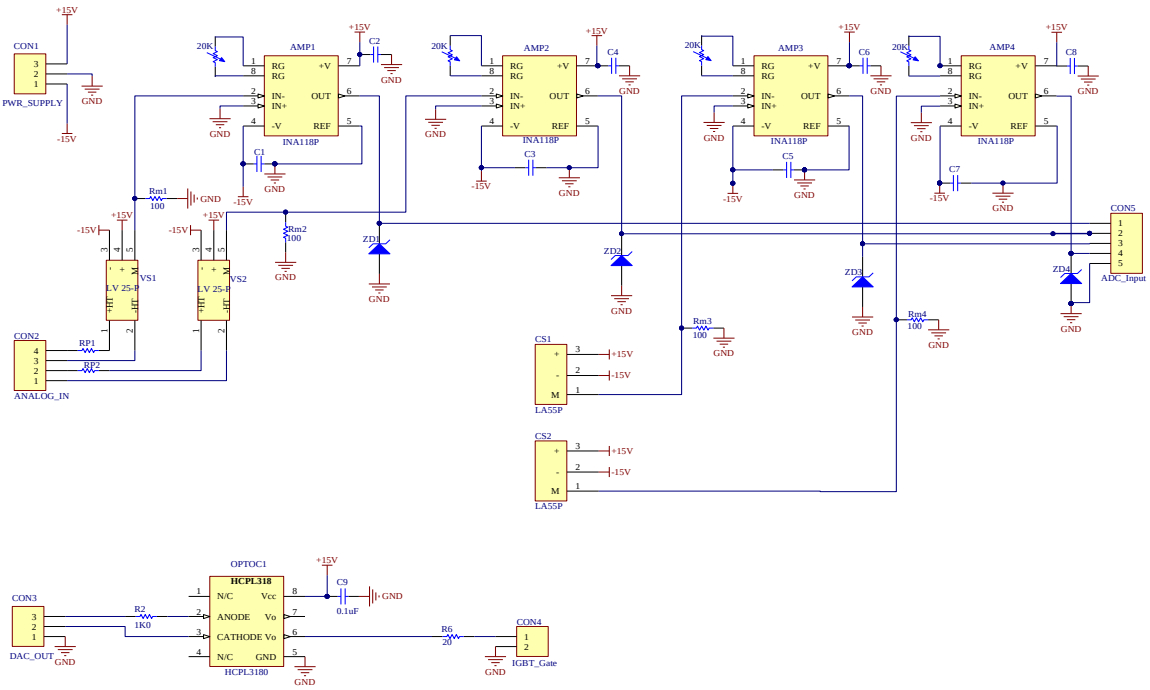

Fig. 7.8: Schematic diagram in Altium Designer software of the four-channel sensor board for the SEPIC converter.

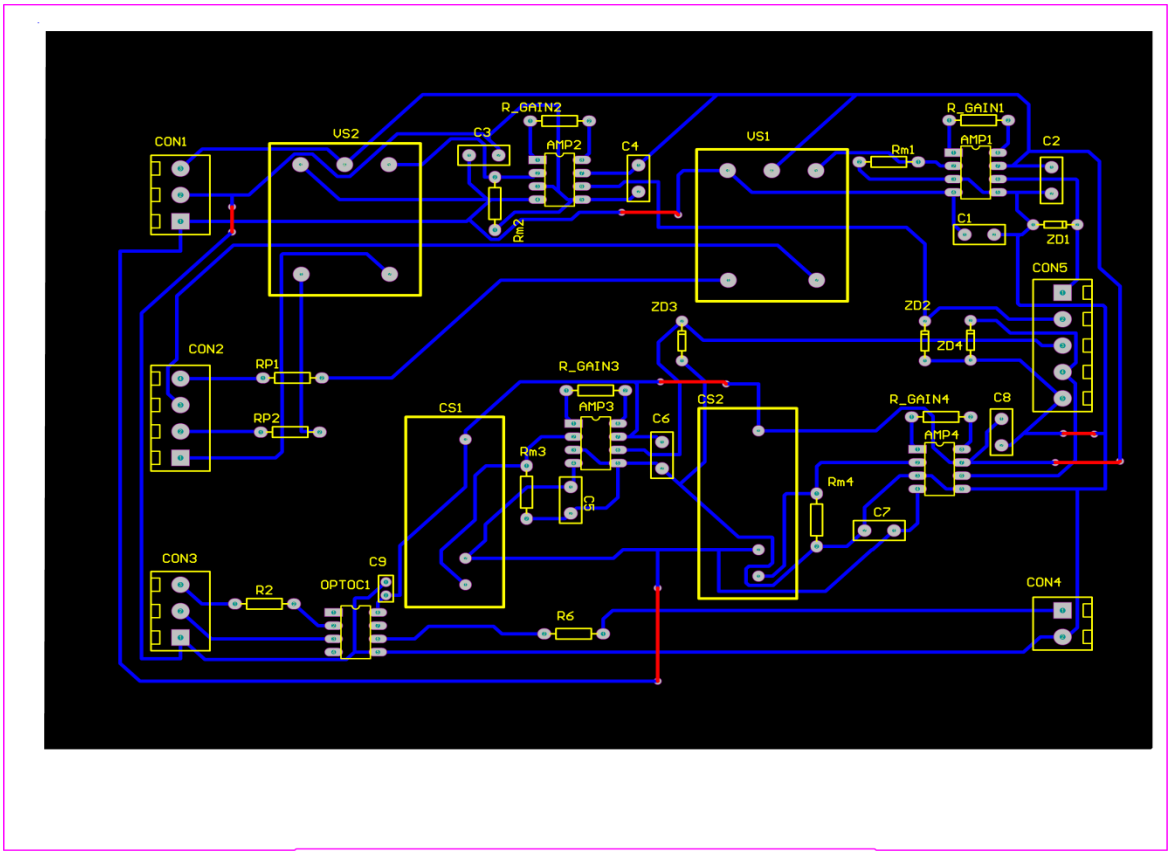

Fig.7.9: Layout drawing in Altium Designer software showing the four-channel PCB for the SEPIC converter.

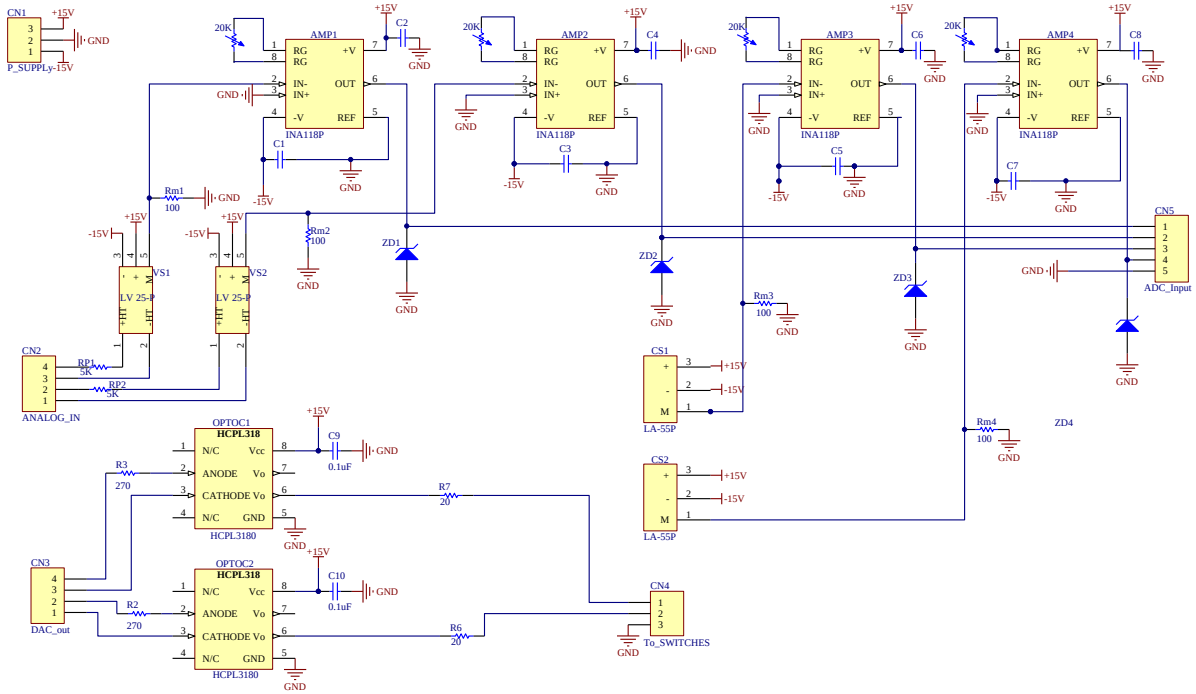

Fig. 7.10: Schematic diagram in Altium Designer of the sensor board for the bidirectional dc-dc converter.

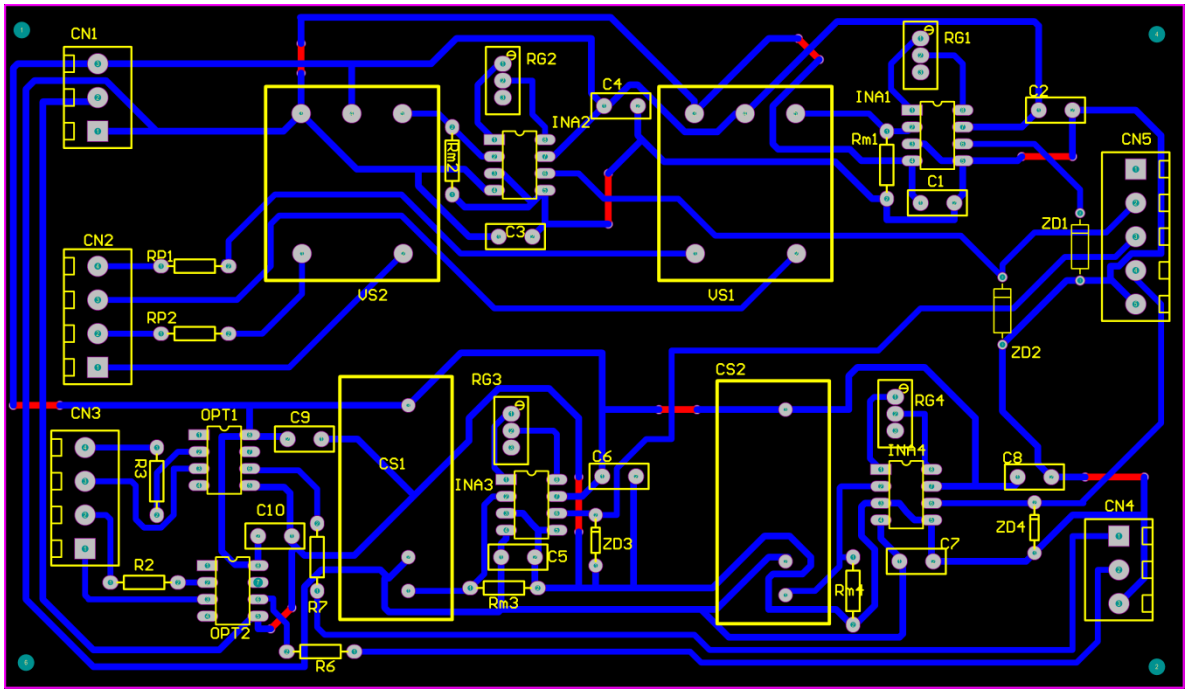

Fig. 7.11: Layout drawing in Altium Designer software showing the four-channel PCB for the bidirectional dc-dc converter.

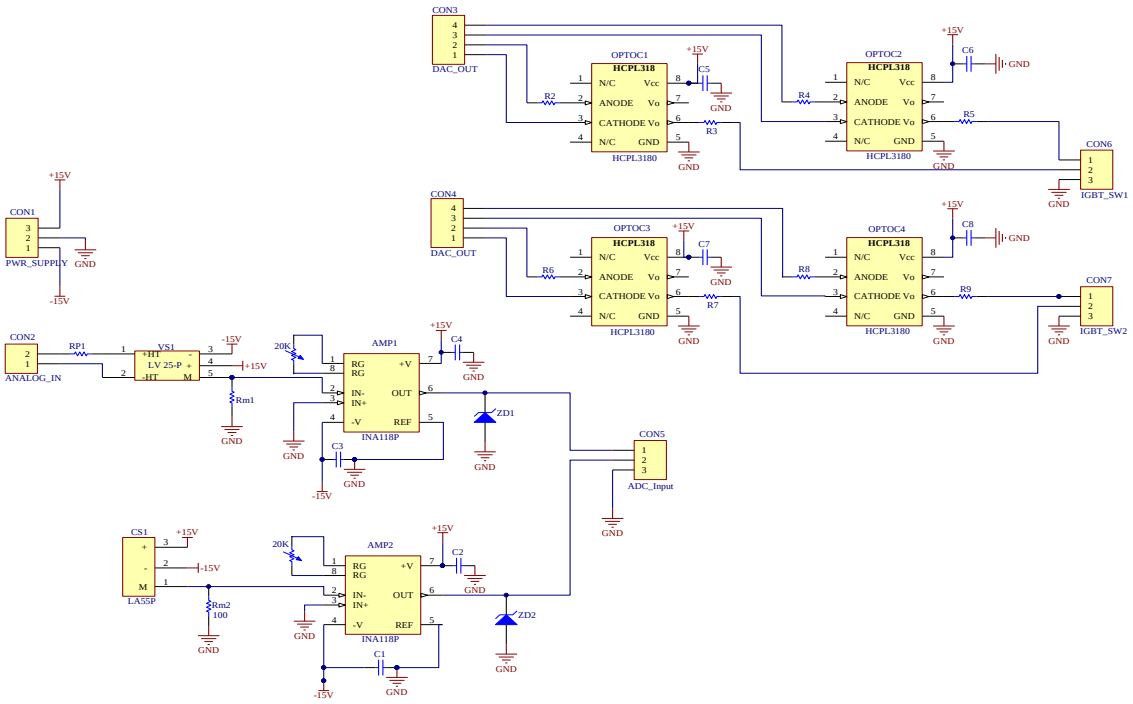

Fig. 7.12: Schematic diagram in Altium Designer of the sensor board for the inverter.

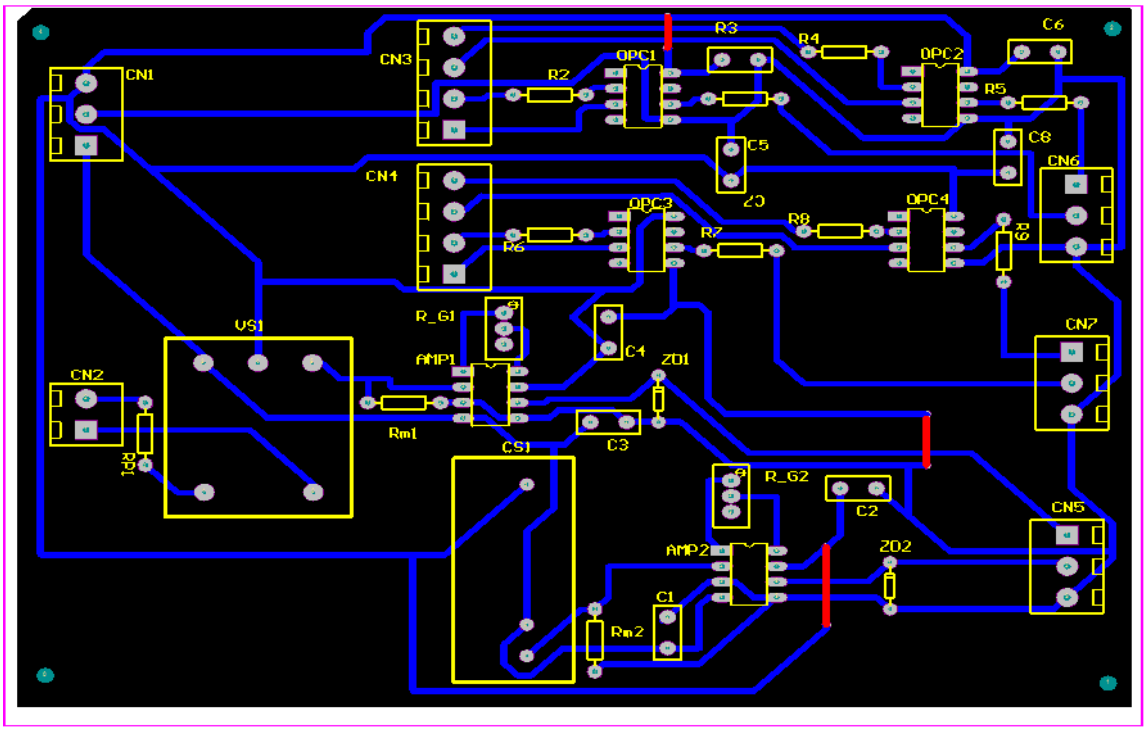

Fig. 7.13: PCB layout drawing in Altium Designer of the sensor board for the inverter.

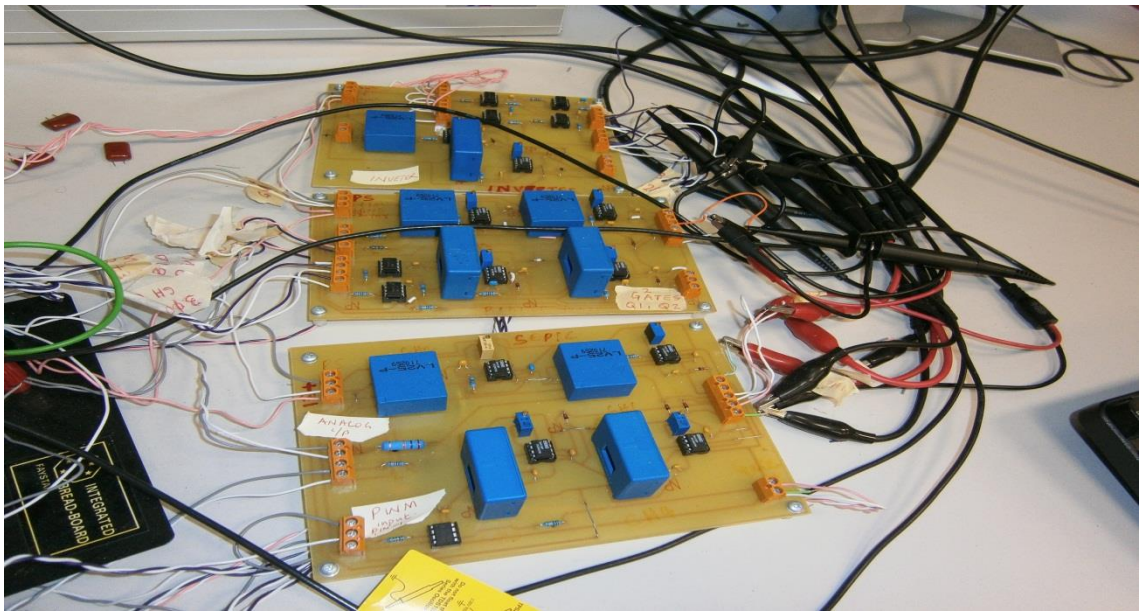

Fig. 7.14: The finished PCBs for the three converters.

7.3.4 Construction of the Power Converters

Stray inductances are present in various parts of a power converter. The presence of these stray inductances results in an overvoltage during the switch turn-off. Similarly, during the turn-on transition these inductances lead to a rise in the switch current. Thus, the power switch, IGBT as used in this study, experiences high electrical stresses at both turn-on and turn-off transitions when both its voltage and current are high simultaneously. This sudden rise in voltage and current causes high instantaneous power dissipation in the power switch and is also accompanied by the propagation of electromagnetic interference (EMI) in the system [124], [116], [150]. To minimise these negative consequences of stray inductances the following circuit layout issues are adopted in this study [116], [151]:

- Use of short conductor lengths from the controller to the gate of the IGBT power switches.
- Use of shielded or twisted conductors for the control circuits links.
- Minimal use of unshielded leads.
- Use of heat sinks for the mounting of the IGBT power switches for efficient dissipation of generated heat by natural convection.

Also, the following "*good design practices*" are used to achieve electrical safety because of the voltage levels involved in the switching operation [150]:

- Sufficient spacing between uninsulated live parts of components: This is necessary for electrical safety and voltage isolation. The use of proper *creepage distance* (shortest path between two conductive materials measured along the surface of an insulator between them) and *clearance distance* (shortest distance between two conductive materials measured through air) is adequate in this regard.
- Provision of thermal interface materials and use of isolation foils: To achieve proper thermal management that allows adequate power dissipation, the IGBT power switches are mounted on heatsinks. An isolation material in the form of isolation foil is inserted between the heatsink and the component. This foil provides both isolation and thermal interface functionalities.
- Proper use of assembly methods: The methods by which the discrete power devices (power switches, inductors, diodes, and capacitors) are assembled impact the electrical safety and isolation level of the finished power converter. Hence the following assembly methods are used: a) screw-mounting assembly method for the

IGBT power switches to the heatsinks with the integrated isolation foils; and b) soldering for the discrete components to leads and to banana sockets.

The above considerations are applied in the construction of the power converters. For the construction of the SEPIC converter, a 600V/60A IGBT (IRGP35B60PDPbF) by International Rectifier is used [152]. The IGBT with integrated freewheeling diode is mounted on a T0-220 heatsink with thermal insulation (isolation foil) in-between. The T0-220 heatsink is chosen for proper dissipation of the heat losses caused by both the conduction and the switching processes. The generated heated is dissipated using natural convection process. With the marking and drilling of the mounting holes done, the IGBT, the inductors and capacitors are mounted on a 4mm-thick Perspex project box using banana sockets. Figure 7.15 shows the constructed power board of the SEPIC converter.

Similarly, the H-bridge based inverter to produce 240V ac at 50 Hz is constructed using the same 600V/60A IGBTs and housed on a separate perspex project box as shown in Fig. 7.16. Figure 7.16 is configured such that it can be used for either single-phase operation (as in this project) or for three-phase operation, if desired. Also, the bidirectional dc-dc converter is constructed on a separate board, Fig. 7.17.

Table 7.1 shows the major components used for the construction of the three power converters.

Fig. 7.15: Prototype of the SEPIC converter in perspex housing.

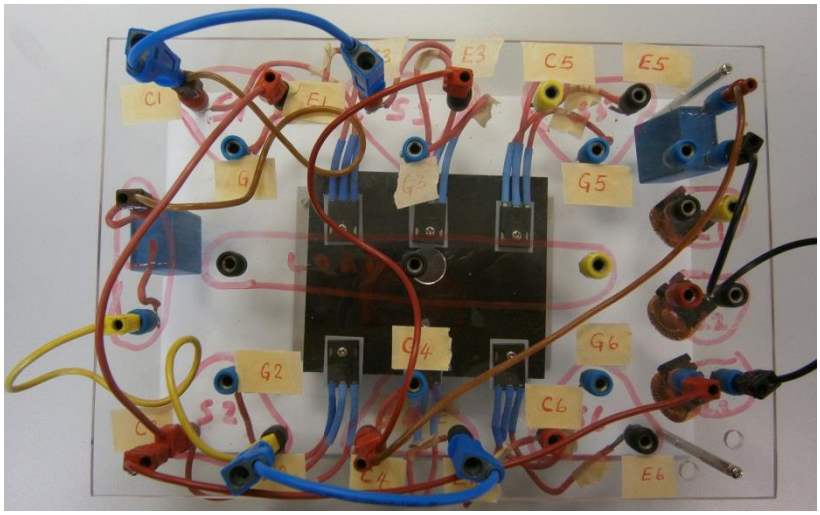

Fig. 7.16: Prototype of the inverter board in perspex housing.

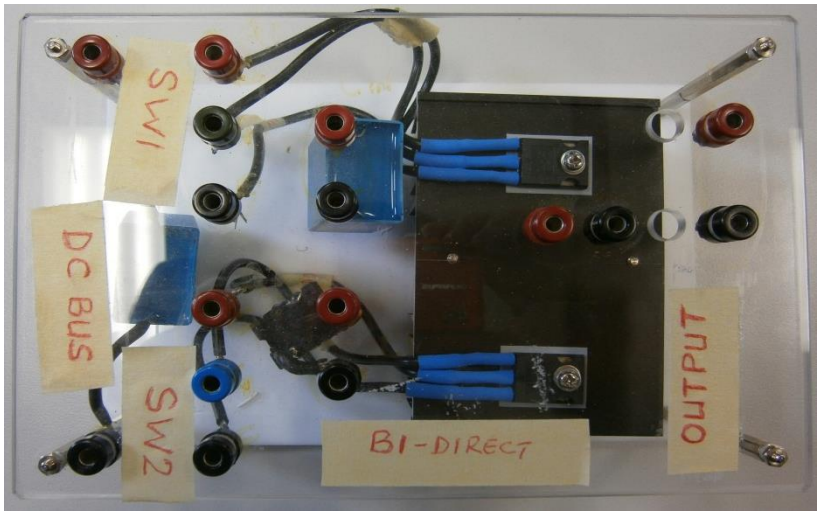

Fig. 7.17: Prototype of the bidirectional dc-dc converter.

Table 7.1: Major components used for the power converters.

	SEPIC Converter	
S/N	Component	Value
1.	IGBT Power Switch (IRGP35B60PDPbF): with co-pack diode.	600V/60A.
2.	Inductor, L1	100µH.
3.	Inductor, L2	1000µH.
4.	Coupling Capacitor, C1	6.8 µF.
5.	Output Capacitor	6.8 µH, 400VDC, ESR: 3.7mΩ.
6.	Input Capacitor	120µF, 250VDC
Bidirectional DC-DC Converter		
7.	IGBT Power Switch (IRGP35B60PDPbF): with co-pack diode.	600V/60A.
8.	Inductor, L1	330 µH
9.	Output Capacitor	4.0 µF, 100V.
DC-AC Converter (Inverter)		
10.	IGBT Power Switches: same as in the SEPIC converter	600V/60A.
11.	Filter Capacitor	70 µF, 350VAC.
12.	Filter Inductor	18mH, 250VAC.

7.4 System Integration and Experimental Setup

7.4.1 Graphical User Interface Development in ControlDesk Software

For real-time implementation of the entire PV power system, the Simulink control models are interfaced with the real-time function blocks. With this interfacing, the following control algorithms are then implemented:

- MPPT control implementation via the SEPIC converter.
- Voltage and current control of the converters.
- Unipolar sinusoidal pulse width modulation of the inverter.

- Protection functions: overcurrent and overvoltage protection of the power switch.

The automatic code generation feature of the Real Time Workshop (RTW) subset of MATLAB enables easy conversion of these codes into the equivalent C codes. The C codes are subsequently compiled into executable codes, assembled, linked and then downloaded to the DS1104 controller.

With the codes already downloaded into the embedded controller, the ControlDesk software (software for DS1104 controller) on the host computer is then used for the development of the graphical user interface (GUI). The GUI enables real time interaction with the embedded DSP controller and allows the user to: 1) change system parameters and, 2) display and monitor waveforms on the host computer. Via the GUI of the ControlDesk, the parameters of the various PI (proportional-integral) blocks are tuned in real time to achieve desired output values. Because of the frequency limitations of the controller, a switching frequency of 15 kHz is chosen for the converters and a deadtime of 500 nanoseconds chosen for the inverter.

7.4.2 Installation of Solar Panels

To achieve optimum energy harvesting from sunlight by the solar array, the exact location of the array in the immediate vicinity of the laboratory is critical. The exact position of the array (group of solar panels) is location-specific. It dependents on the following factors [153]: 1) orientation – facing geographical north or south, 2) angle of tilt from the horizontal surface, 3) shading avoidance from trees and buildings and, 4) length of cable runs to minimize voltage drop between the array and the converters.

To minimize losses from shading, the following sets of rules are adopted [153]:

- Avoiding all obvious obstructions, like trees, buildings or TV aerials so that the array is in no way obstructed.
- Avoiding high northern obstruction. This is because in the southern hemisphere, over a daily cycle, the sun rises roughly in the east, sets roughly in the west and spends most of its time in the northern part of the sky.
- Avoiding obstructions in the north-eastern and north western part of the array to avoid encroaching into the solar window.
- Maximising the array mounting height.

Also, a general rule of thumb that the array should face north in southern hemisphere, and that the minimum angle of tilt with the horizontal should be at least 10 degrees to ensure self-cleaning is adopted. A clinometer is used to get this angle. Moreover, all installations are done in accordance with the relevant Australian standard for PV installation - AS 4509. The two-panel array used is based on the BP 380 solar array, as in the simulation studies.

7.4.3 Experimental Setup

In order to validate the simulation results discussed in the previous chapters, an experimental setup is arranged. The experimental setup for this PV power system is shown in Fig. 7.18, and specifically includes the following key components:

- The DS1104 hardware/software platform: for implementation of the control algorithms to generate the logic level commands for the power switches.
- The fabricated boards for data acquisition, conditioning and gate driver interfacing discussed earlier.
- Laboratory dc power supply (GPC-3030): this is needed to energise the DS1104 hardware system, the sensors, the analogue interface circuitry, and the gate driver circuits. A +5V supply is used for the DS1104 system, ±15V for the analogue circuitry and +15V for the gate driver supply.
- The constructed power converter boards: SEPIC, bidirectional dc-dc, and the inverter.
- A two-panel PV array based on the solar module: BP380, installed outside the laboratory.
- A 48V 200Ah sealed lead acid (SLA) battery bank for energy storage.
- A four channel digital storage oscilloscope (TPS 2024B by Tektronix).
- A power analyser (PM1000+ by Voltech).
- High voltage differential probe (P5200 by Tektronix).
- AC/DC current probe (A622 by Tektronix).
- A resistive load bank.

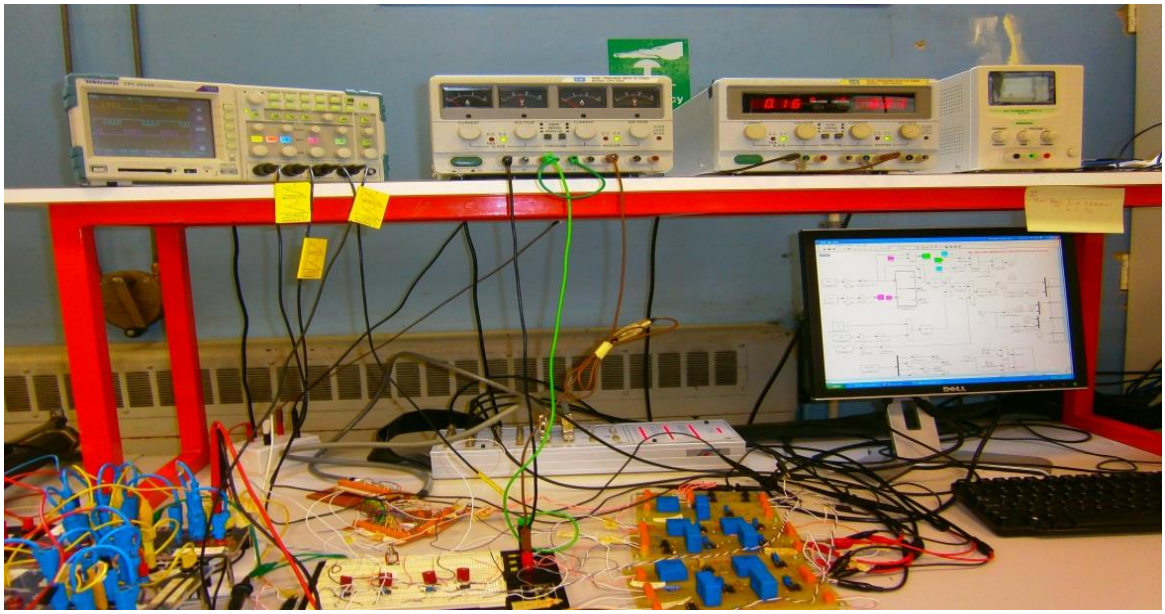

Fig.7.18: Experimental setup for the PV system

7.5 Experimental Results and Discussions

The built prototypes were tested with the controller to determine the performance of the system. The testings involved two levels:

- Unit-level testing to determine the performance of the individual subsystems and the associated control algorithms.
- System-level testing to determine the performance of the entire integrated system and the interactions of the subsystems.

The details are discussed in the subsections below.

7.5.1 Generation of Switching Pulses

Figure 7.19 shows the gating signals used to turn on the SEPIC converter based on the duty cycle generated automatically by the closed-loop operation of the DS1104 controller to maintain the desired output voltage of 180V. The topmost pulse train (yellow) is the direct logic level output of the controller (5V), while the bottom pulse train (blue) is the output of the optocoupler which has been conditioned to 15V suitable to drive the low side power switch of the SEPIC converter.

Similarly, the pulse trains for driving the two phase legs of the H-bridge based inverter are shown in Fig.7.20. The unipolar switching scheme used has generated the four pulse trains –

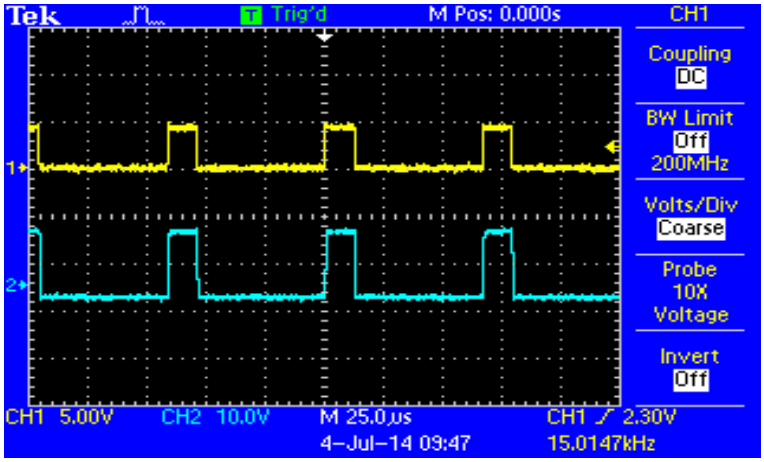

Fig.7.19: SEPIC converter gating signals.

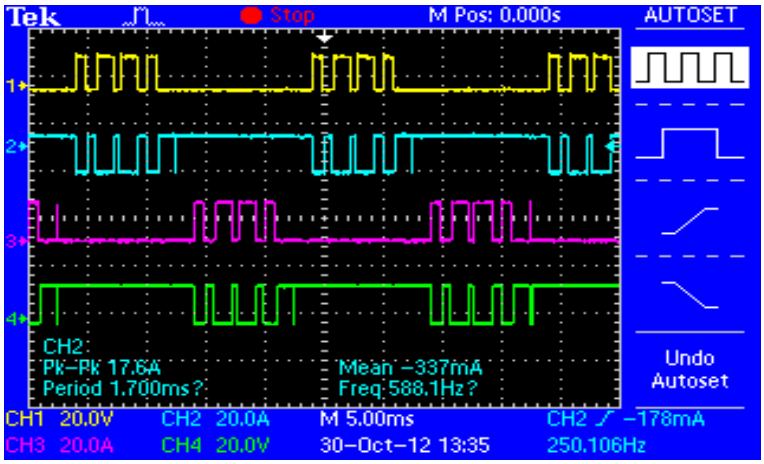

Fig. 7.20: Inverter gating signals.

two are complementary signals for each phase leg to ensure that the two switches of a phase leg are never turned on at the same time. This ensures the avoidance of the problem of shoot-through (a short circuit condition within a phase leg).

7.5.2 Effects of Changing Ambient Temperature

Changes in the ambient temperature and solar irradiation are common environmental variables that affect the performance of a photovoltaic power plant, as explained previously in chapter 2. These variables result in the intermittency and variability associated with such a photovoltaic power plant, and consequently the reliability of such plants. However, a well-designed control system is able to mitigate these problems. Fig. 7.21 shows the effects of changing ambient temperature on system performance for a given solar irradiance. For an

ambient temperature of 30°C at 600W/m^2, the array voltage is 32V while the controller maintains the dc link voltage at the desired value of 180V as in Fig. 7.21(a). In Fig. 7.21(c) for a fall in ambient temperature to 20°C at the same irradiance of 600W/m^2, the array voltage rises to 42V while the controller still regulates the dc link voltage at the desired value of 180V. This is an attestation to the ability of the controller to mitigate this problem of variability arising from changes in the environmental variable.

Fig. 7.21(b) shows the extracted maximum power of 80W from the array at an irradiance of 600W/m^2, while Fig. 7.21(d) shows the extracted maximum power at 100W for an irradiance of 800W/m^2. Thus, the control algorithm for the maximum power extraction is seen to be able to follow changes in the solar irradiation and to extract the power changes accordingly.

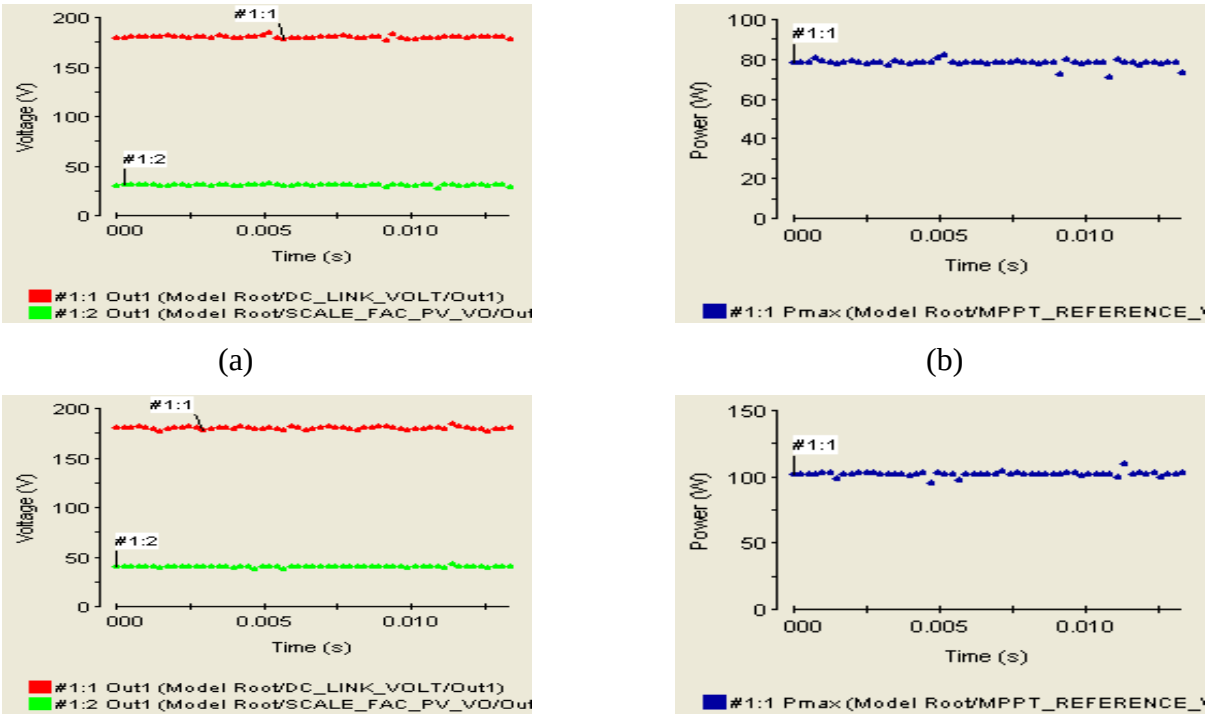

Fig. 7.21: Effects of changing ambient temperature on system performance as displayed in ControlDesk. (a) Dc link voltage (red) and array voltage (green) at an ambient temperature of 30°C and irradiance of 600W/m^2 (b) Extracted maximum power from array at 600W/m^2. (c) Dc link voltage (red) and array voltage (green) at an ambient temperature of 20°C and irradiance of 600W/m^2 (d) Extracted maximum power at 800W/m^2.

7.5.3 Operation of the Bidirectional Converter

For the mitigation of reliability problems of a photovoltaic power system, an energy storage system is often integrated. The bidirectional dc-dc converter is integrated in this work to interface the battery bank used for the energy storage function. Fig. 7.22 shows the output of the bidirectional converter in both charging and discharging modes. In Fig. 7.22(a) the converter output voltage (battery side) is maintained at 60V to charge the battery bank of 48V, while in Fig. 22(b) the converter maintains the dc link voltage at the desired value of 180V when operating in the boost mode (discharging).

Fig. 7.23 is the battery bank voltage profile during charging logged using LabView software. Comparisons of the experimental results of Figs. 7.22 and 7.23, with the simulation results of Figs. 5.11 and 5.12 in section 5.7, show that the experimental results are in agreement with the simulation results. It also shows the reliability of the battery charging algorithm adopted.

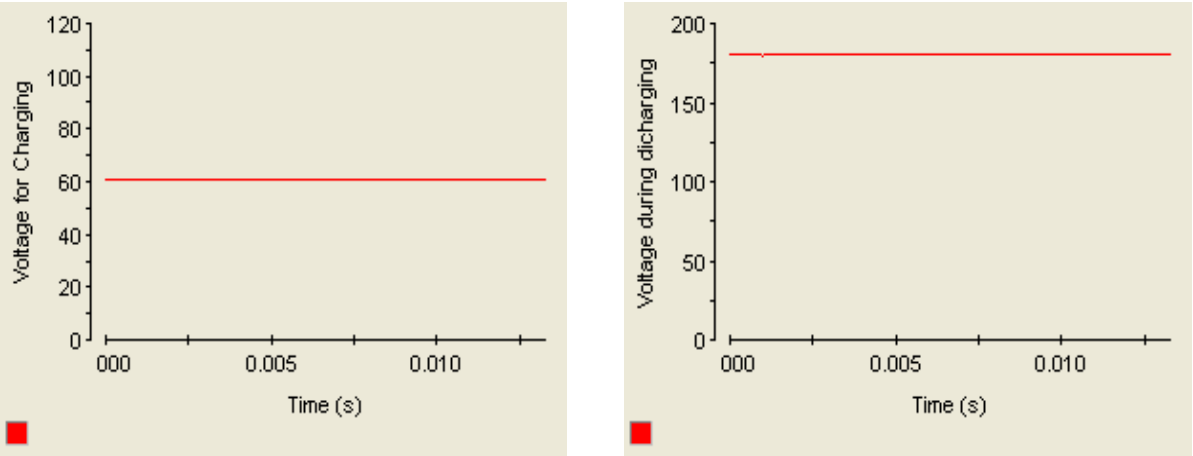

(a) (b)

Fig. 7.22**:** Output of bidirectional dc-dc converter. (a) Charging mode. (b) Discharging mode.

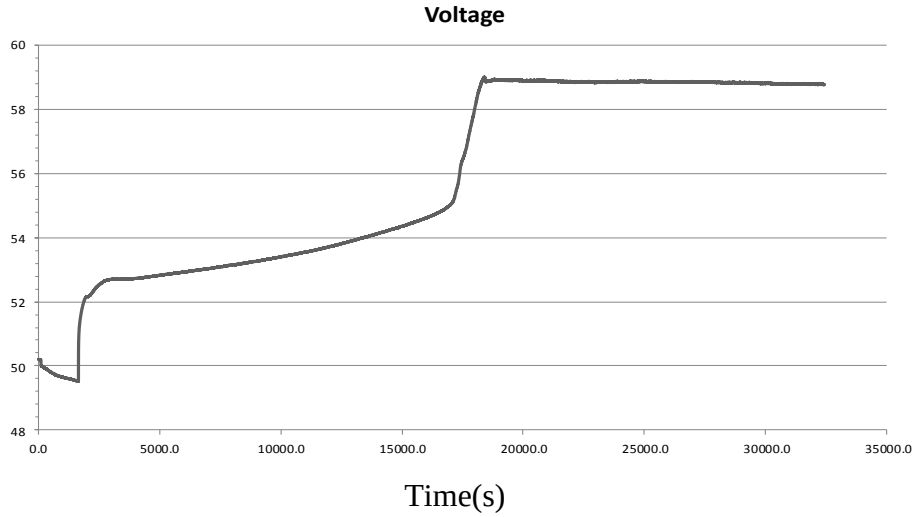

Fig. 7.23: Battery bank terminal voltage during charging: ramping up from bulk to absorption phase after load recovery captured with LabView software.

7.6 Conclusions

This chapter has presented the hardware implementation of the three power converters and their associated control algorithms presented in this study. The experimental setup is used for the validation of the simulation studies. The actual generated gating signals necessary for switching the converters and the effects of ambient temperature changes on system performance have been presented. Similarly, the practical performance of the bidirectional dc-dc converter as the interface for energy storage system has been presented. Moreover, the DS1104 DSP controller used for the study has shown its capability and flexibility in using complex control algorithms to achieve the desired performance outcomes for the converters.

It is seen from the experimental results of this chapter that the results obtained from the hardware implementation almost match those of the simulation results documented in chapters 2 through 6. Thus, the simulation results are validated.

Chapter 8

Summary and Suggestions for Future Research

8.1 Summary

The intention of this chapter is to present a summary of the work carried out so far in this study and then present the conclusions drawn, while at the same time proposing some future areas of research. This research work becomes more relevant as more and more countries in the advanced world embark on ambitious energy agendas to reduce their carbon emission and ultimately become carbon neutral by mid-century, and as engineers in such countries deploy an array of technologies to replace aging coal-fired power plants and to ensure a more sustainable energy future. The importance is even more relevant in developing nations since renewable energy is the key to unshackle their energy poverty.

This thesis has investigated the performances of some control algorithms for power converters used in a photovoltaic power plant for the conversion of solar energy into ac voltage that can be used to power ac loads such as home appliances, lighting and power tools and for possible integration into a microgrid. The PV power plant comprises a photovoltaic generator (solar array), a SEPIC converter for interfacing the solar array, a bidirectional dc-dc converter for interfacing the backup energy storage system, and a dc-ac converter for generating the necessary ac output and for interfacing to the micro grid.

In summary, the conclusions from this study are as follow:

PV Modelling and Software Tool for PV Plant Design

- A well-developed PV simulation model is an invaluable tool to the engineer in accurately predicting the performance of the PV system when deployed in operation.
- The major environmental variables affecting the PV array performance are solar irradiation and ambient temperature. While there is a linear relationship between the output current/power of the array and solar irradiation, there is an inverse linear relation between the array output voltage and the ambient temperature.
- A user-friendly design platform for standalone PV system helps the system designer not only to get the design job done in the shortest possible time, but

most importantly to accurately size the system's components using site-specific design parameters. This ensures system reliability, easy maintainability, durability and system's safety.

Regulation of the DC Link Voltage

- A well-designed control system using the current mode approach ensures a robust regulation of the output voltage of the converter regardless of changes in the input voltage variations, load changes and component's parameter variations. It also ensures good transient and steady state performance while also providing system safety since the current is also controlled.

Maximum Power Point Extraction

- Accuracy and speed of response are the two main considerations in the implementation of any reliable MPPT algorithm, since the changes in ambient temperature and solar irradiation are so unpredictable and happen so quickly. Such accuracy and speed ensure that the maximum power point is tracked irrespective of changes in weather, and thus improving the efficiency of the photovoltaic system.

Management of Energy Storage System

- The mitigation of issues of variability and intermittency of renewable power generators requires the integration of energy storage system with the associated dc-dc power converter with bidirectional power flow capabilities. A well-designed control algorithm when integrated with such a system ensures proper matching of the dc link voltage and the voltage of the energy storage system in both the discharge and charging modes of operation, while providing both over-charge and over-discharge protections. It also must ensure the required power balance between the various subsystems.

Voltage and Frequency Regulation

- To ensure the reliable delivery of ac power to consumers from the renewable energy sources, the photovoltaic inverter has to ensure that the frequency and magnitude of the generated ac voltage are within the acceptable limits. The ability to produce a perfect sinusoidal waveform with minimal distortion at the desired frequency of 50 Hz for both single-phase and three-phase operation depends on the robustness of the inverter's control system.

8.2 Contributions to Engineering Knowledge

Sustainable electricity future will depend on innovations in the following key technologies, among others, 1) energy storage, 2) renewables, 3) microgrids, 4) smart grids, 5) energy efficient schemes, 5) power converters and 6) control algorithms for power converters. The modest contributions of this thesis to such a sustainable energy future in which fossil fuels play a gradually declining role, and to the dissemination of engineering knowledge are summarized below:

- The development of an experimentally validated simulation model for photovoltaic module suitable for characterisation studies, so that better insight of the PV system's behaviour is gained.
- Development of a complete simulation model with associated controllers for a photovoltaic power plant incorporating the PV array, the SEPIC converter, the bidirectional converter, the inverter, and the backup battery energy storage system.
- Development of unique control algorithms for maximum power point tracking, dc and ac voltage and current regulation, and battery management for the backup energy storage system. These algorithms make it easier for the system to mitigate the effects of the inevitable variations in solar power.
- Simplified design approaches to both the SEPIC dc-dc converter and the bidirectional dc-dc converter. Such converters are increasing becoming invaluable in the harnessing of photovoltaic power.
- Physical implementations of the three interfacing converters and the associated controllers. Such implementations help in bridging the knowledge gap between simulation results and experimental results and to help in visualisation of the PV system in real time.
- Better understanding of PV subsystems integration issues. Such knowledge helps engineers to understand and predict the perturbations of the individual subsystems on the grid and for effective integration of distributed generation to the central grid.
- User-friendly design platform for the sizing of PV standalone PV power plants. Such design platforms not only hasten the design process, but also ensure the deployment of reliable, safe and cost-competitive PV power plants.
- Improved understanding of the control of both single-phase and three-phase photovoltaic inverters.

8.3 Suggestions for Future Research

Despite the achievement of some promising results that help in better understanding of photovoltaic power systems, the work done in this thesis may be further improved via the following approaches:

- Research on incorporating a multi-chemistry charging algorithm for the backup energy storage system so that any type of battery would be used.
- Research on the inclusion of a transformerless inverter topology to achieve reduction in physical size of the entire photovoltaic system.
- Research on using the developed system as a practical platform for the comparison of the performance of different maximum power point tracking techniques.
- Implementation and incorporation of an MPPT method capable of tracking maximum power point under shading conditions.
- Studying of the effects of PV cell parameter variations on the MPPT performance.
- Extension of the control strategy to grid connected PV system with smart grid functionality.
- Improvement of the control strategy for a hybrid system to incorporate other renewable energy sources.

References

[1] P. Gevorkian, *Large-scale Solar Power System Design: An Engineering Guide for Grid-connected Solar Power Generation*, New York: McGraw-Hill, 2011.

[2] D.Y. Goswani, F. Kreith, and J.F. Kreider, *Principles of Solar Engineering*, London: Taylor & Francis Group, 2000.

[3] T. Faunce, "Here's to hydrogen: Australia is missing the potential of solar fuels," *Engineers Australia*, vol. 85, no.5, pp. 68-69, May 2013.

[4] A. Goetzberger and V.U. Hoffmann, *Photovoltaic Solar Energy Generation*, Berlin, Germany: Springer, 2005.

[5] M.R. Patel, "Wind and Solar Power Systems: Design, Analysis, and Operation," 2nd ed., New York: CRC Press, 2006.

[6] K.H. Remmers. (2013, March). Inverter, Storage and PV System Technology: Industry Guide 2013. Solarpraxis AG, Berlin. [Online]. Available://www.pv-system-tech.com/fileadmin/user_upload/2013/pdf/InSyst13_GW-ES.pdf.

[7] K. H. Remmers, H. Kundert, & P. Fath. (2012, May).Engineering the Solar Age – Suppliers for Photovoltaics. Solarpraxis AG, Berlin. [Online]. Available: http://www.suppliers-pv.com/fileadmin/user_upload/2012/pdf/esa12_GW-ES-Screen.pdf.

[8] A. Jager-Waldau. (2013, Sept.).PV Status Report 2013. European Community, DG Joint Research Centre. Ispra (VA), Italy. [Online]. Available: http://iet.jrc.ec.europa.eu/remea/sites/remea/files/jrc-pvreport2013-web.pdf.

[9] K.H Remmers and W. Hoffman. (2013, May). PV Power Plants 2013: Industry Guide. Solarpraxis AG, Berlin. [Online]. Available: http://www.solarpraxis.de/en/publishing/industry-guidesreni/.

[10] B.B.F. Wittneben. (2012). The impact of the Fukushima nuclear accident on European energy policy. *Elsevier Journal of Environmental Science & Policy*, Vol.15. [Online]. Available: http://www.elsevier.com/locate/envsci.html.

[11] M. Bhunia, and R. Gupta, "Voltage regulation of stand-alone photovoltaic system using boost SEPIC converter with battery storage system," in Proc. *2013 IEEE Students Conference on Engineering and Systems*, pp. 1-6.

[12] J. P. Barton and D. G. Infield, "Energy storage and its use with intermittent renewable energy," *IEEE Transactions on Energy Conversion,* vol. 19, no. 2, June 2004, pp: 441 – 448.

[13] A. M. O. Haruni, A. Gargoom, M. E. Haque, and M. Negnevitsky, "Dynamic operation and control of a hybrid wind-diesel standalone power systems," *Twenty-Fifth Annual IEEE Applied Power Electronics Conference and Exposition(APEC)*, Palm Springs, California, *21-25 Feb. 2010,* pp. 162-169.

[14] A. A. Setiawan, Y. Zhao, and C. V. Nayar, "Design, economic analysis and environmental considerations of mini-grid hybrid power system with reverse osmosis desalination plant for remote areas," *Journal on Renewable Energy*, vol. 34, 2009, Pages 374–383.

[15] S. Diaf, M. Belhamel, M. Haddadi, A. Louche, "Technical and economic assessment of hybrid photovoltaic/wind system with battery storage in Corsica island," *Journal on Energy Policy*, vol. 36, 2008, pp: 743–754.

[16] M. El Mnassri, M.; A. S. Leger; "Stand alone photovoltaic solar power generation system: A case study for a remote location in Tunisia," *IEEE Power and Energy Society General Meeting*, Minneapolis, 25-29 July 2010, pages 1-4.

[17] C. Wang, and M. H. Nehrir, "Power Management of a Stand-Alone Wind/Photovoltaic/Fuel Cell Energy System," *IEEE Transaction on Energy Conversion,* vol. 23, no. 3, pp. 957-967, September 2008.

[18] K. L. Wang and P. Kundur, "Power system security assessment," *IEEE Power and Energy Magazine*, vol. 2, No. 5, September/ October, 2004, pp. 30 – 39.

[19] S. D. G. Jayasinghe, D. M. Vilathgamuwa, and U. K. Madawala, "Direct Integration of Battery Energy Storage Systems in Distributed Power Generation," *IEEE Transaction on Energy Conversion*, vol. 26, No. 2, pp. 977-685, June 2011.

[20] R. Chedid, H. Akiki, and S. Rahman, "A decision support technique for the design of hybrid solar-wind power systems," IEEE Transaction on Energy Conversion, vol. 13, no. 1, pp. 76–83, Mar. 1998.

[21] B. Borowy and Z. Salameh, “Methodology for the optimally sizing the combination of a battery bank and PV array in a wind/PV hybrid system,” IEEE Transaction on Energy Conversion., vol. 11, no. 2, pp. 367–375, Jun. 1996.

[22] J. A. Greatbanks, D. H. Popovic, M. Begovic, A. Pregelj, T. C. Green, “On optimization for security and reliability of power systems with distributed generation,” *IEEE Power Tech Conference Proceedings*, Bologna, Italy, 23-26 June, 2003.

[23] I. Ziari, G. Ledwich, A. Ghosh, and G. Platt, “Integrated distribution systems planning to improve reliability under load growth”, *IEEE Transaction on Power Delivery*, vol. 27, no. 2, April 2012, pp. 757-765.

[24] T. Markvart and L. Castaner, *Solar Cells: Materials, Manufacture and Operation*, Biddles Ltd, 2006.

[25] F. Lasnier and T.G. Ang, *Photovoltaic Engineering Handbook*, IOP Publishing Ltd, Bristol, 1990.

[26] S.R. Wenham, M.A. Green, M.E. Watt, and R. Corkish, *Applied Photovoltaics*, 2nd ed., TJ International Ltd, 2007.

[27] R.A. Messenger and J.Ventre, *Photovoltaic Systems Engineering*, 2nd ed., CRC Press, 2004.

[28] F. A. Farret and M. G. Simoes, *Integration of Alternative Sources of Energy*, Wiley & Sons, New Jersey, 2006.

[29] S.C. Krauter, *Solar Electric Power Generation-Photovoltaic Energy Systems*, Springer, 2006.

[30] P. Fairley, “Heavy metal power,” IEEE Spectrum, p.11, June 2010.

[31] H. Tsai, C. Tu and Y. Su, “Development of generalized photovoltaic model using matlab/simulink,” Proceedings of the World Congress on Engineering and Computer Science, Oct 22-24, 2008.

[32] R. Hernanz, C. Martin, Z. Belver, L. Lesaka, Z. Guerrero and P. Perez, “Modelling of photovoltaic module,” International Conference on Renewable Energies and Power Quality, Granada, Spain, March 23-25, 2010.

[33] A. E. Shahat, “PV cell module modelling & ann simulation for smart grid Applications," *Journal of theoretical and Applied Information Technology*, 2010.

[34] A. D. Hansen, P. Sorensen, L. H. Hansen and H. Binder, "Models for a Stand-Alone PV System," Riso National Laboratory, Roskilde, Dec 2000.

[35] M. G. Villalva, J.R. Gazoli and E.R. Filho, "Comprehensive approach to modeling and simulation of photovoltaic arrays," *IEEE Transactions on Power Electronics*, vol.24, no.5, May 2009.

[36] P. Maffezzoni, L. Codecasa and D. D'Amore, "Modeling and simulation of a hybrid photovoltaic module equipped with a heat-recovery system," *IEEE Transactions on Industrial Electronics*, vol.56, no.11, Nov.2009.

[37] J. Wiles, "Designing and installing safe, durable and cost-effective photovoltaic power systems" in *Proceedings of IEEE 4th world photovoltaic energy conference*, Waikoloa, Hawaii, pp. 2355-2358, 2006.

[38] H. Matsukawa, P. Pimentel, T. Izawa, S. Ike, H. Koizumi, and K. Kurokawa, "An integrated design software for photovoltaic systems" in *Proceedings of IEEE 3rd world photovoltaic energy conversion conference*, Osaka, Japan, pp. 1930-1933, 2003.

[39] T. Kerekes, E. Koutroulis, D. Sera, R. Teodorescu, and M. Katsanevakis, 'An optimization method for designing large PV plants', *IEEE Transactions on Photovoltaics*, Vol. 3, No. 2, pp.814-22, 2013.

[40] P. Monsour, *Photovoltaic Power Systems Resource Book*, NUER02 edition, Renewable Energy Centre, Brisbane, 2003.

[41] Y. Ru, J. Kleissl, and S. Martinez, "Storage size determination for grid-connected photovoltaic systems", *IEEE Transactions on Sustainable Energy*, Vol. 4, No.1, pp. 68-81, 2013.

[42] A. Purvins, I.T Papaioannou, and L. Debarberis, "Application of battery-based storage system in household-demand smoothening in electricity-distribution grids", *Journal of Energy Conversion & Management*, Vol. 65, pp.272- 84, 2013.

[43] K.M. Tsang, and W.L. Chan, (2013) "State of health detection for Lithium ion batteries in photovoltaic system", *Journal of Energy Conversion & Management*, vol. 65, pp.7-12, 2013.

[44] G.M Masters, *Renewable and Efficient Electric Power Systems*, John Wiley, New Jersey, 2004.

[45] A. Labouret, and M. Villoz, *Solar Photovoltaic Energy*, IET, London, 2010.

[46] P. Monsour, *Hybrid Energy Systems Resource Book*, Renewable Energy Centre, Brisbane, 2003.

[47] W. Kramer, S. Chakraborty, B. Kroposki, and H. Thomas, "Advanced power electronic interfaces for distributed energy systems. Part 1: Systems and topologies," National Renewable Energy Lab., Golden, CO, Tech. Rep. NREL/TP-581-42672, March 2008.

[48] J.M. Carrasco, L.G. Franquelo, J.T. Bialasiewicz, E. Galvan, R.C. Portillo, M. Guisado, A.M. Prats, J.I. Leon, and N. Moreno-Alfonso, "Power-electronic systems for the grid integration of renewable energy sources: a survey," *IEEE Trans. Industrial Electronics*, vol. 53, no. 4, pp. 1002-1016, August, 2006.

[49] M.H. Rashid, *Power Electronics: Circuits, Devices, and Applications*, 3rd ed., Pearson Education Inc., Upper Saddle River, NJ, USA, 2004.

[50] S. Winder, *Power Supplies for LED Driving*, Elesevier Inc., Oxford, 2008.

[51] D.W. Hart, *Power Electronics*, McGraw-Hill, New York, 2011.

[52] N. Kularatna, *Power Electronics Design Handbook: Low-Power Components and Applications*, Butterworth-Heinemann, Woburn, USA, 1998.

[53] R. Ridley, "Analyzing the Sepic converter," *Power Systems Design Europe*, pp. 14-18, Nov. 2006.

[54] R.W. Erickson & D. Maksimovic, *Fundamentals of Power Electronics*, 2nd ed., Kluwer Academic Publishers, Massachussetts, USA, 2001.

[55] J. Falin. (2008, 4Q). Designing dc/dc converters based on the SEPIC topology. Texas Instruments, Dallas, Texas. [Online]. Available: http://www.ti.com/lit/an/slyt309/slyt309.pdf.

[56] A. Ezhilarasi and M. Ramaswamy, "A strategy for assessing the stability of SEPIC converter," *Intl Journal of Eng. Science & Tech*, vol. 2, no. 5, pp. 866-877, 2010.

[57] N.S. Nise, *Control Systems Engineering*, 3rd ed., John Wiley & Sons, Inc., New York, 2000.

[58] S. Buso & P. Mattavelli, *Digital Control in Power Electronics*, Morgan & Claypool, Nebraska-Lincoln, USA, 2006.

[59] S.J. Chiang, H. J. Shieh, and M.C. Chen, "Modelling and control of PV charger system with SEPIC converter," IEEE Trans. Industrial Electronics, vol. 56, no. 11, pp. 4344-4353, Nov. 2009.

[60] K.M. Tsang and W.L. Chan, "Cascade controller for dc/dc buck convertor," in *IEE Proc. Electr. Power Appl*. 2005, pp. 827-831.

[61] C. Restrepo, J. Calvente, A. Cid-Pastor, A. E. Aroudi, and R. Giral, "A noninverting buck-boost dc-dc switching converter with high efficiency and wide bandwidth," *IEEE Trans. Power Electronics*, vol. 26, no. 9, pp. 2490-2503, Sept. 2011.

[62] M. Veerachary, "Power tracking for nonlinear pv sources with coupled inductor SEPIC converter," *IEEE Trans. Aerospace & Electronic Systems*, vol.41, no. 3, pp. 1019-1029, July 2005.

[63] A. Pandey, N. Dasgupta, and A. K. Mukerjee, "High-performance algorithms for drift avoidance and fast tracking in solar mppt systems," *IEEE Trans. Energy Conversion*, vol. 23, no. 2, June 2008.

[64] K. N. Hasan, "Control of power electronic interfaces for photovoltaic power systems," M.S thesis, Dept. Electr. Eng., Univ. of Tasmania, Hobart, Australia, 2009.

[65] S. Jianping and L. Xiaozheng, "A new mppt control strategy," in *Proc. Intl Conf. on Mechatronic Science, Electric Eng. & Computer (MEC)*, 2011, pp. 239-242.

[66] B. Liu, S. Duan, F. Liu, and P. Xu, "Analysis and improvement of maximum power point tracking algorithm based on incremental conductance method for photovoltaic array," in *Proc. 7th Intl Conf. on Power Electronics & Drives Systems*, 2007, pp. 637-641.

[67] T. Esram and P. L. Chapman, "Comparison of photovoltaic array maximum power point tracking techniques," *IEEE Transactions on Energy Conversion*, vol. 22, no. 2, June 2007, pp. 439–449.

[68] M. K. Hossain and M. H. Ali, "Overview on maximum power point tracking (mppt) techniques for photovoltaic power systems*," International Review of Electrical Engineering (IREE),* vol. 8, no. 4, August 2013, pp. 1363-1378.

[69] R. Faranda and S. Leva, "Energy comparison of mppt techniques for photovoltaic systems," *WSEAS Trans. Power Systems*, vol. 3, issue 6, pp. 446-455, June 2008.

[70] H. Cha and S. Lee, "Design and implementation of photovoltaic power conditioning system using a current based maximum power point tracking," in *Proc. IEEE Ind. Applications Society Annual Meeting*, 2008, pp.1-5.

[71] A. K. Abdelsalam, A. M. Massoud, S. Ahmed, and P. Enjeti, "High performance adaptive perturb and observe mppt technique for photovoltaic based microgrids, *IEEE Trans. Power Electronics*, vol. 26, no.4, pp.1010-1021, April 2011.

[72] M.G. Villalva and F.E. Ruppert, "Analysis and simulation of the P&O mppt algorithm using the linearized PV array model," in *Proc. 35th Annual Conf. IEEE Industrial Electronics*, 2009, pp. 231-236.

[73] N. Fermia, G. Petrone, G. Spagnuolo, and M. Vitelli, "Optimization of perturb and observe maximum power point tracking method," *IEEE Trans. Power Electronics*, vol. 20, no. 4, pp.963-973, July 2005.

[74] N. Femia, D. Granozio, G. Petrone, G. Spagnuolo, and M. Vitelli, "Predictive and adaptive mppt perturb and observe method," *IEEE Trans. Aerospace & Electronic Systems*, vol. 43, no. 3, July 2007.

[75] A. Safari and S. Mekhilef, "Incremental conductance mppt method for pv systems," in *Proc. Canadian Conf. on Electrical & Computer Engineering*, 2011, pp. 000345-000347.

[76] W. Ping, D. Hui, D. Changyu, and Q. Shengbiao, "An improved mppt algorithm based on traditional incremental conductance method," in *Proc. 4th Intl Conf. on Power Electronics Systems & Applications (PESA)*, 2011, pp. 1-4.

[77] D. Menniti, A. Burgio, N. Sorrentino, A. Pinnarelli, and G. Brusco, "An incremental conductance method with variable step size for mppt: design and implementation," in *Proc. 10th Intl Conf. on Electrical Power Quality & Utilisation*, Lodz, Poland, 2009, pp. 1-5.

[78] Z. Yan, L. Fei, Y. Jinjun, and D. Shanxu, "Study on realizing mppt by improved incremental conductance method with variable step-size," in *Proc. IEEE 3rd Conf. on Industrial Electronics & Applications*, 2008, pp.547-550.

[79] Y. Xiong, S. Qian, and J. Xu, "Research on constant voltage with incremental conductance mppt method," *in Proc. Asia-Pacific Power & Energy Engineering Conf. (APPEEC)*, 2012, pp.1-4.

[80] J. Li and H. Wang, "A novel stand-alone pv generation system based on variable step size inc mppt and svpwm control," in *Proc. IEEE 6th Intl Conf. on Power Electronics & Motion Control*, 2009, pp. 2155-2160.

[81] A. Safari and S. Mekhilef, "Simulation and hardware implementation of incremental conductance mppt with direct control method using Cuk converter," *IEEE Trans. Ind. Electronics*, vol. 58, no. 4, pp. 1154-1161, April 2011.

[82] T. Esram, J.W. Kimball, P. T. Krein, P.L. Chapman, and P. Midya, "Dynamic maximum power point tracking of photovoltaic arrays using ripple correlation control," *IEEE Trans. Power Electronics*, vol. 21, no. 5, pp. 1282-1291, Sept. 2006.

[83] A. M. Bazzi and P. T. Krein, "Ripple correlation control: an extremum seeking control perspective for real-time optimization," *IEEE Trans. Power Electronics*, vol. 29, no. 2, pp. 988-995, Feb. 2014.

[84] J. W. Kimball and P.T. Krein, "Digital ripple correlation control for photovoltaic applications," in *Proc. Power Electronics Specialists Conf*., 2007, pp. 1690-1694.

[85] G. Zhou, J. Xu and J. Wang, "Constant-frequency peak-ripple-based control of buck converter in CCM: review, unification, and duality," *IEEE Transactions on Industrial Electronics*, vol. 61, no. 3, pp.1280-1291, March 2014.

[86] Y. R. Yang, "A fuzzy logic controller for maximum power point tracking with 8-bit microcontroller," in Proc. *IEEE Industrial Electronics Society Annual Conference*, 2010, pp. 2895-2900.

[87] B. N. Alajimi, K. H. Ahmed, S. J. Finney, and B.W. Williams, "Fuzzy logic controlled approach of a modified hill climbing method for maximum power point in microgrid stand-alone photovoltaic system," *IEEE Trans. Power Electronics*, vol.26, no.4, pp. 1022-1030, April 2011.

[88] C. Cecati, F. Ciancetta, and P. Siano, "A multilevel inverter for photovoltaic systems with fuzzy logic control," *IEEE Trans. Industr. Electronics*, vol. 57, no. 12, pp. 4115-4125, Dec., 2010.

[89] K. Wu, “Switch-mode Power Converters: Design and Analysis,” San Diego, USA: Elsevier Academic Press, 2006.

[90] Y. Yan, F.C. Lee, P. Mattavelli, and P. Liu, “I^2 Average current mode control for switching converters,” *IEEE Trans. Power Electronics*, vol. 29, no. 4, pp. 2027-2036, April 2014.

[91] Y. Yan, F.C. Lee and P. Mattavelli, “Analysis and design of average current mode control using a describing-function-based equivalent circuit model,” *IEEE Transactions on Power Electronics*, vol. 28, no. 10, pp. 4732-4741, Oct. 2013.

[92] N.D. Ghatpande and A. Anand, “50W dc-dc converter-cascaded buck current fed push-pull topology with average current mode control,” *IEEE International Conference on Power Electronics, Drives and Energy Systems*, 2012.

[93] B. Choi, W. Lim, S. Choi, and J. Sun, “Comparative performance evaluation of current-mode control schemes adapted to asymmetrically driven bridge-type pulse width modulated dc-dc converters,” *IEEE Trans. Industrial Electronics*, vol. 55, no. 5, pp. 2033-2042, May 2008.

[94] C. Restrepo, T. Konjedic, J. Calvente, M. Milanovic, and R. Giral, “Fast transitions between current control loops of the coupled-inductor buck-boost dc-dc switching converter,” *IEEE Trans. Power Electronics*, vol. 28, no. 8, pp. 3648-3652, Aug., 2013.

[95] M. Bragard, N. Soltau, S. Thomas, and R. W. De Doncker, “The balance of renewable sources and user demands in grids: power electronics for modular battery energy storage systems,” in Proc.2010 IEEE Trans. Power Electronics, vol. 26, pp. 3049-3056.

[96] L. A. Barroso, H. Rudnick, F. Sensusfuss, and P. Linares, “The green effect,” *IEEE Power & Energy Magazine*, vol. 8, pp. 22-35, Sep. /Oct., 2010.

[97] D. Lew, G. Brinkman, N. Kumar, S. Lefton, G. Jordan, and S. Venkataraman, “Finding flexibility: cycling the conventional fleet,” *IEEE Power & Energy Magazine*, vol. 11, no. 6, Nov/Dec., 2013.

[98] S. C. Smith, P. K. Sen, B. Kroposki, and K. Malmedal, “Renewable energy and energy storage systems in rural electrical power systems: issues, challenges and applications guidelines,” in Proc. 2010 IEEE Rural Electric Power Conf., pp.B4-B4-7.

[99] A. Nasiri, “Integrating energy storage with renewable energy systems,” in Proc. 2008 *IEEE Industrial Electronics Conf.*, pp. 17-18.

[100] D.T. Ton, C.J. Hanley, G.H. Peek, and J.D. Boyes, “Solar energy grid integration systems – energy storage (SEGIS – ES),” Sandia National Laboratories, USA. Rep. SAND2008-4247, July 2008.

[101] A. Nourai and C. Schafer, “Changing the electricity game,” *IEEE Power & Energy Magazine*, pp. 42-47, July/Aug., 2009.

[102] T. Moore and J. Douglas. (Spring 2006). Energy Storage: big opportunities on a smaller scale. EPRI.

[103] S. Vazquez, S. M. Lukic, E. Galvan, L. G. Franquelo, and J. M. Carrasco, “Energy storage systems for transport and grid applications,” in Proc. 2010 IEEE Trans. Industrial Electronics, vol. 57, no. 12, pp. 3881-3895.

[104] S.T. Kim, B.K. Kang, S.H. Bae, and J.W. Park, “Application of SMES and grid code compliance to wind/photovoltaic generation system,” *IEEE Transactions on Applied Superconductivity*, vol. 23, no. 3, June 2013.

[105] E. Koutroulis, and K. Kalaitzakis, “Novel battery charging regulation system for photovoltaic applications,” *IEEE Trans. Electric Power Applications*, vol.151, no. 2, pp.191-197, March 2004.

[106] Electropaedia. Battery and energy technologies. [Online]. Available: http://www.mpoweruk.com/nickel_iron

[107] J. McDowall, P. Biensan, and M. Broussely, “Industrial lithium ion battery safety-what are the trade-offs?,” in Proc. 2007 IEEE Telecommunications Energy Conf., pp. 701-707.

[108] A. Nourai, “Large-scale electricity storage technologies for energy management,” in Proc. 2002 *IEEE Power Engineering Society Summer Meeting*, pp. 310-315.

[109] A. Bito, “Overview of the sodium-sulfur battery for the IEEE stationary battery committee,” in Proc. 2005 *IEEE Power Engineering Society General Meeting*, pp.1-4.

[110] B. Tamyurek, D. K. Nichols, and H. T. Vollkommer, “Sodium sulfur battery applications,” in Proc. 2001 IEEE Power Engineering Society General Meeting, pp. 2323-2324.

[111] London Research International Ltd. Survey of energy storage options in Europe. [Online]. Available: http://www.londonresearchinternationa.com.

[112] J.M. Miller, *Ultracapacitor Applications*, London: The Institution of Engineering & Technology, 2011.

[113] J. Arai, K. Iba, T. Funabashi, Y. Nakanishi, K. Koyanagi, and R. Yokoyama, "Power Electronics and its application to renewable energy in Japan," *IEEE Circuits and Systems Magazine*, vol. 8, no. 3, 2008.

[114] R.G. Lawrence, K.L. Craven, and G.D. Nichols, "Flywheel UPS: an economical energy storage device that bridges the gap caused by voltage sags and temporary voltage loss," *IEEE Industry Applications Magazine*, May/June, 2003.

[115] J. Zhang, "Bidirectional dc-dc power converter design optimization, modelling and control," PhD. dissertation, Dept. Elect. Eng., Virginia Polytechnic Institute & University, 2008.

[116] N. Mohan, T.M. Undeland, and W.P. Robbins, *Power Electronics: Converters, Applications, and Design*, 3rd ed. Hoboken, NJ: John Wiley & Sons, 2003.

[117] P. Pany, R.K. Singh, and R.K. Tripathi, "Bidirectional dc-dc converter fed drive for electric vehicle system," I*ntl. Journal of Eng., Science & Tech*., vol. 3, no. 3, pp. 101-110, April 2011.

[118] B. Hauke, "Basic Calculation of a Buck Converter's Power Stage," Texas Instruments, Dallas, Texas, Tech. Rep. SLVA477, Dec. 2011.

[119] B. Hauke, "Basic Calculation of a Boost Converter's Power Stage," Texas Instruments, Dallas, Texas, Tech. Rep. SLVA372B, July. 2010.

[120] C. A. Hill, M. C. Such, D. Chen, J. Gonzalez, and W. M. Grady, "Battery energy storage for enabling integration of distributed solar power generation*," IEEE Trans. Smart Grid*, vol. 3, no. 2, pp. 850-857, June 2012.

[121] IEA PVPS Task 3 (2004). *Management of Batteries Used in Stand-Alone PV Power Supply Systems*. International Energy Agency. [Online]. Available: http://www.iea-pvps.org.

[122] L. Freris and D. Infield, *Renewable Energy in Power Systems*, London: John Wiley & Sons, 2008.

[123] A. Keyhani, *Design of Smart Power Grid Renewable Energy Systems*, New Jersey: John Wiley & Sons, 2011.

[124] D. G. Holmes and T. A. Lipo, *Pulse Width Modulation for Power Converters: Principles and Practice*, Piscataway, New Jersey: IEEE Press, 2003.

[125] R. Teodorescu, M. Liserre, and P. Rodriguez, *Grid Converters for Photovoltaic and Wind Power Systems*, West Sussex: John Wiley & Sons, 2011.

[126] A. Khaligh, and O. C. Onar, *Energy Harvesting: Solar, Wind, and Ocean Energy Conversion Systems*, New York: Taylor & Francis Group, 2010.

[127] F. Blaabjerg. (2010). Power Electronics in Renewable Energy Systems. Institute of Energy Technology, Aalborg University, Denmark. [Online]. Available: //www.icit2010.usm.cl/doc/plenary/blaabjerg.pdf.

[128] R. Gonzalez, J. Lopez, P. Sanchis, and L. Marroyo, "Transformerless inverter for single-phase photovoltaic systems," *IEEE Trans. Power Electronics*, vol. 22, no. 2, pp. 693-697, March 2007.

[129] B. Gu, J. Dominic, J. Lai, C. Chen, T. Labella, and B. Chen, "High reliability and efficiency single-phase transformerless inverter grid-connected photovoltaic systems," *IEEE Trans. Power Electronics*, vol.28, no. 5, pp. 2235-2245, May 2013.

[130] S.V Araujo, P. Zacharias, and R. Mallwitz, "High efficient single-phase Transformerless inverters for grid-connected photovoltaic systems," *IEEE Trans. Industrial Electronics*, vol. 57, no. 9, pp. 3118-3128, Sept 2010.

[131] B. Wu, Y. Lang, N. Zargari and S. Kouro, Power Conversion and Control of Wind Energy Systems, John Wiley and Sons, 2011.

[132] F. Blaabjerg, R. Teodorescu, M. Liserre, and A. V. Timbus, "Overview of control and grid synchronization for distributed power generation systems," *IEEE Transactions on Industrial Electronics*, vol. 53, pp. 1398–1409, 2006.

[133] K. J. Astrom and T. Hagglund, *PID controllers: Theory, Design and Tuning.* Research Triangle Park, NC: Instrument Society of America, 1995.

[134] P.C. Krause, O. Wasynczuk and S. D Sudhoff, "Analysis of Electric Machinery", IEEE press, New York, 2002.

[135] *IEEE Standard for Interconnecting Distributed Resources with Electric Power Systems*, IEEE Standard 1547, 2003.

[136] R.C. Dugan, T. S. Key, and G.J. Ball, "Distributed resources standards," *IEEE Industry Applications Magazine*, vol. 12, no. 1, pp. 27-34, Feb. 2006.

[137] *IEEE Recommended Practice for Utility Interface of Photovoltaic (PV) Systems*, IEEE Standards 929, 2000.

[138] Photovoltaic *(PV) Systems – Characteristics of the Utility Interface*, IEC 61727 Ed.2, 2004.

[139] *Automatic Disconnection Device between a Generator and the Public Low-Voltage Grid*, VDE V 0126-1-1, 2006.

[140] *Electromagnetic Compatibility (EMC) – Part 3-2: Limits for Harmonic Current Emission (Equipment input Currents ≤ 16A per Phase)*, IEC 61000-3-2 Ed. 3.0, Nov. 2005.

[141] *Voltage Characteristics of Public Distribution System*, Standard EN 50160, Nov. 1999.

[142] *DS1104 R&D Controller Board: Hardware Installation and Configuration*, Release 5.2, dSPACE GmbH, Paderborn, Germany, 2006.

[143] Hall Effect Sensing and Application, Honeywell Inc, Freeport, Illinois.[Online]. Available:http://sensing.honeywell.com/honeywell-sensing-sensors-magnetoresistive-hall-effect-applications-005715-2-en.pdf.

[144] *Real-Time Interface (RTI and RTI-MP): Implementation Guide*, Release 5.3, dSPACE GmbH, Paderborn, Germany, 2007.

[145] *Voltage Transducer LV 25-P, ver.18, LEM Components*, 2012. [Online]. Available: http://www. Lem.com/docs/products/lv% 2025-p.pdf.

[146] *INA118: Precision, Low Power Instrumentation Amplifier*, Burr-Brown Corporation, 1998. [Online]. Available: http://www.ti.com/lit/ds/symlink/ina118.pdf.

[147] *Current Transducer LA 55-P, ver.18, LEM Components*, 2012. [Online]. Available: http://www. Lem.com/docs/products/la% 2055-p %20e.pdf.

[148] *HCPL-3120: 2.0 Amp Output Current IGBT Gate Drive Optocoupler*, Agilent

Technologies. [Online]. Available:http://www.tme.eu/en/Document/dde4b33e41c14c71ffd1089c37a0b6d6/HCPL3120.pdf.

[149] *IR2110: High and Low Side Driver*, Data Sheet No. PD60147 rev.U, International Rectifier, California, 2005. [Online]. Available: //www. Irf.com/product-info/datasheets/data/ir2110.pdf.

[150] R. Strzelecki, and G. Benysek, *Power Electronics in Smart Electrical Energy Networks*, London: Springer, 2008.

[151] P. Wolfgang and B. Fabio, "Electrical safety and isolation in high voltage discrete components applications and design hints," Infineon Technologies, Austria, Application Note AN2012-10(V1.0), Oct. 2012.

[152] IRGP35B60PDPbF: Warp2 Series IGBT with Ultrafast Soft Recovery Diode, International Rectifier, California. [Online]. Available: http://www.irf.com/product-info/datasheets/data/irgp35b60pdpbf.pdf.

[153] ACRE, Photovoltaic Installations (NUER15): Learning Guide, 1st ed., Brisbane: Renewable Energy Centre, 2003.